

A STUDY ON THE BENEFITS OF INCLUDING NEAR-FIELD EFFECTS IN  
ACTIVE-SOURCE SURFACE WAVE DATA COLLECTION AND INTERPRETATION

---

A Thesis

presented to

the Faculty of the Graduate School

at the University of Missouri-Columbia

---

In Partial Fulfillment

of the Requirements for the Degree

Master of Science

---

by

ALEXANDER MCCASKILL

Dr. Brent Rosenblad, Thesis Supervisor

DECEMBER 2014

© Copyright by Alexander McCaskill 2014

All Rights Reserved

The undersigned, appointed by the dean of the Graduate School, have examined the thesis entitled

A STUDY ON THE BENEFITS OF INCLUDING NEAR-FIELD EFFECTS IN  
ACTIVE-SOURCE SURFACE WAVE DATA COLLECTION AND INTERPRETATION

presented by Alexander McCaskill,

a candidate for the degree of master of science,

and hereby certify that, in their opinion, it is worthy of acceptance.

---

Professor Brent L. Rosenblad

---

Professor J. Erik Loehr

---

Professor Justin Legarsky

This thesis is dedicated to

My parents,

Stuart and Patty McCaskill

whose love, encouragement, and prayers  
carried me through the entire thesis process,

My sister,

Sarah McCaskill

who was always available to talk  
when I most needed it,

My best friends,

Matthew Boraas and  
Daniela Gemignani

true friends at the deepest level,  
whom I shall never forget

and My Lord and Savior,

Jesus Christ

without whom I would not have made it even this far,  
and in whose presence "is the fullness of joy"

## ACKNOWLEDGEMENTS

I would like to express my sincere gratitude to my advisor, Dr. Brent Rosenblad, for his continual guidance, counsel, and mentoring in the development of this thesis, and, in some ways, even the development of my career. He is truly an expert in the field of surface wave analyses for geotechnical engineering, and it has been an honor to work with him closely on this research. It was Dr. Rosenblad who first introduced me to the field of soil dynamics and later inspired my interest in surface wave analyses. His enthusiasm and passion for this field is contagious. Dr. Rosenblad was also instrumental in helping me to develop a foundational understanding of surface wave analyses, as I knew very little about the subject when I first approached this research. I would also like to thank Dr. Rosenblad for his extensive and detailed revisions of my work, which made this thesis what it is today. Thanks to Dr. Rosenblad, my newfound interest in soil dynamics led me to pursue the career that I now enjoy in dynamic testing and analysis of deep foundations.

I would like to thank Dr. John Bowders for his encouragement, support, and mentoring during my time at the University of Missouri. It was Dr. Bowders who first introduced and welcomed me to the Geotechnical program, and I have always appreciated his concern and care for others. Although Dr. Bowders was unable to join the thesis committee due to an unfortunate bicycle accident (from which he is presently recovering), he has certainly influenced me for the better in a number of ways.

I would like to thank Dr. J. Erik Loehr and Dr. Justin Legarsky for joining my thesis committee. I thank Dr. Loehr, especially, for stepping in to fill Dr. Bowders' place on the committee on such short notice. Having had the opportunity to be a student in some of his classes, I also appreciate Dr. Loehr's balanced and practical outlook as both a professor and a practitioner. I have not had a chance to work closely with Dr. Legarsky, but I am very grateful for his willingness to come onboard as a committee member from outside of civil engineering.

I would like to thank Dr. Sung-ho Joh, currently of Chung-An University in South Korea, for developing the WinSASW computer program. Unlike many other programs available for surface wave analysis, Dr. Joh's program is one of the few (and perhaps the only) to contain an implementation of the 3D array inversion. With WinSASW, it was possible to perform all of the analytical work for this research (especially the simulation study) in a practical and generally efficient manner.

Finally, I would also like to thank my fellow graduate students in MUGEO for their support and perspective throughout my time at Mizzou. I particularly appreciate their support regarding the practical aspects of developing this thesis (formatting, page numbers, figure cross-references, etc.). I especially appreciate the assistance of Tayler Day and Dan Iffrig in this regard.

## TABLE OF CONTENTS

ACKNOWLEDGEMENTS.....	ii
LIST OF TABLES.....	ix
LIST OF FIGURES.....	x
ABSTRACT.....	xx
1 INTRODUCTION.....	1
1.1 Overview and Motivation .....	1
1.2 Objective and Hypotheses .....	3
1.3 Outline of Thesis .....	3
2 BACKGROUND.....	4
2.1 Introduction .....	4
2.2 Body Wave and Surface Wave Fundamentals .....	4
2.3 Active-source Surface Wave Methods for Geotechnical Engineering .....	7
2.3.1 Spectral Analysis of Surface Waves (SASW).....	9
2.3.1.1 SASW Data Collection .....	9
2.3.1.2 SASW Data Processing .....	10
2.3.1.3 SASW Inversion Analyses .....	12
2.3.2 Multi-channel Surface Wave Methods .....	13
2.3.2.1 Introduction to Multi-channel Methods.....	13
2.3.2.2 Data Collection for Multi-channel Methods .....	13
2.3.2.3 Processing of Multi-channel Data .....	14
2.3.2.4 Inversion Analyses for Multi-channel Methods.....	15
2.4 Near-field Effects in Active-source Surface Wave Measurements .....	15
2.4.1 Introduction to Near-field Effects .....	15

2.4.2	Previous Studies on Near-field Effects in SASW .....	16
2.4.3	Previous Studies on Near-field Effects in Multi-channel Methods .....	19
2.5	Previous Studies on Poisson’s Ratio and Surface Waves .....	24
2.5.1	Introduction to Poisson’s Ratio and Surface waves .....	24
2.5.2	Assessing Sensitivity of Surface Wave Measurements to Poisson’s Ratio .....	25
2.5.3	Inferring Poisson’s Ratio from Surface Wave Measurements .....	28
2.5.4	Relevance of Past Studies: Inferring Poisson’s Ratio from the Near-field .....	30
3	METHODOLOGY .....	31
3.1	Introduction .....	31
3.2	Theoretical Models .....	31
3.2.1	Two-dimensional Solution (2D).....	32
3.2.2	Three-Dimensional (3D) Complete Solution .....	33
3.3	Surface Wave Analyses with WinSASW .....	34
3.3.1	Dispersion Processing/Phase Unwrapping .....	35
3.3.2	Averaging Experimental Dispersion Data .....	37
3.3.3	Forward Modeling.....	41
3.3.4	Inversion Analysis.....	42
3.3.4.1	Global Versus Array Inversion.....	42
3.3.4.2	Starting Model Computation .....	43
3.3.4.3	Maximum Likelihood Inversion Method .....	46
3.4	Processing of Multi-channel Data .....	48
3.4.1	Definition of the Spatospectral Correlation Matrix .....	49
3.4.2	Dispersion Processing by the Frequency-Domain Beamformer (FDBF) Method... 50	
3.5	Preliminary Sensitivity Study .....	51
3.5.1	Selection of Study Profiles .....	52
3.5.2	Forward Modeling Procedures .....	52

3.6	Surface Wave Analyses with Simulated Data .....	54
3.6.1	Simulation of Ground Motions .....	55
3.6.2	Experimental Dispersion Curve Calculations .....	57
3.6.3	Inversion Analysis.....	58
3.6.4	Poisson’s Ratio Study .....	59
3.7	Surface Wave Analyses with Real Data.....	60
3.7.1	Data Collection Procedures.....	60
3.7.1.1	Field Site Location and Geology .....	60
3.7.1.2	Field Equipment .....	62
3.7.1.3	Receiver Arrays .....	65
3.7.2	Experimental Dispersion Curve Calculations .....	66
3.7.3	Inversion Analysis.....	67
4	RESULTS AND DISCUSSION – SIMULATION STUDIES .....	68
4.1	Introduction .....	68
4.2	Preliminary Sensitivity Study .....	68
4.2.1	Near-field Sensitivity Study Results .....	69
4.2.1.1	Halfspace Velocity.....	70
4.2.1.2	$V_s$ Profile Gradient .....	72
4.2.1.3	Halfspace Depth.....	74
4.2.1.4	Layer Transition Gradient .....	76
4.2.1.5	Poisson’s Ratio ( $\nu$ ) .....	78
4.2.2	Discussion of Near-field Sensitivity Study.....	83
4.3	Results from Analysis of Simulated Surface Wave Data .....	86
4.3.1	Results of Profile Recovery Study with Simulated SASW Data .....	87
4.3.1.1	Case A – Uniform $V_s$ Profile ( $\nu = 0.30$ ).....	89
4.3.1.2	Case B – Power Function $V_s$ Profile ( $\nu = 0.30$ ).....	91

4.3.1.3	Case C – Linear $V_S$ Profile ( $\nu = 0.30$ ) .....	93
4.3.1.4	Case D – Steep Power Function $V_S$ Profile ( $\nu = 0.30$ ) .....	95
4.3.1.5	Case B* – “Saturated” Power Function $V_S$ Profile ( $\nu = 0.45$ ).....	97
4.3.2	Discussion of SASW Profile Recovery Study.....	99
4.3.3	Results of Poisson’s Ratio Study with Simulated SASW Data .....	103
4.3.3.1	Case A – Uniform $V_S$ Profile ( $\nu = 0.30$ ).....	105
4.3.3.2	Case B – Power Function $V_S$ Profile ( $\nu = 0.30$ ).....	108
4.3.3.3	Case C – Linear $V_S$ Profile ( $\nu = 0.30$ ) .....	111
4.3.3.4	Case D – Steep Power Function $V_S$ Profile ( $\nu = 0.30$ ) .....	114
4.3.3.5	Case B* – “Saturated” Power Function $V_S$ Profile ( $\nu = 0.45$ ).....	117
4.3.4	Discussion of Poisson’s Ratio Study with Simulated SASW data .....	120
4.3.5	Results from Analysis of Simulated Multi-channel Data.....	123
4.3.5.1	Case A – Uniform $V_S$ Profile, ( $\nu = 0.30$ ).....	124
4.3.5.2	Case B – Power Function $V_S$ Profile ( $\nu = 0.30$ ).....	125
4.3.5.3	Case C – Linear $V_S$ Profile ( $\nu = 0.30$ ) .....	126
4.3.5.4	Case D – Steep Linear $V_S$ Profile ( $\nu = 0.30$ ).....	127
4.3.6	Discussion of Surface Wave Analysis with Simulated Multi-channel Data .....	128
5	RESULTS AND DISCUSSION – EXPERIMENTAL STUDY .....	131
5.1	Introduction .....	131
5.2	Results from the Analysis of Mississippi Embayment Data .....	131
5.2.1	Results from SASW Analyses using Alternative Near-field Filtering .....	131
5.2.2	Results of Multi-channel Analyses with Real Data.....	135
5.3	Discussion of Analyses with Mississippi Embayment Data .....	136
6	SUMMARY AND CONCLUSIONS .....	138
6.1	Summary .....	138
6.2	Conclusions .....	139

6.3	Significance and Future Research .....	140
	Appendix .....	142
A.	Variations in Halfspace (i.e. "Layer 2") Shear Wave Velocity .....	143
B.	Variations in the Shear Wave Velocity Gradient for Linear Profiles .....	148
C.	Variations in Halfspace (i.e. "Layer 2") Depth .....	153
D.	Variations in the Layer Transition Gradient .....	158
E.	Variations in Poisson's Ratio for a Uniform Profile .....	163
F.	Variations in Poisson's Ratio for a "Soft-Over-Stiff" Profile.....	168
G.	Variations in Poisson's Ratio for a Linear Profile .....	173
	REFERENCES.....	178
	VITA.....	182

LIST OF TABLES

Table	Page
Table 2.1 Summary of SASW data collection criteria used to avoid the near-field. Adapted from Yoon and Rix (2009) .....	16
Table 2.2 Comparison of (A) current practice in SWM and (B) method considered in this study.	19
Table 3.1 Summary of receiver spacings and wavelength ranges for forward modeling sensitivity study.....	54
Table 3.2 Profile information for "simulated" data used in inversion analyses. Adapted from Li (2011).....	56
Table 3.3 Summary of SASW receiver spacings used for simulated data collection .....	56
Table 3.4 Summary of SASW receiver spacings used for data collection at Site 1 (MORT).....	65
Table 3.5 Summary of multi-channel arrays used for data collection at Site 1 (MORT) .....	66
Table 4.1 Summary of Inversion Approach/Filtering Criterion Combinations for the first inversion study.....	88

## LIST OF FIGURES

Figure	Page
Figure 2.1 Schematic representation of types of body waves (left) and surface waves (right) (Exploratorium 2014) .....	4
Figure 2.2 P-wave, S-wave, and Rayleigh wave propagation in an elastic halfspace (Richart et al. 1970) .....	5
Figure 2.3 Rayleigh wave amplitude decreases significantly with depth (Richart et al. 1970) .....	6
Figure 2.4 Comparison of P-wave, S-wave and Rayleigh wave (R-Wave) velocities (Richart et al. 1970) .....	7
Figure 2.5 Data collection setups for (a) SASW and (b) multi-channel measurements and data processing (c and d) .....	8
Figure 2.6 Data collection arrangement for Spectral Analysis of Surface Waves (SASW) testing ...	9
Figure 2.7 An example of SASW source-receiver spacings using a constant centerline .....	10
Figure 2.8 SASW processing flowchart illustrating conversion of time-series data to an experimental dispersion curve .....	11
Figure 2.9 Data collection arrangement for multi-channel surface wave testing .....	14
Figure 2.10 Processing flow for multi-channel data using the phase-shift method, including (a) time-series receiver data, (b) dispersion image generation and (c) interpretation of modes. Adapted from Xu et al. (2006) .....	15
Figure 2.11 Evolution of the time history of surface displacements due to an impulse load, showing (a and b) the combination of all wave contributions in the near-field and (c) domination of surface waves in the far-field (Mera 1995) .....	17
Figure 2.12 A far-field “plane wave” solution (black triangles, at left) fits the experimental data well at short wavelengths, while significant deviations – near-field effects – are evident at longer wavelengths. The “array” approach (black circles, at right) fits a theoretical curve to the individual dispersion curve from each receiver pair, thereby accounting for both the near-field and the far-field. ....	19
Figure 2.13 Near-field effects theoretically considered as (A) the interaction of direct SV-waves and reflected P-waves and (B) a reflected SV-wave producing P and SV-waves at the surface.	

Minimum offset curves (C) are shown as a function of upper layer $V_p/V_s$ contrast and depth. Adapted from Xu et al. (2006). .....	20
Figure 2.14 Schematic representation of the Normalized Array Center (NAC) parameter for a 24 receiver array .....	21
Figure 2.15 $V_s$ Profiles used to study near-field effects for unsaturated conditions (Yoon and Rix 2009) .....	22
Figure 2.16 Normalized comparison of numerical, laboratory, and field test results. Adapted from Yoon and Rix (2009) .....	22
Figure 2.17 Minimum size and location required to truly avoid near-field effects with a multi-channel receiver array .....	23
Figure 2.18 Effect of Poisson's ratio on the near-field in terms of (A) the amount of "radiated power" in body waves and surface waves for various Poisson's ratio values, and (B) normalized curves of vertical displacement versus average radial distance from the point load source – all lines represent near-field conditions unless otherwise noted. (Mera 1995) .....	26
Figure 2.19 Normalized dispersion curves from a parametric study of source-to-first-receiver spacing ( $r$ ), receiver-to-receiver spacing ( $\Delta x$ ), and Poisson's ratio ( $\nu$ ) performed by Chen et al. (2004) .....	27
Figure 2.20 $V_s$ profiles used to study near-field effects in saturated conditions. Adapted from Li (2011) .....	28
Figure 2.21 Saturated versus unsaturated dispersion curves for the non-dispersive case (Rosenblad and Li 2011) .....	28
Figure 3.1 Example of wrapped phase plot (i.e. transfer function) imported into WinSASW for processing .....	35
Figure 3.2 Measurement settings window in WinSASW .....	36
Figure 3.3 Example of "masking out" near-field effects (left side) and poor quality data (right side) in WinSASW .....	36
Figure 3.4 Single dispersion curve from a 4m SASW spacing, as calculated from the wrapped phase plot of Figure 3.3 .....	37
Figure 3.5 Composite dispersion curve generated from SASW spacings of 4m, 10m, 20m, 40m, 80m, 160m, and 300m .....	37
Figure 3.6 Illustration of the averaging scheme used in WinSASW (Joh 1996) .....	38
Figure 3.7 User interface for experimental dispersion curve averaging in WinSASW .....	40

Figure 3.8 Global average experimental dispersion curve computed in WinSASW for the composite dispersion curve of Figure 3.5, with the parameters indicated in Figure 3.7 .....	40
Figure 3.9 Array experimental dispersion curve – with a separate average curve for each spacing – computed in WinSASW for the composite dispersion curve of Figure 3.5, with the parameters indicated in Figure 3.7.....	41
Figure 3.10 Forward modeling (a) profile parameter input and (b) theoretical dispersion curve output (red) in WinSASW.....	42
Figure 3.11 Profile parameter input windows for (a) global inversions and (b) array inversions in WinSASW .....	43
Figure 3.12 Development of Phase 1 starting model profile from experimental dispersion data (Joh 1996).....	44
Figure 3.13 Development of Phase 2 starting model profile from a Phase 1 profile (Joh 1996)...	45
Figure 3.14 Interface for starting model computation and inversion analysis in WinSASW .....	45
Figure 3.15 Selection of starting model with the lowest RMS error prior to starting an inversion analysis in WinSASW .....	46
Figure 3.16 Partial derivative matrix computation for the array inversion method (Joh 1996) ...	47
Figure 3.17 Completed maximum likelihood inversion analysis in WinSASW, showing final $V_s$ profile – the starting model is shown in Figure 3.15 .....	48
Figure 3.18 Completed maximum likelihood inversion analysis in WinSASW, showing layer resolution results – the starting model is shown in Figure 3.15.....	48
Figure 3.19 Graphical representation of a spatio-spectral correlation matrix (Yoon 2005).....	49
Figure 3.20 Example of a steered power response spectrum at a frequency of 10 Hz (Li 2011; Yoon 2005).....	51
Figure 3.21 Base case profiles and variations selected for sensitivity study .....	53
Figure 3.22 Shear wave velocity ( $V_s$ ) profiles used as “simulated” data for inversion analyses. Adapted from Li (2011).....	56
Figure 3.23 Visual representation of the SASW receiver spacings used to generate simulated data .....	56
Figure 3.24 Visual representation of the multi-channel array used to generate simulated data .	57
Figure 3.25 Examples of composite dispersion curves (for Case D) derived from four different filtering criteria .....	58

Figure 3.26 Site locations in the Mississippi Embayment – only “Site 1” data was used in this study (Bailey 2008).....	61
Figure 3.27 Google maps image of Site 1 (MORT) – the black line is the array location (Bailey 2008) .....	61
Figure 3.28 Estimated Soil Lithography at Site 1 (Bailey 2008) .....	62
Figure 3.29 An instrumented sledgehammer (PCB Piezotronics Model 086D50) was used to excite high-frequency energy (Bailey 2008) .....	63
Figure 3.30 Low frequency mobile vibrator "Liquidator" developed under the NSF-funded Network for Earthquake Engineering Simulation (NEES) Program (Bailey 2008).....	63
Figure 3.31 Mark Products L-4 High-sensitivity 1Hz Geophone (Li 2008) .....	64
Figure 3.32 Field data acquisition setup, including a VXI digital signal analyzer and a laptop computer (Li 2008).....	65
Figure 3.33 Visual representation of the SASW receiver spacings used to collect data at Site 1 (MORT).....	66
Figure 3.34 Visual representation of the multi-channel arrays used to collect data at Site 1 (MORT).....	66
Figure 4.1 Sensitivity study results derived from the 2D Plane wave solution for a simple “soft-over-stiff” profile with a variable lower layer $V_s$ .....	70
Figure 4.2 Sensitivity study results derived from the 3D solution with a traditional SASW arrangement with a 16m receiver spacing for a simple “soft-over-stiff” profile with a variable lower layer $V_s$ .....	71
Figure 4.3 Sensitivity study results derived from the 3D solution with an alternative approach using a stationary 4m receiver spacing for a simple “soft-over-stiff” profile with a variable lower layer $V_s$ .....	71
Figure 4.4 Sensitivity study results derived from the 2D Plane wave solution for a variable $V_s$ profile transition gradient.....	72
Figure 4.5 Sensitivity study results derived from the 3D solution with a traditional SASW arrangement with a 16m receiver spacing for a variable $V_s$ profile transition gradient .....	73
Figure 4.6 Sensitivity study results derived from the 3D solution with an alternative approach using a stationary 4m receiver spacing for a variable $V_s$ profile transition gradient .....	73
Figure 4.7 Sensitivity study results derived from the 2D Plane wave solution for a simple “soft-over-stiff” profile with a variable lower layer depth .....	74

Figure 4.8 Sensitivity study results derived from the 3D solution with a traditional SASW arrangement with a 16m receiver spacing for a simple “soft-over-stiff” profile with a variable lower layer depth.....	75
Figure 4.9 Sensitivity study results derived from the 3D solution with an alternative approach using a stationary 4m receiver spacing for a simple “soft-over-stiff” profile with a variable lower layer depth.....	75
Figure 4.10 Sensitivity study results derived from the 2D Plane wave solution for a simple “soft-over-stiff” profile with a variable layer transition gradient.....	76
Figure 4.11 Sensitivity study results derived from the 3D solution with a traditional SASW arrangement with a 16m receiver spacing for a simple “soft-over-stiff” profile with a variable layer transition gradient .....	77
Figure 4.12 Sensitivity study results derived from the 3D solution with an alternative approach using a stationary 4m receiver spacing for a simple “soft-over-stiff” profile with a variable layer transition gradient .....	77
Figure 4.13 Sensitivity study results derived from the 2D Plane wave solution for a uniform $V_s$ profile with a variable Poisson’s ratio.....	79
Figure 4.14 Sensitivity study results derived from the 3D solution with a traditional SASW arrangement with a 16m receiver spacing for a uniform profile with a variable value of Poisson’s ratio.....	79
Figure 4.15 Sensitivity study results derived from the 3D solution with an alternative approach using a stationary 4m receiver spacing for a uniform profile with a variable value of Poisson’s ratio.....	80
Figure 4.16 Sensitivity study results derived from the 2D Plane wave solution for a simple “soft-over-stiff” profile with a variable value of Poisson’s ratio.....	80
Figure 4.17 Sensitivity study results derived from the 3D solution with a traditional SASW arrangement with a 16m receiver spacing for a simple “soft-over-stiff” profile with a variable value of Poisson’s ratio .....	81
Figure 4.18 Sensitivity study results derived from the 3D solution with an alternative approach using a stationary 4m receiver spacing for a simple “soft-over-stiff” profile with a variable value of Poisson’s ratio.....	81
Figure 4.19 Sensitivity study results derived from the 2D Plane wave solution for a linear profile with a variable value of Poisson’s ratio .....	82

Figure 4.20 Sensitivity study results derived from the 3D solution with a traditional SASW arrangement with a 16m receiver spacing for a linear profile with a variable value of Poisson’s ratio.....	82
Figure 4.21 Sensitivity study results derived from the 3D solution with an alternative approach using a stationary 4m receiver spacing for a linear profile with a variable value of Poisson’s ratio .....	83
Figure 4.22 Visual comparison of data collection arrays for the “Traditional SASW” and “Alternative SASW” approaches over the same range of wavelengths .....	84
Figure 4.23 Visual representation of the receiver arrays used to measure a maximum wavelength of 64m (blue line) with each of the four filtering criteria. ....	88
Figure 4.24 Comparison of the “true” $V_S$ profile for Case A with $V_S$ profiles inverted by 2D Global, 3D Global and 3D Array methods for the inversion sensitivity study, with the filtering criteria indicated in each column.....	89
Figure 4.25 Percent error between inverted and "true" $V_S$ profiles at each layer for the uniform (Case A) profile.....	90
Figure 4.26 Comparison of the “true” $V_S$ profile for Case B with $V_S$ profiles inverted by 2D Global, 3D Global and 3D Array methods for the inversion sensitivity study, with the filtering criteria indicated in each column.....	91
Figure 4.27 Percent error between inverted and "true" $V_S$ profiles at each layer for the power function (Case B) profile .....	92
Figure 4.28 Comparison of the “true” $V_S$ profile for Case C with $V_S$ profiles inverted by 2D Global, 3D Global and 3D Array methods for the inversion sensitivity study, with the filtering criteria indicated in each column.....	93
Figure 4.29 Percent error between inverted and "true" $V_S$ profiles at each layer for linear $V_S$ increase (Case C).....	94
Figure 4.30 Comparison of the “true” $V_S$ profile for Case D with $V_S$ profiles inverted by 2D Global, 3D Global and 3D Array methods for the inversion sensitivity study, with the filtering criteria indicated in each column.....	95
Figure 4.31 Percent error between inverted and "true" $V_S$ profiles for the steep power function (Case D) profile.....	96

Figure 4.32 Comparison of the “true”  $V_s$  profile for Case B\* with  $V_s$  profiles inverted by 2D Global, 3D Global and 3D Array methods for the inversion sensitivity study, with the filtering criteria indicated in each column ..... 97

Figure 4.33 Percent error between inverted and "true"  $V_s$  profiles in each layer for the “saturated” (Case B\*) profile ..... 98

Figure 4.34 WinSASW screenshots from one of the analyses in the profile recovery study (Case D, 180° near-field criterion, 2D global inversion), illustrating the likely causes of significant misfit for the 2D and 3D global inversions in both the (a) data processing and (b) inversion steps..... 101

Figure 4.35 WinSASW screenshot from one of the analyses in the Poisson’s ratio study (Case D, 180° near-field criterion, 3D array inversion), illustrating an excellent fit between theoretical (red) and experimental (blue) dispersion curves after an inversion analysis (and the correspondingly low RMS error), where the assumed value of Poisson’s ratio exactly matched the “true” value of 0.30 ..... 104

Figure 4.36 WinSASW screenshot from one of the analyses in the Poisson’s ratio study (Case D, 180° near-field criterion, 3D array inversion), illustrating a poor fit between theoretical (red) and experimental (blue) dispersion curves after an inversion analysis (and the correspondingly high RMS error), where the assumed Poisson’s ratio value of 0.45 did *not* match the true value of 0.30 ..... 104

Figure 4.37 Comparison of the “true”  $V_s$  profile for Case A with  $V_s$  profiles inverted by 2D Global, 3D Global and 3D Array methods – these data were processed using the 360° filtering criteria..... 105

Figure 4.38 Comparison of the “true”  $V_s$  profile for Case A with  $V_s$  profiles inverted by 2D Global, 3D Global and 3D Array methods – these data were processed using the 180° filtering criteria..... 106

Figure 4.39 Comparison of the “true”  $V_s$  profile for Case A with  $V_s$  profiles inverted by 3D Array methods – these data were processed by alternative filtering criteria including more of the near-field (90° top row and 45° bottom row) ..... 106

Figure 4.40 RMS error in fit between theoretical and experimental dispersion curves for Case A, covering the range of inversion methods, filtering criteria, and Poisson’s ratio values encompassed by Figure 4.37, Figure 4.38, and Figure 4.39 – arrows indicate abscissa location of the “true” Poisson’s ratio value ..... 107

Figure 4.41 Comparison of the “true”  $V_s$  profile for Case B with  $V_s$  profiles inverted by 2D Global, 3D Global and 3D Array methods – these data were processed by the 360° filtering criteria.... 108

Figure 4.42 Comparison of the “true”  $V_s$  profile for Case B with  $V_s$  profiles inverted by 2D Global, 3D Global and 3D Array methods – these data were processed by the 180° filtering criteria.... 109

Figure 4.43 Comparison of the “true”  $V_s$  profile for Case B with  $V_s$  profiles inverted by 2D Global, 3D Global and 3D Array methods – these data were processed by alternative filtering criteria including more near-field (90° top row and 45° bottom row)..... 109

Figure 4.44 RMS error in fit between theoretical and experimental dispersion curves for Case B, covering the range of inversion methods, filtering criteria, and Poisson’s ratio values encompassed by Figure 4.41, Figure 4.42, and Figure 4.43 – arrows indicate abscissa location of the “true” Poisson’s ratio value ..... 110

Figure 4.45 Comparison of the “true”  $V_s$  profile for Case C with  $V_s$  profiles inverted by 2D Global, 3D Global and 3D Array methods – these data were processed by the 360° filtering criteria.... 111

Figure 4.46 Comparison of the “true”  $V_s$  profile for Case C with  $V_s$  profiles inverted by 2D Global, 3D Global and 3D Array methods – these data were processed by the 180° filtering criteria.... 112

Figure 4.47 Comparison of the “true”  $V_s$  profile for Case C with  $V_s$  profiles inverted by 2D Global, 3D Global and 3D Array methods – these data were processed by alternative filtering criteria including more near-field(90° top row and 45° bottom row) ..... 112

Figure 4.48 RMS error in fit between theoretical and experimental dispersion curves for Case C, covering the range of inversion methods, filtering criteria, and Poisson’s ratio values encompassed by Figure 4.45, Figure 4.46, and Figure 4.47 – arrows indicate abscissa location of the “true” Poisson’s ratio value ..... 113

Figure 4.49 Comparison of the “true”  $V_s$  profile for Case D with  $V_s$  profiles inverted by 2D Global, 3D Global and 3D Array methods – these data were processed by the 360° filtering criteria.... 114

Figure 4.50 Comparison of the “true”  $V_s$  profile for Case D with  $V_s$  profiles inverted by 2D Global, 3D Global and 3D Array methods – these data were processed by the 180° filtering criteria.... 115

Figure 4.51 Comparison of the “true”  $V_s$  profile for Case D with  $V_s$  profiles inverted by 2D Global, 3D Global and 3D Array methods – these data were processed by alternative filtering criteria including more near-field (90° top row and 45° bottom row)..... 115

Figure 4.52 RMS error in fit between theoretical and experimental dispersion curves for Case D, covering the range of inversion methods, filtering criteria, and Poisson’s ratio values

encompassed by Figure 4.49, Figure 4.50, and Figure 4.51 – arrows indicate abscissa location of the “true” Poisson’s ratio value .....	116
Figure 4.53 Comparison of the “true” $V_S$ profile for Case B* - a saturated version of Case B - with $V_S$ profiles inverted by 2D Global, 3D Global and 3D Array methods – these data were processed by the 360° filtering criteria.....	117
Figure 4.54 Comparison of the “true” $V_S$ profile for Case B* - a saturated version of Case B - with $V_S$ profiles inverted by 2D Global, 3D Global and 3D Array methods – these data were processed by the 180 ° filtering criteria.....	118
Figure 4.55 Comparison of the “true” $V_S$ profile for Case B* - a saturated version of Case B - with $V_S$ profiles inverted by 2D Global, 3D Global and 3D Array methods – these data were processed by alternative filtering criteria including more near-field (90° top row and 45° bottom row) ...	118
Figure 4.56 RMS error in fit between theoretical and experimental dispersion curves for Case B* - a saturated version of Case B - covering the range of inversion methods, filtering criteria, and Poisson’s ratio values encompassed by Figure 4.53, Figure 4.54, and Figure 4.55 – arrows indicate abscissa location of the “true” Poisson’s ratio value .....	119
Figure 4.57 WinSASW screenshot of the composite dispersion curve for Case B*, with a 360° filtering criterion, showing the sharp “kinks” in the curves of the longer spacings required for this criterion.....	122
Figure 4.58 WinSASW screenshot of the composite dispersion curve for Case B*, with a 45° filtering criterion, showing the gradual undulations in the near-field region of each curve .....	122
Figure 4.59 Comparison of the “true” $V_S$ profile for Case A with $V_S$ profiles inverted from multi-channel data by 2D Global and 3D Global methods.....	124
Figure 4.60 Comparison of the “true” $V_S$ profile for Case B with $V_S$ profiles inverted from multi-channel data by 2D Global and 3D Global methods.....	125
Figure 4.61 Comparison of the “true” $V_S$ profile for Case C with $V_S$ profiles inverted from multi-channel data by 2D Global and 3D Global methods.....	126
Figure 4.62 Comparison of the “true” $V_S$ profile for Case D with $V_S$ profiles inverted from multi-channel data by 2D Global and 3D Global methods.....	127
Figure 4.63 Normalized dispersion curves for Case C with a multi-channel array having a 10m source-to-first-receiver distance, a receiver-to-receiver of 1m and 30 total receivers (i.e. 10SR1RR-30) from Li 2011 .....	129

Figure 5.1 Experimental dispersion curve generated from the Mississippi Embayment data using a 90° filtering criteria with a 180m long array .....	132
Figure 5.2 $V_s$ profiles inverted from the Mississippi Embayment data by the 3D array method using alternative filtering criteria including more of the near-field .....	132
Figure 5.3 Comparison of the $V_s$ profile derived for the “saturated” ( $V_p = 1600$ m/s) case with the profile determined by Rosenblad et al. (2010), who processed the same experimental dataset with traditional SASW criteria.....	133
Figure 5.4 RMS error in fit between theoretical and experimental dispersion curves from Mississippi Embayment data, for the inversion methods and Poisson’s ratio values encompassed by Figure 5.2 – average Poisson’s ratio values are plotted for the saturated case ( $V_p = 1600$ m/s) .....	134
Figure 5.5 Comparison of experimental and inverted dispersion curves for the “saturated” ( $V_p = 1600$ m/s) case .....	134
Figure 5.6 $V_s$ profiles inverted from real multi-channel data by 2D Global and 3D Global methods .....	135
Figure 5.7 RMS error in fit between theoretical and experimental dispersion curves for real multi-channel data .....	135

A STUDY ON THE BENEFITS OF INCLUDING NEAR-FIELD EFFECTS IN  
ACTIVE-SOURCE SURFACE WAVE DATA COLLECTION AND INTERPRETATION

Alexander McCaskill

Dr. Brent Rosenblad, Thesis Supervisor

ABSTRACT

Geotechnical analyses for earthquake engineering and other applications are often predicated on the accurate determination of shear wave velocity ( $V_s$ ) profiles. Surface wave methods (SWM) are a non-invasive approach to developing  $V_s$  profiles that involve measurement of Rayleigh wave propagation between a wave-generating source and a receiver array placed on the ground surface. There are several variations of SWM, but all utilize the same three-step process for developing a  $V_s$  profile, namely: (1) data collection – measuring ground surface vibrations emanating from a source; (2) data processing – developing an experimental dispersion curve relating wave velocity to wavelength or frequency; and (3) inversion – finding the  $V_s$  profile that produces a theoretical dispersion curve matching the experimental dispersion curve. In current practice, the theoretical model used to fit the experimental data is a far-field model that only simulates motions from planar Rayleigh waves. Therefore, the receiver array used to collect the data in step 1 must be located far from the source (or “far-field”), where body waves have largely dissipated (due to greater damping) and Rayleigh wavefronts are nearly planar. Closer to the source – in the so-called “near-field” – the ground motions include coupled interactions of body waves and non-planar Rayleigh waves and is inconsistent with a far-field theoretical model.

The primary objective of this study was to investigate the effectiveness and potential benefits of including near-field contributions in both the surface wave data collection and modeling. First, it was hypothesized that source offset distance criteria currently used to

mitigate near-field effects could be greatly reduced without affecting the quality of surface wave results. Second, it was hypothesized that additional information about the soil profile could be determined if the near-field portion of the dispersion curve was included in both the data collection and theoretical modeling. Three different studies were performed for this research, namely: (1) a preliminary sensitivity study, to study the sensitivity of the near-field portion of the dispersion curve to changes in various profile parameters, (2) surface wave analysis using simulated experimental data, to assess both profile recovery effectiveness and the possibility of inferring additional profile parameters (specifically, Poisson's ratio), and (3) surface wave analysis with real data, to validate the profile findings from the study using simulated data. Experimental data were collected and/or simulated using both the Spectral-Analysis-of-Surface-Waves (SASW) method and multi-channel surface wave methods, but the primary focus of this study was on the SASW method.

The results from the study showed that surface wave analyses that included near-field contributions in both data collection and theoretical modeling were as effective or more effective at recovering the  $V_s$  profile as conventional far-field approaches, with the benefit of shorter arrays and smaller sources. This study also showed that surface wave measurements that included near-field data were sensitive to changes in Poisson's ratio of the profile, as compared with the known insensitivity of conventional far-field surface wave methods. The results from the limited experimental study were less conclusive, but generally confirmed the findings from the study performed using simulated data.

# 1 INTRODUCTION

## 1.1 Overview and Motivation

Geotechnical analyses for earthquake engineering and other applications are often predicated on the accurate determination of shear wave velocity ( $V_s$ ) profiles. Traditional in-situ test methods, such as crosshole or downhole measurements, provide a profile of  $V_s$  with depth. Such tests, however, require drilling one or more boreholes and can be very expensive to perform. Surface wave methods (SWM) offer a non-invasive approach to developing  $V_s$  profiles from measurements at the ground surface, without the need for boreholes. In addition to traditional applications in earthquake site response analysis (e.g. Woods and Stokoe 1985) and liquefaction analyses (e.g. Stokoe and Nazarian 1985), surface wave methods have also been extensively utilized for subsurface profiling and detection. They have proven to be a valuable tool for subsurface profiling of pavements (e.g. Nazarian et al. 1988), dams (e.g. Oh et al. 2003), levees (e.g. Ivanov et al. 2010), and solid waste landfills (e.g. Kavazanjian et al. 1996), to name a few. Surface wave methods have also been used to detect shallow voids (e.g. Phillips et al. 2000), abandoned coal mines (e.g. Avar and Luke 1999), and unexploded ordnance (e.g. Pulli et al. 2000).

Surface wave methods involve measurement of Rayleigh wave propagation between a wave-generating source and a receiver array placed on the ground surface. The source can be either “active”, where waves are actively generated by an impact or shaker, or “passive”, where ambient wave propagation (due to traffic, tidal motions, random noise, etc.) is measured. This thesis will focus solely on “active-source” methods. Advances in technology and engineering practice have brought about many variations of SWM, but all SWM generally utilize the same three-step process for developing a  $V_s$  profile, namely: (1) data collection – exciting and measuring ground surface vibrations emanating from a source; (2) data processing – developing an experimental dispersion curve relating wave velocity to wavelength or frequency; and (3) inversion – finding the  $V_s$  profile that produces a theoretical dispersion curve matching the experimental dispersion curve. Step 1 involves on-site measurements of surface wave propagation with an array of at least two receivers. In step 2, experimental data from step 1 are processed to produce a “dispersion curve” relating wavelength (or frequency) to surface wave

velocity. In step 3, a model  $V_s$  profile corresponding to a theoretical dispersion curve is adjusted until the theoretical and experimental dispersion curves match. It is important that the theoretical model used in step 3 is consistent with the experimental data collected in step 1.

The issue of model compatibility is a central focus of this thesis: a model that is incompatible with experimental data collection procedures will produce an erroneous  $V_s$  profile, which will adversely affect analyses that depend on the results (e.g. site response, liquefaction). The theoretical model (step 3) in nearly all commercial surface wave analysis programs is a “plane wave” Rayleigh mode model (i.e. far field), which does not include body wave contributions. Therefore, to ensure model compatibility, the receiver array in step 1 must be located far from the source (or “far-field”), where body waves have largely dissipated (due to greater damping) and Rayleigh wavefronts are nearly planar. Closer to the source – in the so-called “near-field” – the ground motion is composed of coupled interactions of body waves and non-planar Rayleigh waves, which is incompatible with a plane wave model. Several past studies (e.g. Heisey et al. 1982; Sanchez-Salinero et al. 1987; Xu et al. 2006) have examined how far the receivers must be placed from the source to avoid near-field contributions. Some recent studies (Bodet et al. 2009; Rosenblad and Li 2011; Yoon and Rix 2009) have shown that this distance is strongly site-dependent and, in some cases, larger than previously thought.

A different approach to dealing with the near-field issue was proposed by Joh (1996): he developed a more advanced theoretical model for an existing SWM – the active-source, two-receiver method known as the Spectral-Analysis-of-Surface-Waves (SASW) method. His theoretical model calculates the complete response at each receiver location due to all wave contributions. Therefore, the near-field need not be avoided in the data collection stage, as it is included in the theoretical model. This approach, however, is not widely used in current practice – when it is used, data collection criteria originally developed to avoid the near-field are often applied. Two aspects of this approach have the potential to provide significant benefit in practice, but have not been studied in detail. First, the extent to which the near-field can be included in the data collection and analysis while maintaining quality in the results needs to be studied. Pushing the lower-limit of the source offset distance would allow for a more economical implementation of SWM by decreasing the size of sources needed to excite the energy and decreasing the space required to perform SWM. Second, the extent to which additional information about the profile can be derived by including near-field effects in the analysis needs to be studied. The ability to determine additional profile parameters that must be

assumed with current methods would serve to improve the accuracy of the methods and provide valuable information for geotechnical analyses.

## **1.2 Objective and Hypotheses**

The primary objective of this study is to investigate potential benefits of including the near-field in surface wave data collection and analysis. Two hypotheses are investigated in this study. First, it is hypothesized that limiting criteria currently used to remove near-field from SWM measurements can be greatly reduced without affecting the quality of surface wave results. The extent to which the source offset distance can be reduced is investigated. Second, it is hypothesized that the near-field portion of the dispersion curve will be more sensitive to changes in additional profile parameters than the far-field portion used in current practice. Sensitivity of the near-field and far-field portions of the dispersion curve to changes in several additional profile parameters is investigated. Although this study will focus primarily on the SASW method, the findings will likely provide valuable insight into possible improvements in multi-channel surface wave methods. If these hypotheses are shown to be true, then the current state-of-the-practice could be improved by developing more economical and effective implementations of SWM.

## **1.3 Outline of Thesis**

This thesis is organized into five chapters. Chapter 2 provides background information on data collection and interpretation for common SWM, with a focus on near-field effects. Chapter 3 describes the methods and theoretical models used to perform: (1) a preliminary sensitivity study, (2) surface wave analyses with simulated data, and (3) surface wave analyses with real data. Results of the first two studies, which extensively utilized surface wave simulations, are presented and discussed in Chapter 4. Results of the study using real data are presented and discussed in Chapter 5. Chapter 6 presents conclusions derived from this work and considerations for future research.

## 2 BACKGROUND

### 2.1 Introduction

Chapter 2 provides a theoretical background and describes the current state-of-the-practice in geotechnical engineering for active-source surface wave measurements. Section 2.2 opens with a review of fundamental aspects of body waves and surface waves. The principles of wave propagation in an elastic halfspace are reviewed in Section 2.3. Section 2.4 provides background information on data collection, data processing, and inversion analyses for the active-source surface wave methods (SWM) considered in this study – including spectral analysis of surface waves (SASW) and multi-channel methods. Sections 2.5 and 2.6 summarize previous studies on near-field effects and sensitivity to Poisson’s ratio, respectively.

### 2.2 Body Wave and Surface Wave Fundamentals

Two types of waves can propagate in an elastic, isotropic, homogeneous material of infinite extent in all directions (i.e. a “wholespace”). Collectively known as “body waves”, the two types of body waves are dilational waves (P-waves) and distortional waves (S-waves). P-waves are also known as primary waves, compression waves, and irrotational waves; S-waves are also known as secondary waves, shear waves, and equivoluminal waves (Richart et al. 1970). A “halfspace,” is contained by a free boundary but infinite below it in all directions. The surface boundary in a halfspace allows for the development of an altogether different wave type – surface waves.

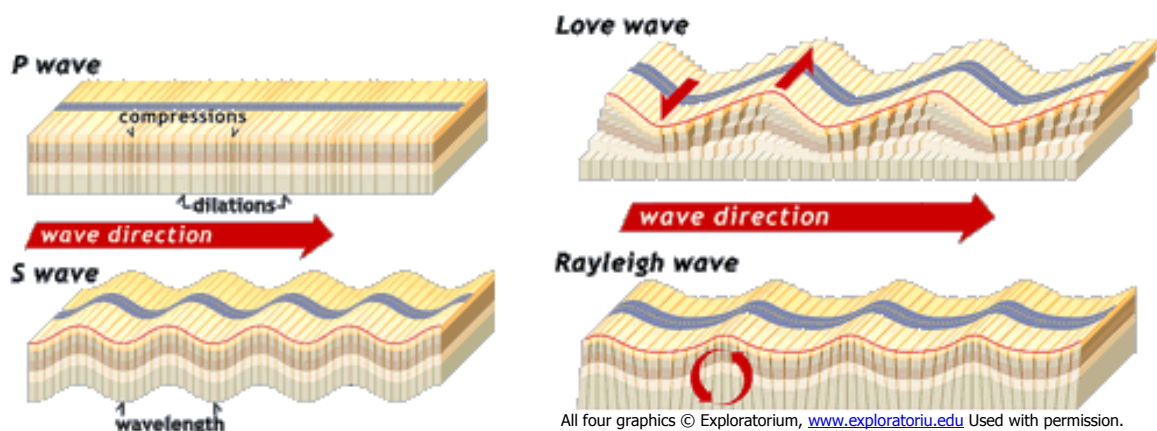
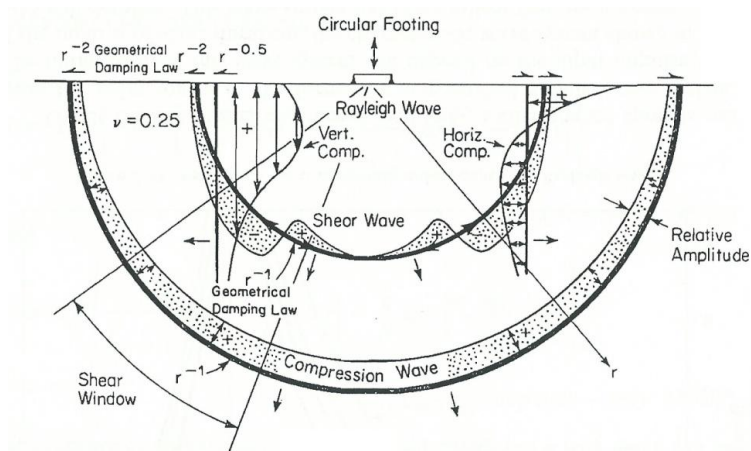


Figure 2.1 Schematic representation of types of body waves (left) and surface waves (right) (Exploratorium 2014)

The fundamental properties of body waves are the same for propagation through both wholespace and halfspace regions. Localized particle motion induced by P-waves is in the same direction as wave propagation, resulting in alternating zones of compression and dilation that oscillate in the direction of wave propagation, as shown in Figure 2.1. For S-waves, particle motion oscillates transverse to the direction of wave propagation, producing a shearing motion (Figure 2.1). S-waves can be either horizontally (SH) or vertically (SV) polarized, corresponding to particle motion in the horizontal or vertical plane, respectively. Both P and S-waves spread spherically from their origin point and damp out (i.e. dissipate or attenuate) at a rate inversely proportional to the square of distance from the origin, as noted in Figure 2.2.

In 1885, Lord Rayleigh discovered a third type of wave resulting from the interaction of P-waves and vertically polarized S-waves at the surface boundary of a halfspace (Lamb 1904; Rayleigh 1885). The so-called “Rayleigh wave” appears to an observer standing on the surface as a “ground roll” moving in the direction of wave propagation. Particle motion in Rayleigh waves takes the form of a retrograde ellipse, with particle motion rotating opposite the direction of wave propagation, as shown in Figure 2.1. Rayleigh waves spread cylindrically and damp out at a rate inversely proportional to the square root of distance from the origin, which is much slower than body waves (as noted in Figure 2.2). Rayleigh wave amplitude is high at the surface and decreases substantially with depth, as illustrated in Figure 2.3.



**Figure 2.2** P-wave, S-wave, and Rayleigh wave propagation in an elastic halfspace (Richart et al. 1970)

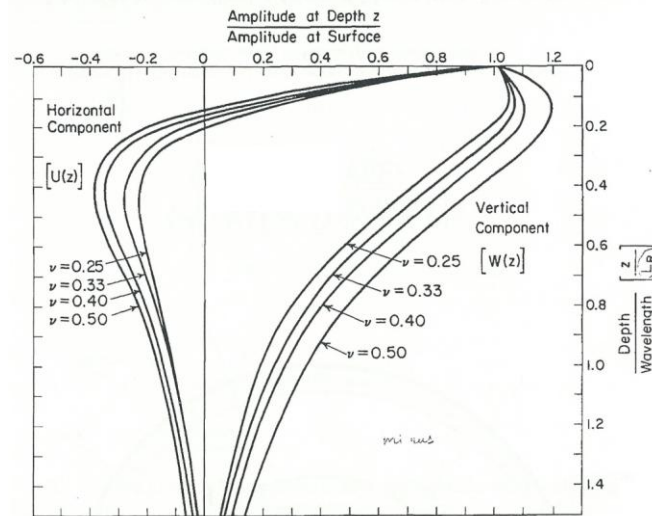


**Figure 2.3** Rayleigh wave amplitude decreases significantly with depth (Richart et al. 1970)

Another type of surface wave resulting from the interaction of horizontally polarized S-waves with the surface boundary was later discovered by Love (1911). Ewing et al. (1957) described the Love wave as a “horizontally polarized shear wave trapped in a superficial layer and propagated by multiple total reflections.” For Love waves to occur, Richart et al. (1970) note that “the phase velocity of the Love wave must be less than the shear wave velocity of the next lower layer.” Surface wave methods involving Love waves have been the subject of some recent research – for example, Xia et al. (2012) – but only Rayleigh-wave-based SWM are considered in this thesis.

It is well known that P-wave velocity ( $V_p$ ) and S-wave velocity ( $V_s$ ) are directly related to the constrained modulus ( $M$ ) and shear modulus ( $G$ ), respectively, by Equations 2.1 and 2.2 – where  $\rho$  is mass density. Well-known relationships between elastic constants may be used to infer other values – for instance Poisson’s ratio ( $\nu$ ) in Equation 2.3 – from  $M$  and  $G$ .

$$V_p = \sqrt{\frac{M}{\rho}} \quad (2.1)$$

$$V_s = \sqrt{\frac{G}{\rho}} \quad (2.2)$$

$$\nu = \frac{M - 2G}{2(M - G)} \quad (2.3)$$

Poisson's ratio and  $V_p$  are good indicators of fluid saturation in soils. Fully saturated conditions in soft soils correspond to Poisson's ratio values close to 0.5 and of  $V_p$  values of approximately 1600 m/s (5000 ft/s), the wave velocity of water. Unsaturated values of Poisson's ratio and  $V_p$  are considerably lower, as shown in Figure 2.4, while most unsaturated soils have  $\nu$  values in the range of 0.25 to 0.40.

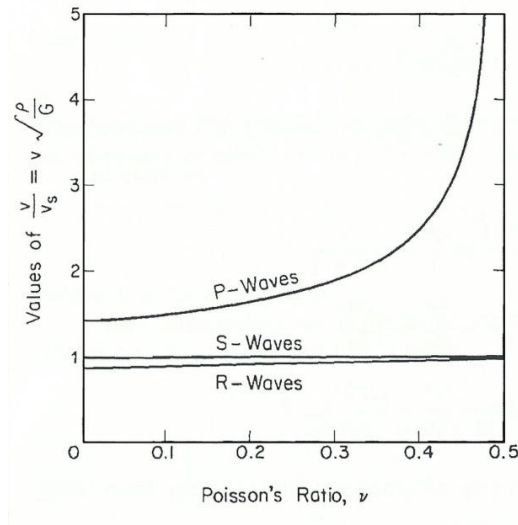


**Figure 2.4** Comparison of P-wave, S-wave and Rayleigh wave (R-Wave) velocities (Richart et al. 1970)

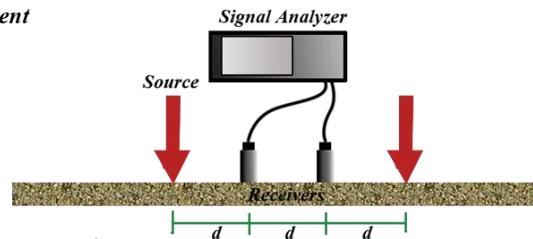
P-waves, S-waves and Rayleigh waves are generated simultaneously from a source applied at the surface. For most soils in an unsaturated condition, the value of  $V_p$  is in the range of 1.8 to 2.2 times that of  $V_s$ . At distances far from the source ("far-field"), P-waves and S-waves have mostly damped out and wave propagation is dominated by the Rayleigh wave. In the far-field, the cylindrically-spreading Rayleigh wavefront has spread out to such an extent that it can be approximated as a vertical plane – a "plane wave" – moving in the direction of wave propagation. In geotechnical literature, the term "near-field" generally refers to the region closer to the source, where the body waves have not damped out and surface waves are spreading along a cylindrical wavefront.

### 2.3 Active-source Surface Wave Methods for Geotechnical Engineering

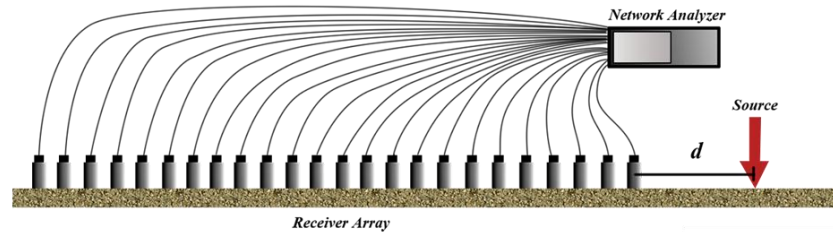
Surface wave methods (SWM) involve measurement of Rayleigh wave propagation between a wave-generating source and a receiver array. The source can be either "active", where waves are actively generated by an impact or other source of vibration, or "passive", where ambient

wave propagation (from traffic, tidal motions, random noise, etc.) is recorded. Most SWM utilize the same three-step process for developing a  $V_s$  profile: (1) data collection – measuring ground vibrations from a source; (2) data processing – developing an experimental dispersion curve; and (3) inversion – finding the  $V_s$  profile that produces a theoretical dispersion curve matching the experimental dispersion curve. Step 1 involves on-site measurements of surface wave propagation (Figure 2.5 a and b) with an array of at least two receivers. In step 2, experimental data from step 1 are processed to produce a “dispersion curve” (Figure 2.5c) relating the surface wave velocity to wavelength (or frequency). In step 3, a model  $V_s$  profile corresponding to a theoretical dispersion curve is iteratively adjusted until the theoretical and experimental dispersion curves match (Figure 2.5d). It is important that the theoretical model used in step 3 is consistent with the experimental data collected in step 1.

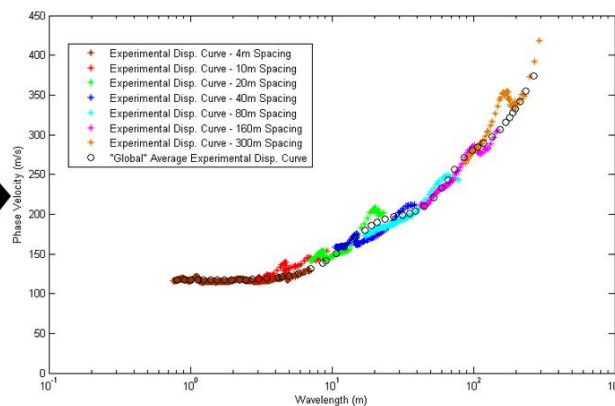
(a) SASW Measurement



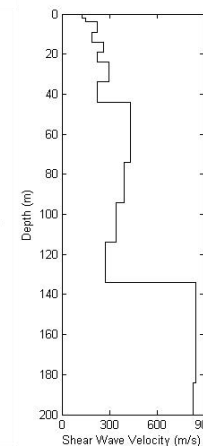
(b) Multi-channel Measurement



(a)  
OR  
(b)



(c) Generate Experimental Dispersion Curve  
(An example from SASW is shown here)



(d) Inversion Analyses  
to Determine  $V_s$  Profile

Figure 2.5 Data collection setups for (a) SASW and (b) multi-channel measurements and data processing (c and d)

### 2.3.1 Spectral Analysis of Surface Waves (SASW)

The early 1980s saw the development of the first practical surface wave method for geotechnical engineering applications, known as the Spectral-Analysis-of-Surface-Waves (SASW) method. Early research on the SASW method demonstrated its utility in pavement profiling (Heisey et al. 1982), liquefaction analyses (Stokoe and Nazarian 1985), and earthquake site response computations (Woods and Stokoe 1985). The steps involved in SASW data collection, data processing, and inversion are described below.

#### 2.3.1.1 SASW Data Collection

Experimental SASW data are collected with the arrangement shown in Figure 2.6 including: an active source, two receivers, and a signal analyzer. The receivers (geophones) are spaced at a distance (“d”) about a centerline, while the source is located the same distance “d” away from one of the receivers. The source, which can be either an impact (e.g. drop weight), shaker (e.g. vibroseis truck), or random noise (e.g. bulldozer), is then activated and ground motions are recorded by the geophone receivers. A second measurement may be recorded with the position of the source mirrored about the centerline as shown (Stokoe and Nazarian 1985). The spacing “d” is then doubled, moving the source away while maintaining the same centerline between receivers, and a new measurement is recorded (Figure 2.7). The process is repeated until data is obtained to cover the desired wavelength range. Rayleigh waves profile to a depth of approximately one-half to one-third of a wavelength of the “longest” wave used in the analysis, as previously shown in Figure 2.3. The largest wavelength value is generally controlled by data collection criteria, which are discussed further in Section 2.4.2. Other things being equal, larger spacings (“d” values) allow for longer wavelengths and, hence, deeper profiling depths.

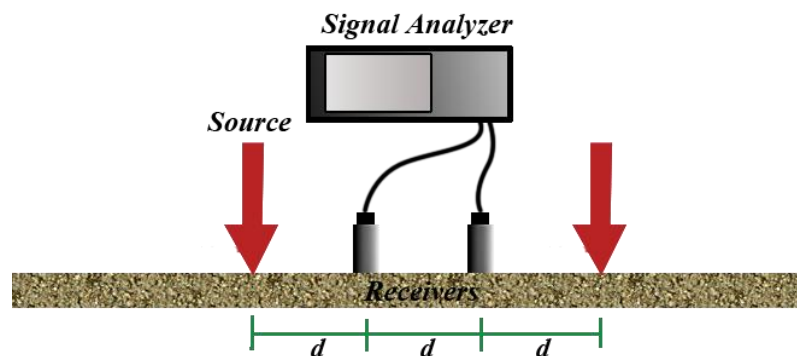
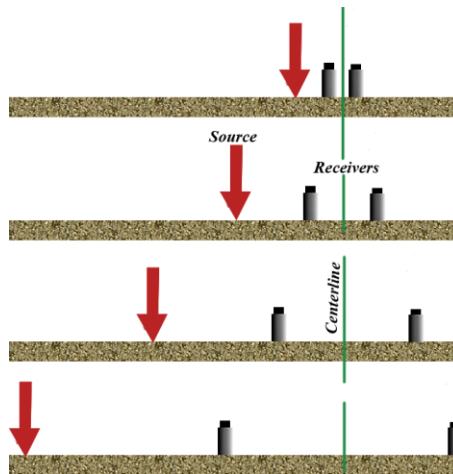


Figure 2.6 Data collection arrangement for Spectral Analysis of Surface Waves (SASW) testing



**Figure 2.7** An example of SASW source-receiver spacings using a constant centerline

### 2.3.1.2 SASW Data Processing

In the SASW data processing stage, recorded ground motions are converted into an experimental dispersion curve using signal processing techniques, as shown in Figure 2.8. First, time-series experimental data from the data collection stage (Figure 2.8a) are converted to a frequency-domain representation using a Fourier series transformation, typically utilizing the fast Fourier transform (FFT) algorithm (Figure 2.8b). In cases where a controlled stepped-sine source is used, data are collected directly in the frequency domain. Second, the phase difference (lead or lag of 180 degrees) between the two receivers is computed and plotted as a function of frequency, producing a “wrapped phase plot” (Figure 2.8c). Third, some portion of the data is omitted (e.g. “masked out”) according to commonly accepted filtering criteria (Figure 2.8d), to avoid regions of low signal coherence and so-called “near-field effects” (see Section 2.4.2). Fourth, the process of “phase unwrapping” (Figure 2.8e) is performed to yield a relationship between frequency and unwrapped phase angle (e.g. an “absolute” phase angle) – The wavelength can be computed from unwrapped phase angle and known receiver spacing (Equation 2.4). Fifth, knowing the frequency and wavelength, the phase velocity is computed by Equation 2.5 and plotted versus wavelength, or sometimes frequency, to generate an experimental dispersion curve (Figure 2.8f) corresponding to a particular receiver spacing (i.e. a particular distance “ $d$ ” in Figure 2.6). These five steps are repeated to process data corresponding to each receiver spacing, thus yielding a “composite” dispersion curve (Figure 2.8g) combining data from multiple receiver spacings. The composite dispersion curve, however, often has more data points than can be practically used in an inversion analysis, necessitating the use of an averaging scheme. In current practice, a “global” average experimental dispersion

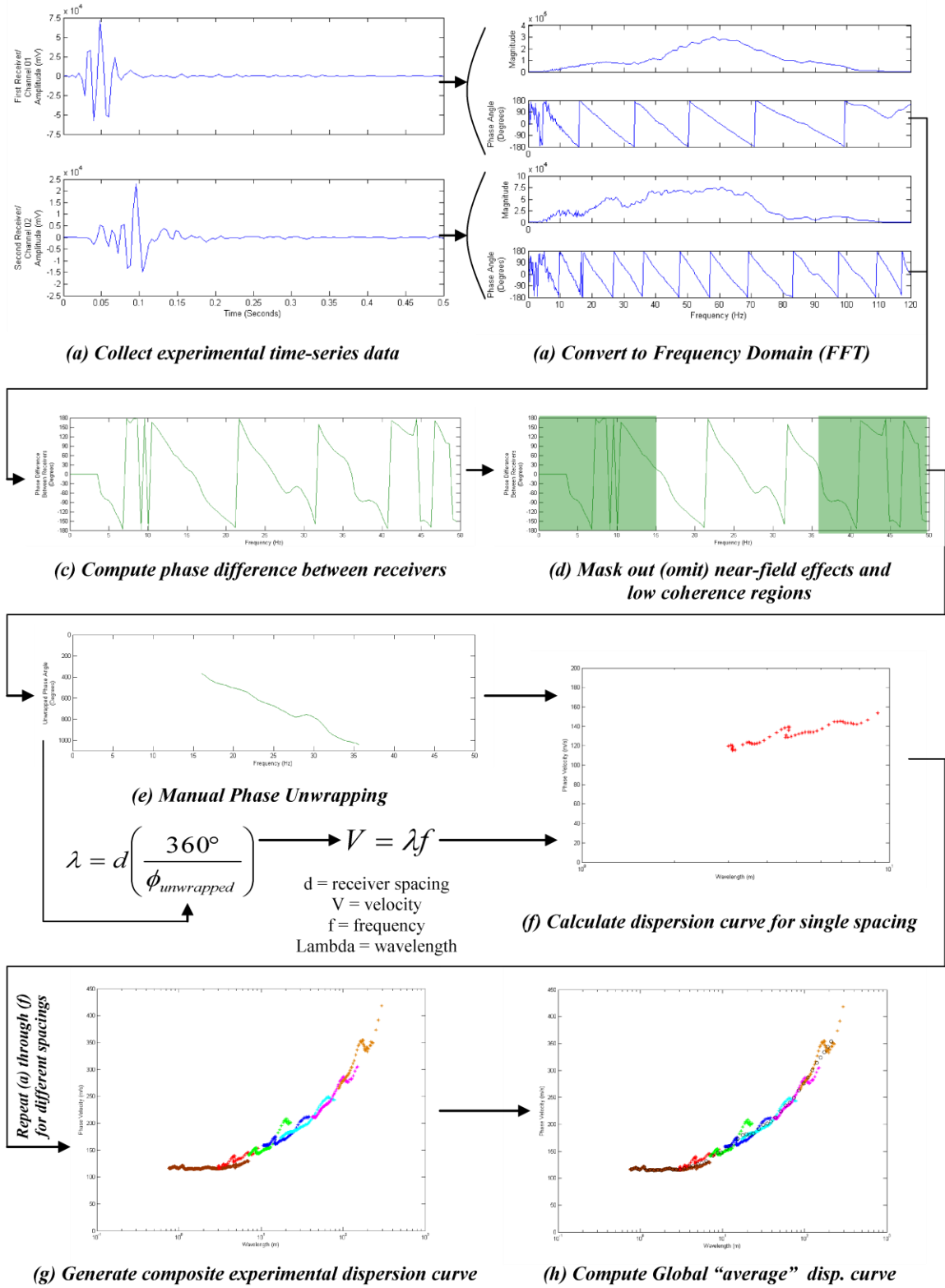


Figure 2.8 SASW processing flowchart illustrating conversion of time-series data to an experimental dispersion curve

curve is generated by determining average values from overlapping windowed portions of the composite dispersion curve. An alternative approach using several individual dispersion curves is also discussed in this thesis and implemented in the research described here.

$$\lambda = d \left( \frac{360^\circ}{\phi_{Unwrapped}} \right) \quad (2.4)$$

$$V = \lambda f \quad (2.5)$$

### **2.3.1.3 SASW Inversion Analyses**

Historically, three different theoretical models (termed “2D Global”, “3D Global”, and “Array”) have been used to perform the inversion analysis to determine the  $V_s$  profile from SASW data. The term “Global” refers to the fact that the theoretical model is fit to the “global” experimental dispersion curve determined in the data processing stage (i.e. a single curve determined from all receiver pairs). The “2D global” theoretical model, also known as the far-field or plane wave solution, produces a theoretical dispersion curve composed solely of (two-dimensional) plane Rayleigh waves. The dispersion curve generated by this approach is considered to correspond to the fundamental mode of Rayleigh wave propagation. With the 2D global approach, experimental data must be collected in the far-field to be compatible with the model and yield an accurate inversion of the  $V_s$  profile.

The theoretical model utilized in both the “3D global” and “array” approaches accounts for three-dimensional wave propagation effects and the presence of body waves by means of a Green’s function solution. The Green’s function provides the complete response at a given location relative to the source due to all wave types. This is also considered to be an “effective mode” solution, since fundamental and higher modes from multiple wave types (body waves and surface waves) are superimposed, producing a velocity that may not correspond to any single Rayleigh mode. The theoretical dispersion curve from the 3D global is still a single global experimental dispersion curve. Since this dispersion curve does not correspond to any single receiver location, the typical approach is to compute the Green’s function response at distances corresponding to 2 and 4 wavelengths from the source (at each frequency). This inconsistency between experimental data collection and the theoretical model led to the recent development of the array approach proposed by Joh (1996). With the array approach, multiple average experimental dispersion curves are produced (instead of a single global dispersion curve) – one

for each receiver pair used in the data collection stage. Multiple theoretical dispersion curves are simultaneously calculated and fit to the experimental curves in an array inversion analysis, such that the theoretical response simulates the in-situ experimental response.

## **2.3.2 Multi-channel Surface Wave Methods**

### ***2.3.2.1 Introduction to Multi-channel Methods***

By the late 1990s, computing power had advanced to the point that data from large receiver arrays could be quickly and efficiently processed for geotechnical applications. Park et al. (1999) introduced the first multi-channel surface wave method for engineering applications – Multi-channel Analysis of Surface Waves (MASW). In addition to applications in pavement profiling (Park et al. 2001) and liquefaction analysis (Lin et al. 2004), MASW has also been used to calibrate compaction instrumentation (Ryden and Mooney 2007) and profile solid waste landfills (Smith et al. 2012).

The data collection, data processing, and inversion procedures utilized for MASW (and other active-source multi-channel methods) are described below.

### ***2.3.2.2 Data Collection for Multi-channel Methods***

Experimental data are collected for multi-channel methods, at a field site location, with the arrangement shown in Figure 2.9: including an active source and a stationary receiver array (typically 24 to 48 channels). For most applications, the receivers are equally spaced in a linear array, while the source is located a specified distance (“d”) away from one side of the array. The source, which can be either an impact or shaker, is then activated and ground motions are recorded by the array of geophone receivers. The geophones can be placed directly on the ground (or embedded slightly), as they are for SASW, or connected together in a device known as a “landstreamer.” In either case, the array is stationary while the test is being performed, but the landstreamer allows for quick relocation of the array when recording multiple measurements at a large site.

Data collection practices for multi-channel surface wave methods are dictated by the requirements of the data processing techniques. For instance, the ability to separate Rayleigh wave modes in the data processing stage is one of the key motivations for choosing multi-channel methods over SASW. Modal separation, however, requires a long receiver array (i.e. aperture) to adequately resolve and separate fundamental and higher modes. Some multi-

channel processing techniques require multiple source impacts (e.g. “shots”) at increasing distances (e.g. “offsets”) from the array.

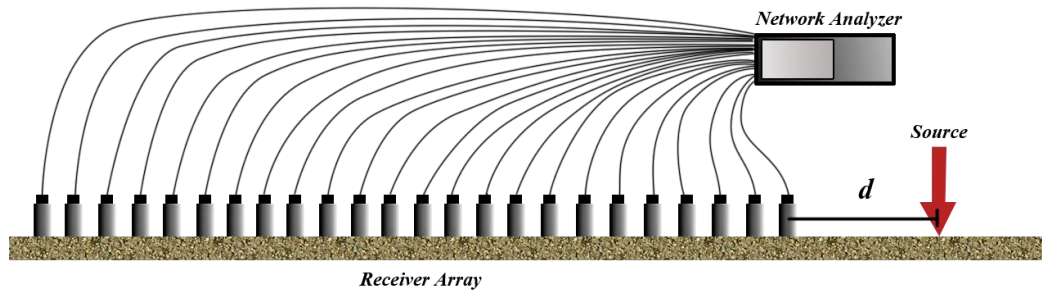


**Figure 2.9** Data collection arrangement for multi-channel surface wave testing

### 2.3.2.3 Processing of Multi-channel Data

In the data processing stage of multi-channel methods, raw field data are converted into an experimental dispersion curve by means of array processing techniques. Pelekis and Athanasopoulos (2011) identified four different variations on processing techniques for multi-channel methods: (1) the frequency-wavenumber (f-k) transform, (2) the frequency-slowness (f-p) transform, (3) the phase-shift transform, and (4) the cylindrical beamformer transform. With the f-k transform, time-series data from each receiver is converted to the frequency domain by an FFT, while the spatial arrangement of the receivers is converted to the wavenumber domain by use of a second FFT. The f-p transform combines “slant-stack transformation of receiver time histories and the sum of power spectra of transformed traces for each frequency.” The phase-shift method (i.e. plane wave beamformer) is “a composite of the slant-stack and f-k methods.” The cylindrical beamformer approach used by Zywicki and Rix (2005) is the only method that considers the experimental data to take the form of a cylindrical wave field, all others assume a planar Rayleigh wave. All four data processing approaches ultimately produce a dispersion image from time-series receiver data, as shown in Figure 2.10. Fundamental and higher modes are then interpreted from the dispersion image.

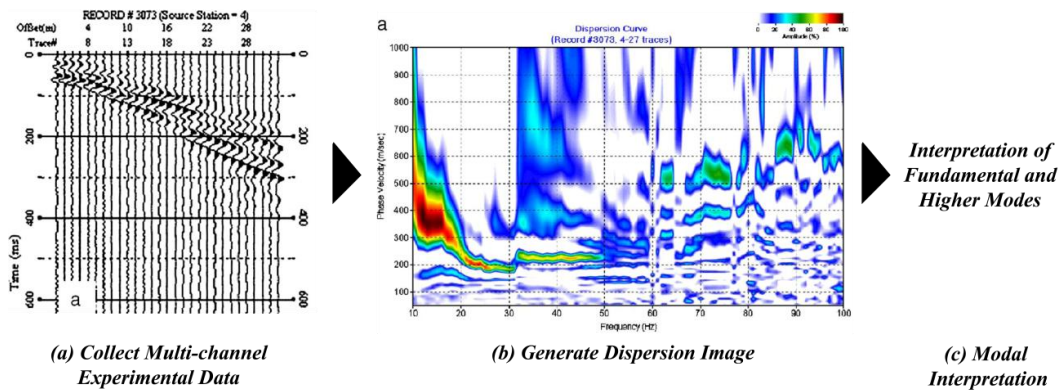


**Figure 2.10** Processing flow for multi-channel data using the phase-shift method, including (a) time-series receiver data, (b) dispersion image generation and (c) interpretation of modes. Adapted from Xu et al. (2006)

### 2.3.2.4 Inversion Analyses for Multi-channel Methods

Unlike SASW, only one theoretical model, the “2D” approach, has typically been used to invert the  $V_s$  profile from multi-channel data. The critical processing step for multi-channel methods is the separation of modes and the interpretation of fundamental and higher modes. One or more of these modes are used as the experimental dispersion curve(s) for the inversion. Multi-channel inversion analyses can use a fundamental mode or a “multi-modal” (fundamental and higher modes) solution. In either case, the inversion analysis still uses a “far-field” plane wave (e.g. 2D) model to fit a theoretical dispersion curve to each mode of the experimental dispersion curve. Therefore, experimental multi-channel data must be collected in the far-field to ensure compatibility between the experimental data and the theoretical model, and modal separation procedures must accurately identify fundamental and higher modes.

## 2.4 Near-field Effects in Active-source Surface Wave Measurements

### 2.4.1 Introduction to Near-field Effects

The term “near-field effects” in geotechnical SWM applications refers to non-planar wave propagation and coupled interactions of body and surface waves near the source. Yoon and Rix (2009) distinguished between the terms “near-field” and “near-field effects”: *near-field* refers to the region where a plane Rayleigh wave assumption are no longer valid, while *near-field effects* refers to “any adverse effect resulting from the invalid assumption.” In practice, however, the two terms are often used interchangeably. Most SWM research to date has been concerned with avoiding or eliminating near-field effects, ultimately to validate continued use of the simple far-field plane wave model used in the inversion analyses which are ubiquitous in current practice.

In a study of dynamic pavement testing methods and the progression of ground motions away from the source, Mera (1995) provided a practical illustration of near-field effects. A time history of vertical displacements, from simulations involving an impulse source at the surface of a halfspace, is shown in Figure 2.11. At large distances (Figure 2.11c), the Rayleigh wave is clearly the primary source of displacements and body waves have substantially damped out, requiring 10x amplitude magnification to be visible on the plot. Close to the source – in the near-field – (Figure 2.11a and b) body wave and surface wave contributions are superimposed into a single disturbance propagating at a velocity that is different from that of the Rayleigh wave.

#### 2.4.2 Previous Studies on Near-field Effects in SASW

Early in the development of SASW, near-field effects were only considered in view of establishing data collection (or filtering) criteria to avoid the near-field. These criteria are usually expressed in terms of the number of wavelengths between the source and first receiver. A summary of these criteria adapted from the work of Yoon and Rix (2009) is shown in Table 2.1 – many of these criteria are still widely used in current SASW practice. Park and Shawver (2009) observe that such criteria offer no guarantee that the results will be completely free of near-field effects. Joh (1996) developed an altogether different approach to deal with the issue of near-field effects in SASW measurements, which is described in detail in Chapter 3.

**Table 2.1** Summary of SASW data collection criteria used to avoid the near-field. Adapted from Yoon and Rix (2009)

Reference	Filtering Criterion	Phase Plot Masked Out	Receiver Configuration	Type of Study
Heisey et al. (1982)	$d/\lambda_R = 1/3$	First 120°	$\Delta d/d = 1$	Numerical
Sanchez-Salinerio et al. (1987)	$d/\lambda_R = 2$	First 720°	$\Delta d/d = 1$	Numerical
Roesset et al. (1990)	$d/\lambda_R = 1/2$	First 180°	$\Delta d/d = 0.2-2$	Numerical
Hiltunen and Woods (1990)	$d/\lambda_R = 1/2$	First 180°	$\Delta d/d = 1$	Experimental
Gucunski and Woods (1992)	$d/\lambda_R = 1$	First 360°	$\Delta d/d = 1$	Numerical
Al-Hunaidi (1993)	N/A	N/A	$\Delta d/d = 1$	Numerical

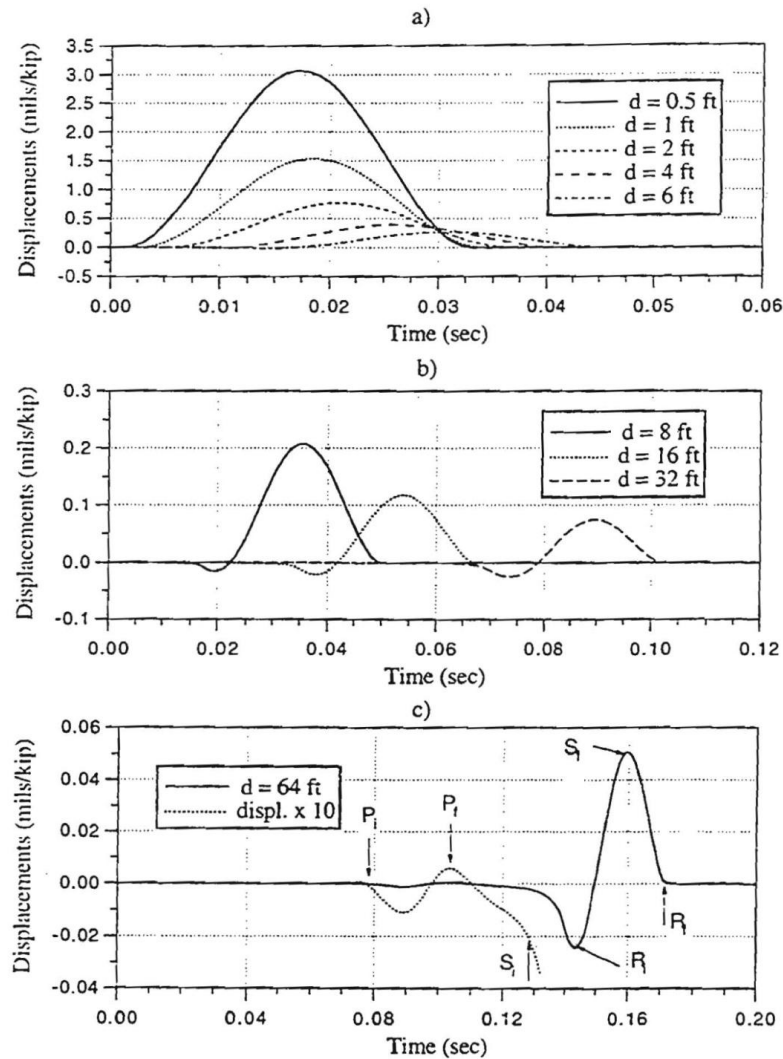


**Figure 2.11** Evolution of the time history of surface displacements due to an impulse load, showing (a and b) the combination of all wave contributions in the near-field and (c) domination of surface waves in the far-field (Mera 1995)

Sanchez-Salinero et al. (1987) simulated SASW measurements by means of a Green's function solution (including near-field effects) and compared the results to a far-field-only plane Rayleigh wave approach. They noted that body wave contributions are completely ignored in the far-field solution and sought to study the issue in greater depth. They also noted that, while the experimental dispersion curve was a product of all wave contributions from a point source, the inversion procedure used at the time was still based solely on plane Rayleigh waves. They performed a parametric study on data collection criteria to identify an optimum configuration of source and receivers. They ultimately recommended receiver spacing to wavelength ( $d/\lambda$ ) ratio of at least 2.0 (first 720 degrees of phase plot omitted) to completely avoid the near-field for a

typical SASW setup with equal source-receiver and receiver spacings. They noted, however, that a  $d/\lambda$  of 1.0 (first 360 degrees of phase plot omitted) or greater could be used if more low-frequency data were required.

Gucunski and Woods (1992) observed discrepancies among previously published SASW filtering criteria and performed several numerical simulations to evaluate these criteria. They modeled four typical profiles with finite element techniques, including the effects of body waves and higher mode Rayleigh waves. They examined the effects of source-receiver arrangements and filtering criteria on SASW results. They considered both equal and unequal spacings and found good agreement between unfiltered dispersion curves developed from different spacings, except at frequencies below 10 to 20 Hz (i.e. in the “near-field”), for most of the profiles they studied. They performed simulations with several filtering criteria, including that of Heisey et al. (1982), and proposed an alternative filtering criterion of  $d/\lambda \geq 1.0$  (first 360 degrees of phase plot omitted) to eliminate near-field effects. They noted that their numerical simulations assumed ideal conditions and, therefore, recommended performing a series of SASW field tests to validate the proposed criteria.

Joh (1996) proposed a different approach to deal with near-field effects in SASW: he applied a more advanced theoretical model and inversion method that could account for near-field effects (the array inversion approach described in Section 2.3.1.3). The theoretical model used by Joh involves a computation of the Green’s function solution, the complete response due to all wave contributions, at each receiver location. The computer program WinSASW, described in Chapter 3, contains an implementation of Joh’s approach. Therefore, the near-field need not be avoided in the data collection stage, as it is included in the theoretical model. Joh’s approach, however, is not widely used in current practice – when it is used, data collection criteria originally developed to avoid the near-field are often applied.

Joh (1996) also introduced the “array” inversion approach, whereby each segment of the experimental dispersion curve (corresponding to a particular spacing) is individually averaged to obtain multiple dispersion curves. In the plane wave analyses prevalent in current practice, all data are averaged into a single “global” experimental dispersion curve. The array inversion approach, which includes near-field effects, is compared with the plane wave approach, which only considers far-field planar Rayleigh waves, in Table 2.2. The same comparison is illustrated graphically in Figure 2.12 – dispersion data from each SASW receiver spacing are shown in a separate color and theoretical dispersion curves are shown in black. The

plane wave solution provides a correct global average fit to experimental data when only far-field (i.e. short wavelength) data are present and can be severely skewed by the presence of near-field effects (i.e. at longer wavelengths), as noted at left in Figure 2.12. The array inversion approach, however, fits experimental data for each SASW spacing with a separate average dispersion curve, thereby accounting for both the near-field and far-field, as shown at right in Figure 2.12.

**Table 2.2** Comparison of (A) current practice in SWM and (B) method considered in this study

		Measurement	Model	Advantages	Disadvantages
<b>A</b>	Plane Wave Approach	Must avoid near-field (Keep source far from receivers)	Plane Rayleigh wave only	Fast, simple plane wave model	Large array spacing and large sources needed
<b>B</b>	Alternative Approach (Array)	May include near-field	Complete wavefield, including near-field terms	Near-field in theoretical model and measurement	Computation time for model is large

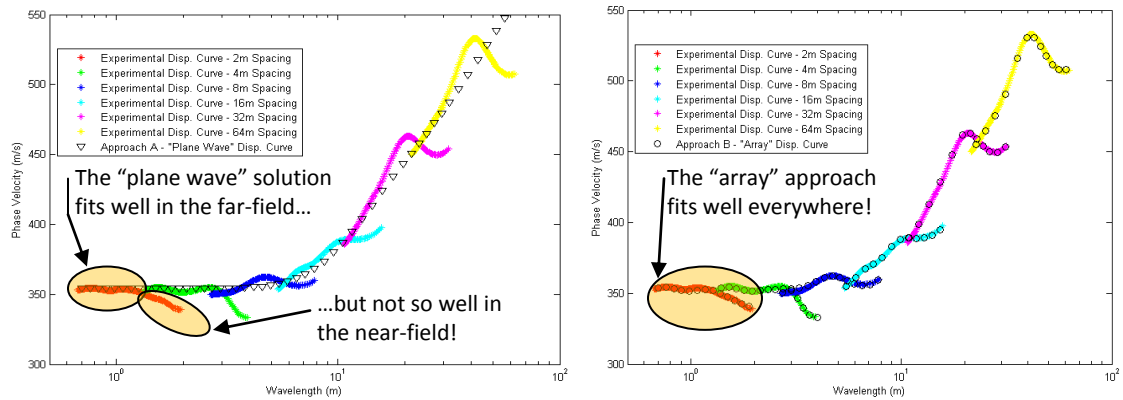


**Figure 2.12** A far-field “plane wave” solution (black triangles, at left) fits the experimental data well at short wavelengths, while significant deviations – near-field effects – are evident at longer wavelengths. The “array” approach (black circles, at right) fits a theoretical curve to the individual dispersion curve from each receiver pair, thereby accounting for both the near-field and the far-field.

### 2.4.3 Previous Studies on Near-field Effects in Multi-channel Methods

Over the past decade, research has been devoted to understanding how to avoid near-field effects in multi-channel measurements. Researchers such as Xu et al. (2006), Yoon and Rix (2009), and Li (2011) have conducted thorough investigations with the aim of finding a minimum “offset” (i.e. source-receiver distance) to avoid near-field effects in multi-channel methods. Bodet et al. (2009) considered a minimum value for array length to avoid or average out near-field effects. Others, such as Zywicki and Rix (2005), and more recently Park and Shawver (2009), have developed data processing techniques to directly mitigate near-field effects.

With an aim to find a rigorous solution to the minimum offset problem, Xu et al. (2006) proceeded to study the minimum offset problem for a layered system theoretically. They considered a simple, layered elastic system, consisting of a single layer over a halfspace. Near-field effects were theoretically considered as (1) the interaction of reflected P-waves and direct SV-waves (Figure 2.13a), and (2) the interaction of P- and SV-waves created at the free surface boundary by an incident SV-wave reflecting off the lower layer (Figure 2.13b). They found that both approaches produced the same solution (Equation 2.6), if the incident SV-wave in the latter approach is critically refracted. They developed a series of minimum offset curves as shown in Figure 2.13c. One problem with this approach is that the  $V_p/V_s$  contrast of the upper layer must be known *a priori* – although it is largely a site-dependent value, the authors suggest that  $V_p/V_s = 4.0$  is common for near-surface materials. They admit that most surface wave testing will be controlled by the depth of investigation (i.e. wavelength), without prior knowledge of velocities, but note that the depth-based approach risks omitting high-frequency Rayleigh waves.

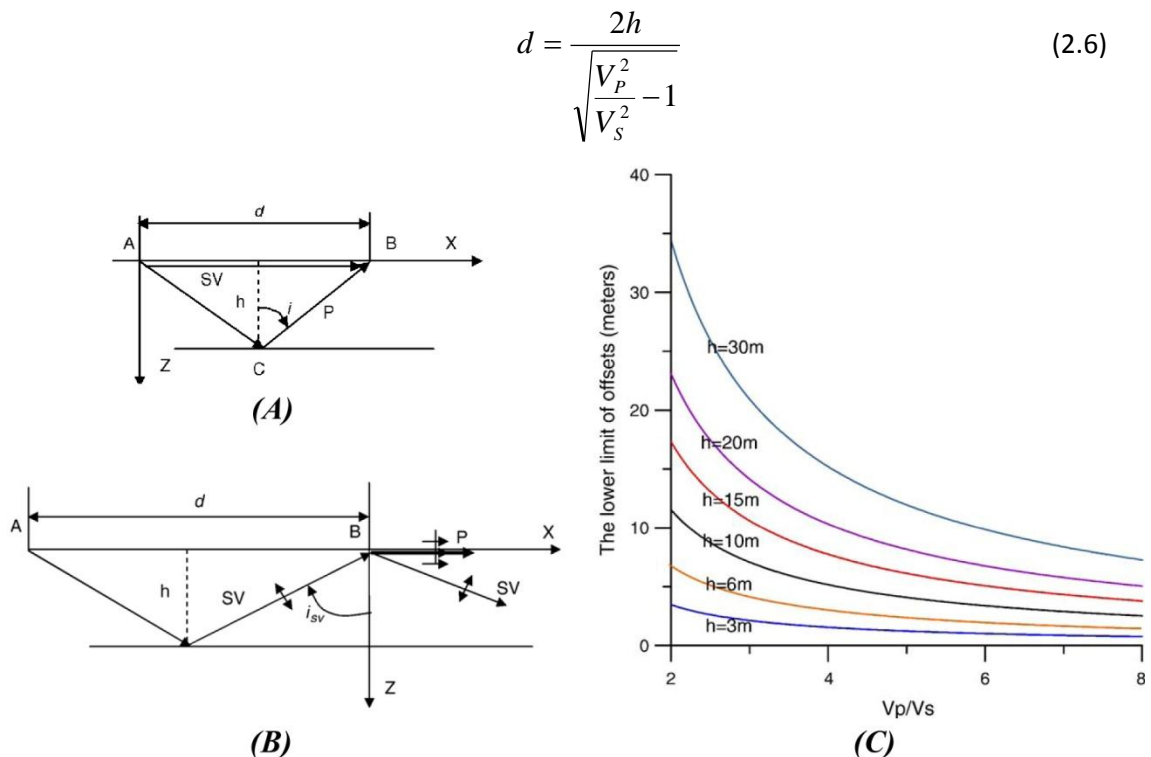


**Figure 2.13** Near-field effects theoretically considered as (A) the interaction of direct SV-waves and reflected P-waves and (B) a reflected SV-wave producing P and SV-waves at the surface. Minimum offset curves (C) are shown as a function of upper layer  $V_p/V_s$  contrast and depth. Adapted from Xu et al. (2006).

Yoon and Rix (2009) performed a thorough study on near-field effects in multi-channel measurements and developed a new parameter, the Normalized Array Center (NAC), for describing the minimum offset distance. They defined the NAC, the ratio between the center of the array and the wavelength of the Rayleigh wave (Equation 2.7) – a visual representation of  $NAC = 2$  is presented in Figure 2.14. They also defined the normalized Rayleigh wave velocity (NRV) as the ratio of the measured velocity to the plane wave velocity (Equation 2.8). An NRV value of 1.0 corresponds to a purely far-field condition, while other values indicate the presence of near-field effects.

$$NAC = \frac{\bar{x}}{\lambda_R} = \frac{\frac{1}{M} \sum_{m=1}^M x_m}{\lambda_R} = \frac{\left( \frac{1}{M} \sum_{m=1}^M x_m \right) f}{V_R} \quad (2.7)$$

$$NRV = \frac{V_R}{V_{R,plane}} \quad (2.8)$$

where  $\bar{x}$  = mean distance of all receivers in an array relative to the source;  $\lambda_R$  = wavelength of the Rayleigh wave;  $M$  = total number of receivers in the array;  $x_m$  = distance of the  $m$ th receiver relative to the source;  $V_R$  = measured Rayleigh wave velocity at frequency  $f$  and  $V_{R,plane}$  = plane Rayleigh wave velocity at the same frequency.

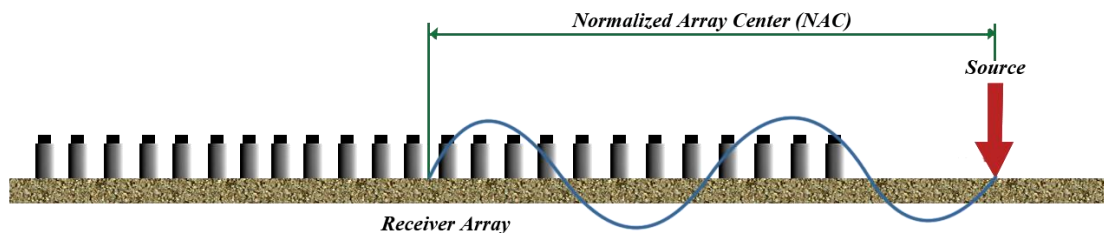


**Figure 2.14** Schematic representation of the Normalized Array Center (NAC) parameter for a 24 receiver array

To study near-field effects, Yoon and Rix (2009) performed extensive numerical modeling of various  $V_s$  profiles (Figure 2.15), laboratory simulations with a “half-space” of synthetic material, and multi-channel field testing at the Oakridge landfill in Dorchester, South Carolina. They found good agreement among methods in the normalized (NAC/NRV) results, as shown in Figure 2.16, but were careful to note that differences in geometry and boundary conditions may influence such comparisons. They attribute much of the scatter to random errors in experimental measurements. From their results, Yoon and Rix (2009) derived the following key conclusions about near-field effects: (1) Near-field effects generally cause an

underestimation of dispersion values; (2) Near-field effects are quite significant for irregular soil profiles, less so in simple profiles; (3) An increased number of receivers greatly reduces the intensity of near-field effects for irregular soil profiles; and (4) To limit the error in surface wave velocity to less than 15% (i.e. error in assuming a far-field solution when near-field effects are indeed present) the NAC values must be greater than 1, and to limit the error to less than 5%, NAC values must be greater than 2.

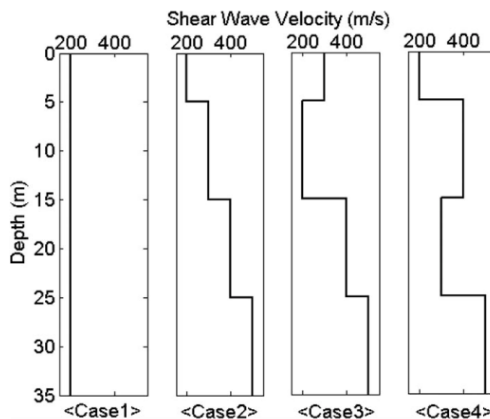


**Figure 2.15**  $V_s$  Profiles used to study near-field effects for unsaturated conditions (Yoon and Rix 2009)

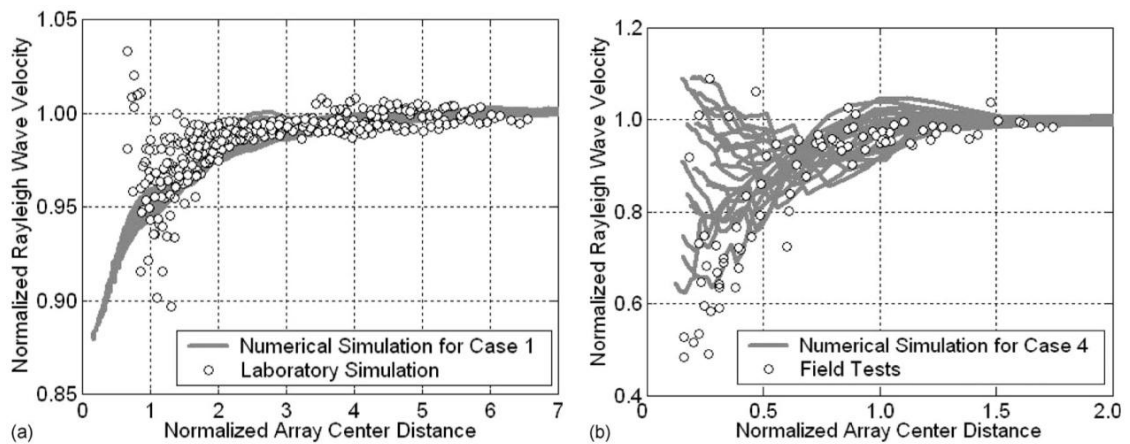


**Figure 2.16** Normalized comparison of numerical, laboratory, and field test results. Adapted from Yoon and Rix (2009)

One limitation of the Yoon and Rix (2009) study was that it only considered unsaturated conditions (Poisson's ratio = 0.30). Li and Rosenblad (2011) showed experimental data that was inconsistent with some of Yoon and Rix's findings and suggested that Poisson's ratio may have a significant effect on near-field criteria. Li (2011) later extended the work of Yoon and Rix (2009) by considering minimum NAC values for saturated conditions. He performed several numerical analyses and compared his results to experimental results from multi-channel surface wave

testing at a field site in the Mississippi Embayment. His simulation results for unsaturated conditions (Poisson's ratio = 0.30) agreed well with the criteria recommended by Yoon and Rix (2009), requiring NAC values of 1 to 2 for near-field avoidance with less than 5% error in NRV. He also showed, however, that the required NAC value varied greatly – ranging from 0.4 to 2.0 – depending on the  $V_s$  profile gradient and the saturation conditions (i.e. Poisson's ratio) of the site.

Bodet et al. (2009) simultaneously considered the effect of array length (i.e. “spread length”) on dispersion resolution and the presence of near-field effects in multi-channel SWM. They performed sensitivity studies with numerical and physical models to study the interaction of near-field effects and “spread length effects”, and determine maximum wavelength criteria for near-field avoidance. They observed that near-field effects become significant when the wavelength exceeds 50% of the spread length and recommended this value as a data collection criterion for multi-channel measurements. They noted, however, that such criteria lead to a loss of recorded data and suggested that alternative approaches should be considered, even to the point of “accepting” near-field effects. A composite interpretation of the near-field avoidance criteria recommended by Yoon and Rix (2009) and Bodet et al. (2009) is presented in Figure 2.17, indicating that the minimum NAC and array length to avoid the near-field is larger than previously thought. Using their criteria, a spread length of 180 m would be required to profile to a depth of 30m – in practice, however, such criteria are rarely applied.

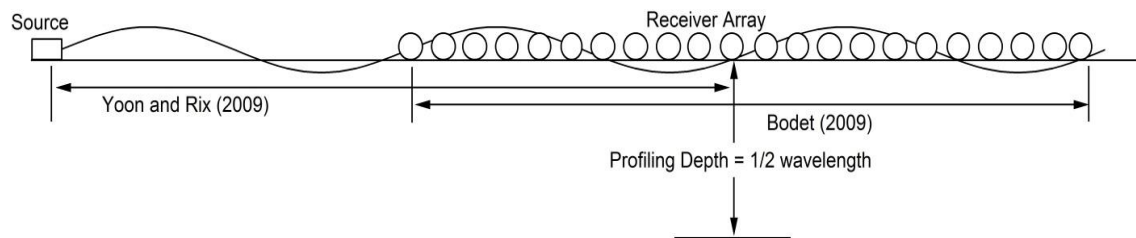


**Figure 2.17** Minimum size and location required to truly avoid near-field effects with a multi-channel receiver array

Zywicki and Rix (2005) abandoned traditional plane wave analyses for a “cylindrical beamforming” processing technique that accounts for the cylindrically spreading nature of the Rayleigh wave in the near-field. They defined three variations of the “near-field effect” problem: (1) *model incompatibility*, between the actual cylindrically spreading wavefront and processing methods that assume a planar wavefront; (2) *near-field body wave effects*, arising from body wave propagation in the near-field that does not contribute higher Rayleigh wave modes; and (3) *far-field body wave effects*, caused by “body wave superposition contributing to additional

surface wave modes.” They observed that, while multi-channel methods do have an advantage over SASW in some areas, all surface wave methods appear to be equally afflicted with the model incompatibility issue.

Therefore, Zywicki and Rix (2005) developed an alternative signal processing approach with an aim to resolve model incompatibility. The so-called “cylindrical beamformer” produces better phase velocity estimates than a traditional plane wave beamformer, but requires greater numerical complexity. Plane wave beamformers utilize the simple and efficient fast Fourier transform (FFT) algorithm, while the cylindrical beamformer requires a numerically-calculated steering vector for each possible wavenumber. Use of the cylindrical beamformer, however, requires accurate separation of Rayleigh wave modes, which can be difficult to establish with absolute certainty. Under the tenuous assumption that such modes can be accurately resolved, Zywicki and Rix further suggest that body wave contributions can also be eliminated, since body wave modes appear orthogonal to Rayleigh wave modes on a dispersion image. Li and Rosenblad (2011) showed only partial removal of near-field effects using the cylindrical beamformer.

Park and Shawver (2009) developed a data processing technique involving stacking MASW dispersion data from multiple source offsets to eliminate near-field effects. They collected experimental data from a stationary multi-channel array with multiple source impacts, the source being located at increasing distances (offsets) from the array with each impact. They used MASW to individually process the data from each impact and stacked the resulting dispersion images to produce a single dispersion image. They reasoned that each offset was subject to the same fundamental and higher modes of the underlying soil, which would lead to increased modal sensitivity. Similar to other variations of the multi-channel method, this approach also depends on the separation of modes, which can be ambiguous as previously noted.

## **2.5 Previous Studies on Poisson’s Ratio and Surface Waves**

### **2.5.1 Introduction to Poisson’s Ratio and Surface waves**

Poisson’s ratio is an elastic constant describing the relationship between deformations of a material in orthogonal directions. In soils, the values of Poisson’s ratio can vary greatly (from 0.2 to nearly 0.5) due to the presence of water in the void space. Typically, values of Poisson’s ratio

are assumed in the inversion stage of the analysis if they are not known *a priori*. This section summarizes past studies concerned with the effect of Poisson's ratio on surface wave analyses.

### 2.5.2 Assessing Sensitivity of Surface Wave Measurements to Poisson's Ratio

Mera (1995) considered the impact of Poisson's ratio on near-field effects, in a theoretical sense, for the simple case of a harmonic point load source on the surface of a homogeneous halfspace. With his model, Mera proceeded to study the effect of Poisson's ratio on wave propagation characteristics: he considered the proportion of "radiated power" in each wave type at a given Poisson's ratio (Figure 2.18a) and differences in "dispersion" properties (both near-field and far-field) at different values of Poisson's ratio (Figure 2.18b). The total radiated power for each wave type was determined by integrating the power per unit area over either a hemisphere of large radius (for body waves) or a cylinder of large radius (for surface waves). From Figure 2.18a, it appears that most of the energy from an impulse load is transmitted as surface waves (roughly 60 to 70 percent of the radiated power). From Figure 2.18b, it is evident that the only effect of Poisson's ratio on the far-field solution is to shift the location of the dispersion curve (translation). In the near-field, however, it is evident that increasing the value of Poisson's ratio results in not only translation, but also increasing undulations in the dispersion curve itself – suggesting that the near-field is more sensitive to changes in Poisson's ratio than the far-field.

Chen et al. (2004) studied the impact of the source-receiver configuration on SASW results, with particular attention to the effect of Poisson's ratio. They performed a parametric study on source-to-first-receiver distance ( $r$ ), receiver-to-receiver distance ( $\Delta x$ ), and Poisson's ratio ( $\nu$ ) with an axisymmetric finite element model of a uniform elastic halfspace. The resulting dispersion curves, shown in Figure 2.19, experience increasingly large fluctuations as the value of Poisson's ratio approaches saturated conditions (near  $\nu=0.5$ ). The effect is most notable when receivers are closely spaced (small  $\Delta x$  values) and close to the source (small  $r$  values). Chen et al. attributed these fluctuations to body wave interference, especially P-waves.

Chen et al. (2004) observed that the validity of a plane Rayleigh wave (e.g. far-field) assumption is strongly dependent on the value of Poisson's ratio: for instance, a minimum source offset of  $r/\lambda > 1$  is valid when  $\nu \leq 0.25$  – larger values of  $\nu$  require larger minimum offsets for the plane wave assumption to be valid. They also noted that, while a large SASW receiver spacing would allow valid use of the plane wave assumption, it would require a larger source

and increase the potential for erroneous phase unwrapping. Solely on the basis of their SASW sensitivity study, they closed with a blanket statement that MASW is better than SASW. Chen et al. did not once use the term “near-field”, but its effect is quite evident in Figure 2.19 – where small spacings ( $r$  and  $\Delta x$ ) correspond to large fluctuations in velocity values.

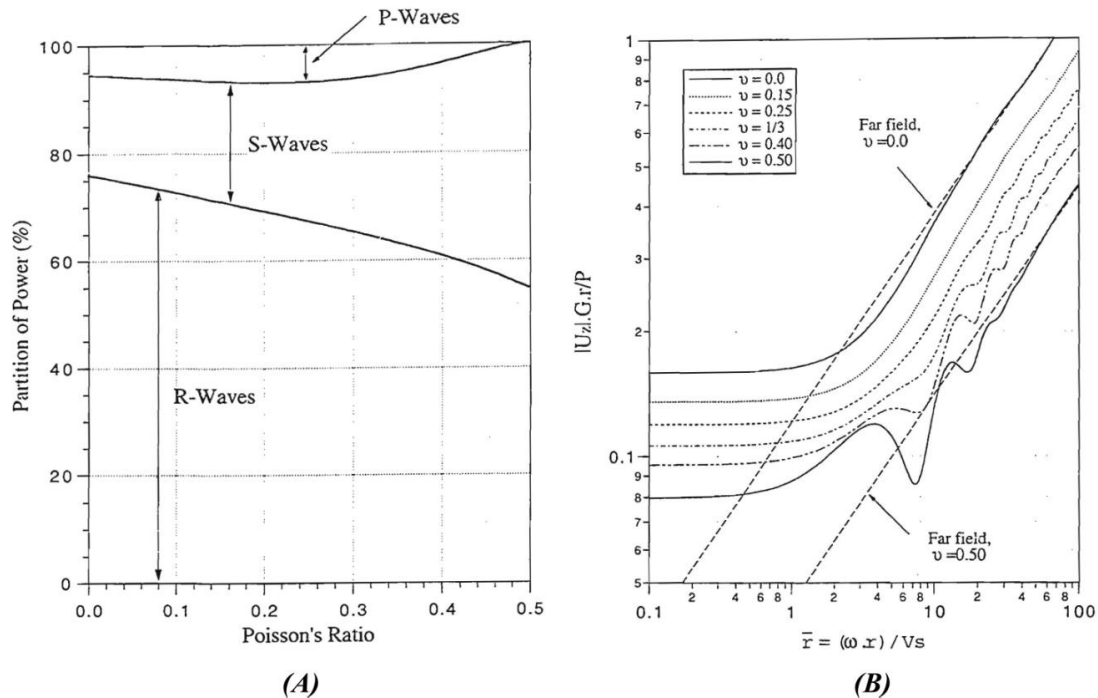


**Figure 2.18** Effect of Poisson's ratio on the near-field in terms of (A) the amount of “radiated power” in body waves and surface waves for various Poisson's ratio values, and (B) normalized curves of vertical displacement versus average radial distance from the point load source – all lines represent near-field conditions unless otherwise noted. (Mera 1995)

Li (2011) studied the impact of Poisson's ratio ( $\nu$ ) on the minimum offset required to avoid the near-field for multi-channel measurements of in saturated conditions ( $V_p = 1600$  m/s). They simulated surface wave measurements for five simple  $V_s$  profiles (Figure 2.20) using a model that includes near-field effects. They studied the Rayleigh wave dispersion characteristics of the three profiles using the normalized parameter (NAC and NRV) approach developed by Yoon and Rix (2009). Defining a 5% in normalized velocity as the near-field threshold, they found good agreement with the recommendations of Yoon and Rix (2009) for the unsaturated case of uniform  $V_s$  profile, with a limiting NAC of 2.0 to avoid the near-field. They found that the NAC value was strongly dependent on the  $V_s$  profile and the value of Poisson's ratio. Some cases required a restrictive limitation on the NAC value to avoid the near-field, while smaller NAC values were permissible for other cases. Depending on the  $V_s$  profile and Poisson's ratio value,

they found limiting NAC values spanning a large range from 2.0 to 0.4. A typical normalized dispersion curve from this study, with a limiting NAC value of approximately 2.0, is shown in Figure 2.21.

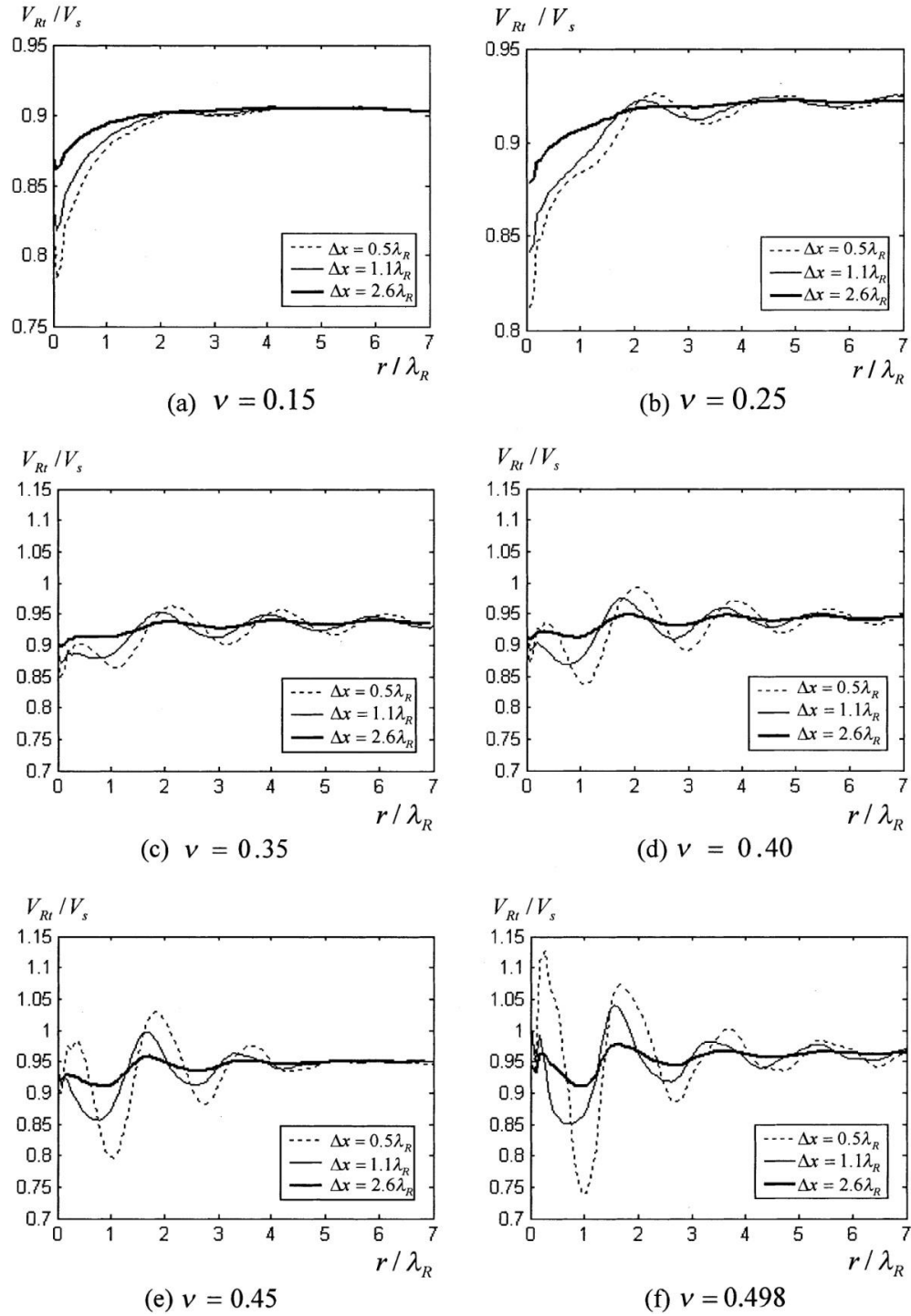


**Figure 2.19** Normalized dispersion curves from a parametric study of source-to-first-receiver spacing ( $r$ ), receiver-to-receiver spacing ( $\Delta x$ ), and Poisson's ratio ( $\nu$ ) performed by Chen et al. (2004)

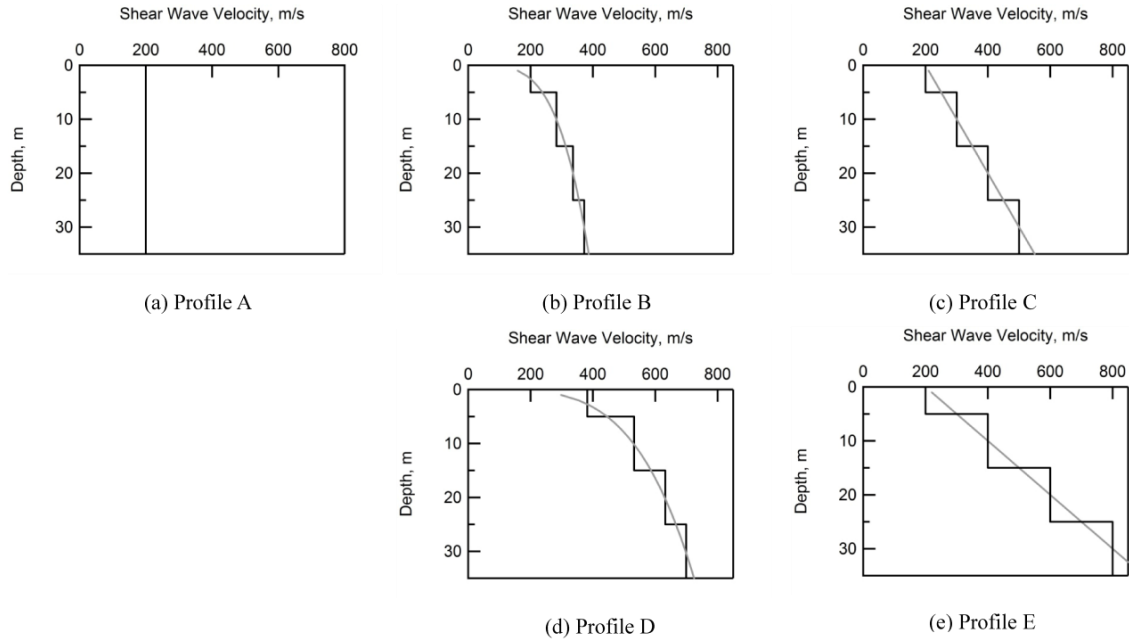


Figure 2.20  $V_s$  profiles used to study near-field effects in saturated conditions. Adapted from Li (2011)

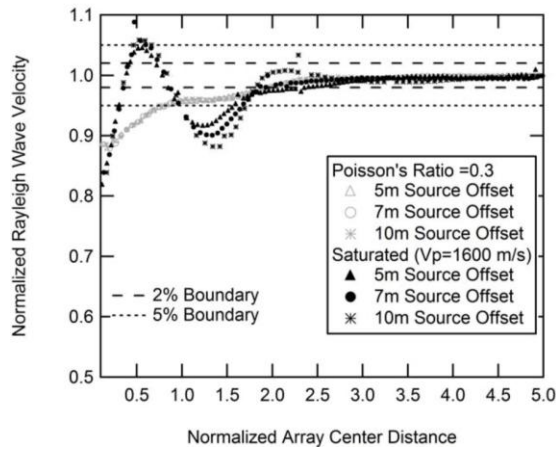


Figure 2.21 Saturated versus unsaturated dispersion curves for the non-dispersive case (Rosenblad and Li 2011)

### 2.5.3 Inferring Poisson’s Ratio from Surface Wave Measurements

As shown in Figure 2.18, the value of Poisson’s ratio affects the energy transmitted by the Rayleigh wave and far-field Rayleigh wave velocity. However, because the shape of the far-field dispersion curve does not change with Poisson’s ratio, it is not possible to infer Poisson’s ratio from far-field Rayleigh waves alone. In other words, the same quality of fit between the experimental and theoretical dispersion curves can be achieved with any value of Poisson’s ratio. Therefore, in current SWM practice using far-field dispersion curves, the value of Poisson’s

ratio must be assumed for SWM analyses if it is not known independently. If the wrong value of Poisson's ratio is assumed, the final  $V_s$  profile determined from the SWM will be incorrect. This error is currently accepted in SWM practice. Only a few studies have considered how to determine Poisson's ratio from surface wave measurements.

Ivanov et al. (2000) used multi-channel data to perform both MASW (to determine the  $V_s$  profile) and a refraction analysis (to determine the P-wave velocity profile from the first arrivals), from which a profile of Poisson's ratio was inferred. This is an example of using a supplementary method (in this case, refraction) to determine Poisson's ratio at the site. Here, data collected from a single long receiver array was processed by both methods. MASW processing was used to determine a contour map of  $V_s$  versus depth and horizontal distance. A distribution of Poisson's ratio (in relation to depth or  $V_s$ ) was assumed and the P-wave velocity model was adjusted until it closely matched the experimental P wave refraction results. The P-wave velocity ( $V_p$ ) profile is assumed to have the variation trends as the  $V_s$  profile (derived from MASW) to provide a starting model and thereby yield a unique solution to the refraction analysis.

The approach of Ivanov et al. (2000) has the advantage of producing a 2D planar profile of Poisson's ratio for a site along the line of the receiver array. However, this method is limited to profiles where velocity increases with depth. In the case of a decrease in velocity with depth, the transmitted wave would become "trapped" in the lower velocity layer and would not refract back to the surface. If layers of increasing velocity are underlain by low velocity layer, then a profile of Poisson's ratio derived from the approach of Ivanov et al. would only be valid above the low velocity layer. A similar problem occurs if the refracting layer is deeper than the profiling depth of the surface wave – in which case a profile of Poisson's ratio would be limited by the latter.

Another approach, using surface wave data alone, was examined by Karray and Lefebvre (2008) using a multi-modal SASW inversion to compute the value of Poisson's ratio for a given profile. They separated modes in the experimental dispersion data by multiple applications of time-variable filters. The multi-modal inversion requires an initial assumption of Poisson's ratio, which is then used to evaluate the fundamental Rayleigh mode; the theoretical (first or higher) mode is compared to a comparable mode determined experimentally. The P-wave velocity profile is then adjusted and the inversion repeated iteratively until the theoretical and experimental modes match. Combining  $V_s$  and  $V_p$  profiles provides a profile of Poisson's ratio.

Error is minimized in the matching of modes by use of a linear optimization (simplex) algorithm controlled by least-squares criteria. They analyzed both simulated and experimental data and found good agreement with the theoretical model.

Karray and Lefebvre (2008) derived three key conclusions regarding Poisson's ratio and surface wave measurements. First, they observed that Poisson's ratio has a greater effect on the theoretical dispersion curve for real profiles than it does for simple (e.g. homogeneous or two-layer) profiles. Second, the magnitude of error in  $V_s$  profile estimation, due to an incorrect value of Poisson's ratio, depends on the  $V_s$  profile gradient and the  $V_s$  pattern in the upper layers. Third, they caution that, if Poisson's ratio is going to be assumed instead of inverted, the greatest care must be taken to select a value based on all available information; further adding that the value of Poisson's ratio above the water table may be the most critical of all. They also note that fundamental mode Rayleigh wave processing of the same data can lead to different  $V_s$  profiles for different assumptions of Poisson's ratio.

#### **2.5.4 Relevance of Past Studies: Inferring Poisson's Ratio from the Near-field**

This thesis examines another approach to inferring Poisson's ratio from surface wave measurements alone. It posits that Poisson's ratio can be inferred from surface wave analyses by intentionally including more of the near-field in both the data collection and inversion stages. Some previous studies (Chen et al. 2004; Li 2011; Rosenblad and Li 2011) have considered the effect of Poisson's ratio on the near-field portion of the dispersion curve. Others (Ivanov et al. 2000; Karray and Lefebvre 2008) have attempted, by various methods, to infer Poisson's ratio from surface wave data. Yet no one, to the author's knowledge, has attempted to infer Poisson's ratio by using the near-field portion of the dispersion curve. One objective of this research is to determine if this is possible.

The data presented by Chen et al. (2004) – for SASW – and Li (2011) – for multi-channel SWM – appear to show that it should be possible to infer Poisson's ratio using the near-field data (although this was not their objective): Referring to Figure 2.19 and Figure 2.21 it is apparent that, the shape of the dispersion curve in the near-field changes with changes in Poisson's ratio. Furthermore, the relative shape of the dispersion curve at different values of Poisson's ratio (see also Figure 2.18) indicates that surface wave analyses, with near-field effects included, should be sensitive to the “correct” value of Poisson's ratio. The presence of such sensitivity suggests that Poisson's ratio can be determined in the inversion stage of the analysis.

## 3 METHODOLOGY

### 3.1 Introduction

Chapter 3 describes the approach used to study the effect of the near-field on active-source surface wave measurements. Section 3.2 describes the two theoretical models used for surface wave analyses in this study. Section 3.3 describes the commercial software program WinSASW, which was extensively used in the surface wave analyses performed for this thesis. Section 3.4 describes the approach used to process multi-channel data for import into WinSASW. Section 3.5 describes the methods used to assess the sensitivity of the near-field portion of the dispersion curve to various changes in profile conditions. Section 3.6 describes the methods used to simulate, process, and invert experimental surface wave data to assess the effectiveness of different data collection and inversion procedures. Section 3.7 describes how experimental data from a real field site were collected, processed, and inverted to assess the effectiveness of different data collection and inversion procedures.

### 3.2 Theoretical Models

Two theoretical models of surface wave propagation were used in this study. The two dimensional “plane wave” solution (termed “2D” in this thesis), as described in Section 3.2.1, computes the normal modes of planar Rayleigh wave propagation in a layered system. This model is commonly used as the theoretical model in the inversion stage of surface wave analysis. The three-dimensional solution (termed “3D” in this thesis) computes displacements from all wave contributions (surface waves and body waves) at a given distance from the source. This model is more computationally extensive than the 2D solution, but provides a realistic model of wave propagation in surface wave measurements. In this study, the 3D solution was used both to simulate experimental surface wave measurements and, in some cases, to compute the theoretical model in the inversion analysis stage. Regardless of the application, the mathematical model assumes a horizontally layered profile over a uniform halfspace. The key characteristic of each solution, as it pertains to this thesis, is the presence of near-field effects in the 3D solution and lack thereof in the 2D solution.

### 3.2.1 Two-dimensional Solution (2D)

The 2D solution is used to calculate the normal modes of Rayleigh wave propagation in a horizontally layered half-space. The modes of propagation are usually presented in terms of dispersion curves expressing the phase velocity of each mode of propagation as a function of frequency or wavelength. The 2D solution can be obtained using either the transfer matrix approach (Haskell 1953; Thompson 1950) or the stiffness matrix approach (Kausel and Roesset 1981). In this study, the 2D solution was obtained using the program WinSASW, which contains an implementation of the stiffness matrix approach.

In the stiffness matrix approach, displacements the top and bottom of each layer in the profile are related to the external loads applied at the same interfaces through a local (i.e. layer-specific) stiffness matrix. The local stiffness matrices of individual layers are combined in a global stiffness matrix, while considering the compatibility of displacements and force equilibrium at each layer interface. The displacements and forces for the layered profile are related as:

$$K\bar{U} = P \quad (3.1)$$

where  $K$  is the dynamic stiffness matrix for the layered medium,  $U$  is a vector of layer interface displacements, and  $P$  is a vector of applied loads at the interfaces. The normal modes of the system can be obtained from Equation 3.1 by setting the force vector equal to zero. A characteristic equation is obtained by equating the determinant of the stiffness matrix to zero. The roots of the characteristic equation are the normal modes of Rayleigh wave propagation. Details of this procedure can be found in Kausel and Roesset (1981).

In the case of a homogeneous half-space, this approach produces a single Rayleigh mode (i.e. the fundamental mode). In a layered system, where properties change with depth, multiple modes of propagation are possible. The 2D solution corresponds to the fundamental mode of Rayleigh wave propagation (i.e. the smallest eigenvalue of the dynamic stiffness matrix), which gives good results for soil deposits with gradually varying shear wave velocities with depth (Joh 1996; Mera 1991). The primary limitation of the 2D model is that it does not account for the cylindrical spreading of the surface waves and it does not include the contributions of body waves. It is an appropriate model only for locations far from the source (the far-field) where these contributions can be considered negligible.

In this thesis, the 2D solution was used for two primary purposes: (1) to serve as a baseline for comparison to 3D results and (2) to evaluate the consequences of using a plane

wave inversion on data that includes near-field effects. For the sensitivity study described in Section 3.5, forward modeling was performed using both 2D and 3D solutions for the same profile conditions. Any result produced by the 3D solution that deviated from the 2D solution was considered as the effect of the near-field. In the inversion analysis studies, with both simulated (Section 3.6) and real data (Section 3.7), the results of 2D and 3D inversions were compared to assess the effectiveness of the inversion process when varying levels of near-field contribution are included in the analysis.

### 3.2.2 Three-Dimensional (3D) Complete Solution

A better simulation of surface wave measurements can be achieved using the so-called three-dimensional (3D) solution, which includes all body wave and surface wave contributions and incorporates three-dimensional wave propagation. By modeling the complete wave field, the 3D solution accurately models wave propagation in both the near-field and the far-field. The 3D solution implemented in WinSASW calculates the dynamic response of a soil profile at a given distance from the source to a vertical disk load applied at the surface. In this way, the 3D model closely simulates the actual surface wave measurement performed in the field. The displacements can be used to calculate a theoretical dispersion curve for the inversion analysis. The dispersion curve obtained in this manner is not necessarily one particular Rayleigh wave mode, but may be a superposition of body waves and modes from surface waves (i.e. “effective” or “apparent” mode). This subsection presents a summary of the 3D method drawing from Roesset et al. (1991). A more detailed presentation of this method can be found in Kausel and Peek (1982).

For axisymmetric loading, the radial and vertical displacements,  $U$  and  $W$ , can be calculated from:

$$U = qR \int_0^{\infty} (\bar{u} J_1(kR) J_1(kr)) dk \quad (3.2)$$

$$W = \int_0^{\infty} (\bar{w} J_1(kR) J_0(kr)) dk \quad (3.3)$$

where  $J_0$  and  $J_1$  are zero and first order Bessel functions,  $k$  is the wave number,  $r$  is the radial distance from the source to the receiver location,  $R$  is the radius of the source, and  $q$  is the magnitude of the uniformly distributed surface load. The displacements  $\bar{u}$  and  $\bar{w}$  are functions of the wave number,  $k$ , which can be obtained by assembling the global stiffness matrix and

solving Equation 3.1 for a harmonic load at the surface. Therefore, solving for the displacements requires assembling the stiffness matrix,  $K$ , of the layered medium, solving Equation 3.1 for many different wavenumbers,  $k$ , and numerically evaluating the integrals of Equations 3.2 and 3.3 (Li 2011; Mera 1995). This approach (termed the continuous formulation) is efficient for simple layered systems, but requires excessive computational resources and is not practical for a system with several layers (Roesset et al. 1991). An alternative approach is the so-called “discrete” formulation, also known as the thin layer method (TLM). For the discrete formulation, a Taylor series expansion is applied to the elements of the dynamic stiffness matrix,  $K$ , and truncated at the second-order term. This is equivalent to assuming that displacements in each layer vary linearly with depth, which requires that layers be subdivided into sufficiently thin layers to produce reliable results. The 3D solution implemented in WinSASW and applied in this study uses the discrete formulation (Joh 1996).

The 3D solution was used extensively in the studies performed for this thesis. Ground motions at various distances from the source were simulated using the 3D solution. Experimental dispersion curves were calculated from the simulated displacements and compared to 2D to assess the influence of near-field contributions. Both the 2D and 3D forward models were used to calculate theoretical dispersion curves in the inversion analysis to assess the ability to recover the original shear wave velocity profile using different data collection criteria and inversion models.

### **3.3 Surface Wave Analyses with WinSASW**

WinSASW is a windows-based surface wave analysis program developed at the University of Texas. The research completed for this thesis made extensive use of WinSASW to study the influence of near-field effects on surface wave measurements. Specifically, the following analyses were performed with WinSASW: (1) development of individual experimental dispersion curves using phase unwrapping, (2) calculating an average experimental dispersion curve from several individual dispersion curves, (3) performing forward modeling using either the 2D or 3D solution (Section 3.2) to calculate theoretical dispersion curves for a given soil profile, and (4) performing inversion analysis to minimize the error between theoretical and experimental dispersion curves by iteratively adjusting the model  $V_s$  profile with an optimization algorithm. The surface wave data processing and analysis procedures implemented in WinSASW, and used in this study, are described below.

### 3.3.1 Dispersion Processing/Phase Unwrapping

Experimental data were imported into WinSASW in the form of a transfer function – a wrapped phase plot showing the phase difference between receivers as a function of frequency – as shown in Figure 3.1. For most of the analyses performed in this study (Section 3.6), experimental data were simulated using the program FitSASW, which produces the transfer function as a direct output (Section 3.6.1). For analyses performed using real experimental data (Section 3.7), transfer functions were computed from time-series data transformed into the frequency domain using a Fast Fourier Transform (FFT) and cross-multiplication. Separate transfer functions were developed or calculated for each receiver spacing used in the simulation or field data collection.

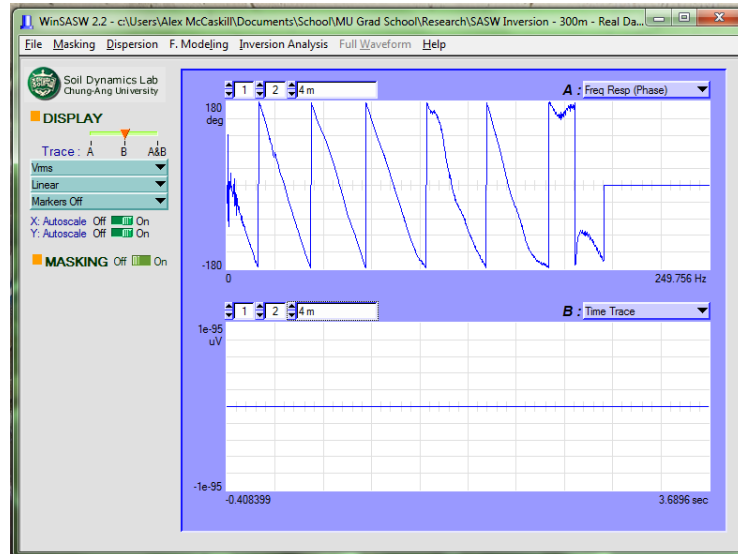


**Figure 3.1** Example of wrapped phase plot (i.e. transfer function) imported into WinSASW for processing

Having input a wrapped phase plot in WinSASW for each receiver spacing, the next step was to omit (i.e. “mask out”) portions of the phase plot corresponding to regions affected by near-field effects. For the examples shown in this section, the near-field criterion of Gucunski and Woods (1992) was applied, which requires that the first  $360^\circ$  of the wrapped phase plot be masked out (i.e.  $d/\lambda = 1.0$ ). The measurement settings window of WinSASW, where the  $d/\lambda$  criterion can be entered directly, is shown in Figure 3.2, while an example of phase plot masking is shown in Figure 3.3. The number of “jumps” from  $-180^\circ$  to  $+180^\circ$  contained by each “masked out” region must be specified during the masking process to produce the correct experimental dispersion curve.

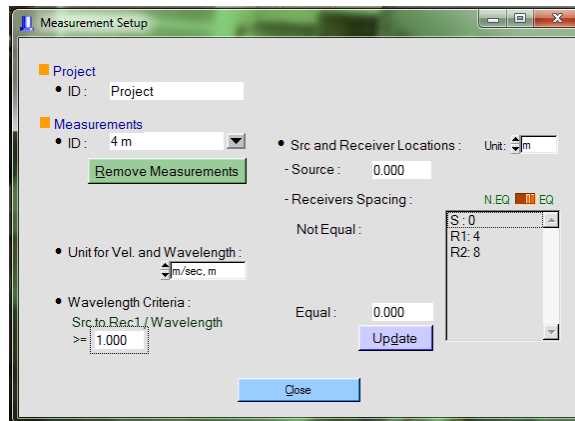


Figure 3.2 Measurement settings window in WinSASW

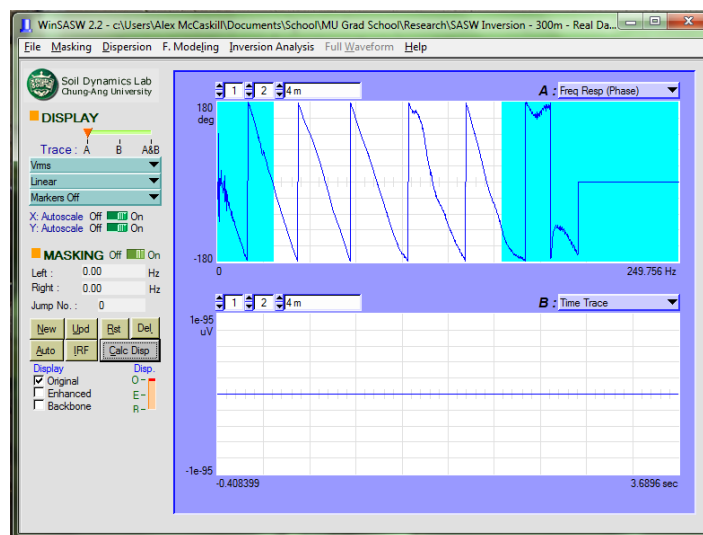
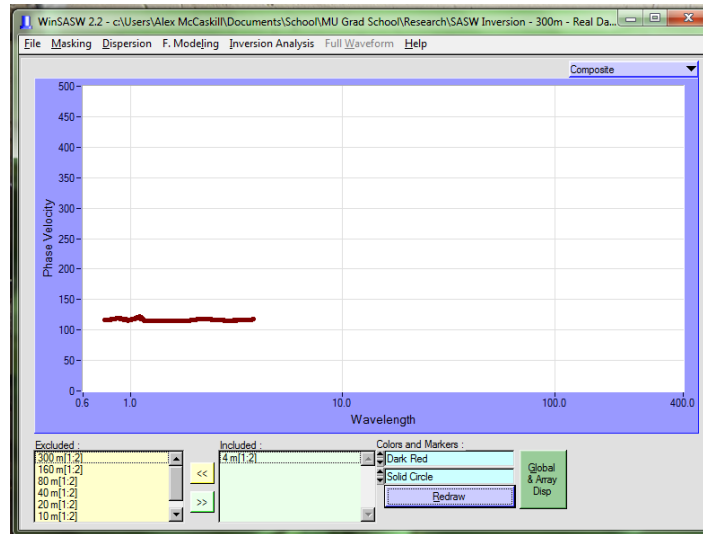
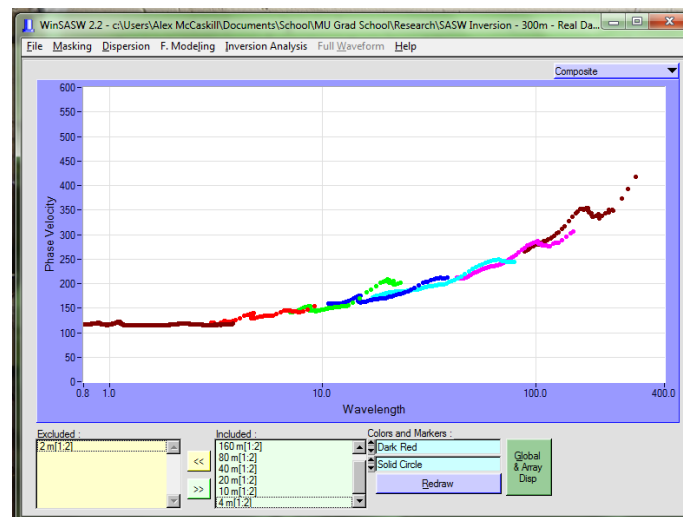


Figure 3.3 Example of “masking out” near-field effects (left side) and poor quality data (right side) in WinSASW

Once the masking process was complete, the next step was to determine the unwrapped phase and produce a dispersion curve. The unwrapping process, itself, was performed internally in WinSASW. A dispersion curve produced from the masked wrapped phase data above (Figure 3.3) is shown in Figure 3.4. The masking and unwrapping processes were repeated with data from several different receiver spacings to produce the individual segments of the “composite” dispersion curve shown in Figure 3.5. The composite dispersion curve, however, may include hundreds of data points, which can be very computationally demanding for an inversion analysis.



**Figure 3.4** Single dispersion curve from a 4m SASW spacing, as calculated from the wrapped phase plot of Figure 3.3



**Figure 3.5** Composite dispersion curve generated from SASW spacings of 4m, 10m, 20m, 40m, 80m, 160m, and 300m

### 3.3.2 Averaging Experimental Dispersion Data

An averaging scheme was applied to the composite experimental dispersion curve to generate an average experimental dispersion curve that can be used in the inversion analyses. WinSASW can average the composite dispersion curve in two different ways, “global” or “array”, depending on the method of inversion analysis to be implemented. Implementation differences between these methods are discussed later in this section, but both of them use the same averaging algorithm. Much of the following description, concerning the averaging algorithm in WinSASW, is drawn from the work of Joh (1996).

The averaging algorithm in WinSASW is based on the principle of a moving average, a linear operation, where an arithmetic average is calculated for  $m$  consecutive data points. The average value of a moving average is assigned to the middle point of the  $m$  consecutive points. For the next average value, the  $m$ -point segment is shifted by one point, such that  $m-1$  points are overlapping the previous segment. WinSASW uses “a polynomial best-fit curve to obtain the average for each segment, combined with the idea of overlapping the segments to extract the basic trends,” as shown in Figure 3.6.

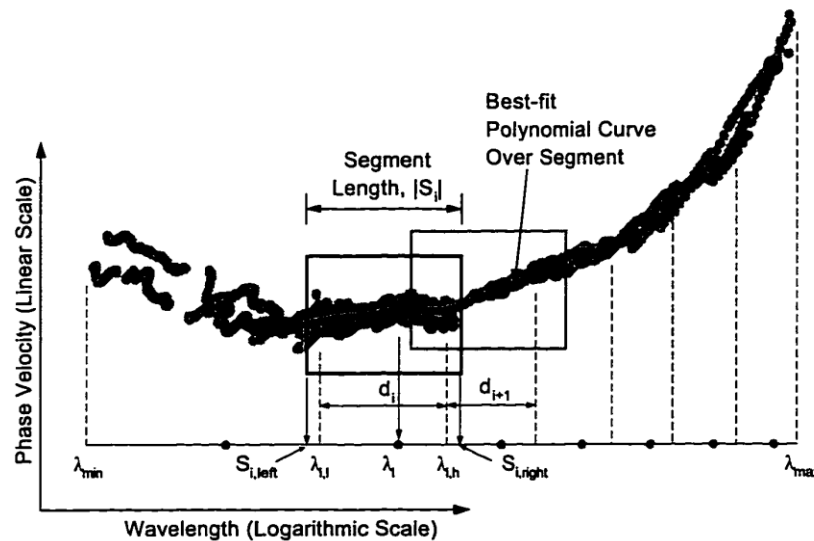


Figure 3.6 Illustration of the averaging scheme used in WinSASW (Joh 1996)

Joh (1996) proceeds to describe the five steps of the averaging process in detail:

1. Determine the distribution of data in the average experimental dispersion curve.

Joh noted that small wavelength data ultimately produces a better  $V_s$  profile. Therefore, he introduced a constant “increment ratio” to distribute “more data in the small wavelength range” and determine “where the average phase velocities are evaluated.” The length of the division,  $d_i$ , which is represented by an average velocity, is increased by a constant ratio,  $r$ , as shown in Equation 3.4.

$$d_{i+1} = r + d_i \quad (3.4)$$

where the increment ratio,  $r$ , typically ranges from 1.01 to 1.20. When the desirable number of points for the average dispersion curve is  $n$ , the  $i$ th wavelength,  $\lambda_i$ , is determined as shown in Equation 3.5.

$$\lambda_i = \frac{\lambda_{i,l} - \lambda_{i,h}}{2} \quad (3.5)$$

where  $\lambda_{i,l}$  and  $\lambda_{i,h}$  are the low and high ends of the  $i$ th division,  $d_i$ , and are related to  $d_i$  as shown in Equation 3.6. The values of  $\lambda_{i,l}$  and  $\lambda_{i,h}$  are determined as shown in Equations 3.7 and 3.8.

$$d_i = \lambda_{i,h} - \lambda_{i,l} \quad (3.6)$$

$$\lambda_{i,l} = \lambda_{\min} + (\lambda_{\max} - \lambda_{\min}) \cdot \left( \frac{r^{i-1} - 1}{r^{n-1} - 1} \right) \quad (3.7)$$

$$\lambda_{i,h} = \lambda_{\min} + (\lambda_{\max} - \lambda_{\min}) \cdot \left( \frac{r^i - 1}{r^{n-1} - 1} \right) \quad (3.8)$$

Here,  $\lambda_{\max}$  and  $\lambda_{\min}$  are the maximum and minimum wavelengths, respectively, of the composite experimental dispersion curve.

2. *Determine the length of the segment of the composite experimental dispersion curve used to evaluate the representative phase velocity for the wavelength  $\lambda_i$ .*

When the desirable number of segments is  $k$ , the length of the segment,  $|S_i|$ , is determined to be constant on the logarithmic scale, as shown in Equation 3.9.

$$|S_i| = \frac{\log \lambda_{\max} - \log \lambda_{\min}}{k} \quad (3.9)$$

The left and right ends of the segment,  $S_{i,left}$  and  $S_{i,right}$ , are determined by Equations 3.10 and 3.11, respectively. Therefore, the average phase velocity for the wavelength  $\lambda_i$  is calculated from the data in the wavelength range given by Equation 3.12.

$$S_{i,left} = \lambda_i \cdot 10^{-|S_i|/2} \quad (3.10)$$

$$S_{i,right} = \lambda_i \cdot 10^{|S_i|/2} \quad (3.11)$$

$$S_{i,left} \leq \lambda \leq S_{i,right} \quad (3.12)$$

3. *Perform a polynomial best-fit analysis for the phase velocities in the segment specified in Step 2 and determine the best-fit polynomial function for the segment.*
4. *Evaluate the average phase velocity by plugging the wavelength  $\lambda_i$  into the estimated polynomial best-fit function.*
5. *Repeat the previous four steps by changing the polynomial order and/or the number of segments until a desirable average dispersion curve is obtained.*

A visual inspection, comparing the composite and average dispersion curves, should be performed to determine whether or not the computed average curve is acceptable.

In WinSASW, the averaging algorithm is activated from the user interface shown in Figure 3.7. The user specifies values for the span width,  $d_i$ , number of segments,  $k$ , increment ratio,  $r$ , and the polynomial order for the best-fit curve. A “Global” average dispersion curve is determined by applying the moving average approach to the entire composite curve as a single dataset, thereby generating a single average dispersion curve. An example of a global average experimental dispersion curve is shown in Figure 3.8, underlain by the original composite dispersion curve (in gray). The “Array” approach, however, applies the moving average approach individually to each segment of the composite dispersion curve, thus producing a series of average dispersion curves – one for each individual receiver spacing. An example of an array average experimental dispersion curve is shown in Figure 3.9, also underlain by the original composite dispersion curve (in gray). In any case, the average dispersion curve is taken as the experimental dispersion curve for the inversion analyses.

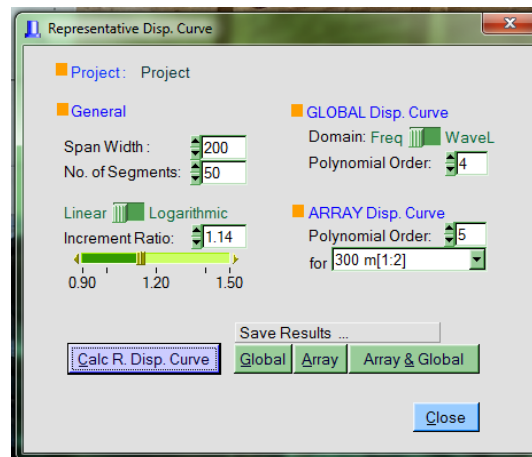


Figure 3.7 User interface for experimental dispersion curve averaging in WinSASW

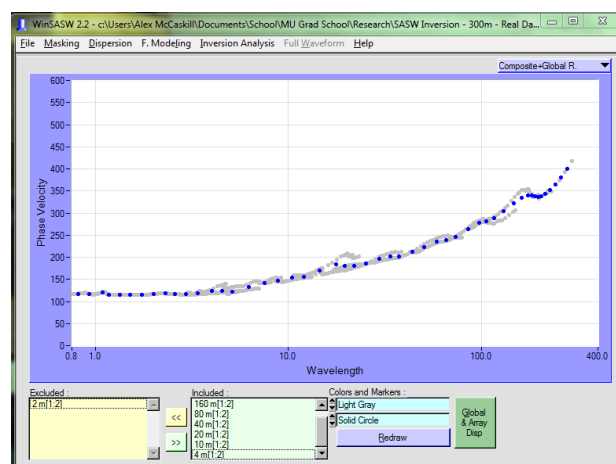
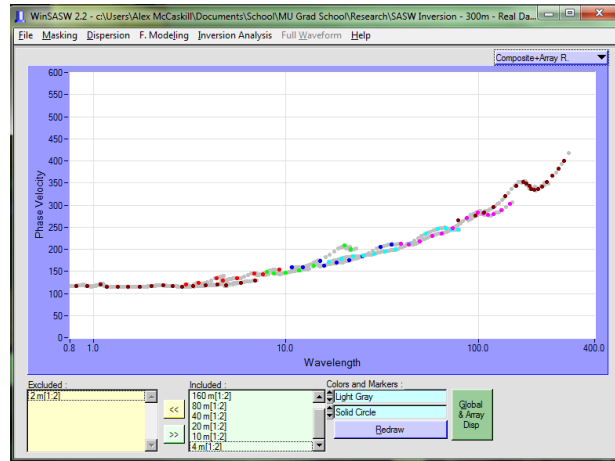


Figure 3.8 Global average experimental dispersion curve computed in WinSASW for the composite dispersion curve of Figure 3.5, with the parameters indicated in Figure 3.7



**Figure 3.9** Array experimental dispersion curve – with a separate average curve for each spacing – computed in WinSASW for the composite dispersion curve of Figure 3.5, with the parameters indicated in Figure 3.7

### 3.3.3 Forward Modeling

Forward modeling proceeds “forward” from assumed profile parameters to produce the corresponding theoretical dispersion curve. In the software program WinSASW (Joh 1996), forward modeling is implemented as shown in Figure 3.10 (taken from version 2.3.1). The WinSASW user enters all forward modeling data in the window shown at left (Figure 3.10a), including: (1) selection of 2D or 3D analysis, (2) entry of profile information, including layer thickness,  $V_p$ ,  $V_s$ , density, Poisson’s ratio, and damping, (3) specification of receiver locations – only applies to 3D analysis – and (4) the wavelength range according to an appropriate data collection criterion.

An example of forward modeling output from WinSASW is shown at right (Figure 3.10b), where the red curve is the theoretical dispersion curve produced by forward modeling. The blue curve in Figure 3.10b is an experimental dispersion curve derived from a “global” average of experimental data. Forward modeling can be used with a manual “trial-and-error” approach to find the profile which produces a good fit between theoretical and experimental dispersion curves. However, several iterations of “trial-and-error” are required to produce a good fit, which makes it a very inefficient and cumbersome method. In this thesis, forward modeling analyses were used in the preliminary sensitivity study (Section 3.5) to perform both 2D and 3D analyses and study the effect of the near-field on the dispersion curve. An automated inversion approach, described below, was used to determine the  $V_s$  profiles.

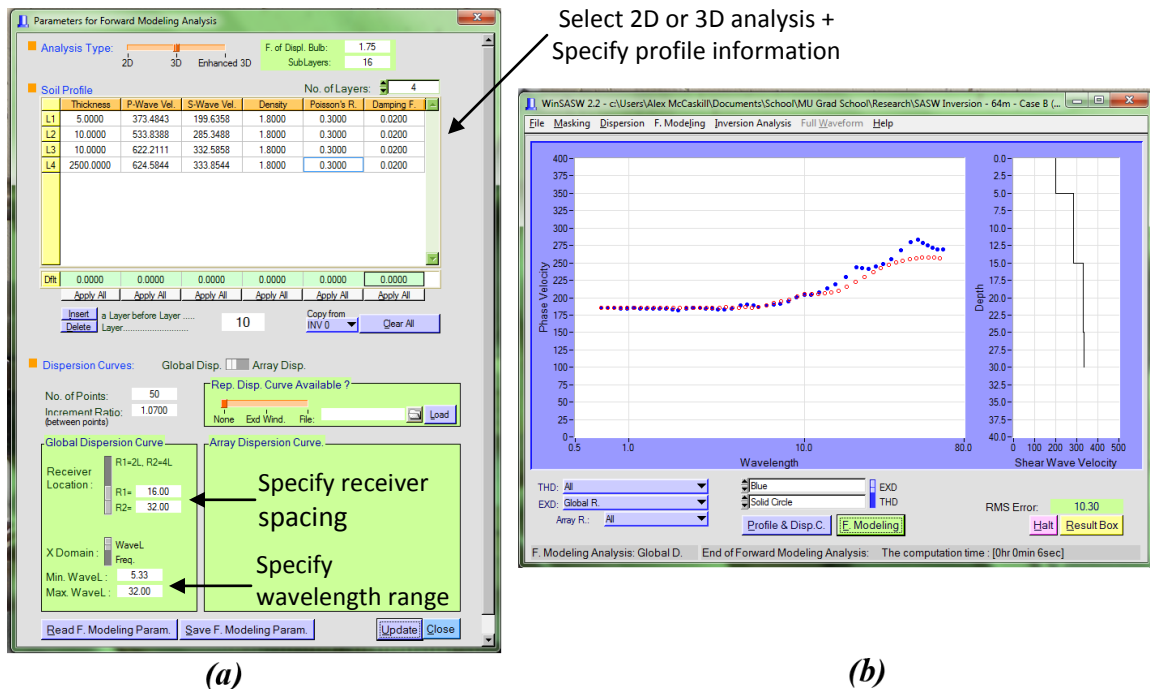


**Figure 3.10** Forward modeling (a) profile parameter input and (b) theoretical dispersion curve output (red) in WinSASW

### 3.3.4 Inversion Analysis

#### 3.3.4.1 Global Versus Array Inversion

Inversion analyses in WinSASW can be one of three types: 2D Global, 3D Global, or 3D Array. The first part of each designation refers to the type of theoretical model, 2D or 3D, used to fit the theoretical dispersion curve (see Section 3.2) in the inversion process. The second part of the designation refers to the type of averaging scheme, Global or Array, used to generate the experimental dispersion curve (see Section 3.3.2) for the inversion process. By extension, then, an experimental dispersion curve derived from a global average must be fit by a global-type theoretical dispersion curve – a “global inversion” – while an array average experimental curve requires an array-type theoretical fit – an “array inversion.”

The 2D global inversion, therefore, assumes far-field plane Rayleigh wave conditions for both experimental and theoretical (global) dispersion curves. Since the 2D solution is a modal solution, no receiver locations are specified for the theoretical model. The 3D global inversion uses the same global experimental curve as used in the 2D inversion, but uses the 3D model to calculate the theoretical dispersion curve. The 3D solution requires knowledge of the receiver locations, but the global experimental curve is not associated with a particular receiver spacing

(i.e. it is assembled from averaging several receiver pairs). Therefore, a common approach has been to assume the receiver locations are two wavelengths and four wavelengths from the source for each of the frequencies calculated. Using this approach, the 3D model is a far-field solution (i.e. calculating the response at locations greater than 2 wavelengths from the source), but the experimental dispersion curve contains data at shorter wavelengths. To avoid this inconsistency, Joh (1996) suggested the 3D array inversion approach, which uses each of the individual average experimental dispersion curves and calculates theoretical dispersion curves for each of the receiver locations used in the experimental data collection. In this way, the 3D array inversion accurately simulates the surface wave measurement for an “array” of receiver spacings. WinSASW interfaces used to specify profile data and inversion type are shown in Figure 3.11.

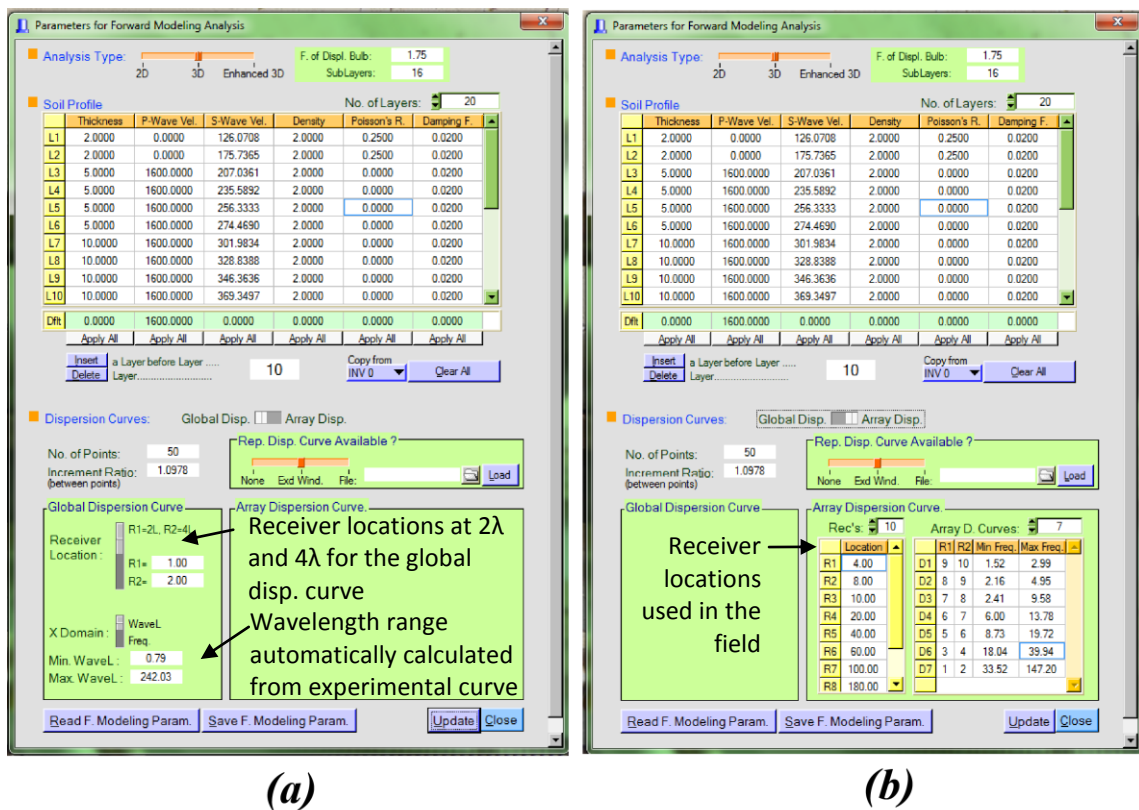
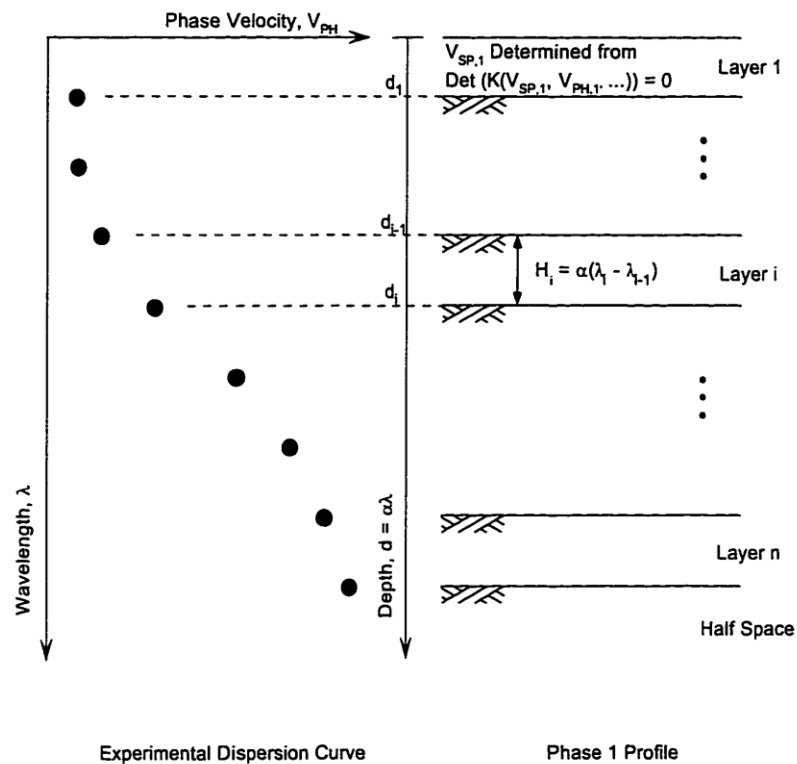


Figure 3.11 Profile parameter input windows for (a) global inversions and (b) array inversions in WinSASW

### 3.3.4.2 Starting Model Computation

The inversion analysis algorithm implemented in WinSASW uses the Newton-Raphson method for non-linear root finding, which requires an initial guess that is close to the true value, so as to avoid numerical traps like local minima. Therefore, a “starting model” profile is computed prior

to initiating an inversion analysis. For WinSASW, Joh (1996) adapted an approach developed by Roesset and Foinquinos (1991) to compute a starting model in two phases. Details of this procedure are presented in Joh (1996) and summarized below. Experimental dispersion data are used to compute a temporary layering arrangement (number of layers and thickness) for a Phase 1 profile, as shown in Figure 3.12. The thickness of each layer is determined from the wavelength of a given dispersion data point and an assumed depth-to-wavelength ratio,  $\alpha$ . The shear wave velocities of each layer are determined one-by-one, starting from the top layer and working down. Initially, a one-layer system is assumed and a stiffness matrix is assembled. The shear wave velocity is varied to make the determinant of the stiffness matrix zero. The same scheme is used working down (two-layered systems, etc.) for each point in the dispersion curve. A Phase 2 profile, which is used as the starting model for the inversion process, is computed from the layering of the Phase 1 profile as shown in Figure 3.13. The procedure is repeated for different values of  $\alpha$ , and the model having the lowest RMS error when compared to the experimental dispersion curve is selected as the starting model for use in the inversion analysis (Figure 3.15).



**Figure 3.12** Development of Phase 1 starting model profile from experimental dispersion data (Joh 1996)

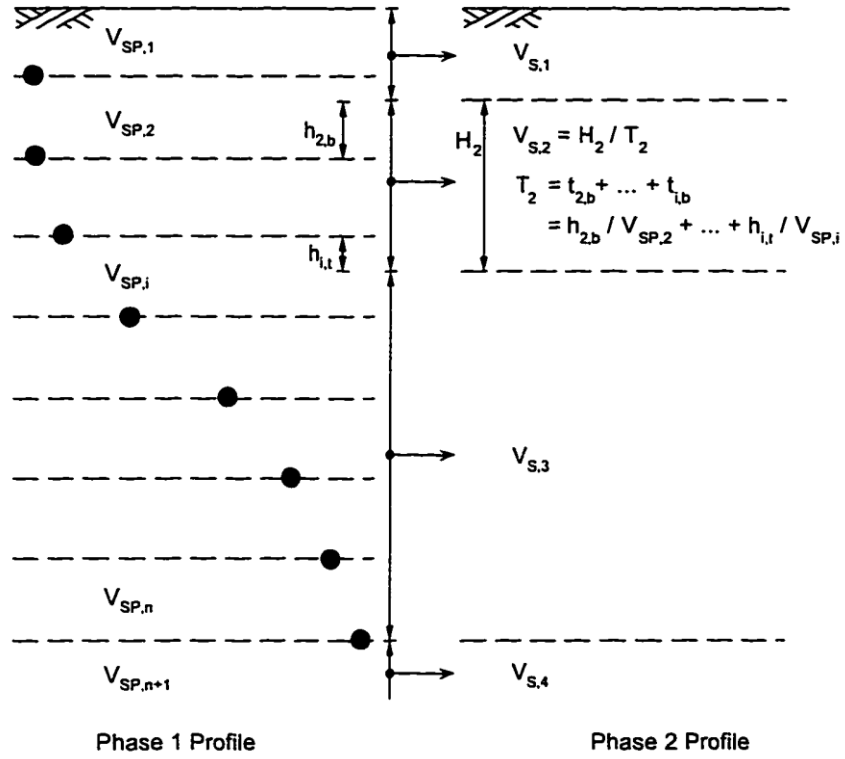


Figure 3.13 Development of Phase 2 starting model profile from a Phase 1 profile (Joh 1996)

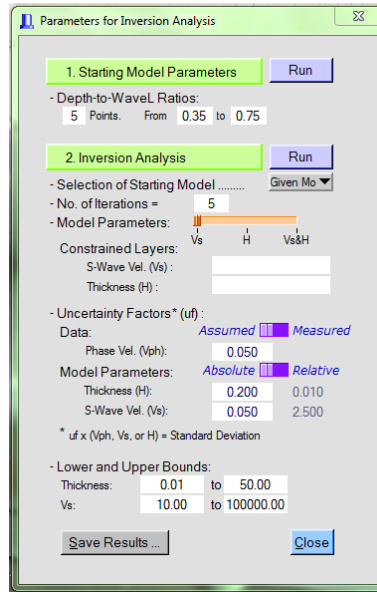
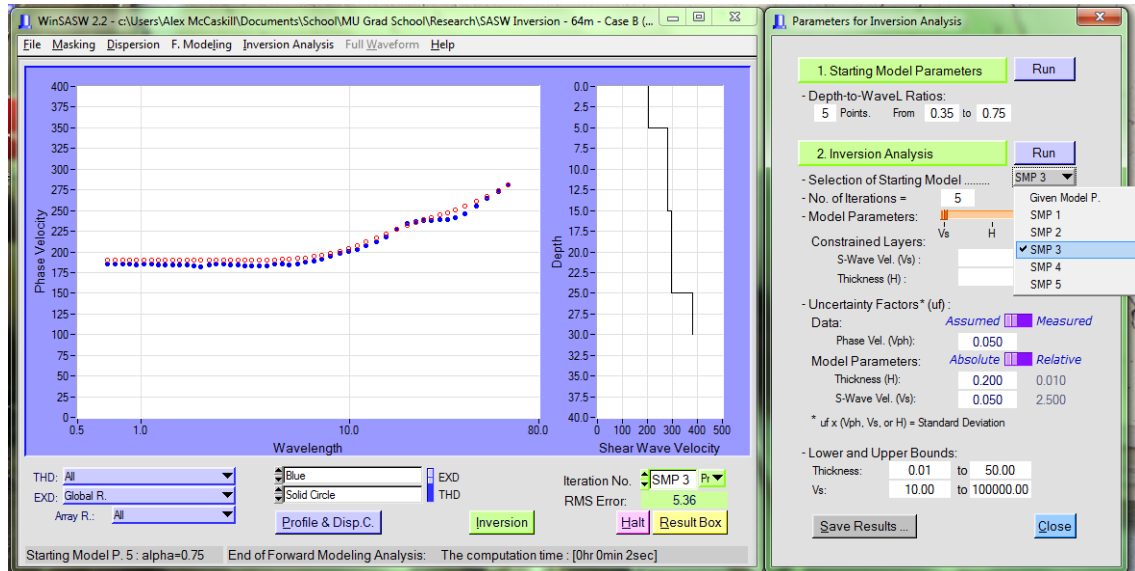


Figure 3.14 Interface for starting model computation and inversion analysis in WinSASW



**Figure 3.15** Selection of starting model with the lowest RMS error prior to starting an inversion analysis in WinSASW

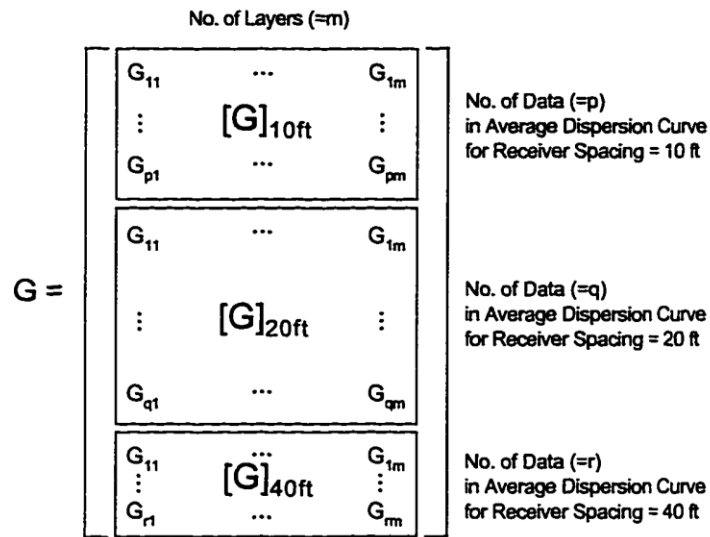
### 3.3.4.3 Maximum Likelihood Inversion Method

WinSASW uses the “maximum likelihood” method to match the theoretical dispersion curve to the experimental curve. The goal of this inversion approach is to find the  $V_s$  profile that has the greatest statistical likelihood of producing a match between the theoretical and experimental dispersion curves. The maximum likelihood method “asserts that the optimum shear wave velocity profile maximizes the probability that the dispersion curve determined by the shear wave velocity is the experimental dispersion curve” (Joh 1996). A detailed description of the maximum likelihood method is beyond the scope of this thesis. For an in-depth discussion of the theoretical and statistical underpinnings of the approach, the reader is referred to the work of Joh (1996), Tarantola (1987), and Menke (1984).

In the WinSASW global inversion approach, a single theoretical dispersion curve from the starting soil profile model is calculated from either the 2D model or the 3D global model. The inversion proceeds by calculating the error between the experimental and theoretical dispersion curves. The sensitivity matrix (i.e. partial derivative of phase velocity relative to shear wave velocity) is calculated and used to improve the fit by iteratively updating the soil model. The inversion is completed when the RMS error reaches a sufficiently low value. As noted above, the model requires several soil parameters, including: (1) layer thickness, (2) shear wave velocity, (3) Poisson’s ratio (or P-wave velocity), (4) damping, and (5) mass density. In the inversion process, all values except the shear wave velocity are held constant. With the array inversion approach, the 3D forward model is calculated using actual receiver locations from the

experimental data collection stage. Therefore, several individual theoretical dispersion curves are calculated – one for each segment of the experimental dispersion curve (which correspond to specific receiver pairs). The sensitivity matrix is calculated for points in each individual dispersion curve (Figure 3.16). The inversion procedure seeks to minimize the overall misfit between the experimental and theoretical dispersion data (Figure 3.17

An inversion analysis in WinSASW, using the starting model selected in Figure 3.15, is shown as in progress in Figure 3.17 and as completed in Figure 3.18. Using a 2D global inversion, the root-mean-square (RMS) error of the fit between theoretical and experimental dispersion curves was reduced from the starting model value of 5.36 to 1.47 after the final iteration. The inversion is typically completed within five iterations.



Note:  $G_j = \frac{\partial V_{phj}}{\partial V_{s,i}}$   
 = the partial derivative of the  $j$ th phase velocity with respect to the shear wave velocity of the  $i$ th layer  
 $[G]_{10ft}, [G]_{20ft}, [G]_{40ft}$  = the partial derivative matrices corresponding to the array average dispersion curves for receiver spacing of 10ft, 20ft and 40 ft, respectively

Figure 3.16 Partial derivative matrix computation for the array inversion method (Joh 1996)

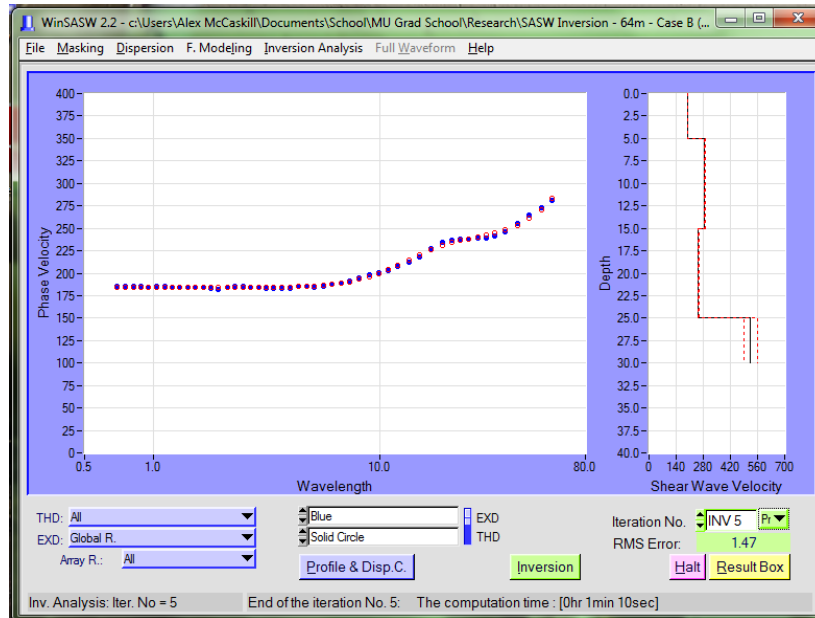


**Figure 3.17** Completed maximum likelihood inversion analysis in WinSASW, showing final  $V_s$  profile – the starting model is shown in Figure 3.15

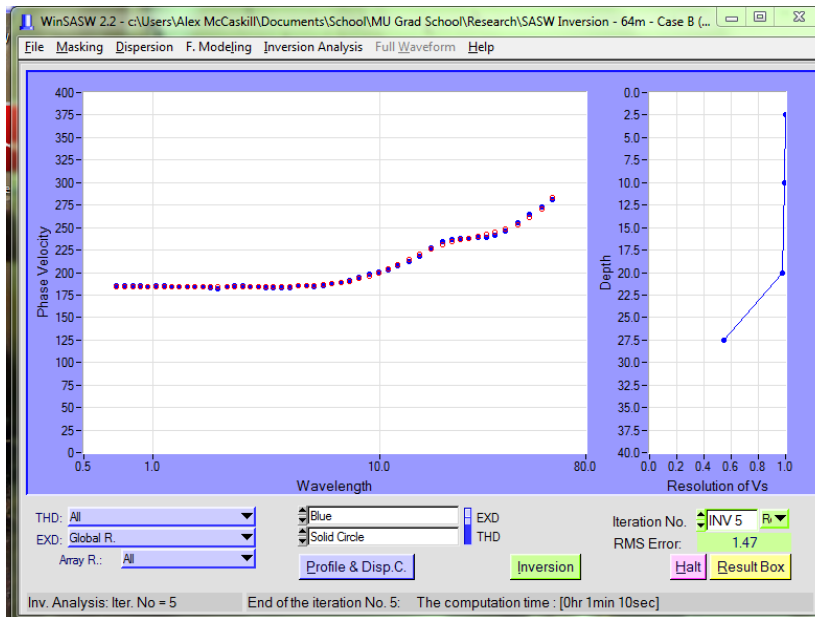


**Figure 3.18** Completed maximum likelihood inversion analysis in WinSASW, showing layer resolution results – the starting model is shown in Figure 3.15

### 3.4 Processing of Multi-channel Data

In addition to the SASW analysis described in the previous section, multi-channel surface wave data was also analyzed in this study. Unlike the SASW method, where the phase difference between receiver pairs is manually unwrapped, multi-channel methods use a single array of

receivers and a wavefield transformation method to develop the dispersion curve. The main advantage of multi-channel methods is the possibility to separate individual modes. Therefore the theoretical model used in multi-channel analyses is almost always a modal solution (2D). In this study, dispersion curves were developed for both real and simulated multi-channel data using the frequency-domain beamformer (FDBF) approach. The dispersion curve produced by the FDBF technique was imported directly into WinSASW and averaged by the averaging approach described in Section 3.4.2. Inversion analyses were then performed in WinSASW, as described in Section 3.4.3, using the 2D global inversion. Sections 3.4.1 and 3.4.2 describe the FDBF method used to develop the experimental dispersion curves and draws extensively from Li (2011).

### 3.4.1 Definition of the Spatospectral Correlation Matrix

Frequency-domain beamforming requires calculation of the spatospectral correlation matrix. The spatospectral correlation matrix is composed of the cross-power spectra (i.e. wrapped phase plots) for the phase difference between every possible two-receiver combination in the array. A graphical representation of the matrix is presented in Figure 3.19, where each row can be considered as the relation of a given receiver to every other receiver in the array. The labeled axes correspond to the axes of each individual subplot, while the long diagonal shows the “phase difference” for a receiver location in relation to itself (auto power spectrum).

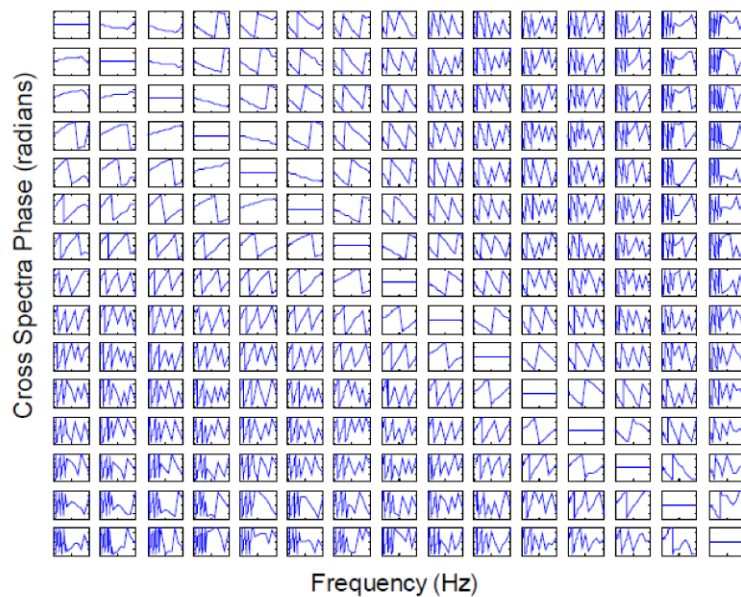


**Figure 3.19** Graphical representation of a spatospectral correlation matrix (Yoon 2005)

Mathematically, the spatio-spectral correlation matrix is computed by use of the following equations. The cross-power spectrum for each receiver pair, the “elements” of the matrix, is computed as shown in the following equation:

$$R_{ij}(\omega) = S_i(\omega)S_j^*(\omega) \quad (3.13)$$

where  $R_{ij}(\omega)$  is the cross-power spectrum between receivers  $i$  and  $j$ ,  $S_i(\omega)$  is the linear spectrum at circular frequency  $\omega$  for the  $i$ th receiver, and  $S_j(\omega)$  is the linear spectrum for the  $j$ th receiver. The (\*) indicates complex conjugation. Therefore, the spatio-spectral correlation matrix,  $R(\omega)$ , is defined as shown in Equation 3.14.

$$R(\omega) = \begin{bmatrix} R_{11}(\omega) & R_{12}(\omega) & \cdots & R_{1n}(\omega) \\ R_{21}(\omega) & R_{22}(\omega) & \cdots & R_{2n}(\omega) \\ \vdots & \vdots & \ddots & \vdots \\ R_{m1}(\omega) & R_{m2}(\omega) & \cdots & R_{mn}(\omega) \end{bmatrix} \quad (3.14)$$

### 3.4.2 Dispersion Processing by the Frequency-Domain Beamformer (FDBF) Method

The FDBF approach essentially involves a phase shifting and summing of receiver responses for different trial wavenumbers,  $k$ , in search of the  $k$  that dominates wave propagation. To identify the dominant  $k$  value, a plot of wavenumber versus power – the steered power spectrum – is constructed for a given frequency,  $f_0$ . The steered power response spectrum is computed as shown in Equation 3.5 (Johnson and Dudgeon 1993).

$$P_{FDBF}(k, \omega) = e^H(k) \times W \times R(\omega) \times W \times e(k) \quad (3.15)$$

where  $^H$  is the Hermitian transpose,  $W$  is a diagonal matrix of receiver weighting factors,  $R(\omega)$  is the spectrospatial correlation matrix defined in Section 3.4.1, and  $e(k)$  is the steering (i.e. phase-shift) vector. The steering vector,  $e(k)$ , is defined as shown in Equation 3.16.

$$e(k) = \left[ \exp(j\bar{k} \cdot x_1) \exp(j\bar{k} \cdot x_2) \cdots \exp(j\bar{k} \cdot x_m) \right]^T \quad (3.16)$$

where  $\bar{k}$  is the wavenumber vector,  $x_m$  is the spatial location of the  $m$ th receiver, and  $^T$  is the transpose vector. The array is steered with exponential phase shift vectors associated with different trial wavenumbers  $\bar{k}$ . An example of a steered power response spectrum is presented in Figure 3.20. The peak wavenumber,  $k_{peak}$ , corresponds to the dominant mode of the steered power response spectrum. Knowing  $k_{peak}$  and the associated frequency,  $f_0$ , (or circular frequency,  $\omega$ ) the phase velocity of the Rayleigh wave,  $V_R$ , can be computed as shown in Equation 3.17. This

yields one point on the dispersion curve relating velocity and frequency (or wavelength). The same procedure is, therefore, repeated for a range of frequencies to produce a complete experimental dispersion curve. If multiple peaks are present, higher modes of propagation can be identified in the power response plot.

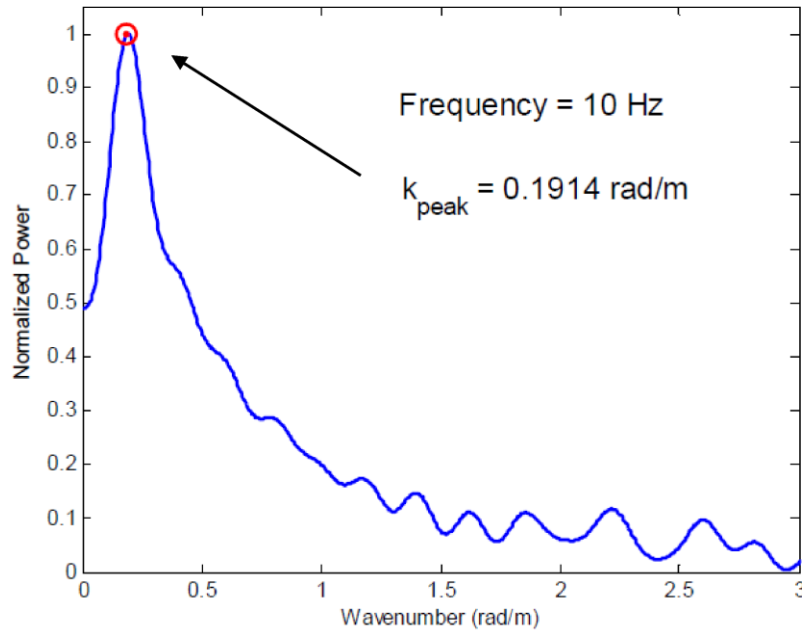


**Figure 3.20** Example of a steered power response spectrum at a frequency of 10 Hz (Li 2011; Yoon 2005)

$$V_R(\omega, k_{peak}) = \frac{\omega}{k_{peak}} = \frac{2\pi f_0}{k_{peak}} \quad (3.17)$$

The preceding sections described the tools that were used to perform this research (models and software). Presented below are the specific procedures used to perform the three studies conducted in this research, namely (1) a preliminary sensitivity study of near-field effects to changes in profile parameters, (2) inversion analyses using simulated experimental data and (3) inversion analyses using real experimental data.

### 3.5 Preliminary Sensitivity Study

As discussed in Chapter 2, most surface wave research to date has been concerned with avoiding the near-field in both the data collection and processing stages, so that a far-field model (i.e. 2D plane wave) can be reliably used for the inversion analysis stage. In these studies (Li and Rosenblad 2011; Sanchez-Salinerio et al. 1987; Yoon and Rix 2009) it has been observed that near-field effects change not only with data collection procedures (i.e. how close the array

is to the source), but also with variations in the profile parameters. It stands to reason that, if near-field effects are sensitive to changes in profile parameters, then including the near-field in the data collection and analysis could help to infer unknown profile conditions. The extent to which parametric variations can be resolved from the near-field portion of the dispersion curve is not well understood.

In the preliminary stages of developing a research plan for this thesis, a sensitivity study was performed to assess the sensitivity of the near-field portion of the dispersion curve to changes in several profile parameters. Parametric variations were analyzed using both the 2D plane wave and 3D theoretical forward models. Results derived from the 3D solution, which includes near-field effects, were compared with those derived from 2D solution. The latter does not include near-field effects, allowing for a comparison of changes in the near-field and far-field portions of the dispersion curve. The purpose of this portion of the study was to identify parameters for further study.

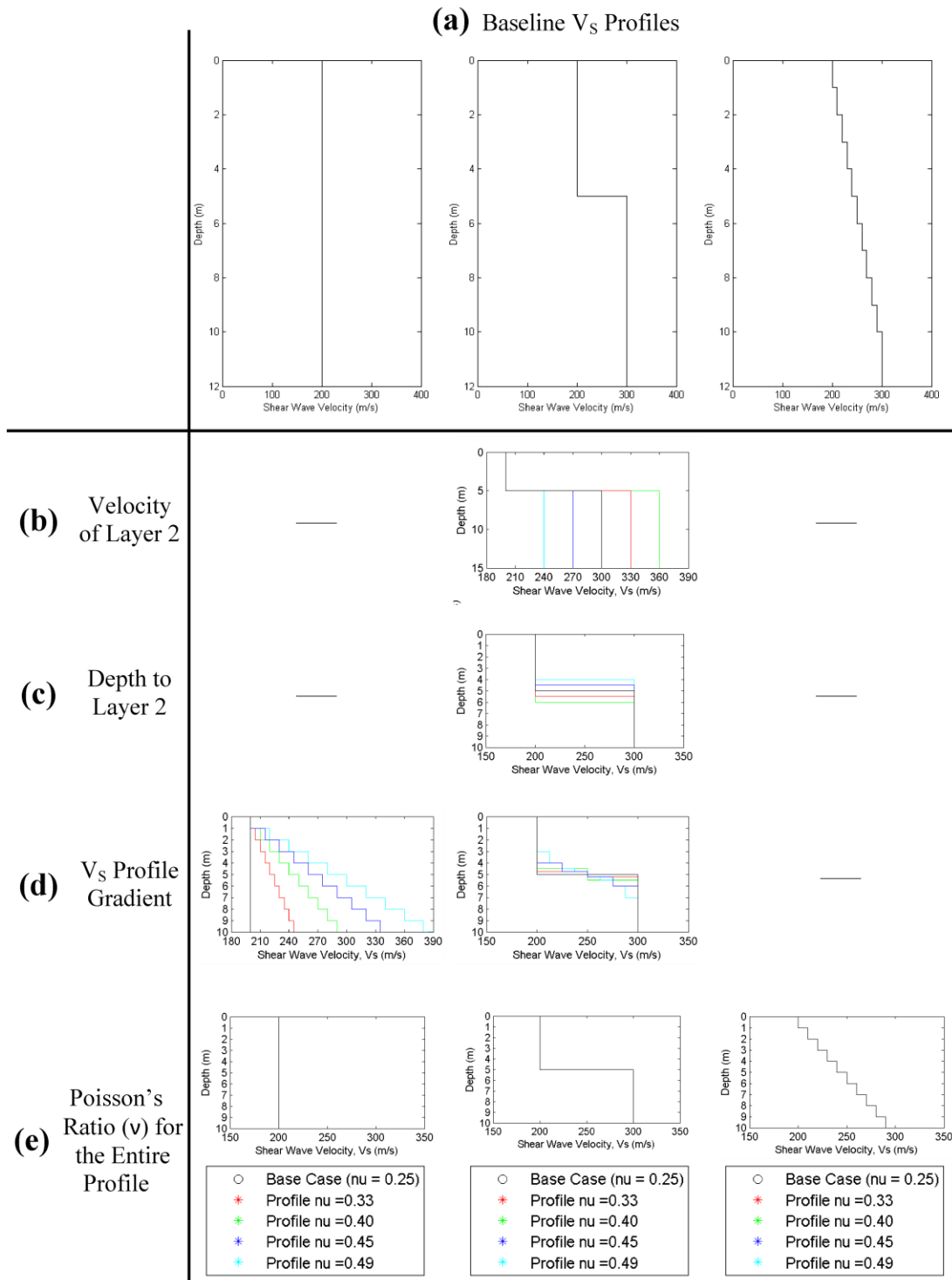
### **3.5.1 Selection of Study Profiles**

Three simple baseline  $V_s$  profiles (Figure 3.21a) were used in the sensitivity study. The baseline profiles included (1) a uniform  $V_s$  profile, (2) a simple soft-over-stiff layered system, and (3) a profile having a linear increase in  $V_s$  with depth, each underlain by a uniform halfspace. The following profile parameters were varied in this study: (1) halfspace velocity ( $\pm 10\%$  and  $\pm 20\%$ ), depth to the lower layer in the soft-over-stiff  $V_s$  profile ( $\pm 10\%$  and  $\pm 20\%$ ), (3) velocity gradient at the soft-over-stiff interface, (4) gradient of the linear  $V_s$  profile, and (5) changes in Poisson's ratio for all profiles (assumed constant with depth). The cases studies are summarized in Figure 3.21b through Figure 3.21e.

### **3.5.2 Forward Modeling Procedures**

For each profile considered, forward modeling computations were performed to simulate both a traditional SASW data collection approach, where near-field effects are largely avoided, and an alternative approach using a single receiver spacing, where the near-field is included in the data analysis. For the traditional SASW approach, receiver spacings of 2m, 4m, 8m, and 16m were used in the simulations with a near-field criterion limiting usable data to wavelengths between 1/3 and 2 times the receiver spacing. The wavelength range interpreted for each of the traditional SASW receiver spacings are summarized in Table 3.1 **Error! Reference source not**

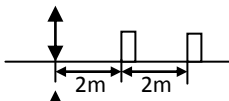
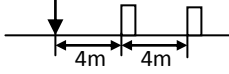
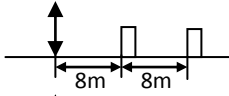
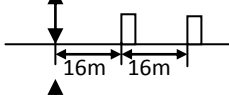
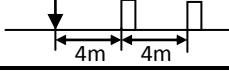
**found..** The alternative approach used a single receiver pair with a spacing of 4m and calculated the dispersion curve for the same total span of wavelengths (1/3m to 32m) as was interpreted with five receiver pairs using the traditional approach.



**Figure 3.21** Base case profiles and variations selected for sensitivity study

For each wavelength range, both the 2D and 3D dispersion curves were computed by forward modeling in WinSASW. This procedure was repeated for each profile variation shown in Figure 3.21. Default values for Poisson's ratio, mass density and damping were 0.25, 1.8 kg/m<sup>3</sup>, and 0.02%, respectively, for all profiles. All profile values were held constant except for the parameter being studied. The dispersion curve for each profile variation was computed separately and the dispersion curves for each set were plotted together in Matlab. Dispersion curves were plotted both as phase velocity versus frequency and percent difference in phase velocity (from the base case) versus frequency. Results of the sensitivity study described in this section are presented in Section 4.2.

**Table 3.1** Summary of receiver spacings and wavelength ranges for forward modeling sensitivity study

	SASW Spacing*	Wavelength Range (m)
Traditional SASW 2m Spacing		2/3 to 4
Traditional SASW 4m Spacing		4/3 to 8
Traditional SASW 8m Spacing		8/3 to 16
Traditional SASW 16m Spacing		16/3 to 32
Alternative Approach with a Single 4m Spacing		1/3 to 32

\*As noted in Section 3.2.1, the 2D solution, being a far-field model, does *not* require knowledge of receiver locations

### 3.6 Surface Wave Analyses with Simulated Data

In the second stage of this study, simulated surface wave measurements were used to assess the influence of data collection, data processing, and inversion analysis procedures on the quality of the results (i.e. the ability to recover the original profile. The objective of this portion of the study was to determine if current surface wave measurement procedures could be made more efficient and effective. In addition, this portion of the study examined if other profile parameters (specifically Poisson's ratio) could be inferred by using alternative methods of collection, processing, and analysis of the data.

### 3.6.1 Simulation of Ground Motions

Simulated ground motions from a vertical disk load at the surface of an assumed soil profile were generated using the program FitSASW, developed at the University of Texas. FitSASW uses the 3D forward model solution (described in Section 3.2.2) and therefore includes all surface wave and body wave modes in both the near- and far-field. FitSASW requires the input of a known soil profile (specifically layer thickness, shear wave velocity, Poisson's ratio, mass density, and damping) and receiver locations relative to the source. FitSASW computes the ground motion in both the time and frequency domains, corresponding to a given profile at specified receiver locations relative to the source. The transfer function (i.e. wrapped phase plot) between any receiver pair can be output from FitSASW. The transfer functions output from FitSASW were used as the simulated experimental data for analysis in WinSASW.

To avoid the complexities associated with higher modes (which typically occur with strong impedance contrasts and "stiff-over-soft" layering conditions), this study was limited to only uniform and normally dispersive profiles (i.e. increasing shear wave velocity with depth). Four profiles with different  $V_s$  gradients were used in this portion of the study (Figure 3.22 and Table 3.2). These profiles were the same as the "A", "B", "C", and "D" profiles used by Li (2011) in his study of near-field effects (the "E" profile of Li (2011) was omitted from this study, as FitSASW encountered a numerical anomaly when generating simulated data for the longest receiver spacing). Default values for Poisson's ratio, mass density and damping in the simulated data were 0.30,  $1.8 \text{ kg/m}^3$  and 2%, respectively, on all profiles. The only exception was a "saturated" version of profile B, which had a Poisson's ratio value of 0.45, but the same values of mass density and damping as the other profiles. The values of mass density and damping were held constant while assumed values of Poisson's ratio varied from 0.15 to 0.45.

Simulated data were generated with six SASW receiver spacings (Table 3.3 and Figure 3.23) and a single multi-channel array (Figure 3.24). Using the FitSASW program described above, "experimental" SASW data were simulated for receiver spacings of 2m, 4m, 8m, 16m, 32m, and 64m, with a maximum wavelength of 64m. Multi-channel data were simulated in FitSASW using an array of 30 receivers, spaced at 1m center-to-center, and a source-to-first-receiver distance of 10m. Li (2011) used the same multi-channel array setup in his study on near-field effects – using his notation, this array would be designated 10SR1RR-30. The same procedures and array setups were used to generate simulated data for all profiles shown in Figure 3.22.

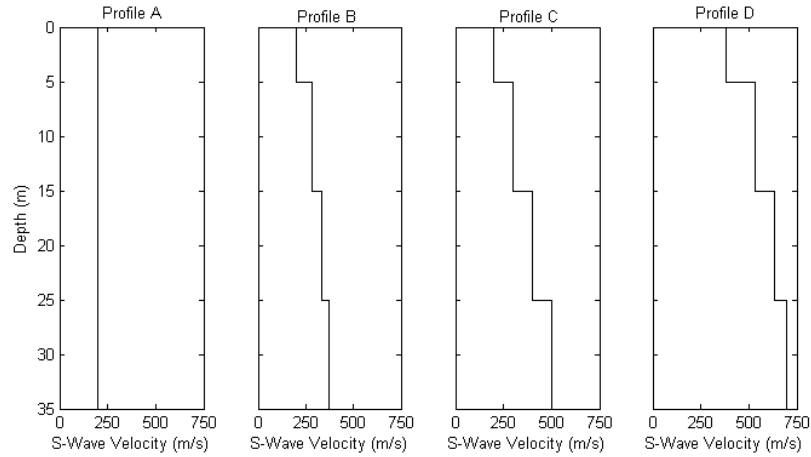


Figure 3.22 Shear wave velocity ( $V_s$ ) profiles used as “simulated” data for inversion analyses. Adapted from Li (2011)

Table 3.2 Profile information for "simulated" data used in inversion analyses. Adapted from Li (2011)

	Profile A	Profile B	Profile C	Profile D
	“Uniform”	“Power Function”	“Linear”	“Steep Power Function”
Depth (m)	$V_s$ (m/s)	$V_s$ (m/s)	$V_s$ (m/s)	$V_s$ (m/s)
0 – 5	200	200	200	382
5 – 15	200	283	300	532
15 – 25	200	336	400	632
25 – 35	200	372	500	699

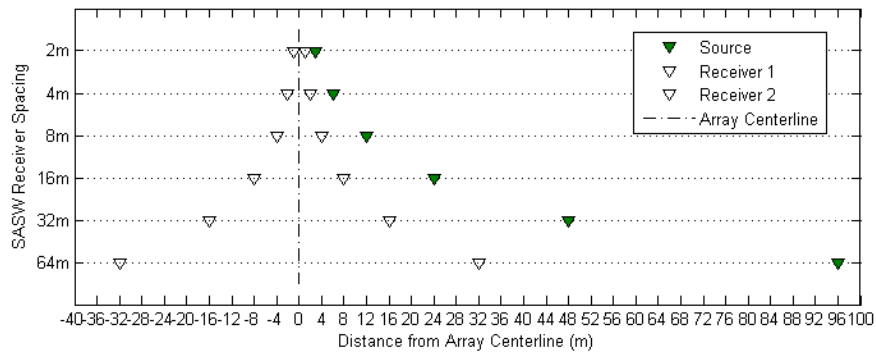
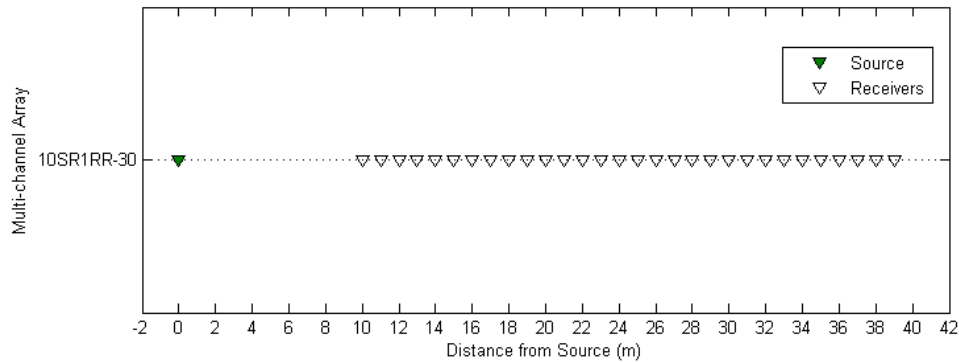


Figure 3.23 Visual representation of the SASW receiver spacings used to generate simulated data

Table 3.3 Summary of SASW receiver spacings used for simulated data collection

Spacing Name	S-R1(m)	R1-R2 (m)	Max. Freq. Range (Hz)	Included in composite disp. curve?			
				360°	180°	90°	45°
2m	2	2	18 to 540	Y	Y	Y	Y
4m	4	4	9 to 260	Y	Y	Y	Y
8m	8	8	6 to 130	Y	Y	Y	Y
16m	16	16	3 to 66	Y	Y	Y	N
32m	32	32	2 to 36	Y	Y	N	N
64m	64	64	1 to 21	Y	N	N	N



**Figure 3.24** Visual representation of the multi-channel array used to generate simulated data

### 3.6.2 Experimental Dispersion Curve Calculations

Data from simulated SASW measurements (generated in FitSASW) were processed in WinSASW to produce a composite experimental dispersion curve by the methods described Section 3.3.1. The simulated data were first imported into WinSASW as transfer functions (i.e. wrapped phase plots) and masking was applied to each wrapped phase plot, according to four different filtering criteria. The filtering criteria used in this study are referred to by extent to which the low frequency range of the wrapped phase plot is “masked out” (see Figure 2.8d) to avoid near-field effects: 360°, 180°, 90°, and 45°. As the extent of masking decreases (i.e. smaller numbers), the influence of near-field effects increases. Masking out the first 360° of the wrapped phase plot (i.e. requiring that the first receiver is a distance of at least one wavelength from the source) corresponds to the filtering criterion recommended by Gucunski and Woods (1992), and the 180° case (i.e. requiring that the first receiver is a distance of at least one-half of a wavelength from the source) corresponds to that recommended by Hiltunen and Woods (1990) – both of which are commonly used in current practice. The 90° and 45° cases, although not derived from specific filtering criteria in the literature, were included to study the effect of including more near-field in the dispersion curve. Using the same experimental dataset (collected as shown in Figure 3.23), a separate composite dispersion curve was produced for each filtering criterion applied. In all cases, the maximum wavelength was limited to 64m. As shown in Figure 3.25 and the right side of Table 3.3, the benefit of using a less restrictive near-field criteria is that the same range in wavelength (up to 64m in this case) can be achieved with fewer receiver setups and much less space (e.g. 128 m for the 360° criterion versus only 16m for the 45° criterion). The same process was repeated with simulated SASW data for each profile shown in Figure 3.22.

Simulated multi-channel data were processed according to the frequency-domain beamformer (FDBF) approach described in Section 3.4 and imported into WinSASW for dispersion processing. The FDBF approach yields a single experimental dispersion curve for each multi-channel array. Experimental dispersion curves generated in this way were imported directly into WinSASW (as segments of a composite dispersion curve). For this study, only one multi-channel array was modeled, yielding a single “composite” experimental dispersion curve.

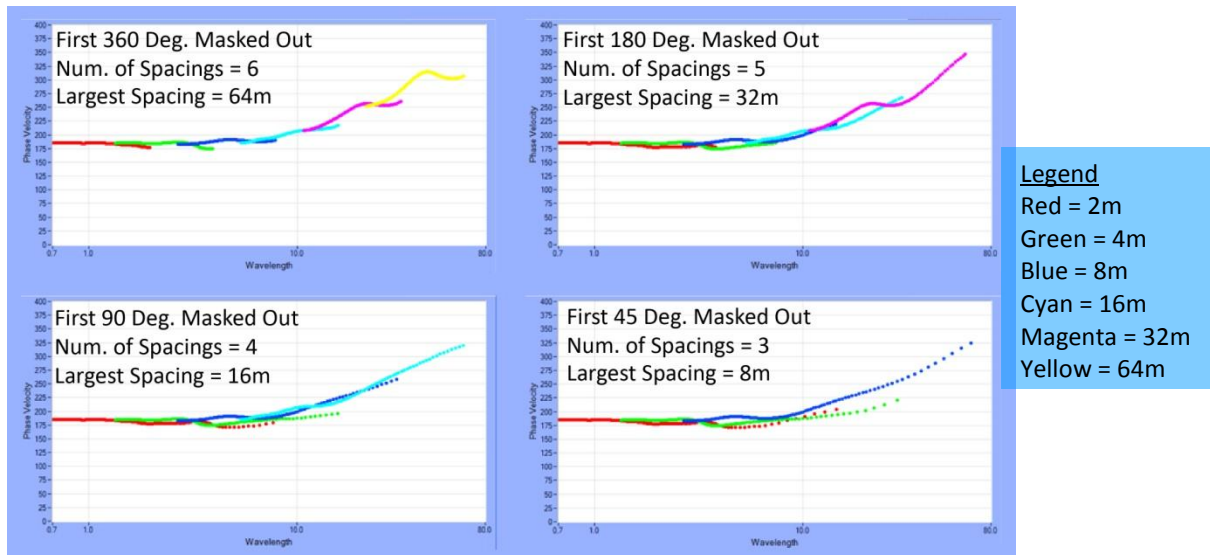


**Figure 3.25** Examples of composite dispersion curves (for Case D) derived from four different filtering criteria

The composite dispersion curve was then averaged according to the global averaging scheme described in Section 3.3.2 to produce an experimental dispersion curve that can be used for inversion analysis.

### 3.6.3 Inversion Analysis

In this study, several inversion analyses were performed using WinSASW as described in Section 3.3.4. Three previously-described inversion methods (“2D Global”, “3D Global”, and “3D Array”) were used to invert data processed with the 360° and 180° filtering criteria. Data processed by the 90° and 45° filtering criteria were inverted using only the 3D array approach since the 2D approach is clearly not valid for these cases. The  $V_s$  profile produced by the inversion analysis, with all other parameters being held constant, was compared with the “true”  $V_s$  profile to assess the effectiveness of each approach. Similar analyses were also performed with multi-channel data: simulated multi-channel data were processed as described in the previous section and inverted by 2D global and 3D global analyses.

The 2D global approach uses a 2D theoretical model, a modal plane Rayleigh wave solution (see Section 3.2.1), to fit a theoretical dispersion curve to an experimental dispersion curve produced by a global average. The 2D global model is, by far, the most-used inversion approach in current practice. In this study, the 2D global inversion implemented in WinSASW was used to invert simulated data processed by two SASW filtering criteria currently in common use (360° and 180°). This was done for all simulated profiles. The 2D global inversion was used to invert dispersion curves derived from multi-channel data. The FitSASW model used to simulate the experimental data for this study (and therefore all experimental dispersion curves) includes near-field contributions, but the 2D global inversion analysis does not.

The 3D Global approach uses a 3D theoretical model (see Section 3.2.2), to fit a *single* theoretical dispersion curve to a *single* experimental dispersion curve produced by a global average. Like the 2D global inversion, the 3D global inversion in WinSASW was used to invert data processed according to the 360° and 180° filtering criteria, for all simulated profiles in this study. Experimental dispersion curves processed from multi-channel data were also inverted by the 3D global method.

The 3D Array approach uses a 3D theoretical model (see Section 3.2.2), to fit a *family* of theoretical dispersion curves to a *family* of experimental dispersion curves produced by an array average. For this study, the 3D Array inversion in WinSASW was used to invert data processed by all four filtering criteria (360°, 180°, 90°, and 45°), for all simulated profiles. At the present time, the 3D array approach cannot be used with multi-channel data. The 3D array approach is perhaps the least-used of the three inversion approaches, but it provides, perhaps, the best simulation of the SASW measurement itself.

Results from these analyses with simulated data are presented in Sections 0 and 4.3.3.

#### **3.6.4 Poisson's Ratio Study**

In the preliminary sensitivity study, the near-field was found to have the greatest sensitivity to changes in Poisson's ratio. If a forward model is sensitive to a parametric variation, then it stands to reason that the inversion analysis should also be sensitive to changes in the same parameter. If the inversion analysis is sensitive in this way, then it also stands to reason that this parameter could be inferred to some degree. Therefore, a second inversion study was performed with the simulated data to assess the extent to which Poisson's ratio could be inferred. This second study expanded on the study described in Section 3.6.3, by performing inversion analyses with seven

different assumed values of Poisson's ratio (ranging from 0.15 to 0.45) for the same combination of simulated profiles, filtering criteria, and inversion approaches used in the first study. In each case, one value of Poisson's ratio corresponded to the known "true" value used to generate simulated data (usually  $\nu=0.30$ ), which was the same analysis performed in Section 3.6.3. The other six values of Poisson's ratio essentially corresponded to an incorrect estimation of the "true" Poisson's ratio. Since this study used simulated data, both the assumed and the "true" values of Poisson's ratio were constant with depth over the entire profile. It should be noted that in current surface wave practice (SASW and multi-channel) Poisson's ratio is either assumed or known *a priori*.

### **3.7 Surface Wave Analyses with Real Data**

The final stage of this study used real surface wave data collected at a site on the Mississippi Embayment near Mooring, TN to assess the influence of data collection, data processing, and inversion analysis procedures on the quality of the results. The objective of this final stage was to determine if the procedures used to process simulated data (Section 3.6) would produce similar results when applied to real data. The effect of Poisson's ratio on surface wave analyses was also considered, with particular attention to saturated conditions.

#### **3.7.1 Data Collection Procedures**

##### ***3.7.1.1 Field Site Location and Geology***

Experimental SASW and multi-channel data previously collected by Li (2008) and Bailey (2008) were used in the analyses for this portion of the study. They recorded ground motions from both active and passive sources at eleven sites (Figure 3.26) in a geologic region known as the Mississippi Embayment. The Mississippi Embayment "is a southwest plunging trough encompassing parts of Arkansas, Missouri, Kentucky, Tennessee and Mississippi in the Central United States" (Li 2008). The region is characterized by deep deposits of glacial soils underlain by Dolomitic bedrock, ranging in depth from 470m in New Madrid, Missouri to almost 1000m near Memphis, Tennessee. For this study, only the active-source data from "Site 1" were used. Located in Mooring, Tennessee, the site is also home to a seismic station (designated "MORT") operated by the Center of Earthquake Research and Information (CERI) at the University of Memphis. An estimated lithology of the Site 1/MORT location is presented in Figure 3.28. Due to

the site’s proximity to the Mississippi River, it is known to have a shallow (i.e. within the top few meters) groundwater table.

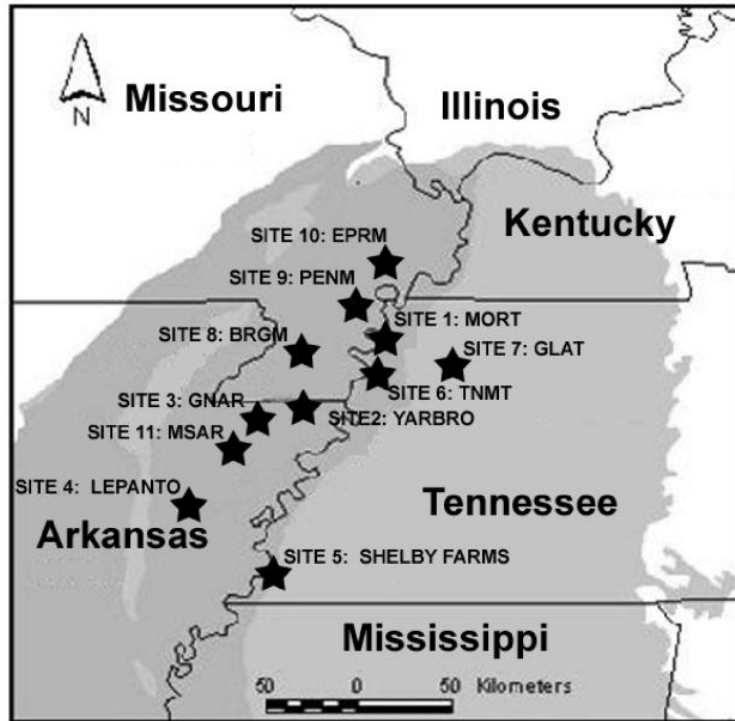


**Figure 3.26** Site locations in the Mississippi Embayment – only “Site 1” data was used in this study (Bailey 2008)



**Figure 3.27** Google maps image of Site 1 (MORT) – the black line is the array location (Bailey 2008)

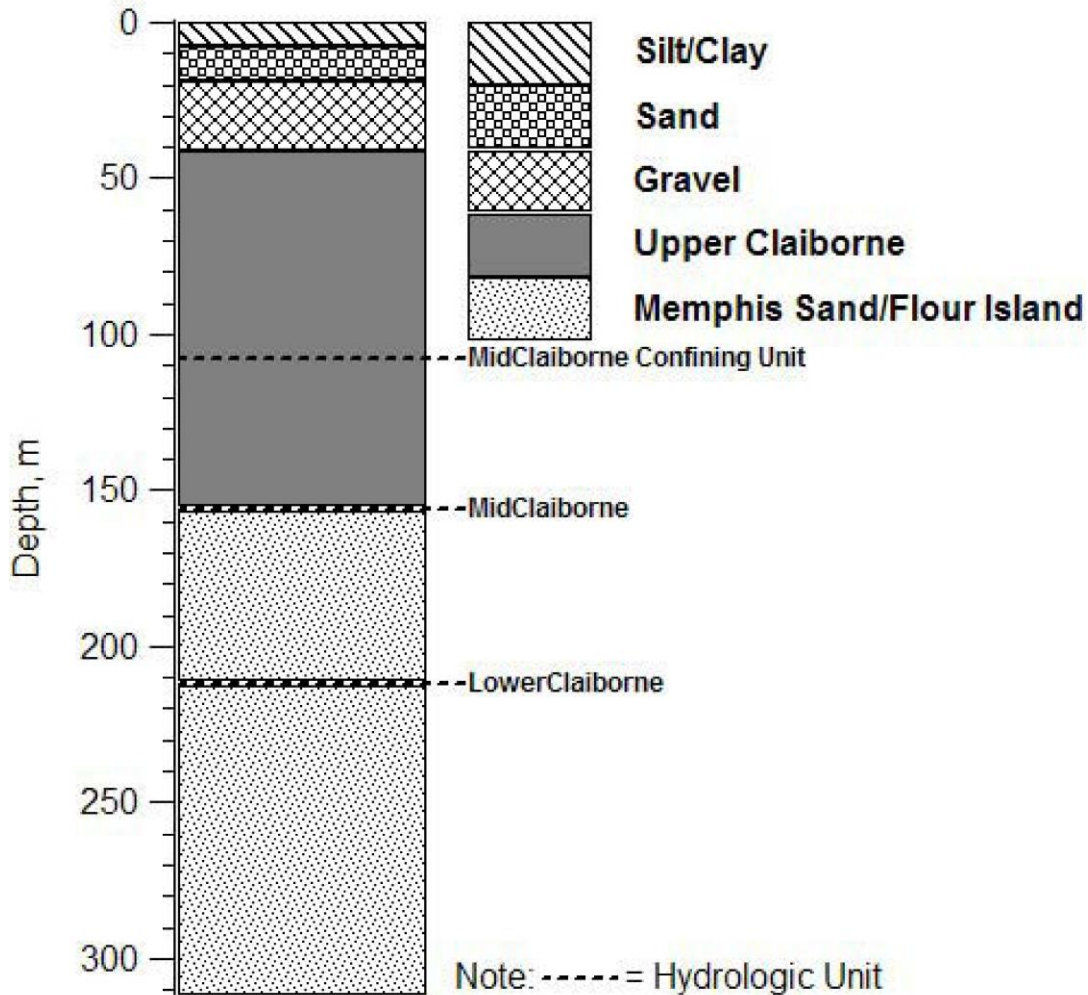


Figure 3.28 Estimated Soil Lithography at Site 1 (Bailey 2008)

### 3.7.1.2 Field Equipment

Li (2008) and Bailey (2008) collected the experimental data at the MORT site in Spring of 2006 using two different active sources, an array of high-sensitivity geophones, and a robust data acquisition system. To collect surface wave data in the high frequency range (i.e. short wavelength range), an instrumented sledgehammer (PCB Piezotronics Model 086D50) was used as an active source. Impact sources, like the sledgehammer, have the advantage of generating energy at several frequencies simultaneously, which can be resolved in the data processing stage by means of a Fourier transformation. The sledgehammer source is shown in Figure 3.29. To obtain low-frequency (i.e. long wavelength) data, a specialized mobile shaker – the “Liquidator” – was used as a source: it can operate at frequencies ranging from about 0.5Hz to 80Hz. Sources of controlled vibration, like the Liquidator, have the advantage of generating one



**Figure 3.29** An instrumented sledgehammer (PCB Piezotronics Model 086D50) was used to excite high-frequency energy (Bailey 2008)



**Figure 3.30** Low frequency mobile vibrator "Liquidator" developed under the NSF-funded Network for Earthquake Engineering Simulation (NEES) Program (Bailey 2008)

frequency at a time, which allows for data collection in the frequency range. The Liquidator was developed through the Network for Earthquake Engineering Simulation (NEES) program funded by the National Science Foundation (NSF), and is operated by the University of Texas at Austin. Complete technical details on the Liquidator can be found in Stokoe et al. (2006).

All geophones used in to collect experimental surface wave data at the MORT site were Mark Products L-4 geophones manufactured by Sercel Incorporated which have a natural frequency of 1.0Hz, a nominal sensitivity of 2.77 Volts/cm/sec, and a coil resistance of 5500 Ohms. Bailey (2008) observes that these geophones have a flat response between 2Hz and 100Hz. He also notes that geophones used at the MORT site were first calibrated in the lab at the University of Texas at Austin. Also, geophone pairs closely matched in phase were selected for use in measurements at the lowest frequencies. Geophone locations were established exactly using a Nikon model NPL-821 total station and each geophone was buried to a depth of about 15cm by hand (Li 2008). Field installation of a geophone is shown in Figure 3.31.

The data acquisition system used to record the geophone outputs during surface wave testing included a digital signal analyzer and a laptop. The signal analyzer “consists of a VXI CT 100C main frame with four 16-channel cards with maximum sampling rate of 50 ksamples/sec, and one 8-channel card with a sampling rate of up to 100 ksamples/sec” (Li 2008). A Panasonic notebook (Toughbook) computer (Model: CF- 29CTPGZKM) was used to control the signal analyzer and record the data. Geophone data is recorded as time-series change in voltage amplitude.



**Figure 3.31** Mark Products L-4 High-sensitivity 1Hz Geophone (Li 2008)



**Figure 3.32** Field data acquisition setup, including a VXI digital signal analyzer and a laptop computer (Li 2008)

### 3.7.1.3 Receiver Arrays

Experimental data collection at the MORT site included seven SASW receiver spacings and two different multi-channel arrays. The SASW data were collected with the arrangement shown in Table 3.4 and Figure 3.33. Unlike the simulated data, many of the SASW spacings had slightly different source-to-first-receiver (S-R1) and receiver-to-receiver (R1-R2) distances. Multi-channel data were collected using two arrays of 14 receivers each: (1) a “short” array with a receiver spacing of 10m and a source-to-first-receiver distance of 50m, and (2) a “long” array with a receiver spacing 20m and a source-to-first-receiver distance of 220m. Using the nomenclature of Li (2011), the short array would be designated 50SR10RR-14, while the long array would be 220SR20RR-14. The arrays used to collect multi-channel data at the MORT site are tabulated in Table 3.5 and demonstrated visually in Figure 3.34.

**Table 3.4** Summary of SASW receiver spacings used for data collection at Site 1 (MORT)

Spacing Name	Active Source	S-R1(m)	R1-R2 (m)	Freq. Range (Hz)	Number of Freq.
4m	Hammer	4	4	6 to 150	Single Impact
10m	Hammer	10	10	4 to 50	Single Impact
20m	Vibrator	40	20	4 to 20	100
40m	Vibrator	60	40	2 to 15	100
80m	Vibrator	100	80	1 to 10	100
160m	Vibrator	180	160	0.7 to 5	100
300m	Vibrator	340	300	0.7 to 3	80

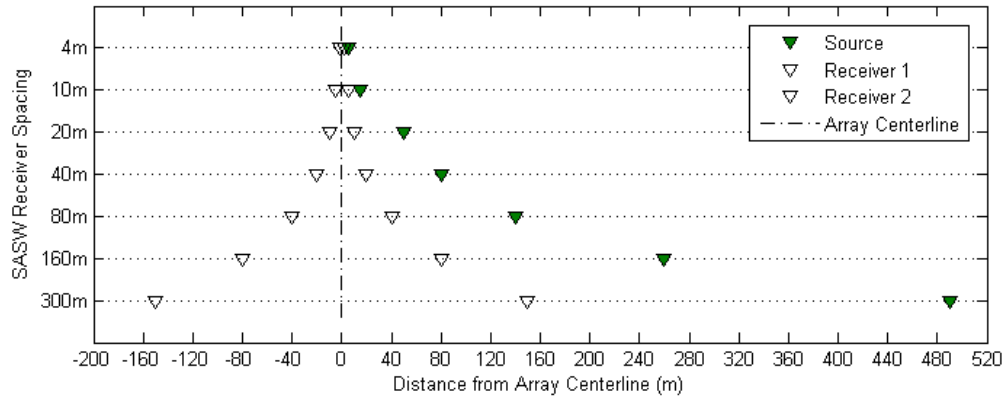


Figure 3.33 Visual representation of the SASW receiver spacings used to collect data at Site 1 (MORT)

Table 3.5 Summary of multi-channel arrays used for data collection at Site 1 (MORT)

Array Type	Active Source	Num. of Receivers	S-R1(m)	R1-R2 (m)	Array Length (m)	Freq. Range (Hz)	Number of Freq.
Short	Vibrator	14	50	10	130	2 to 50 0.7 to 5	200 40
Long	Vibrator	14	220	20	260	2 to 50 0.7 to 5	200 40

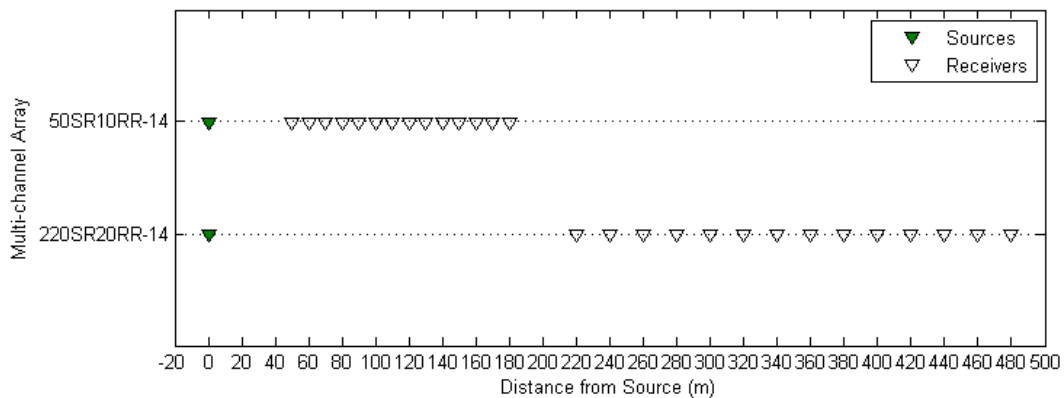


Figure 3.34 Visual representation of the multi-channel arrays used to collect data at Site 1 (MORT)

### 3.7.2 Experimental Dispersion Curve Calculations

The data processing stage for this study was essentially identical to the data processing performed for the simulated data study, as described in Section 3.6.2. For this study, SASW transfer functions computed from real experimental data were imported into WinSASW and masked out according to the data collection criteria used in the previous study. For this study, however, only the following data collection criteria were applied: 360°, 180°, and 90°. The 45° case was omitted due to poor signal quality at very low frequencies in the real data, an occurrence not evident in the simulated data. As previously noted, the angles refer to the extent to which the low frequency range of the wrapped phase plot is masked out (see Figure 2.8d) to

avoid near-field effects. These data were used to compute a composite experimental dispersion curve which was then averaged, by both global and array techniques, to obtain an experimental dispersion curve that can be used in an inversion analysis. For this study, multi-channel data were processed by the same techniques used in the simulated data study; dispersion curves generated by the FDBF technique were imported into WinSASW as segments of a composite dispersion curve and averaged by the global approach.

### **3.7.3 Inversion Analysis**

The inversion analysis stage of this study used essentially the same approach as that of the simulated data study (Section 3.6.3), but with data from one unknown real profile instead of four “perfectly known” simulated profiles. As is usually the case with real surface wave testing the “true” profile was not known *a priori*. This precluded any comparisons of inverted values with “true” values (e.g. the comparison of true and inverted  $V_s$  profiles – a hallmark of the simulated data study), but still allowed for comparisons between different methods. This study also incorporated the approach to studying Poisson’s ratio outlined in Section 3.6.4. However, due to the large spacings, high phase velocities, and the complexity inherent in real data, each inversion analysis had a high computation time demand. Therefore, only four values of Poisson’s ratio were considered (0.20, 0.30, 0.40, 0.45), plus a “saturated” case, where the P-wave velocity was set to 1600 m/s for most of the profile. The top 4m of the “saturated” profile was set to a Poisson’s ratio value of 0.25 to simulate an unsaturated zone above the shallow water table and maintain numerical stability.

## **4 RESULTS AND DISCUSSION – SIMULATION STUDIES**

### **4.1 Introduction**

The results of two simulation-based studies described in the previous chapter (see Sections 3.5 and 3.6) are presented and discussed in Chapter 4. The two studies included: (1) a preliminary sensitivity study and (2) surface wave analyses with simulated data. Preliminary sensitivity study results concerning the sensitivity of the near-field portion of the dispersion curve to changes in various profile conditions are presented and discussed in Section 4.2. Results of complete surface wave analyses using simulated experimental data are presented and discussed in Section 4.3.

### **4.2 Preliminary Sensitivity Study**

The results of a preliminary sensitivity study of near-field effects are presented and discussed in this section. The purpose of this portion of the study was to determine the sensitivity of the near-field portion of the dispersion curve to changes in several profile conditions, including: variations in the shear wave velocity ( $V_s$ ) profile and changes in Poisson's ratio. For the inversion procedure to be effective, changes in the parameter of interest must produce meaningful change in the dispersion curve. Current analysis only considers the far-field portion of the dispersion curve. It was hypothesized that changes in some profile parameters may produce a greater change in the near-field portion of the dispersion curve than the far-field portion, allowing these parameters to be evaluated in the dispersion analysis. Additionally, data collection procedures that use more of the near-field require shorter arrays and smaller sources, resulting in more efficient data collection. This study included 350 forward modeling simulations and was performed using the methods described in Section 3.5, considering the baseline profiles and variations previously shown in Figure 3.21. The effect of these changes on the near-field portion of the dispersion curve was assessed by comparing results of three different modeling approaches: (1) the "idealized" far-field case, (2) the "traditional SASW" case, and (3) the "alternative SASW" case including near-field data. These three approaches are briefly described in Section 4.2.1. Results of these approaches were compared over the same range of wavelengths for five different profile variations, including: (1) changes in the halfspace  $V_s$  and

(2) changes in halfspace depth for the case of a single layer over a halfspace (i.e. a simple “soft-over-stiff” profile), as well as (3) changes in the  $V_s$  gradient at a layer transition, (4) changes in the  $V_s$  gradient of the entire profile, and (5) changes in Poisson’s ratio value (of the entire profile) for several profile conditions. While six different wavelength ranges were considered for this study (see Table 3.1) only the longest wavelengths are of primary interest. Therefore, only the results for the wavelength range of 5.33m to 32m (i.e. receiver spacing = 16m), are shown in this section. Complete sensitivity study results for all wavelength ranges can be found in the Appendix of this thesis.

#### 4.2.1 Near-field Sensitivity Study Results

All of the sensitivity study results are presented in the same format, from Figure 4.1 to Figure 4.21. Three figures are presented for each of the four  $V_s$  profile variations, while the Poisson’s ratio results have three figures for each of the three baseline profiles studied. The first figure in each section shows the simulation results for the “idealized” case where only planar Rayleigh waves are propagating (i.e. 2D solution). The second figure in each section presents the simulation results for the “Traditional SASW” case where the complete wavefield is simulated (i.e. 3D solution), but multiple receiver spacings (i.e. 2m, 4m, 8m, 16m) and typical SASW near-field filtering criteria were used to cover the desired wavelength range while minimizing the near-field contribution. The third figure in each section shows the simulation results for the “Alternative SASW” approach where the complete wavefield is simulated (i.e. 3D solution), but data are collected in the near-field using a single receiver spacing. Only results from the longest spacing are presented for comparison (results from other spacings can be found in the appendix).

On each figure, part (a) shows the profile variations considered, (b) shows the simulated dispersion curves and (c) shows the sensitivity of the dispersion curve (percent difference in phase velocity from the baseline) to changes in profile parameters. On all figures, (b) and (c) are plotted versus frequency instead of wavelength, as WinSASW computes different wavelengths for the 2D and 3D models. The near-field has the most influence on the dispersion curve at low frequencies (i.e. long wavelengths).

#### 4.2.1.1 Halfspace Velocity

Representative sensitivity study results for variations in halfspace (i.e. “Layer 2”) velocity are presented in Figure 4.1, Figure 4.2, and Figure 4.3. This case was selected for the sensitivity study as a representative example of a two-layer system, where the goal of the surface wave measurement is to determine the shear wave velocity ( $V_s$ ) of both the upper and lower (i.e. halfspace) layers. Real in-situ conditions are often approximated by systems of one or more horizontal layers over a halfspace. Dispersion curves derived from surface wave measurements of a layered system must show sensitivity to the  $V_s$  of all layers (particularly the halfspace) for an inversion analysis to be successful.

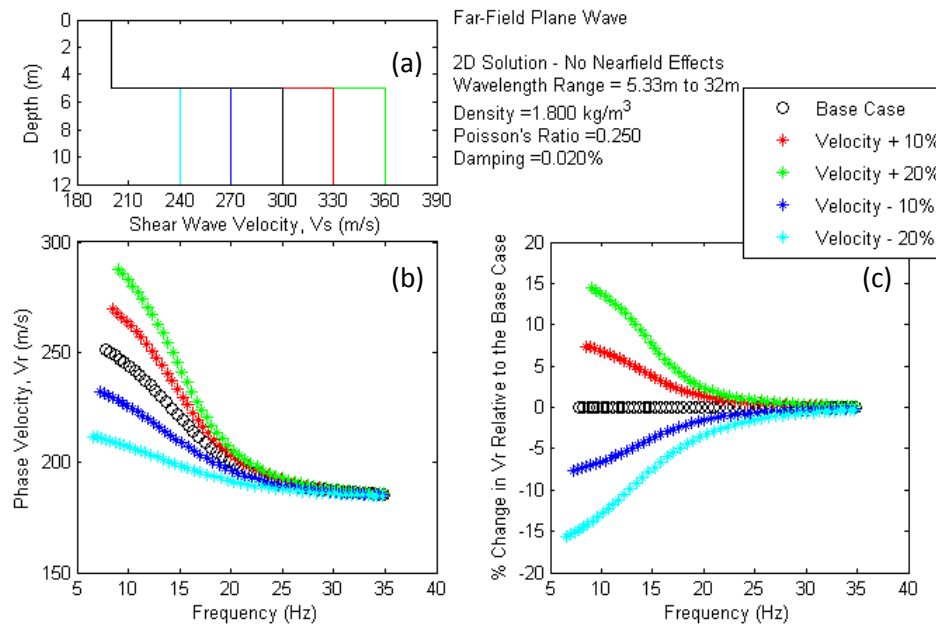


**Figure 4.1** Sensitivity study results derived from the 2D Plane wave solution for a simple “soft-over-stiff” profile with a variable lower layer  $V_s$

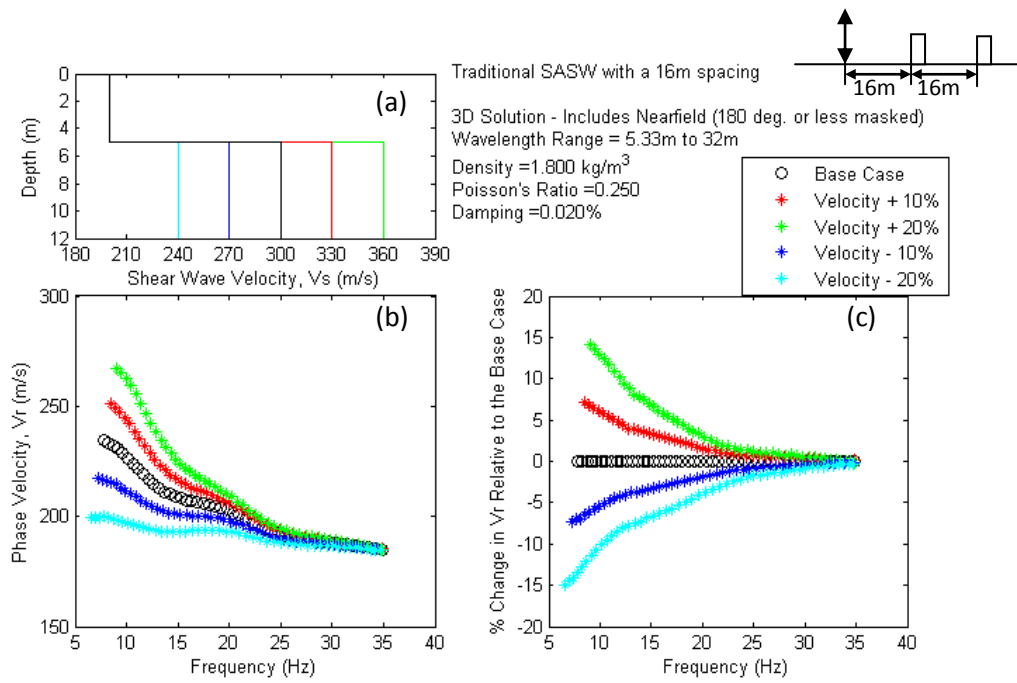


**Figure 4.2** Sensitivity study results derived from the 3D solution with a traditional SASW arrangement with a 16m receiver spacing for a simple “soft-over-stiff” profile with a variable lower layer  $V_s$

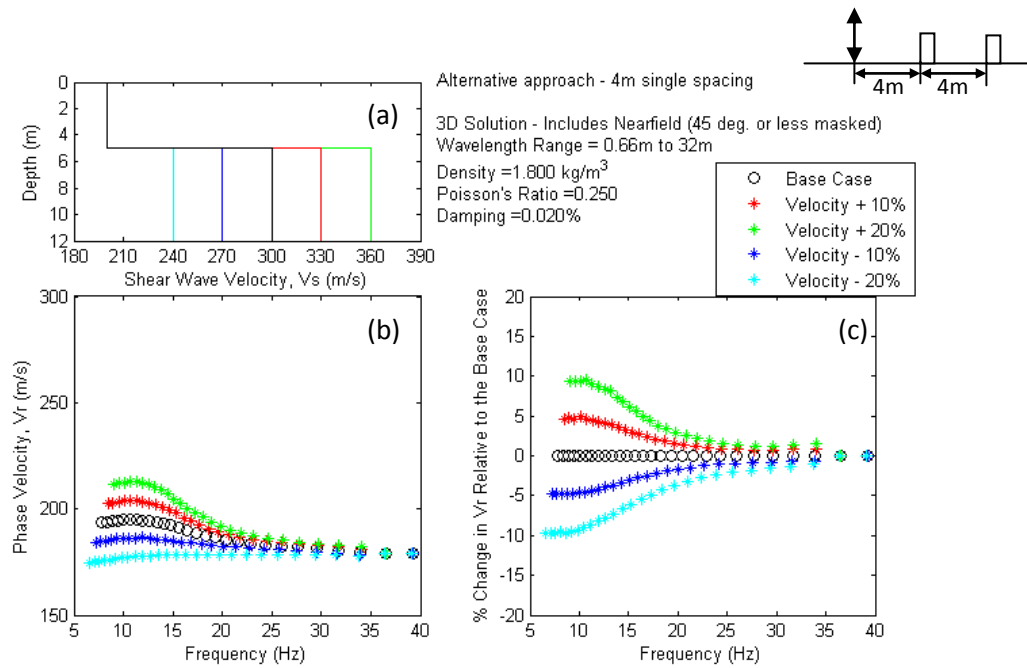


**Figure 4.3** Sensitivity study results derived from the 3D solution with an alternative approach using a stationary 4m receiver spacing for a simple “soft-over-stiff” profile with a variable lower layer  $V_s$

#### 4.2.1.2 $V_s$ Profile Gradient

Sensitivity study results for variations in the  $V_s$  profile gradient are presented in Figure 4.4, Figure 4.5, and Figure 4.6. Gradient values are presented in terms of linear slope (e.g. “10H:1V” means that the  $V_s$  profile increases by 10m/s for every 1m of depth). This case was selected to assess the sensitivity of the dispersion curve to changes in the gradient of the  $V_s$  profile. Inversion analysis requires that the dispersion curve must be sensitive to the profile gradient.

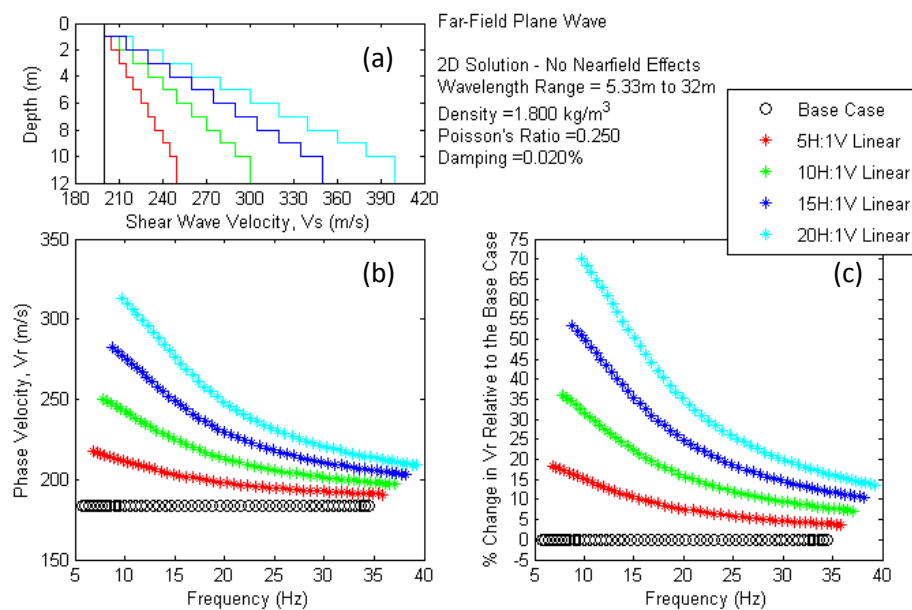


**Figure 4.4** Sensitivity study results derived from the 2D Plane wave solution for a variable  $V_s$  profile transition gradient

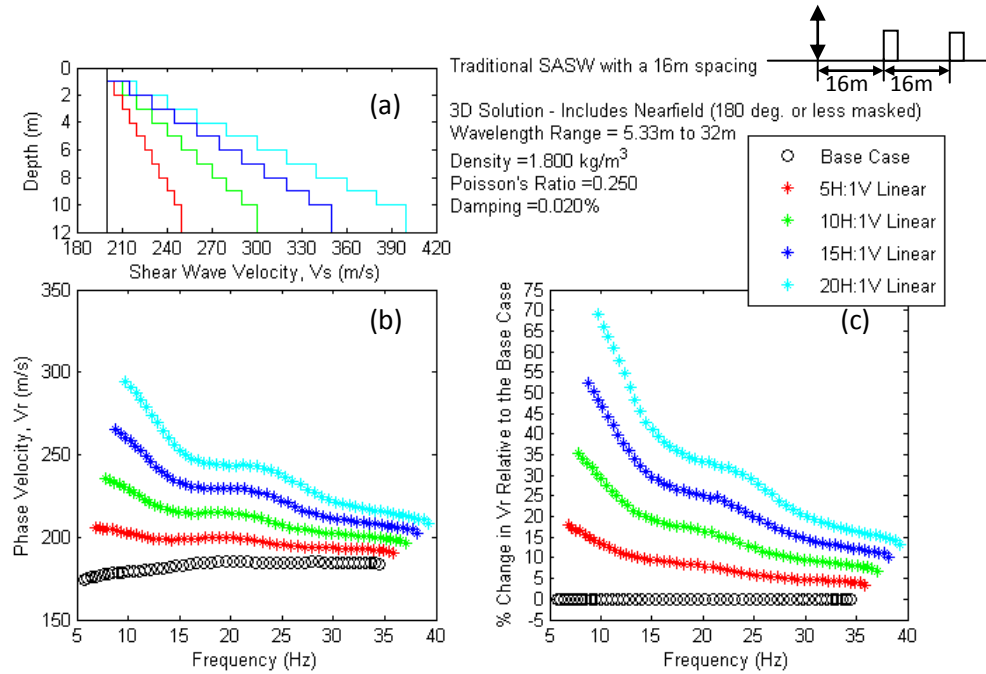


**Figure 4.5** Sensitivity study results derived from the 3D solution with a traditional SASW arrangement with a 16m receiver spacing for a variable  $V_s$  profile transition gradient

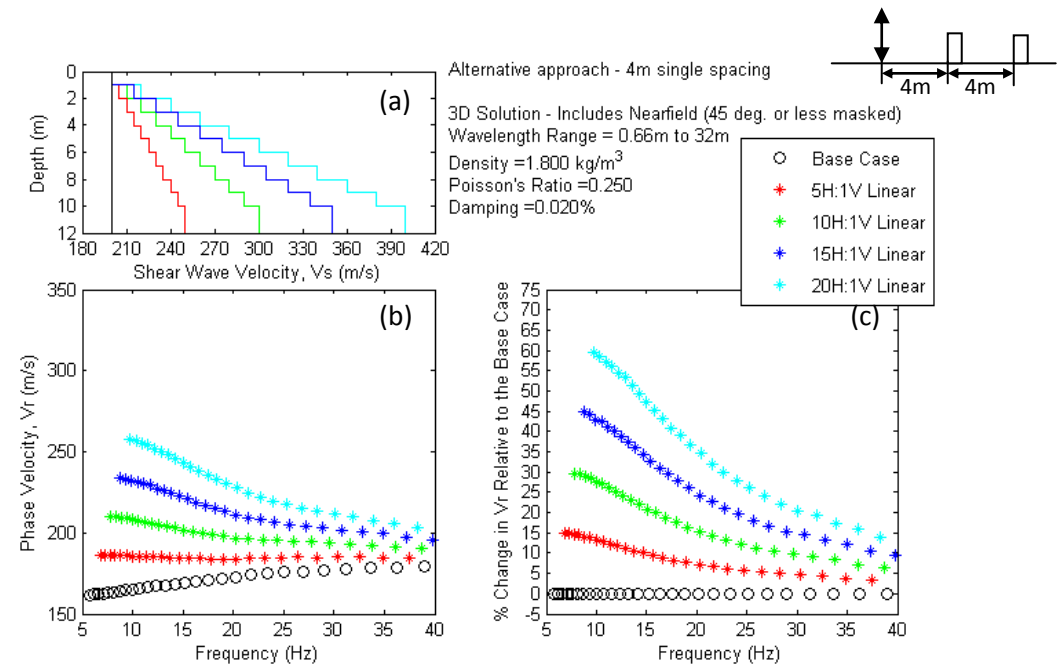


**Figure 4.6** Sensitivity study results derived from the 3D solution with an alternative approach using a stationary 4m receiver spacing for a variable  $V_s$  profile transition gradient

### 4.2.1.3 Halfspace Depth

Sensitivity study results for variations in the depth of the halfspace (i.e. “Layer 2”) are presented in Figure 4.7, Figure 4.8, and Figure 4.9. Having assessed the sensitivity of the dispersion curve to “macro-scale” changes in the  $V_s$  profile, the next two phases of the study considered the effect of changes in  $V_s$  at the layer/halfspace interface. In some cases, the layer velocities may be relatively well constrained but the thickness may be of particular interest (e.g. assessing the thickness of pavement layers). The sensitivity of the dispersion curves to changes in the halfspace depth was studied by varying the depth of the half-space by  $\pm 10\%$  to  $\pm 20\%$ .

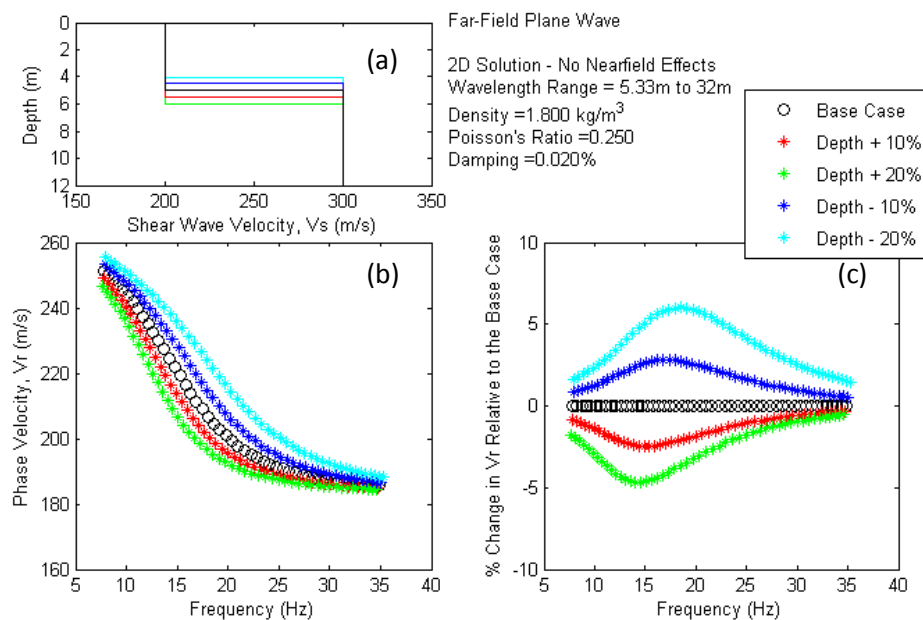


**Figure 4.7** Sensitivity study results derived from the 2D Plane wave solution for a simple “soft-over-stiff” profile with a variable lower layer depth

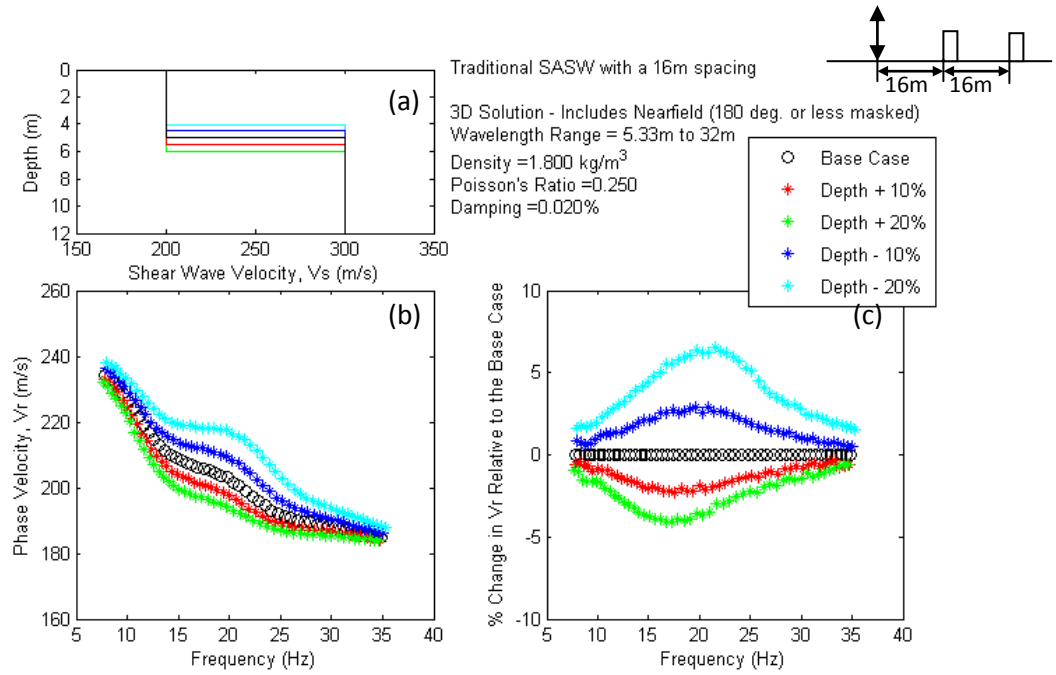


**Figure 4.8** Sensitivity study results derived from the 3D solution with a traditional SASW arrangement with a 16m receiver spacing for a simple “soft-over-stiff” profile with a variable lower layer depth

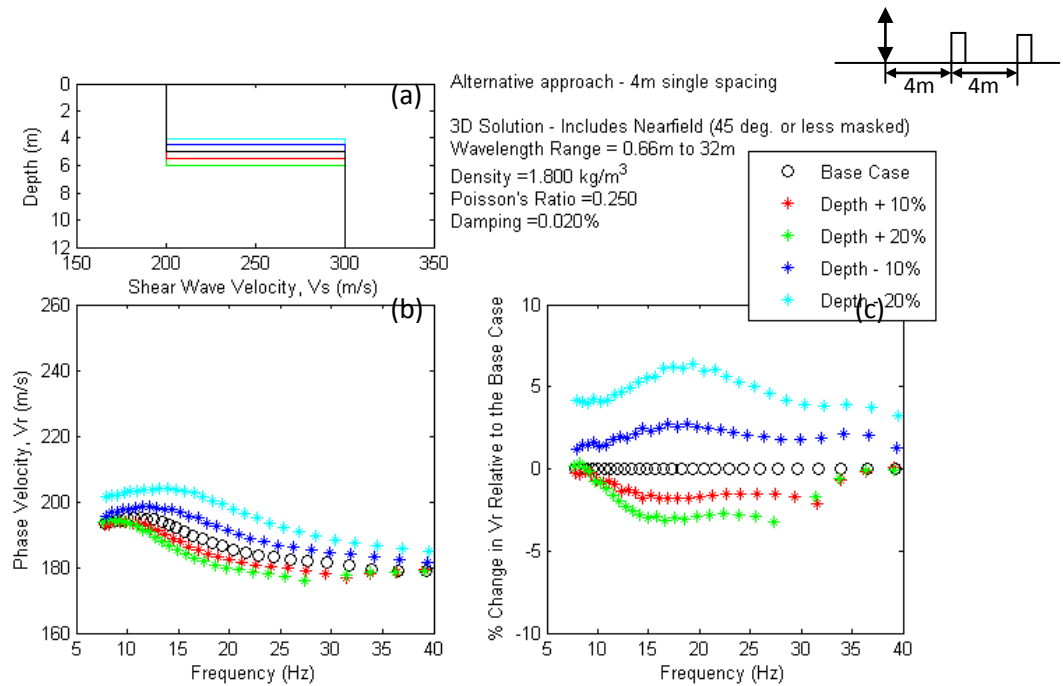


**Figure 4.9** Sensitivity study results derived from the 3D solution with an alternative approach using a stationary 4m receiver spacing for a simple “soft-over-stiff” profile with a variable lower layer depth

#### 4.2.1.4 Layer Transition Gradient

The transition between two layers is often of great interest in geotechnical engineering. For example, in earthquake engineering, site response amplification can be quite different for the case of an abrupt transition (with a large impedance contrast) versus a gradual transition. Sensitivity study results for variations in the transition gradient between the upper layer and the halfspace are presented in Figure 4.10, Figure 4.11, and Figure 4.12. The transition gradient at the layer/halfspace interface was studied with the change varying from instantaneous to varying linearly over a range of thicknesses (as shown below).

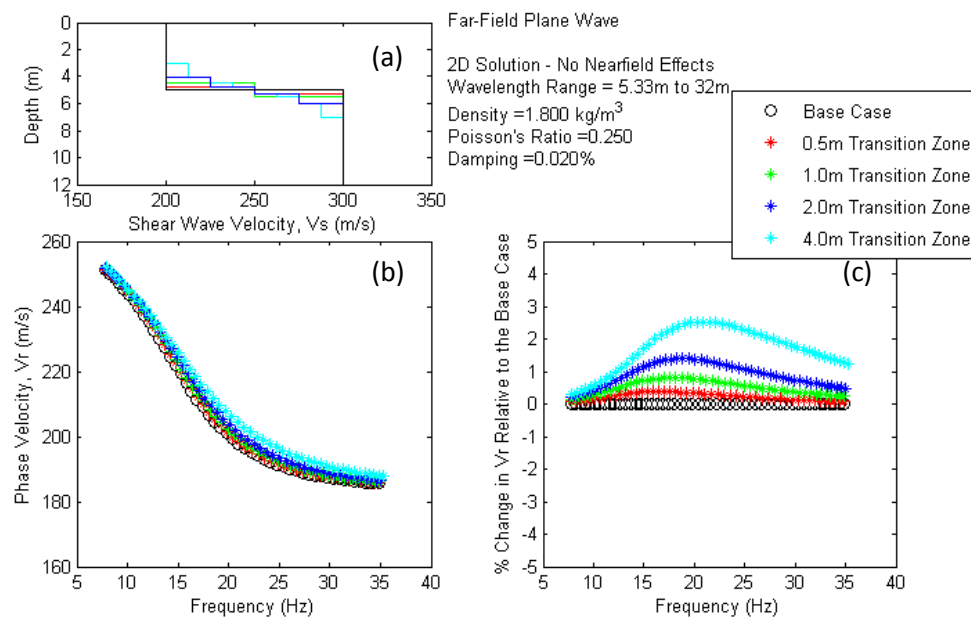


**Figure 4.10** Sensitivity study results derived from the 2D Plane wave solution for a simple “soft-over-stiff” profile with a variable layer transition gradient

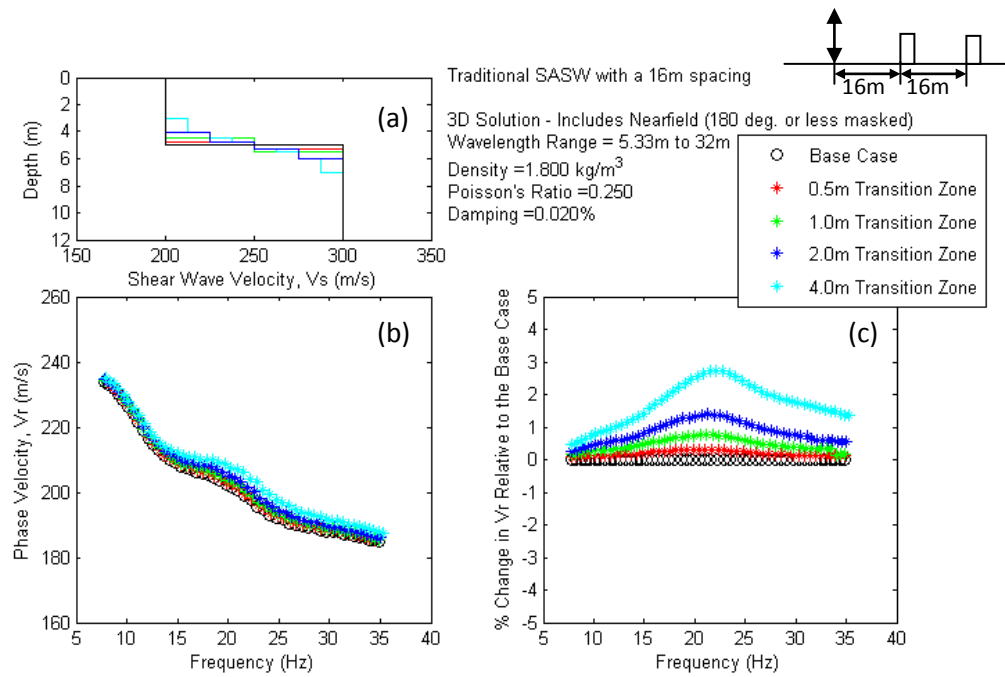


**Figure 4.11** Sensitivity study results derived from the 3D solution with a traditional SASW arrangement with a 16m receiver spacing for a simple “soft-over-stiff” profile with a variable layer transition gradient

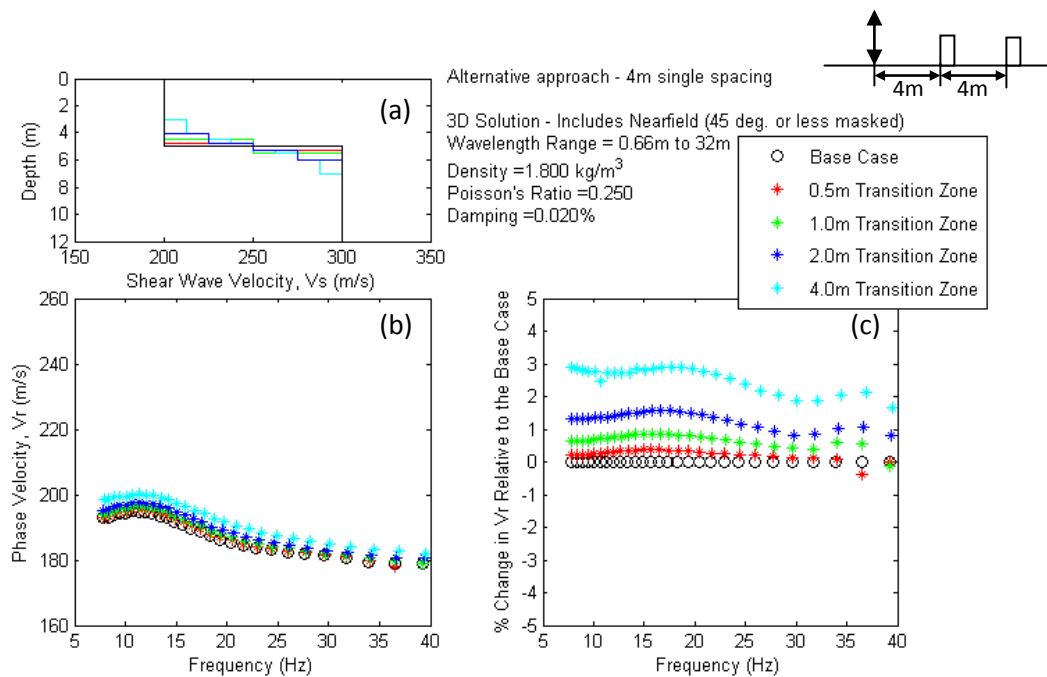


**Figure 4.12** Sensitivity study results derived from the 3D solution with an alternative approach using a stationary 4m receiver spacing for a simple “soft-over-stiff” profile with a variable layer transition gradient

#### **4.2.1.5 Poisson's Ratio ( $\nu$ )**

Having assessed the sensitivity of the dispersion curve to changes in the  $V_s$  profile, this final stage of the sensitivity study considered the effect of changes in Poisson's ratio on the near-field portion of the dispersion curve. Poisson's ratio is an important parameter in geotechnical engineering because, (1) it indicates saturation conditions (fully saturated soft soil will have a Poisson's ratio near 0.5), and (2) incorrect values can have an impact on the reliability of analyses performed due to the large possible range of values (0.15 to 0.499). It should be reiterated at this point that current procedures used in surface wave analysis recognize that it is not possible to infer Poisson's ratio from surface wave measurements alone, so it must be either known *a priori* or, more commonly, assumed. The focus of this study was to examine if this holds true when the near-field is included in the analysis. A range of Poisson's ratio values was selected (0.25, 0.33, 0.40, 0.45, and 0.49) to represent a range of soil types and site conditions. The results for a Poisson's ratio of 0.49 were found to be numerically unstable and were omitted from the figures in this section. Sensitivity study results for variations in the value of Poisson's ratio for the entire profile are presented for the uniform baseline profile in Figure 4.13, Figure 4.14, and Figure 4.15. Results for the simple "soft-over-stiff" baseline profile are shown in Figure 4.16, Figure 4.17, and Figure 4.18, while the results for the linear baseline profile are presented in Figure 4.19, Figure 4.20, and Figure 4.21.

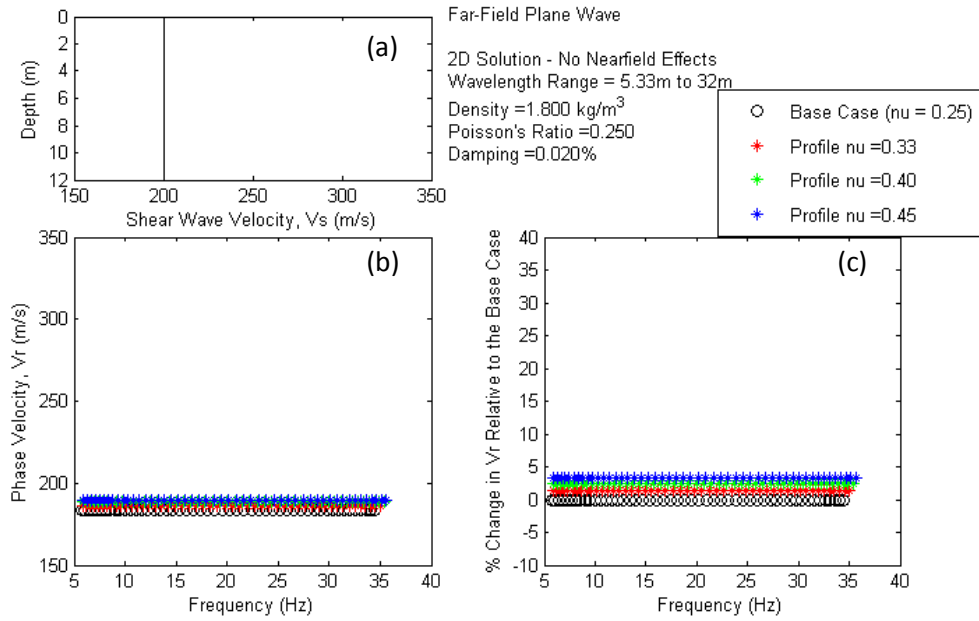


**Figure 4.13** Sensitivity study results derived from the 2D Plane wave solution for a uniform  $V_s$  profile with a variable Poisson's ratio

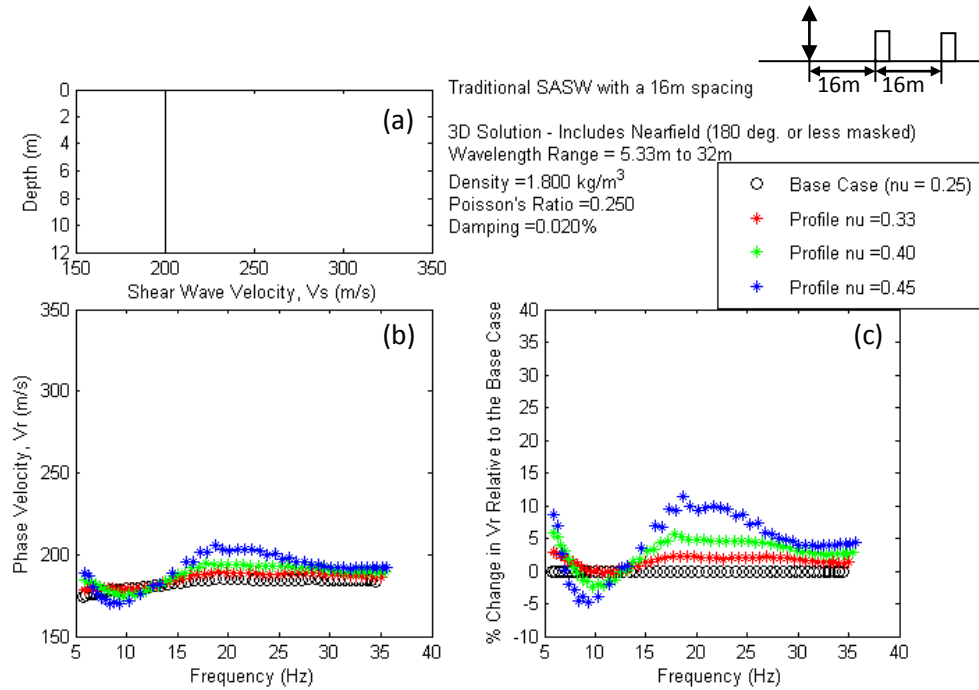


**Figure 4.14** Sensitivity study results derived from the 3D solution with a traditional SASW arrangement with a 16m receiver spacing for a uniform profile with a variable value of Poisson's ratio

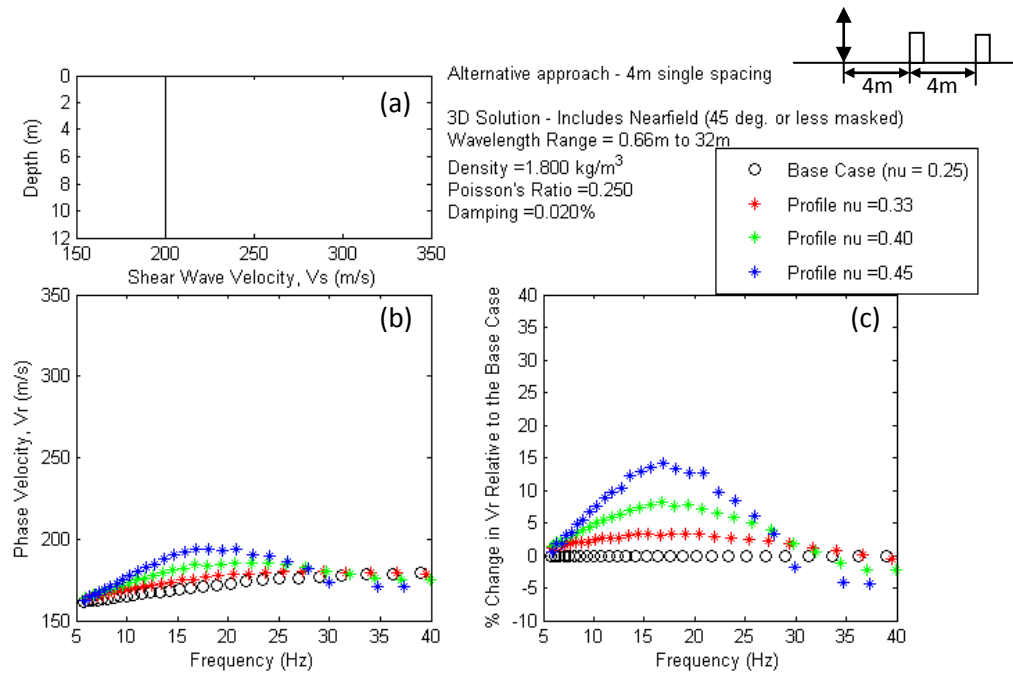


**Figure 4.15** Sensitivity study results derived from the 3D solution with an alternative approach using a stationary 4m receiver spacing for a uniform profile with a variable value of Poisson’s ratio

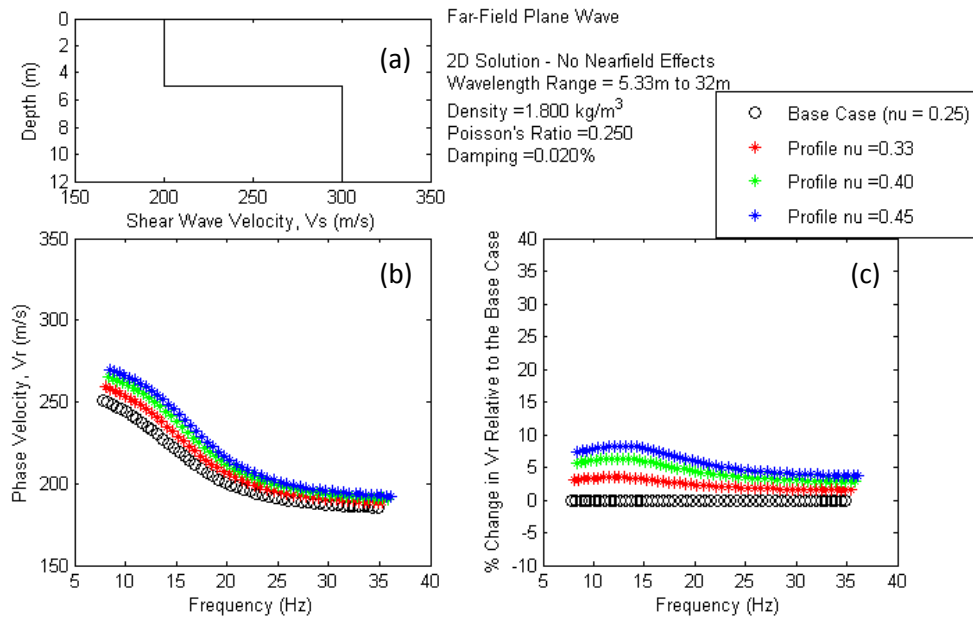


**Figure 4.16** Sensitivity study results derived from the 2D Plane wave solution for a simple “soft-over-stiff” profile with a variable value of Poisson’s ratio

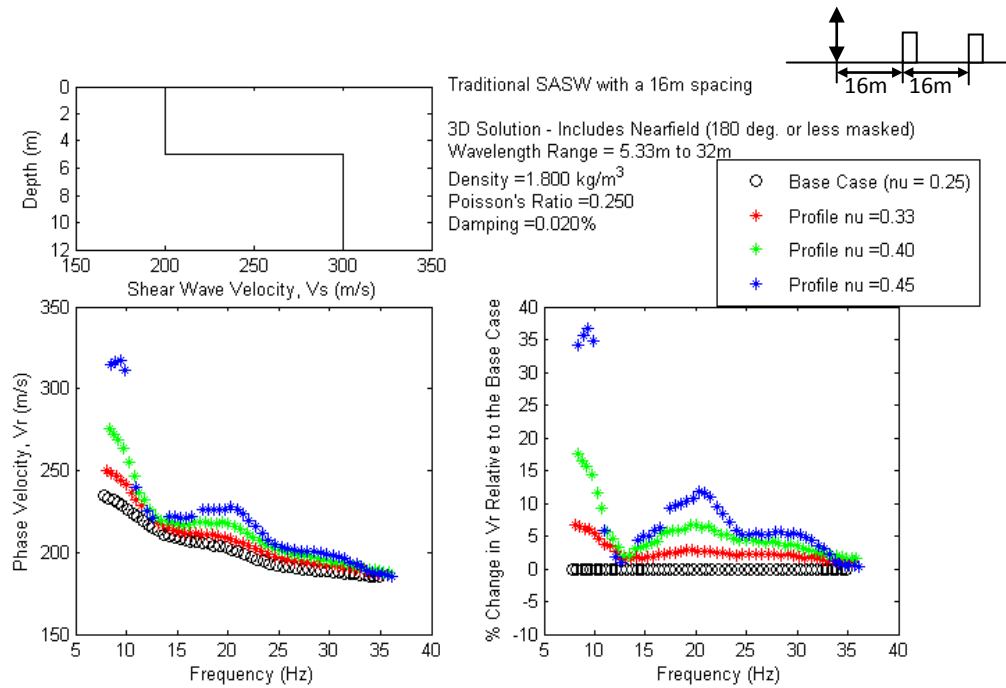


**Figure 4.17** Sensitivity study results derived from the 3D solution with a traditional SASW arrangement with a 16m receiver spacing for a simple “soft-over-stiff” profile with a variable value of Poisson’s ratio

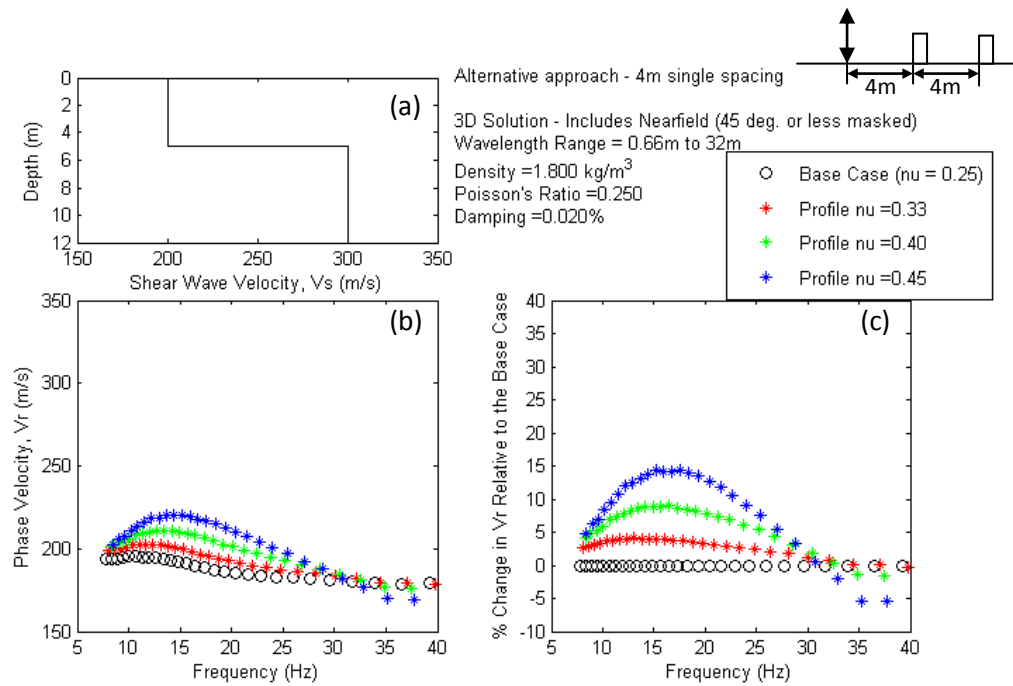


**Figure 4.18** Sensitivity study results derived from the 3D solution with an alternative approach using a stationary 4m receiver spacing for a simple “soft-over-stiff” profile with a variable value of Poisson’s ratio

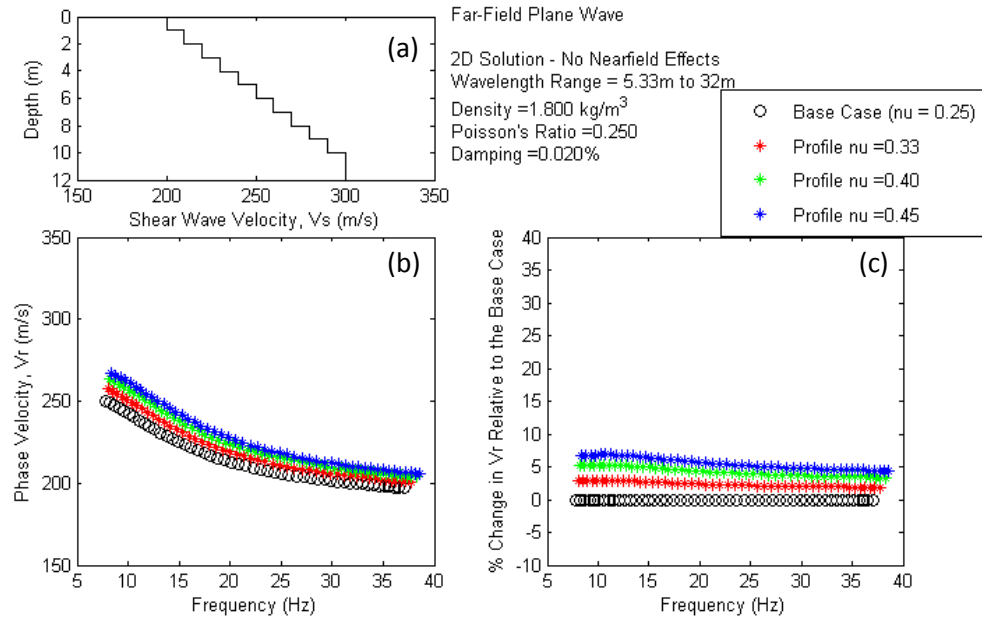


**Figure 4.19** Sensitivity study results derived from the 2D Plane wave solution for a linear profile with a variable value of Poisson's ratio

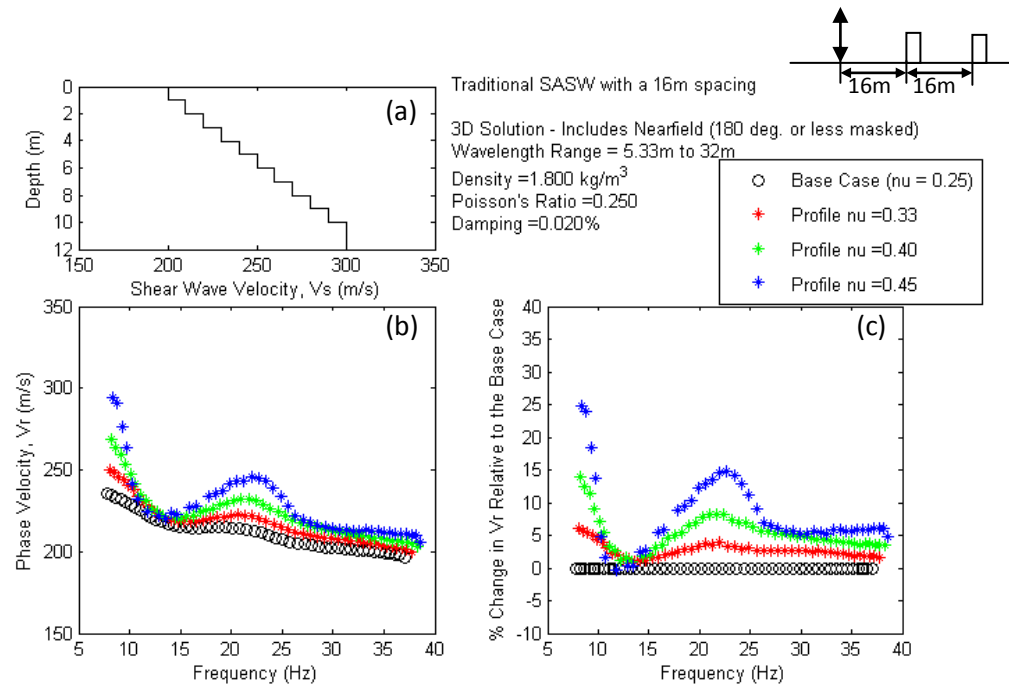


**Figure 4.20** Sensitivity study results derived from the 3D solution with a traditional SASW arrangement with a 16m receiver spacing for a linear profile with a variable value of Poisson's ratio

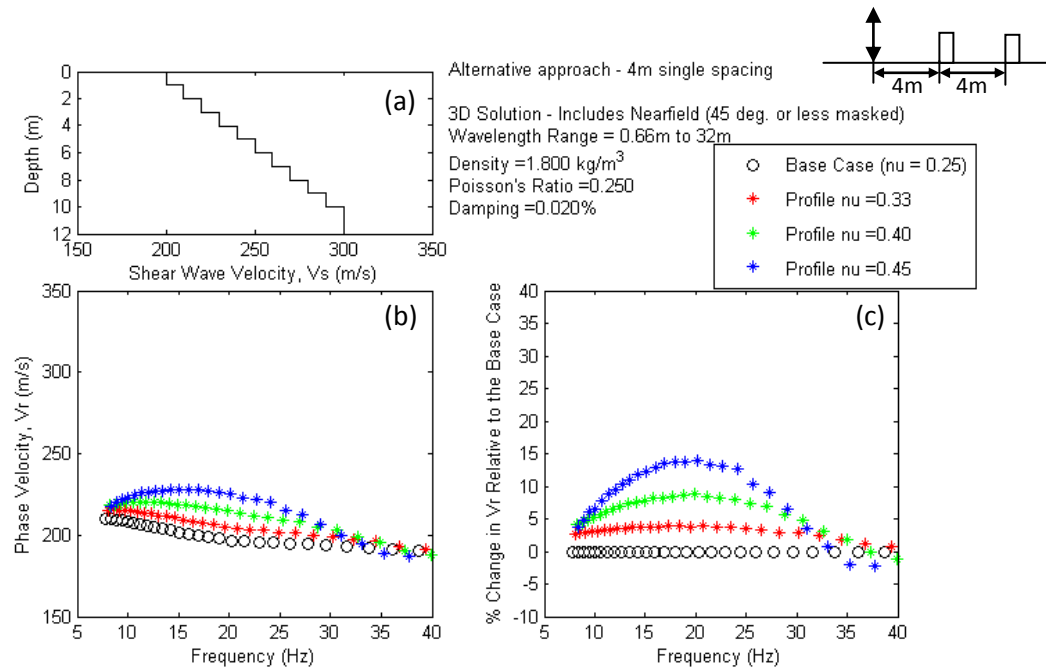


**Figure 4.21** Sensitivity study results derived from the 3D solution with an alternative approach using a stationary 4m receiver spacing for a linear profile with a variable value of Poisson's ratio

#### 4.2.2 Discussion of Near-field Sensitivity Study

The sensitivity study results presented in the Section 0 demonstrate the effect of profile variations on the near-field portion of the dispersion curve. The goal of this study was to determine the sensitivity of the near-field region of the dispersion curve to changes in profile parameters. To this end, three different types of parametric variations were considered: (1) changes in the shear wave velocity ( $V_s$ ) profile, (2) changes in the  $V_s$  transition between layers in the profile, and (3) changes in the value of Poisson's ratio for the entire profile. Three different approaches were used to model dispersion curves for each set of parametric variations: (1) the "Idealized" pure Rayleigh wave simulates a 2D far-field plane wave, (2) the "Traditional SASW" approach common in current practice, which limits near-field effects through masking and receiver locations, and (3) the "Alternative SASW" approach examined in this thesis, using a single short array with extensive inclusion of near-field effects. The practical implications of the alternative SASW approach are illustrated in Figure 4.22, where one receiver spacing is used to collect data that requires four receiver spacings with the traditional SASW approach.

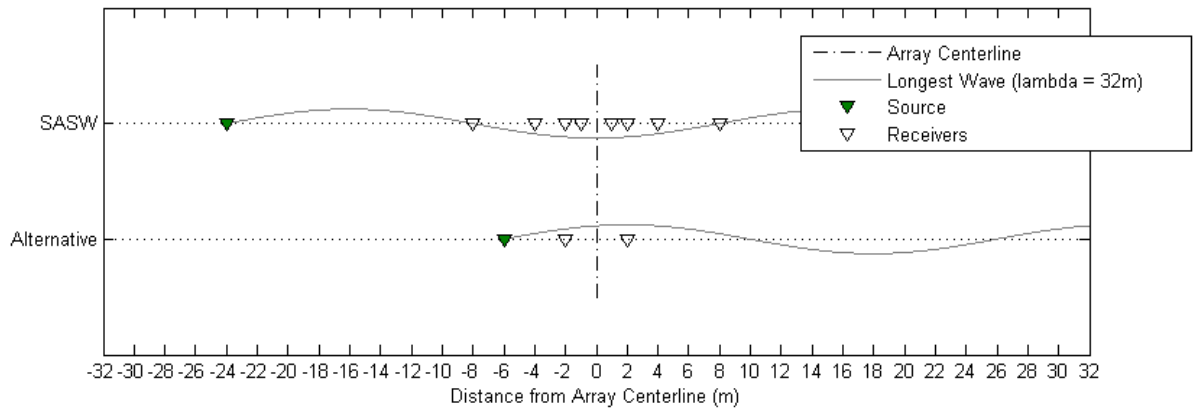


**Figure 4.22** Visual comparison of data collection arrays for the “Traditional SASW” and “Alternative SASW” approaches over the same range of wavelengths

The results from studies involving changes in VS profiles are presented above in Sections 4.2.1.1 and 4.2.1.2. The results from the halfspace study (Section 4.2.1.1) indicate that, as expected, the 2D Rayleigh wave is very sensitive to changes in the shear wave velocity of the lowest layer (Figure 4.1). For example, a 20% change in the shear wave velocity of the halfspace resulted in a change of nearly 15% in the dispersion curve at the lowest frequency (longest wavelengths). Also, as expected, the traditional SASW approach (which is designed to minimize near-field effects) yielded very similar results to the idealized case. Although the dispersion curves were only slightly different from those of the idealized case, the results suggested that the traditional SASW approach is not completely effective in eliminating near-field effects. The results from the alternative approach are quite different in some respects. In comparing the actual dispersion curves (Figure 4.3b) using this approach to those obtained using the idealized (Figure 4.1b) and traditional SASW approach (Figure 4.2b), it can be observed that the phase velocities measured at long wavelengths are still much lower. However, change in phase velocity (as compared to the base condition) is still rather large. In this case, a 20% change in shear wave velocity of the half-space causes a 10% change in phase velocity. Similar trends are evident for the case of the  $V_S$  profile gradient presented in Section 4.2.1.2. In this case, the alternative approach shows much lower velocity values in the dispersion curve at long wavelengths (compare Figure 4.6b to Figure 4.4b and Figure 4.5b), but only slightly lower sensitivity to changes in  $V_S$  (compare Figure 4.6c to Figure 4.4c and Figure 4.5c). These results suggest that although the alternative single-setup approach produces dispersion curves that are inconsistent with the true Rayleigh wave dispersion curves, they are still sensitive to changes in the  $V_S$

profile, suggesting that this single setup may be just as effective as the multiple setups for inferring  $V_s$  profile conditions.

The results from studies involving changes in  $V_s$  transitions are presented above in Sections 4.2.1.3 and 4.2.1.4. As in the previous cases, the idealized and traditional approaches showed similar results (compare Figure 4.7 to Figure 4.8 and Figure 4.10 to Figure 4.11). The alternative approach again produced dispersion curves with much lower phase velocity values (Figure 4.9b and Figure 4.12b), but sensitivity plots (Figure 4.9c and Figure 4.12c) that showed comparable values to those obtained with the idealized and traditional approaches. In addition, the alternative approach showed sensitivity at low frequencies (Figure 4.9c and Figure 4.12c) that was not evident at the same frequencies in the idealized or traditional cases. This suggests that the near-field does have a different (and enhanced) sensitivity to changes in interface characteristics (especially in the gradient between layers) and, thus, could be a better approach to collecting and analyzing the data. However, the changes in all cases are very small (3 to 5% changes in phase velocity) and are likely too small to produce meaningful differences in practice.

The results from the final study involving changes in Poisson's ratio are presented in Section 4.2.1.5. From the results of final phase of the sensitivity study, it is evident that the dispersion curve has a distinct and strong sensitivity to changes in the value of Poisson's ratio when near-field effects are included in the analysis. The same study was repeated for each of the baseline profiles: results for the uniform, "soft-over-stiff", and linear profiles all demonstrated a similar sensitivity. For the idealized case, variations in Poisson's ratio seem to only cause small shifts in the phase velocity (i.e. a "vertical translation") of the dispersion curve at all frequencies (Figure 4.13, Figure 4.16, and Figure 4.19). Practically, this means that the quality of the theoretical fit to the experimental curve is not sensitive to an incorrect value of Poisson's ratio (i.e. a similar quality of fit can be achieved with the wrong value of Poisson's ratio and the wrong  $V_s$  profile). This is consistent with current surface wave practice, which requires assumed or known values of Poisson's ratio. However, results for both the traditional SASW and alternative SASW approaches show not only the "vertical translation" effect, but also significant changes in the shape of the dispersion curve itself, depending on the value of Poisson's ratio (Figure 4.14 and Figure 4.15; Figure 4.17 and Figure 4.18; Figure 4.20 and Figure 4.21). Poisson's ratio values closer to 0.50 have the most profound effect, producing a maximum phase velocity difference in excess of 15 to 20% and large undulations in the dispersion curve. This result is consistent with the figures presented by Mera (1995) and Chen et al. (2004), as shown in Figure

2.18 and Figure 2.19. The Poisson's ratio effect was most pronounced for the alternative SASW setup, where more near-field data was collected.

Two key findings were developed from this preliminary sensitivity study. First, the "Alternative SASW" approach, with a single short receiver spacing, was found to have similar sensitivity to changes in profile properties as those from the "Idealized" and "Traditional SASW" approaches. This suggests that the SASW approach to data collection and analysis could be implemented more efficiently without compromising quality. Second, the near-field region of the dispersion curve (i.e. low frequencies/long wavelengths) was *more* sensitive to some profile changes than the "Idealized" and "Traditional SASW" approaches. Most interestingly, the near-field portion of the dispersion curve was particularly sensitive (in terms of both velocity values and dispersion curve shape) to changes in Poisson's ratio for all  $V_s$  profiles considered. This suggests that the value of Poisson's ratio, which is currently assumed for most analyses, could be inferred by inversion analysis. These two issues were investigated further by analyzing simulated surface wave data obtained from different profile conditions, as reported below.

### **4.3 Results from Analysis of Simulated Surface Wave Data**

The central hypothesis of this research is that the efficiency and effectiveness of surface wave methods can be improved by including more near-field data in the data collection and analysis. To investigate this hypothesis, three different studies were performed using simulated surface wave data for five assumed profile conditions, as described in Section 3.6.1. The first study (Section 0) considered the influence of the near-field on "profile recovery" for SASW, where an inversion analysis was performed on data generated from a known (i.e. "true") profile to assess the feasibility of correctly identifying (i.e. recovering) the "true" profile when near-field effects are present. The second study (Section 4.3.3) considered the effect of Poisson's ratio on SASW analyses, with particular attention to the possibility of inferring the "true" value of Poisson's ratio by inversion analysis. The third study (Section 4.3.5), although somewhat limited in scope, considered both "profile recovery" and Poisson's ratio effects for current approaches to multi-channel surface wave measurements. These studies were performed using the methods described in Section 3.6 (multi-channel data were processed as described in Section 3.4). A total of 280 SASW analyses and 28 multi-channel analyses were completed for this study.

#### 4.3.1 Results of Profile Recovery Study with Simulated SASW Data

This section presents results of the “profile recovery” study, which was performed to address the question of whether surface wave measurements could be performed more efficiently. The results of the preliminary study suggested the possibility of using much shorter arrays with more near-field data (and hence smaller sources). In this study, four different approaches to collecting and processing surface wave data were used to generate experimental dispersion curves having a maximum wavelength of 64m. These approaches are summarized in Table 3.3 and Figure 3.23. Near-field “filtering” criteria of 360°, 180°, 90° and 45° were applied to the data. The 360° criterion represents a very conservative approach to limiting near-field surface wave data and requires a maximum array length (source to far receiver) of 128 m to generate a dispersion curve to a wavelength of 64m. The 180° criterion represents the “traditional” SASW approach to limiting surface wave data and requires a maximum array length (source to far receiver) of 64m to generate a dispersion curve to a wavelength of 64m. The 90° criteria is one alternative approach investigated in this study and requires a maximum array length (source to far receiver) of 32 m to generate a dispersion curve to a wavelength of 64m. The 45° criteria is the other alternative approach investigated in this thesis and requires a maximum array length (source to far receiver) of only 16m to generate a dispersion curve to a wavelength of 64 m. Inversion analysis performed on the experimental dispersion curves obtained with the different filtering criteria, using three different theoretical models as described in Section 3.6.3, including the 2D (with no near-field), 3D global (with limited near-field), and 3D Array inversion approaches. The central question is whether reliable results can be obtained with more efficient data collection methods (e.g. 90° and 45°).

Results for this study are presented in two ways. First, a  $V_s$  profile plot grid is presented, comparing the inverted and “true” profiles for each of the different filtering criteria and theoretical models used in the analysis. Each grid is associated with one of the five profiles used to simulate the experimental data, while the rows correspond to inversion approaches and the columns correspond to filtering criteria. The dispersion curves obtained using the 90° and 45° criteria were not inverted by the 2D and 3D global models, since it is apparent that the far-field models and near-field data collection are incompatible. Second, plots of percent error between the inverted and true profile for each layer in the profile are presented. Plots of percent error in profile recovery are presented based on the numbering scheme described in Table 4.1, for each

combination of inversion approach and filtering criterion. The results of this study are discussed in Section 4.3.4.

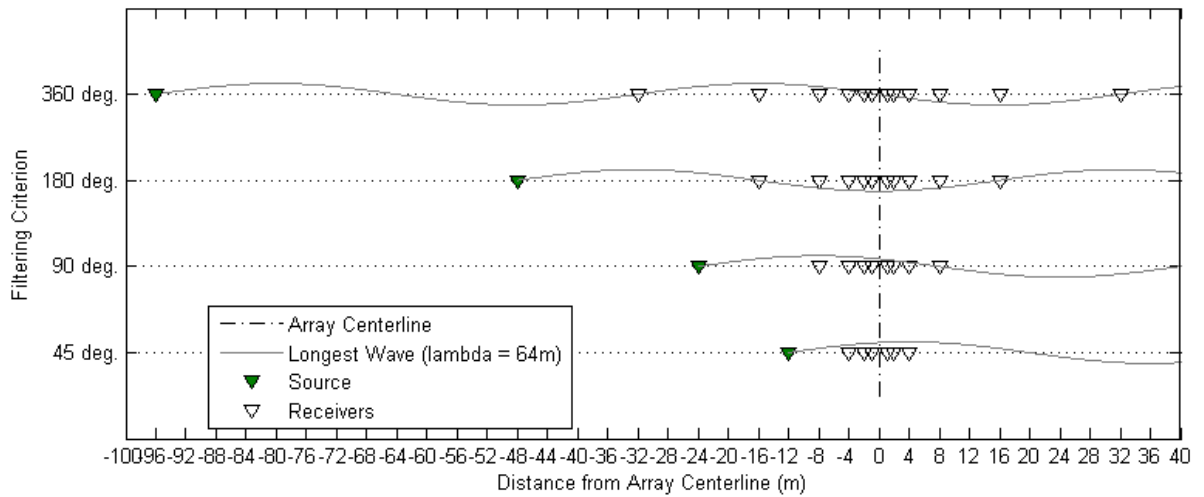


**Figure 4.23** Visual representation of the receiver arrays used to measure a maximum wavelength of 64m (blue line) with each of the four filtering criteria.

**Table 4.1** Summary of Inversion Approach/Filtering Criterion Combinations for the first inversion study

Designation		Filtering Criterion			
		360°	180°	90°	45°
Inversion Approach	2D	<b>(1)</b>	<b>(2)</b>	N/A	N/A
	3D Global	<b>(3)</b>	<b>(4)</b>	N/A	N/A
	3D Array	<b>(5)</b>	<b>(6)</b>	<b>(7)</b>	<b>(8)</b>

#### 4.3.1.1 Case A – Uniform $V_S$ Profile ( $\nu = 0.30$ )

Inversion sensitivity results for the case of a uniform  $V_S$  profile (Case A) are shown in Figure 4.24. The Case A profile was used to generate simulated data in FitSASW, which were processed according to the four filtering criteria indicated (360°, 180°, 90°, and 45°) and inverted by three approaches (2D Global, 3D Global, and 3D Array).  $V_S$  profiles derived from inversion analysis are shown with a solid line, while the “true” Case A profile is shown with a dashed line. Only the value of  $V_S$  in each layer was inverted in this study – the profile layering and all other parameters, including Poisson’s ratio, were held constant.

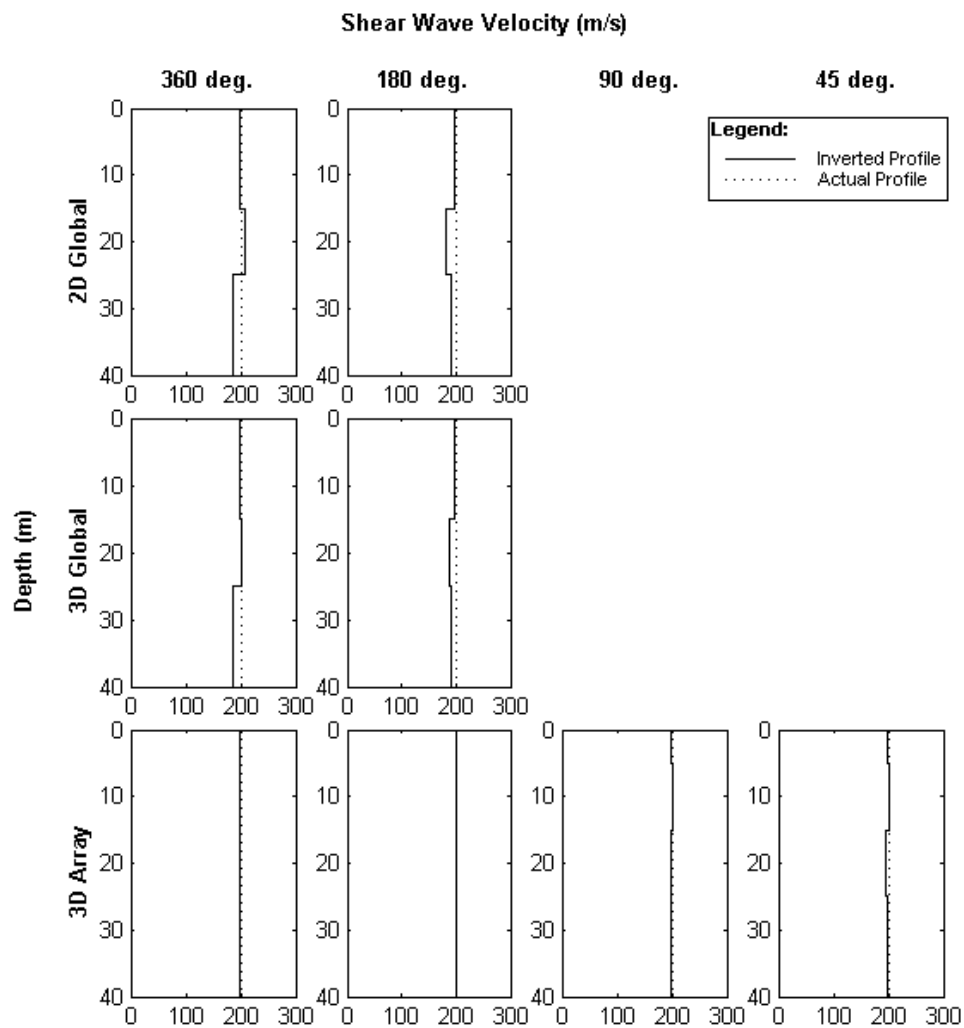


**Figure 4.24** Comparison of the “true”  $V_S$  profile for Case A with  $V_S$  profiles inverted by 2D Global, 3D Global and 3D Array methods for the inversion sensitivity study, with the filtering criteria indicated in each column

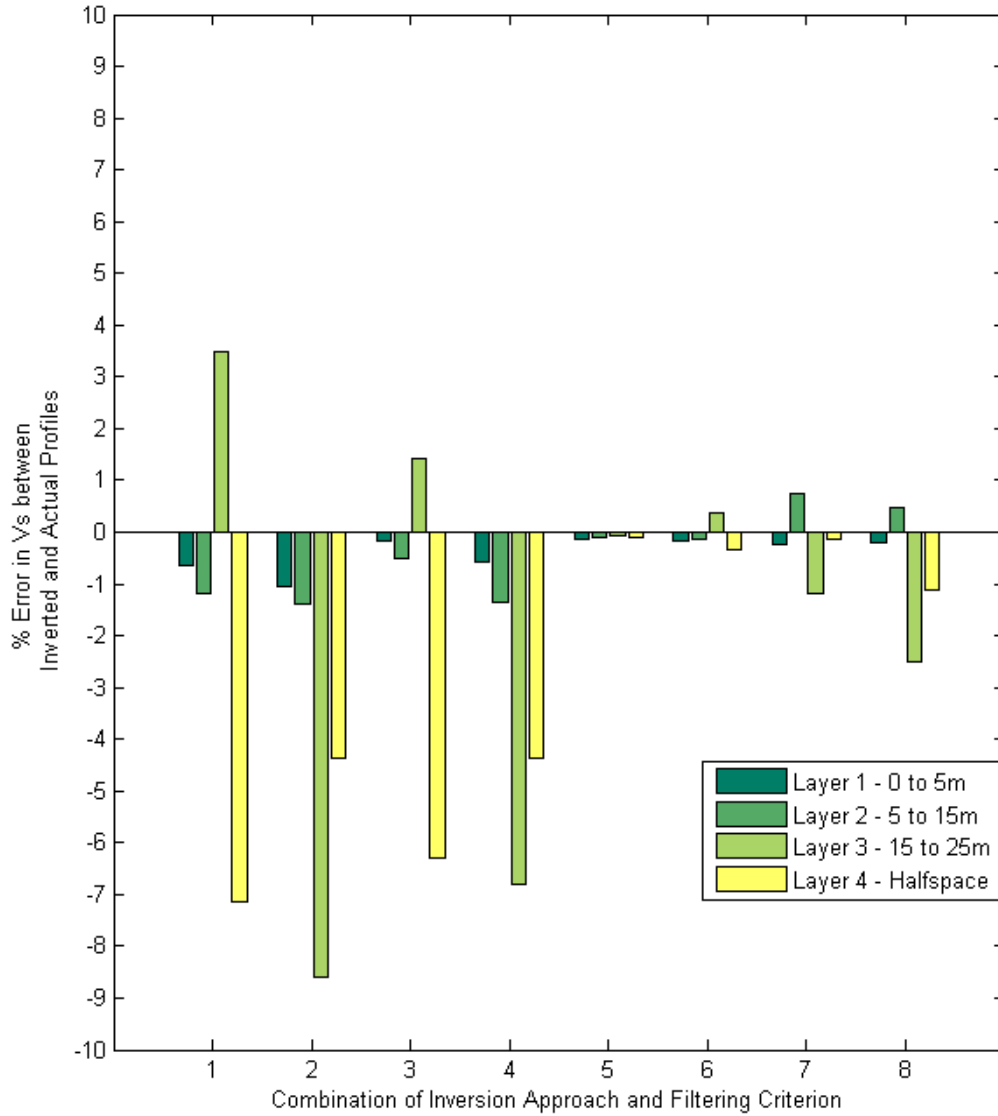


**Figure 4.25** Percent error between inverted and "true"  $V_s$  profiles at each layer for the uniform (Case A) profile

#### 4.3.1.2 Case B – Power Function $V_s$ Profile ( $\nu = 0.30$ )

Inversion sensitivity results for the case of a power function  $V_s$  profile (Case B) are shown in Figure 4.26. The Case B profile was used to generate simulated data in FitSASW, which were processed according to the four filtering criteria indicated (360°, 180°, 90°, and 45°) and inverted by three approaches (2D Global, 3D Global, and 3D Array).  $V_s$  profiles derived from inversion analysis are shown with a solid line, while the “true” Case B profile is shown with a dashed line. Only the value of  $V_s$  in each layer was inverted in this study – the profile layering and all other parameters, including Poisson’s ratio, were held constant.

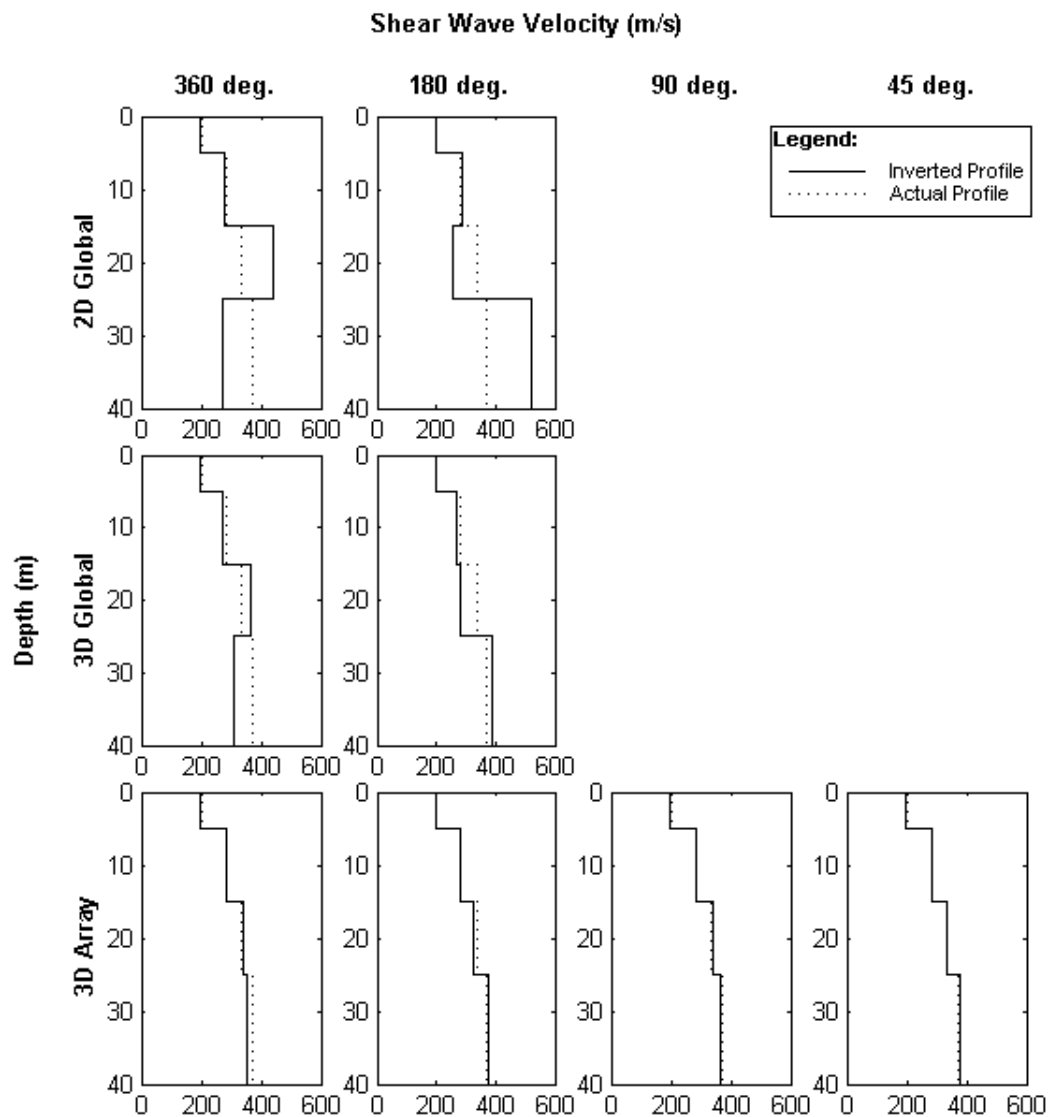


**Figure 4.26** Comparison of the “true”  $V_s$  profile for Case B with  $V_s$  profiles inverted by 2D Global, 3D Global and 3D Array methods for the inversion sensitivity study, with the filtering criteria indicated in each column

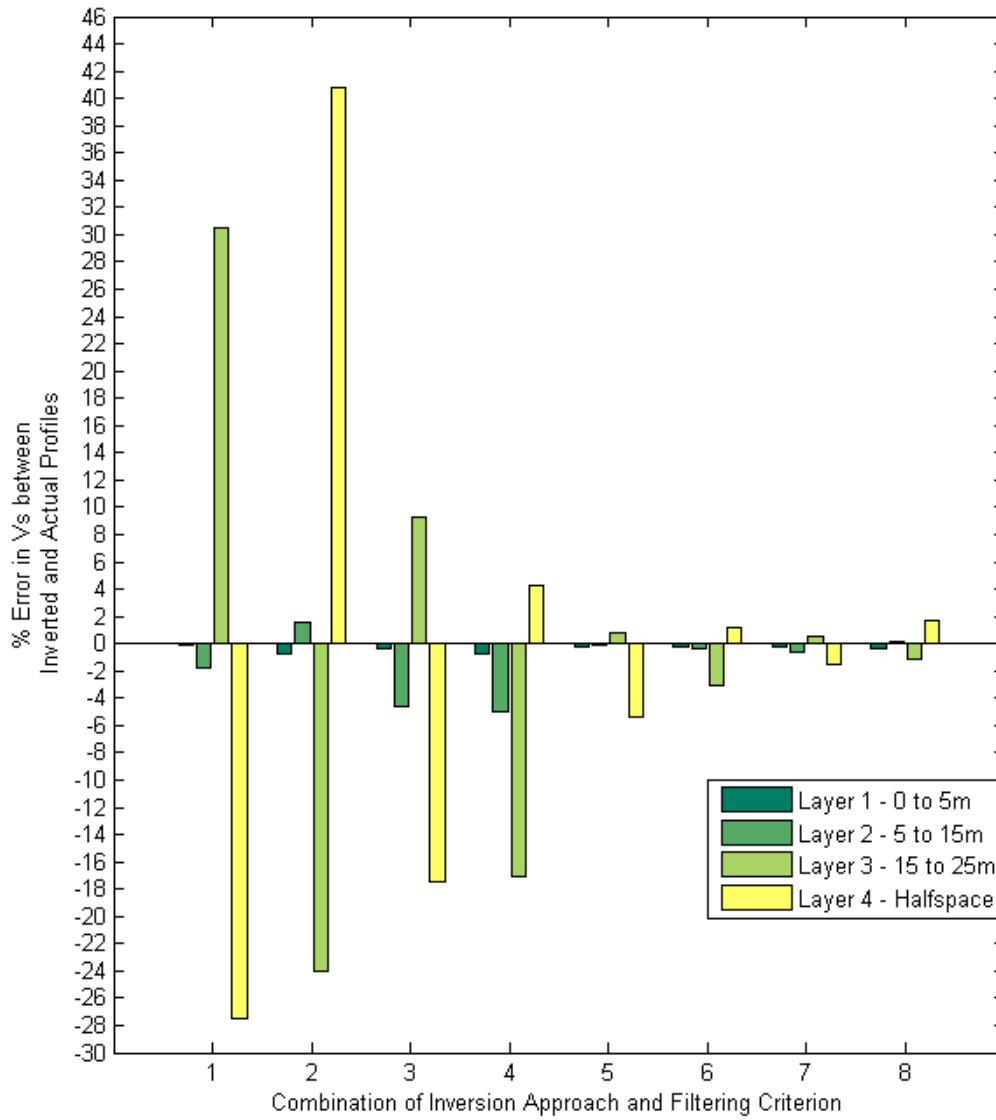


**Figure 4.27** Percent error between inverted and "true"  $V_s$  profiles at each layer for the power function (Case B) profile

#### 4.3.1.3 Case C – Linear $V_s$ Profile ( $\nu = 0.30$ )

Inversion sensitivity results for the case of a linear  $V_s$  profile (Case C) are shown in Figure 4.28. The Case C profile was used to generate simulated data in FitSASW, which were processed according to the four filtering criteria indicated (360°, 180°, 90°, and 45°) and inverted by three approaches (2D Global, 3D Global, and 3D Array).  $V_s$  profiles derived from inversion analysis are shown with a solid line, while the “true” Case C profile is shown with a dashed line. Only the value of  $V_s$  in each layer was inverted in this study – the profile layering and all other parameters, including Poisson’s ratio, were held constant.

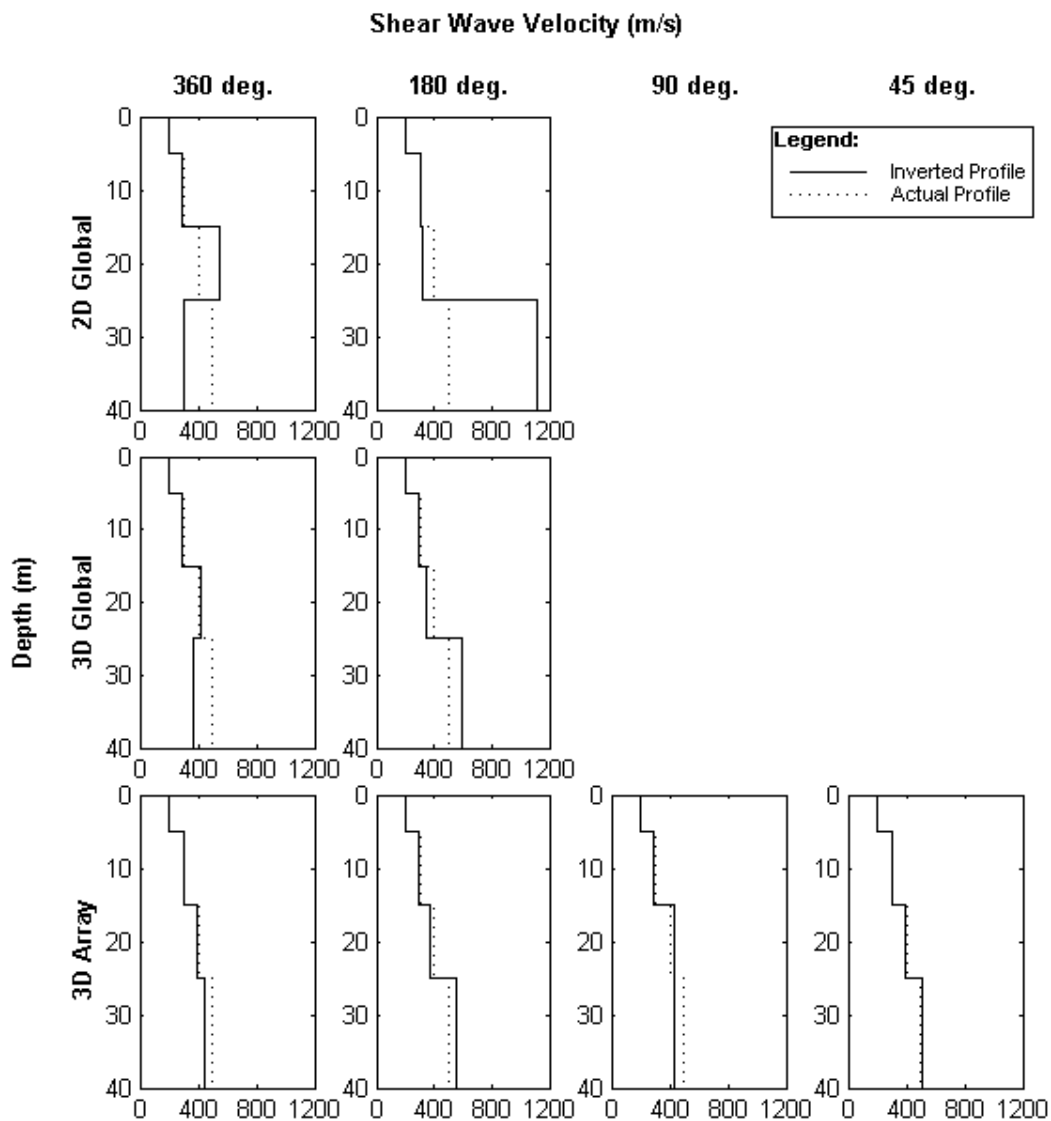


**Figure 4.28** Comparison of the “true”  $V_s$  profile for Case C with  $V_s$  profiles inverted by 2D Global, 3D Global and 3D Array methods for the inversion sensitivity study, with the filtering criteria indicated in each column

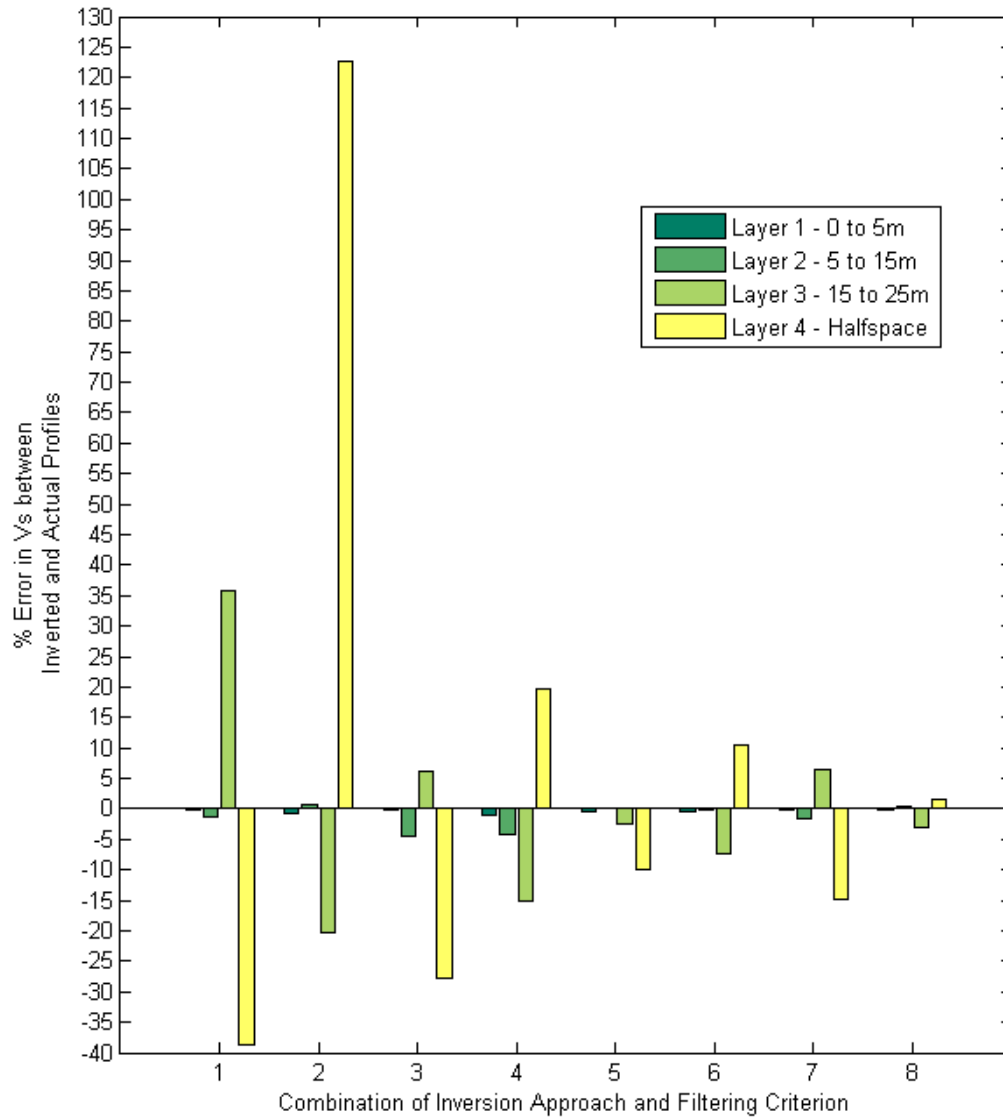


**Figure 4.29** Percent error between inverted and "true"  $V_s$  profiles at each layer for linear  $V_s$  increase (Case C)

#### 4.3.1.4 Case D – Steep Power Function $V_S$ Profile ( $\nu = 0.30$ )

Inversion sensitivity results for the case of a steep power function  $V_S$  profile (Case D) are shown in Figure 4.30. The Case D profile was used to generate simulated data in FitSASW, which were processed according to the four filtering criteria indicated (360°, 180°, 90°, and 45°) and inverted by three approaches (2D Global, 3D Global, and 3D Array).  $V_S$  profiles derived from inversion analysis are shown with a solid line, while the “true” Case D profile is shown with a dashed line. Only the value of  $V_S$  in each layer was inverted in this study – the profile layering and all other parameters, including Poisson’s ratio, were held constant.

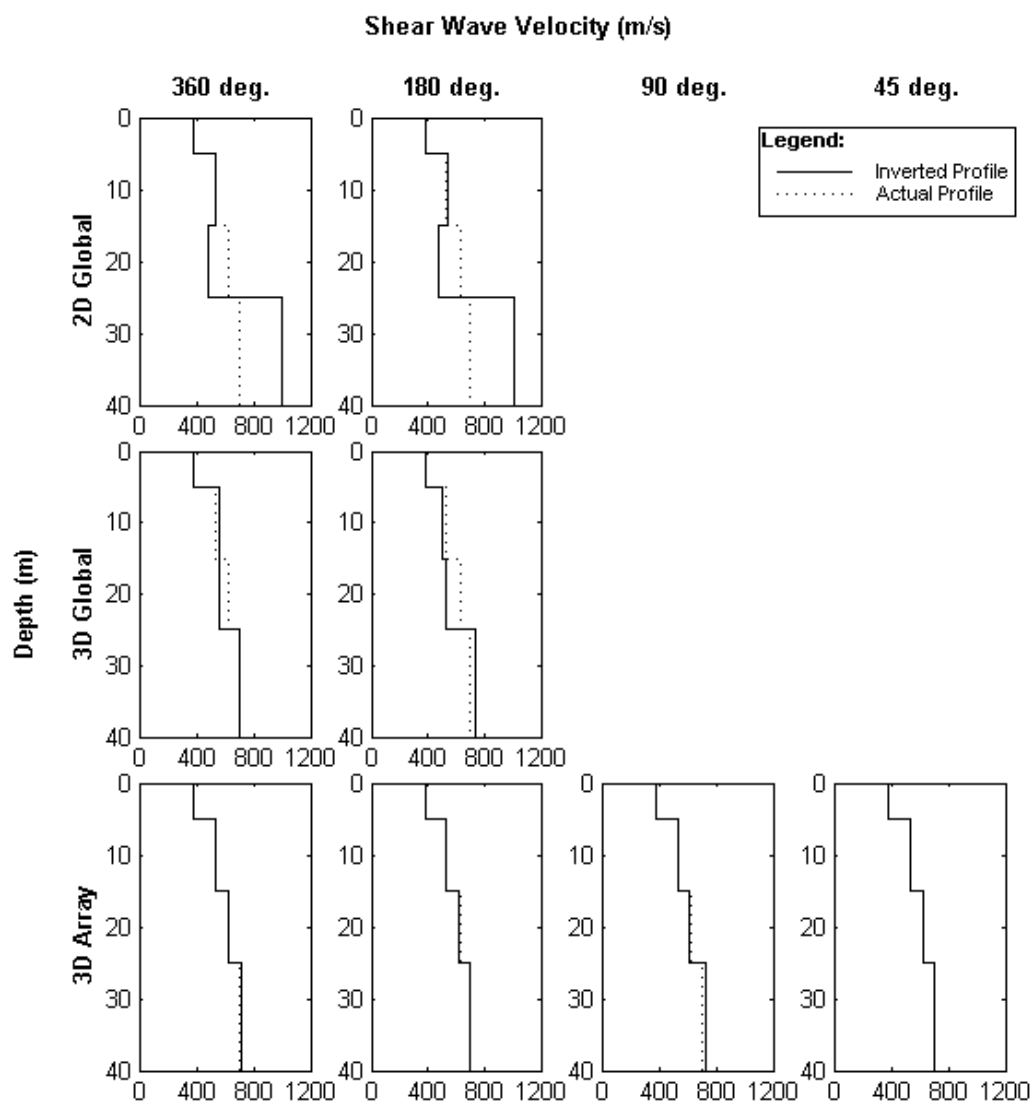


**Figure 4.30** Comparison of the “true”  $V_S$  profile for Case D with  $V_S$  profiles inverted by 2D Global, 3D Global and 3D Array methods for the inversion sensitivity study, with the filtering criteria indicated in each column

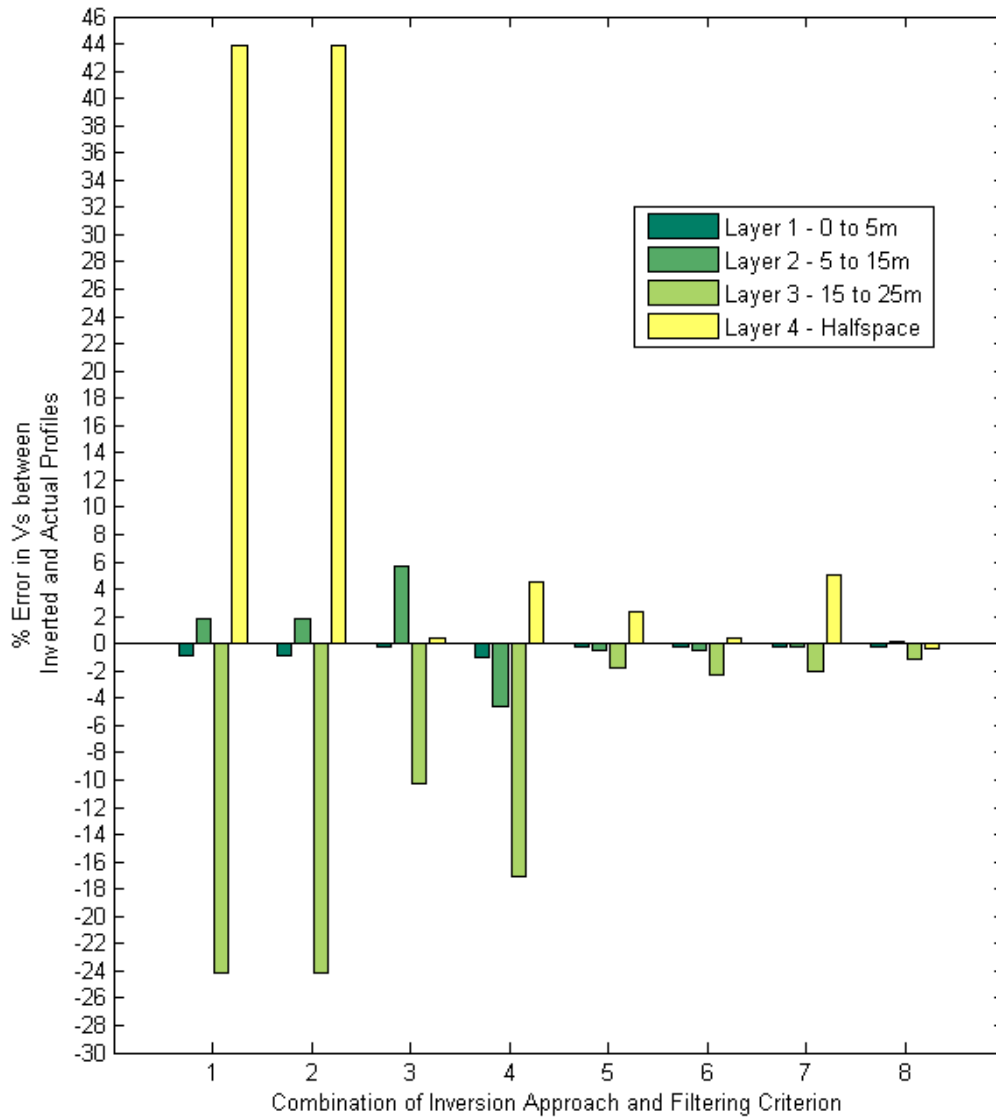


**Figure 4.31** Percent error between inverted and "true"  $V_s$  profiles for the steep power function (Case D) profile

#### 4.3.1.5 Case B\* – “Saturated” Power Function $V_S$ Profile ( $\nu = 0.45$ )

Inversion sensitivity results for the case of a “saturated” power function  $V_S$  profile (Case B\*) are shown in Figure 4.32. The Case B\* profile was used to generate simulated data in FitSASW, which were processed according to the four filtering criteria indicated (360°, 180°, 90°, and 45°) and inverted by three approaches (2D Global, 3D Global, and 3D Array).  $V_S$  profiles derived from inversion analysis are shown with a solid line, while the “true” Case B\* profile is shown with a dashed line. Only the value of  $V_S$  in each layer was inverted in this study – the profile layering and all other parameters, including Poisson’s ratio, were held constant.

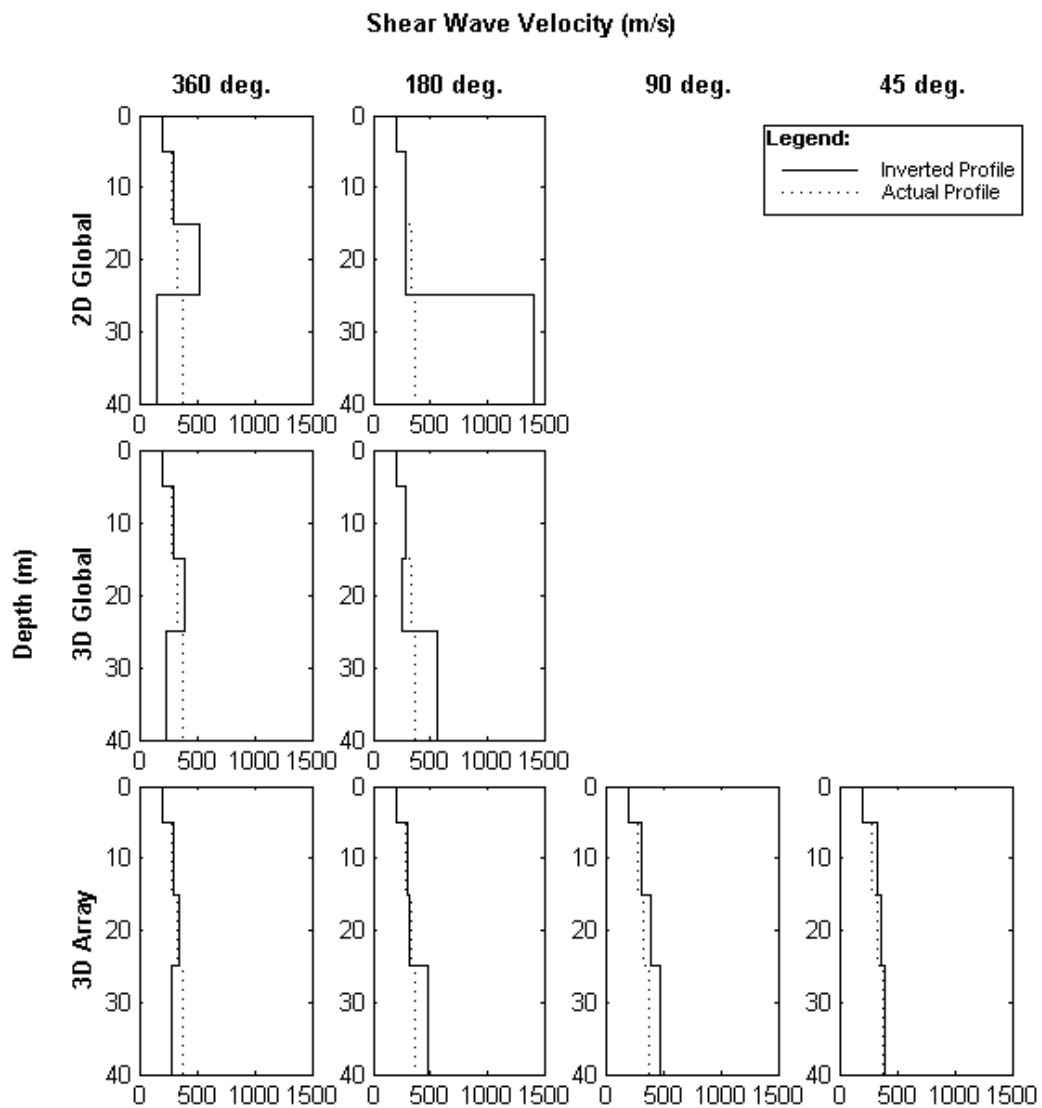


**Figure 4.32** Comparison of the “true”  $V_S$  profile for Case B\* with  $V_S$  profiles inverted by 2D Global, 3D Global and 3D Array methods for the inversion sensitivity study, with the filtering criteria indicated in each column

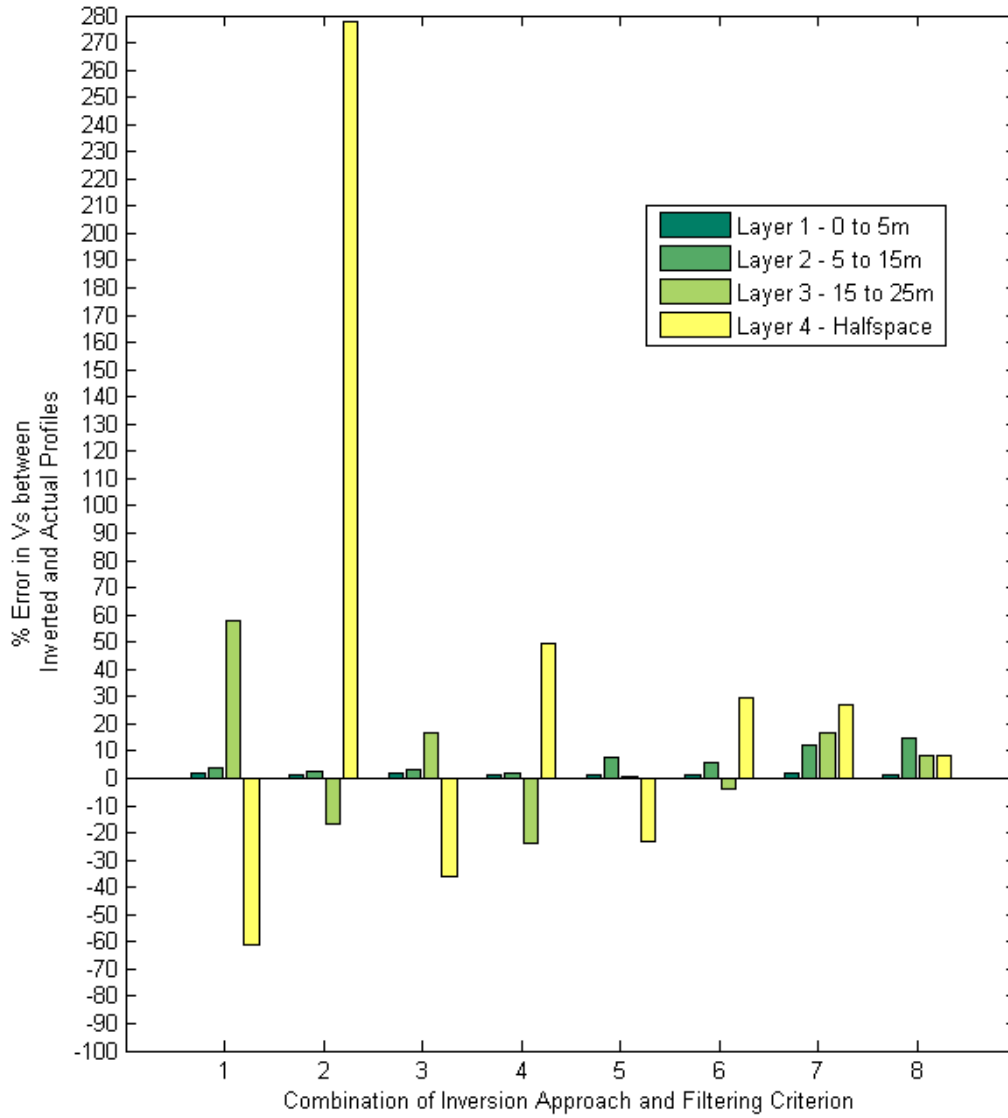


**Figure 4.33** Percent error between inverted and "true"  $V_s$  profiles in each layer for the "saturated" (Case B\*) profile

### 4.3.2 Discussion of SASW Profile Recovery Study

The profile recovery study results presented in Section 0 demonstrate the use of three different inversion approaches to recover the “true”  $V_S$  profile from data processed by various methods. In this study, the “true” profile was the known profile used to generate simulated experimental data in FitSASW. Only the value of the shear wave velocity was changed in the inversion analysis: the layering system and all other parameters, including Poisson’s ratio, were identical to those used to generate the simulated data and were held constant throughout the analysis. The goal of this study was to identify the best combination of data processing and inversion approaches in terms of the efficiency and effectiveness of the approach. An ideal combination would produce the closest fit between inverted and “true” profiles for all profile conditions.

The numbering scheme outlined in Table 4.1, which corresponds somewhat to the historical development of the SASW method, is referenced throughout this discussion. Early implementations of SASW were performed according to combinations 1 and 2, where data were processed by restrictive filtering criteria for use with a far-field, 2D plane wave inversion model. Current practice in SASW is largely encompassed by combinations 3 and 4, where data are processed with the same restrictive criteria, but inverted with a 3D model that accounts for all wave contributions, including near-field effects. Joh (1996) noted the issues with combinations 1 through 4 and proceeded to develop the 3D array approach, which he applied to data processed by the same far-field filtering criteria (i.e. combinations 5 and 6). This thesis aims to consider the feasibility of combinations 7 and 8, extending the work of Joh (1996) with new filtering criteria (i.e. 90° and 45° criteria) that allow for greater use of the near-field and a more efficient application of the SASW approach.

Several observations arise from a comparison of the inverted and “true” profiles shown in Section 0. For Case A, the uniform profile, all combinations of inversion analyses and filtering criteria seem to yield inverted profiles that are close approximations of the “true” profile, with the 3D array inversion producing the best results. For Cases B, C, D, and B\*, the results show three major trends: (1) the quality of the inverted profile is strongly dependent on the inversion method used, (2) for a given inversion method, the quality of the inverted profile does not seem to be greatly affected by the filtering criterion used to process the data, and (3) the deepest layers in the model (i.e. halfspace) appear to be the most critical to the quality of the inverted profile. Some notable instances of these trends are described below.

Of the three inversion methods used, the 2D global inversion (i.e. Combinations 1 and 2) yielded the worst quality fit between inverted and “true” profiles. In some ways, however, this was to be expected, as the (simulated) experimental data includes near-field effects while the 2D global inversion does not. These results indicate that the 360° and 180° filtering criteria do not completely remove the near-field effects, resulting in incompatibility between the experimental data and theoretical solution. The 3D global results (i.e. Combinations 3 and 4) had less overall misfit between the profiles than the 2D results, likely due to the fact that the 3D model accounts for the near-field effects inherent in the experimental data, although it does not account for the actual receiver location. For both approaches, the largest error magnitudes occurred with the “saturated” profile condition (Case B\*), where Poisson’s ratio was known to be 0.45. The quality of inverted profiles produced by both 2D and 3D global methods is very good in shallow layers, but decreases significantly for the deeper layers. From the profile error plots, it is evident that the 2D solution grossly over-predicts the halfspace velocity in most cases and under-predicts (to a lesser degree) the velocity of the layer immediately above the halfspace. The 3D global inversion encountered the same difficulties as the 2D global inversion, but with significantly less error in most cases. This is likely due in part to the mechanics of the global average, as the moving average mechanism (see Section 3.3.2) is considerably affected by the near-field at low frequencies/long wavelengths for the longest receiver spacing, as shown in Figure 4.34. It is evident that near-field effects in the experimental data for the longest receiver spacing can substantially “derail” the averaging scheme for points at the longest wavelengths.

Of the three inversion methods used, the 3D array inversion (i.e. Combinations 5, 6, 7, and 8) yielded the best quality fit between inverted and “true” profiles. Overall, the 3D array inversion produced a close fit to the “true” profile in most cases, regardless of the filtering criteria used. Similar to the other two approaches, the 3D array inversion had some difficulty inverting data produced from the “saturated” profile (Case B\*). Even so, it provided a significantly better fit than any inversion approach based on a global average. Most importantly, it is evident that the 3D array inversion provided a consistent quality result for all four filtering criteria (360°, 180°, 90°, and 45°). The recovery error for the 3D array results was typically less than 5% for each layer and, in some cases, even lower when more of the near-field was included (i.e. 45° criterion). The apparent success of the 3D array inversion in profile recovery is likely due to the fact that this approach simulates the data collection procedure used in actual surface wave measurements, including both near-field and far-field contributions..

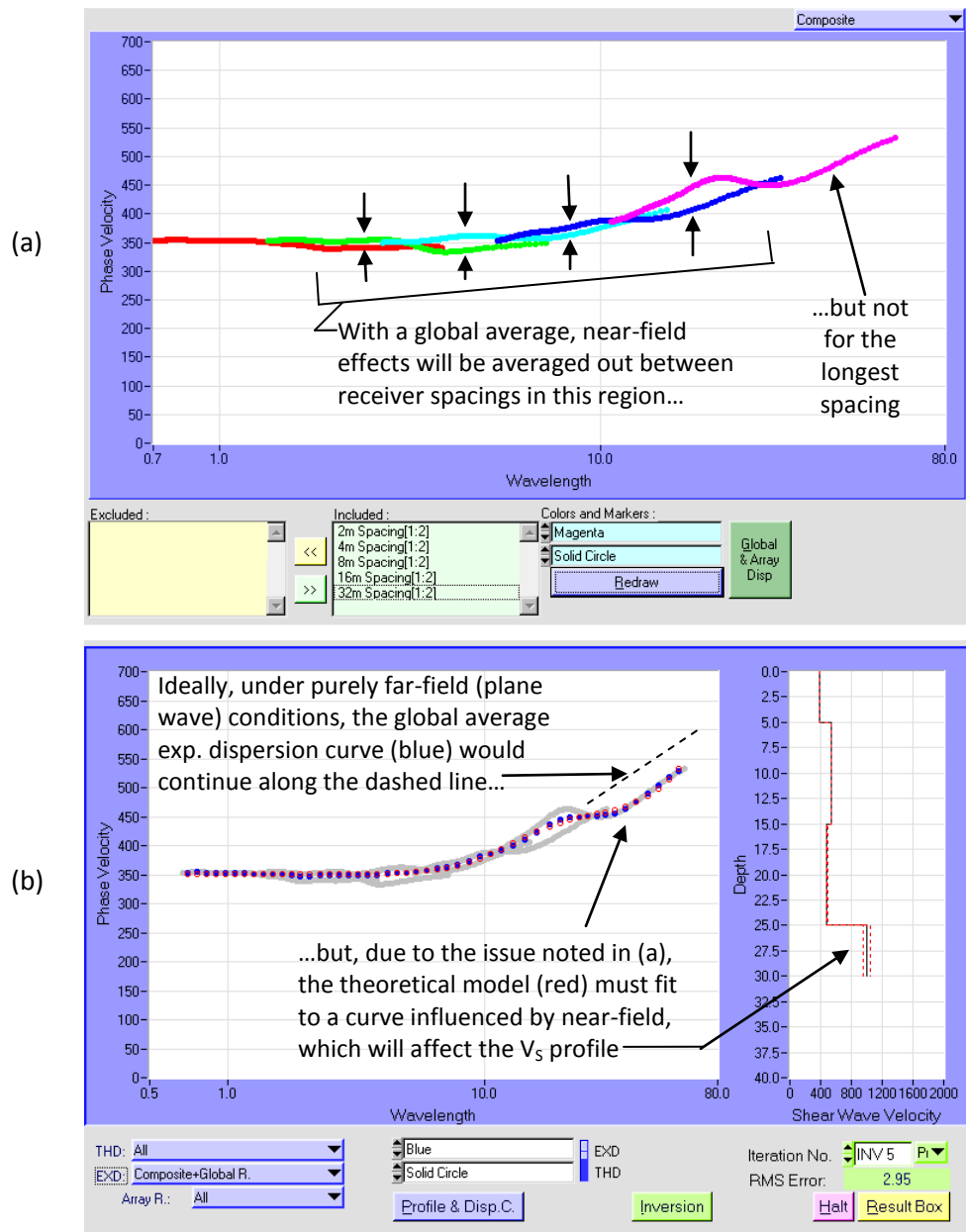


**Figure 4.34** WinSASW screenshots from one of the analyses in the profile recovery study (Case D, 180° near-field criterion, 2D global inversion), illustrating the likely causes of significant misfit for the 2D and 3D global inversions in both the (a) data processing and (b) inversion steps.

Three key conclusions were drawn from the profile recovery study. First, inversion methods based on a global average are negatively affected by near-field effects in experimental data, with a significant decrease in  $V_s$  profile quality with depth. The misfit produced by the 3D global approach is less severe than that of the 2D global approach, but neither approach can effectively estimate the  $V_s$  profile from experimental data collected in the near-field. Second, the 3D array inversion performs admirably in recovering the original profile from data with near-field effects. This suggests that the effectiveness of surface wave measurements can be improved by fully implementing the 3D array approach (instead of the common 3D global approach used with SASW) in engineering practice. Third, while the quality of the profile recovery depended heavily on the inversion approach used, changing the filtering criteria from  $180^\circ$  to  $360^\circ$  had minimal effect on the quality of the results for the global inversion approaches. The 3D array inversion also showed little impact on account of the filtering criteria used and, in fact, showed slightly better results when more of the near-field (i.e.  $90^\circ$ , and especially  $45^\circ$ ) was used as compared to the more restrictive criteria (i.e.  $360^\circ$  and  $180^\circ$ ).

Therefore, it has been demonstrated in this study using simulated data that the efficiency of surface wave measurements can be vastly improved by using shorter receiver spacings (e.g. 16m total array length, instead of 128m – see Figure 4.23) to collect, process, and invert data in the near-field, with no significant change in effectiveness. Shorter array lengths have two benefits. First, the profile obtained is more localized and does not average the profile velocities over long receiver spread length, resulting in better horizontal resolution from multiple measurements. Secondly, energy requirements for the source are reduced, since signal attenuation will be lower over the shorter array distance.

### 4.3.3 Results of Poisson's Ratio Study with Simulated SASW Data

This section presents results from a study performed to determine if additional profile information could be determined from surface wave data that included more near-field contributions. Specifically, this study investigated if it is possible to infer Poisson's ratio of the profile when near-field data are included. As noted in Section 2.5.1, it is accepted in current practice (far-field data collection and theoretical model) that surface waves are not sensitive to changes in Poisson's ratio. Therefore, values of Poisson's ratio must be either assumed or known *a priori* for the analysis. From the results of the preliminary study, it was hypothesized that the quality of fit between experimental and theoretical dispersion curves in the near-field is sensitive to the value of Poisson's ratio. It was considered that an incorrect assumption of Poisson's ratio would yield an inferior fit between dispersion curves as compared to the case where the correct value of Poisson's ratio is used. Inversion analyses were performed with a range of assumed Poisson's ratio values to investigate this hypothesis. Results of this study include three  $V_S$  profile plot grids and a plot of the misfit between theoretical and experimental dispersion curves, for each of the five profiles used to simulate the experimental data. For this study, the rows of each grid represent the different inversion approaches, while the columns represent the assumed values of Poisson's ratio. The root-mean-squared (RMS) error, a measure of the misfit between theoretical and experimental dispersion curves, is plotted versus the assumed value of Poisson's ratio in this section. Each point on the plot corresponds to a complete inversion analysis with an assumed value of Poisson's ratio. A sensitivity to Poisson's ratio would be indicated by a trend of decreased RMS error when the correct Poisson's ratio was used. A practical illustration of the meaning of RMS error in this study is presented in Figure 4.35, where a correct assumption of Poisson's ratio produces a small RMS error, and Figure 4.36, where an incorrect assumption produces a large RMS error. The results of this study are discussed in Section 4.3.4.

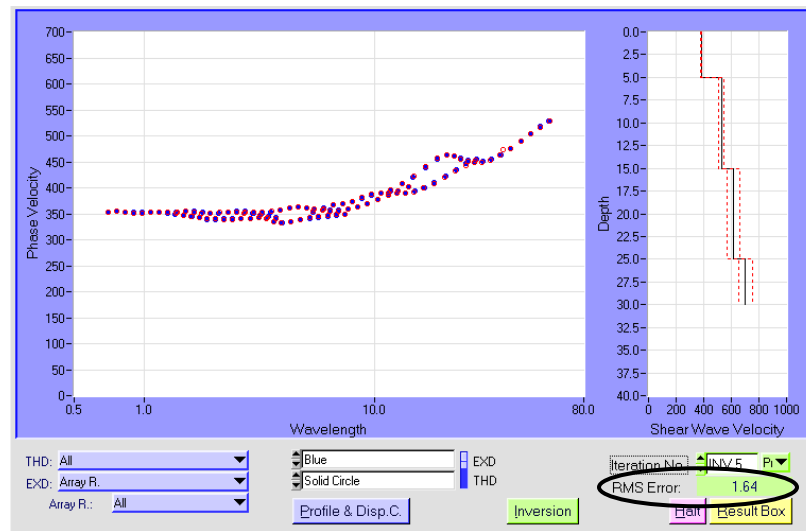


**Figure 4.35** WinSASW screenshot from one of the analyses in the Poisson's ratio study (Case D, 180° near-field criterion, 3D array inversion), illustrating an excellent fit between theoretical (red) and experimental (blue) dispersion curves after an inversion analysis (and the correspondingly low RMS error), where the assumed value of Poisson's ratio exactly matched the "true" value of 0.30

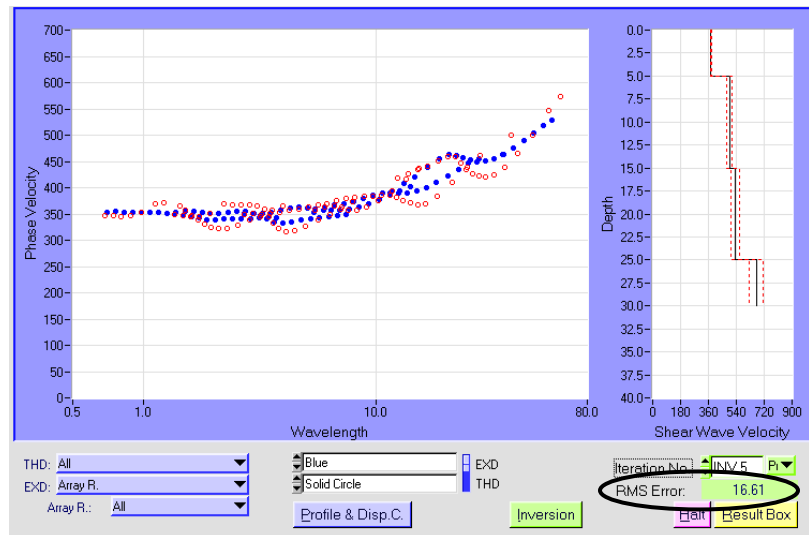


**Figure 4.36** WinSASW screenshot from one of the analyses in the Poisson's ratio study (Case D, 180° near-field criterion, 3D array inversion), illustrating a poor fit between theoretical (red) and experimental (blue) dispersion curves after an inversion analysis (and the correspondingly high RMS error), where the assumed Poisson's ratio value of 0.45 did *not* match the true value of 0.30

#### 4.3.3.1 Case A – Uniform $V_S$ Profile ( $\nu = 0.30$ )

Results of the Poisson’s ratio study for the case of a uniform  $V_S$  profile (Case A) are presented in four different figures as described herein – three sets of  $V_S$  profiles and a plot of RMS error versus Poisson’s ratio.  $V_S$  profiles derived from all inversion analyses are compared with the “true” Case A profile over seven different values of Poisson’s ratio. Specifically,  $V_S$  profiles derived from the 360° and 180° filtering criteria in Figure 4.37 and Figure 4.38, respectively, while those derived from the 90° and 45° filtering criteria are shown together in Figure 4.39.  $V_S$  profiles derived from inversion analysis are shown with a solid line, while the “true” Case A profile is shown with a dashed line. The root-mean-squared (RMS) error in fit between theoretical and experimental dispersion curves is plotted versus the value of Poisson’s ratio in Figure 4.40: a separate curve is plotted for each inversion approach (2D Global, 3D Global, and 3D Array) and each subplot corresponds to one of the four filtering criteria (360°, 180°, 90°, and 45°). Each curve in Figure 4.40 corresponds to an individual row of  $V_S$  profiles in Figure 4.37, Figure 4.38, or Figure 4.39.

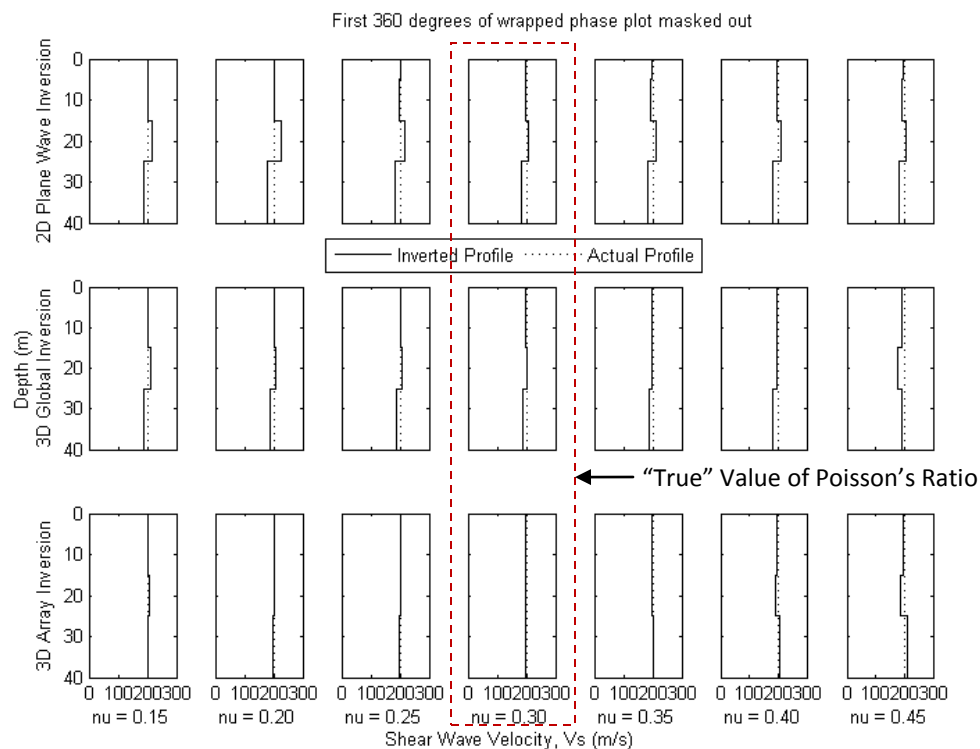


**Figure 4.37** Comparison of the “true”  $V_S$  profile for Case A with  $V_S$  profiles inverted by 2D Global, 3D Global and 3D Array methods – these data were processed using the 360° filtering criteria

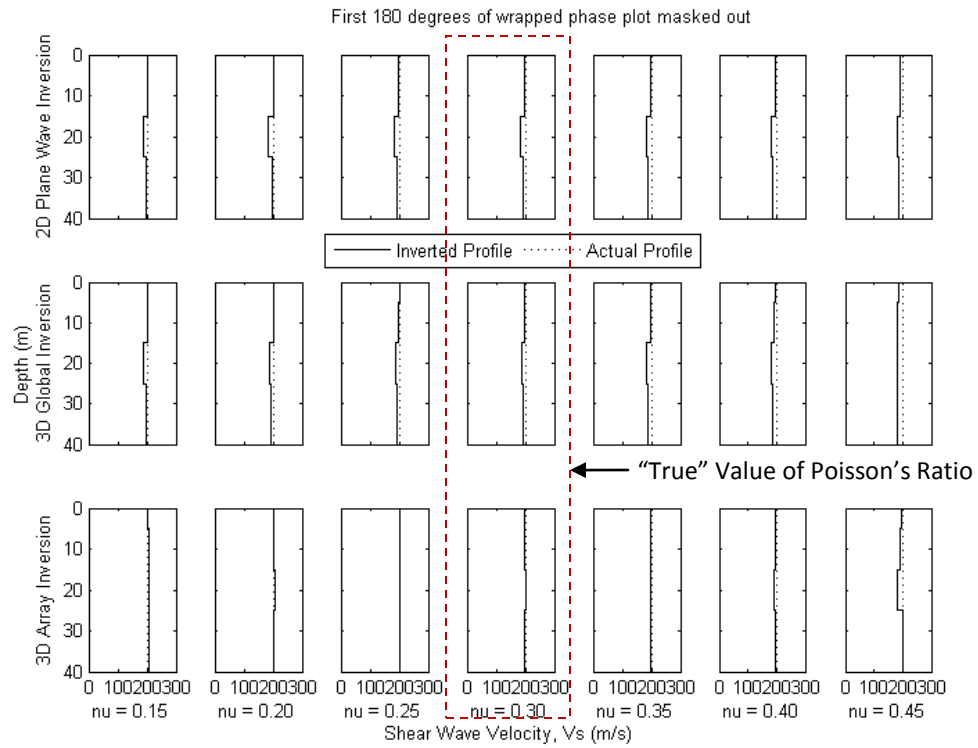


**Figure 4.38** Comparison of the “true”  $V_s$  profile for Case A with  $V_s$  profiles inverted by 2D Global, 3D Global and 3D Array methods – these data were processed using the 180° filtering criteria

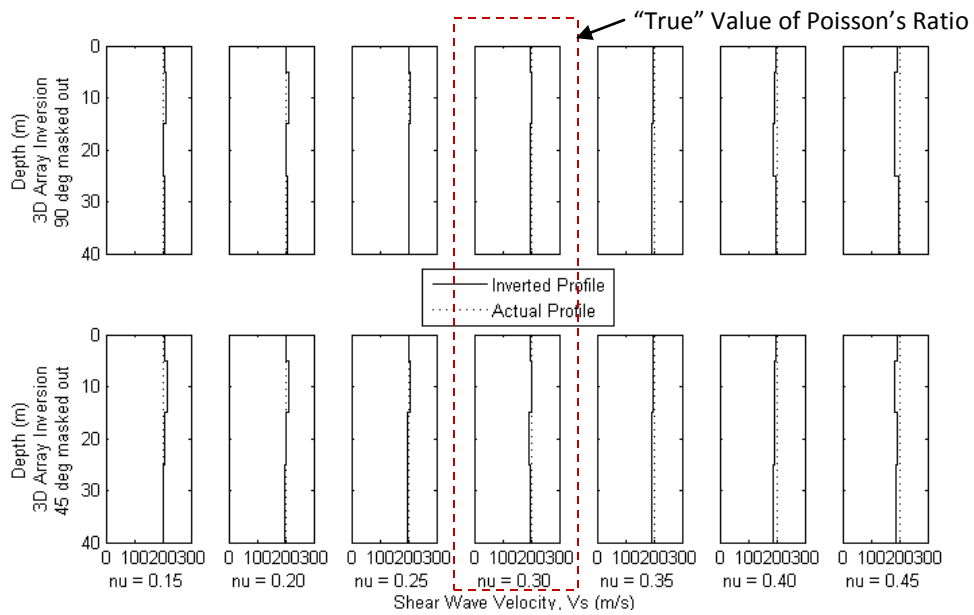


**Figure 4.39** Comparison of the “true”  $V_s$  profile for Case A with  $V_s$  profiles inverted by 3D Array methods – these data were processed by alternative filtering criteria including more of the near-field (90° top row and 45° bottom row)

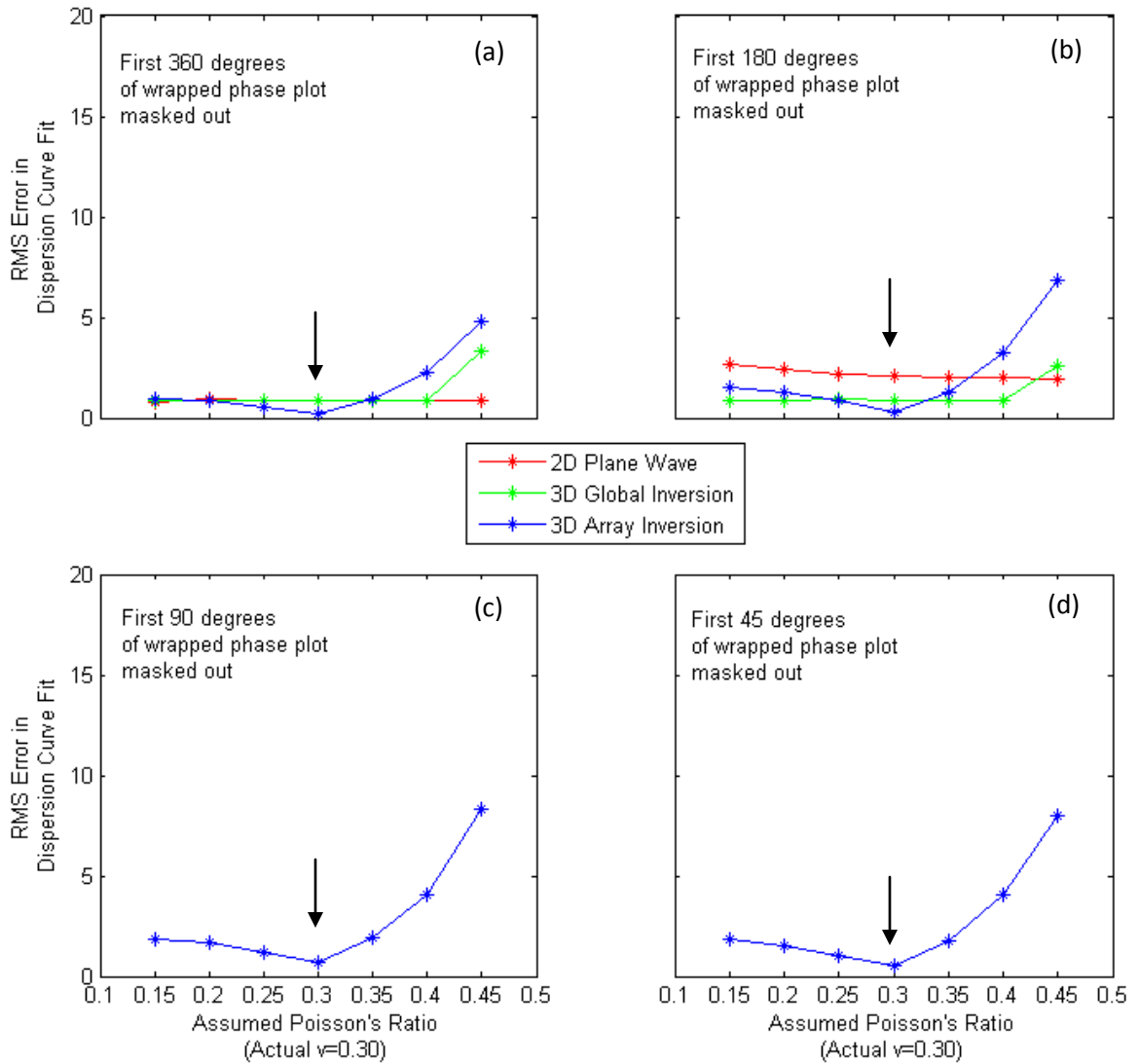


**Figure 4.40** RMS error in fit between theoretical and experimental dispersion curves for Case A, covering the range of inversion methods, filtering criteria, and Poisson’s ratio values encompassed by Figure 4.37, Figure 4.38, and Figure 4.39 – arrows indicate abscissa location of the “true” Poisson’s ratio value

**4.3.3.2 Case B – Power Function  $V_s$  Profile ( $\nu = 0.30$ )**

Results of the Poisson’s ratio study for the case of a power function  $V_s$  profile (Case B) are presented in four different figures as described herein – three sets of  $V_s$  profiles and a plot of RMS error versus Poisson’s ratio.  $V_s$  profiles derived from all inversion analyses are compared with the “true” Case B profile over seven different values of Poisson’s ratio. Specifically,  $V_s$  profiles derived from the 360° and 180° filtering criteria in Figure 4.41 and Figure 4.42, respectively, while those derived from the 90° and 45° filtering criteria are shown together in Figure 4.43.  $V_s$  profiles derived from inversion analysis are shown with a solid line, while the “true” Case B profile is shown with a dashed line. The root-mean-squared (RMS) error in fit between theoretical and experimental dispersion curves is plotted versus the value of Poisson’s ratio in Figure 4.44: a separate curve is plotted for each inversion approach (2D Global, 3D Global, and 3D Array) and each subplot corresponds to one of the four filtering criteria (360°, 180°, 90°, and 45°). Each curve in Figure 4.44 corresponds to an individual row of  $V_s$  profiles in Figure 4.41, Figure 4.42, and Figure 4.43.

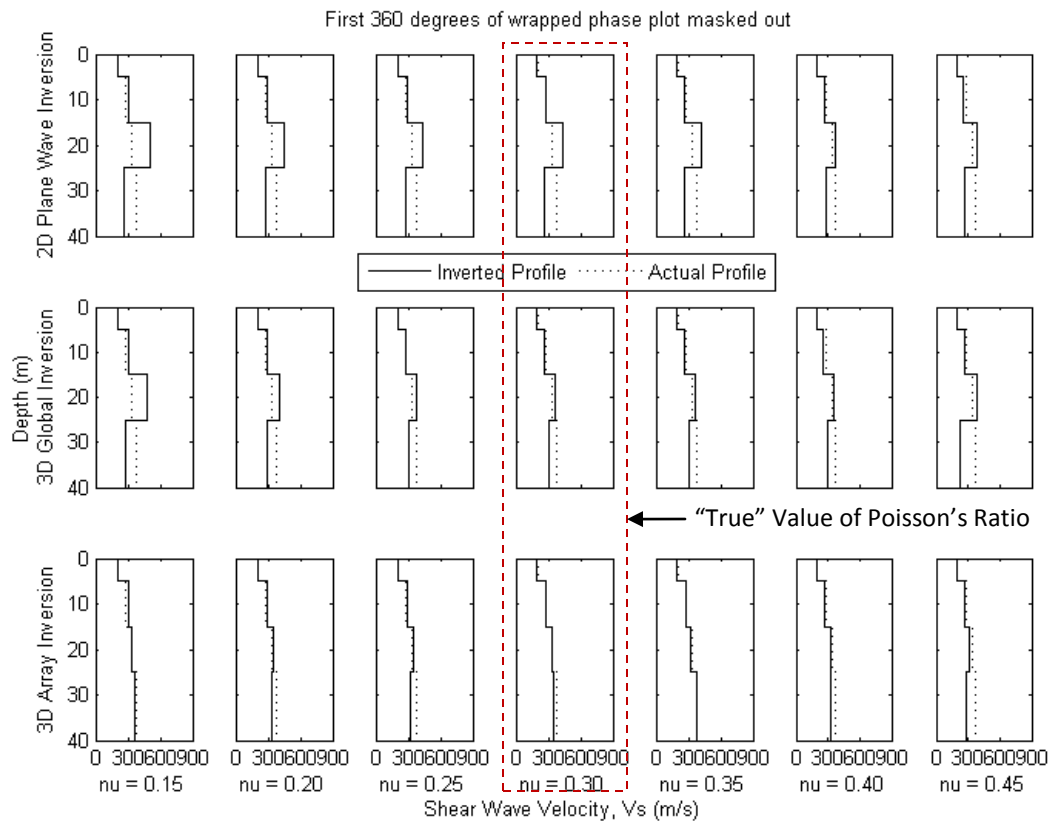


**Figure 4.41** Comparison of the “true”  $V_s$  profile for Case B with  $V_s$  profiles inverted by 2D Global, 3D Global and 3D Array methods – these data were processed by the 360° filtering criteria

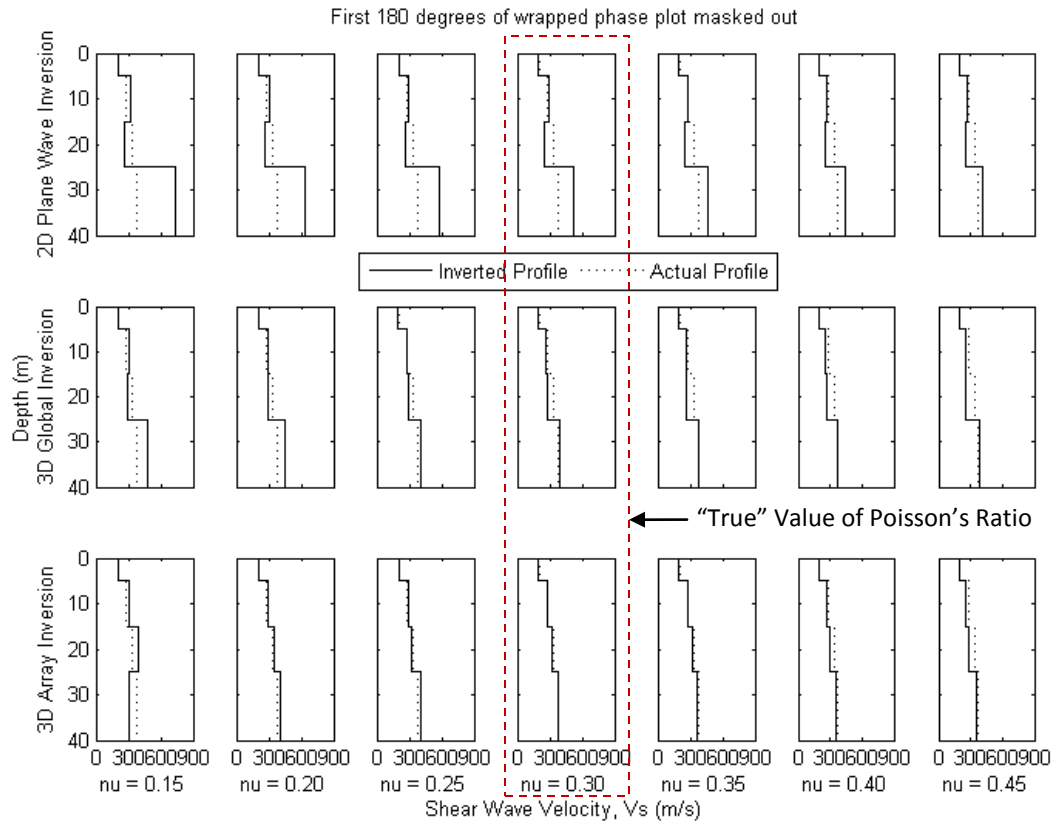


**Figure 4.42** Comparison of the “true”  $V_s$  profile for Case B with  $V_s$  profiles inverted by 2D Global, 3D Global and 3D Array methods – these data were processed by the  $180^\circ$  filtering criteria

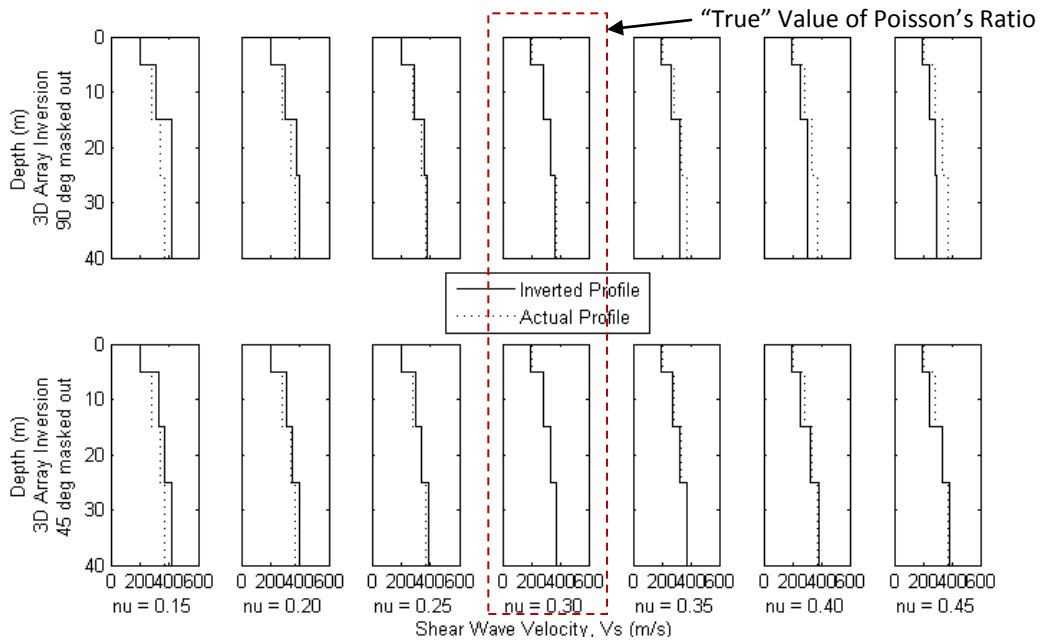


**Figure 4.43** Comparison of the “true”  $V_s$  profile for Case B with  $V_s$  profiles inverted by 2D Global, 3D Global and 3D Array methods – these data were processed by alternative filtering criteria including more near-field ( $90^\circ$  top row and  $45^\circ$  bottom row)

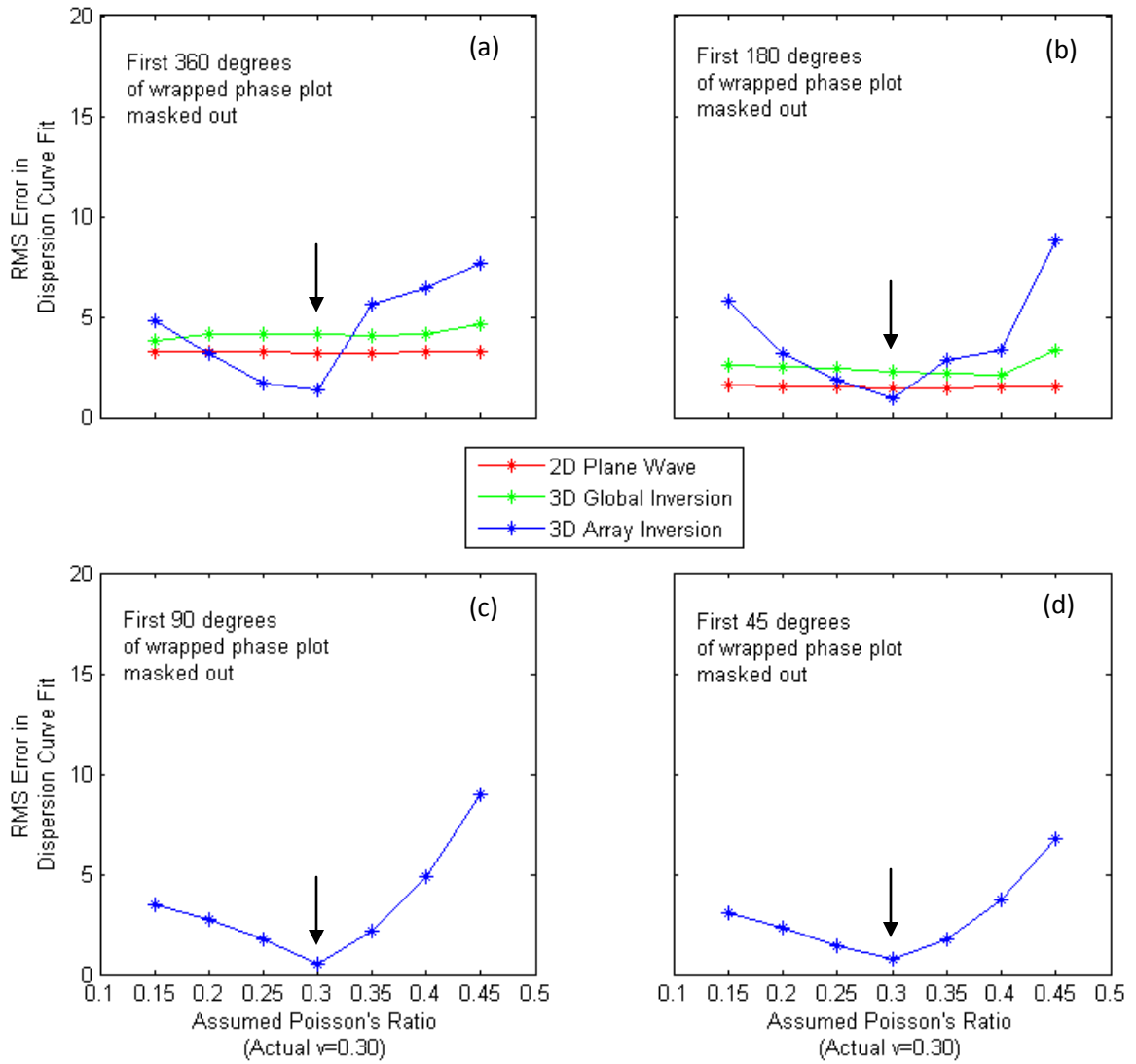


**Figure 4.44** RMS error in fit between theoretical and experimental dispersion curves for Case B, covering the range of inversion methods, filtering criteria, and Poisson's ratio values encompassed by Figure 4.41, Figure 4.42, and Figure 4.43 – arrows indicate abscissa location of the “true” Poisson's ratio value

**4.3.3.3 Case C – Linear  $V_s$  Profile ( $\nu = 0.30$ )**

Results of the Poisson’s ratio study for the case of a linear  $V_s$  profile (Case C) are presented in four different figures as described herein – three sets of  $V_s$  profiles and a plot of RMS error versus Poisson’s ratio.  $V_s$  profiles derived from all inversion analyses are compared with the “true” Case C profile over seven different values of Poisson’s ratio. Specifically,  $V_s$  profiles derived from the 360° and 180° filtering criteria in Figure 4.45 and Figure 4.46, respectively, while those derived from the 90° and 45° filtering criteria are shown together in Figure 4.47.  $V_s$  profiles derived from inversion analysis are shown with a solid line, while the “true” Case C profile is shown with a dashed line. The root-mean-squared (RMS) error in fit between theoretical and experimental dispersion curves is plotted versus the value of Poisson’s ratio in Figure 4.48: a separate curve is plotted for each inversion approach (2D Global, 3D Global, and 3D Array) and each subplot corresponds to one of the four filtering criteria (360°, 180°, 90°, and 45°). Each curve in Figure 4.48 corresponds to an individual row of  $V_s$  profiles in Figure 4.45, Figure 4.46, and Figure 4.47.

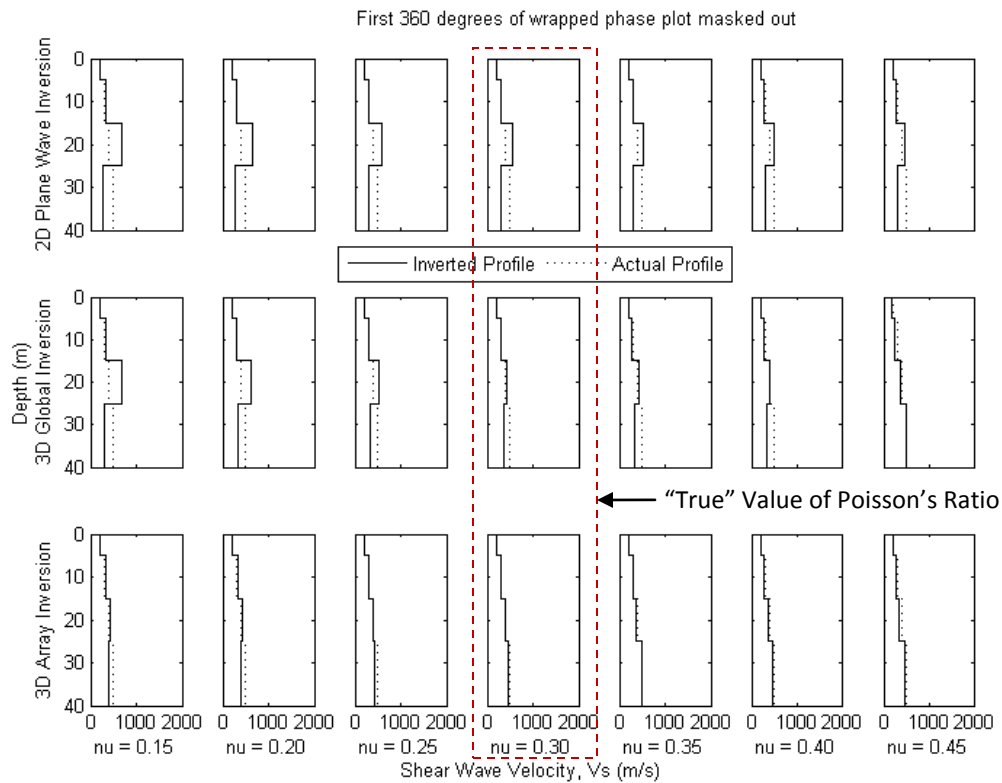


**Figure 4.45** Comparison of the “true”  $V_s$  profile for Case C with  $V_s$  profiles inverted by 2D Global, 3D Global and 3D Array methods – these data were processed by the 360° filtering criteria

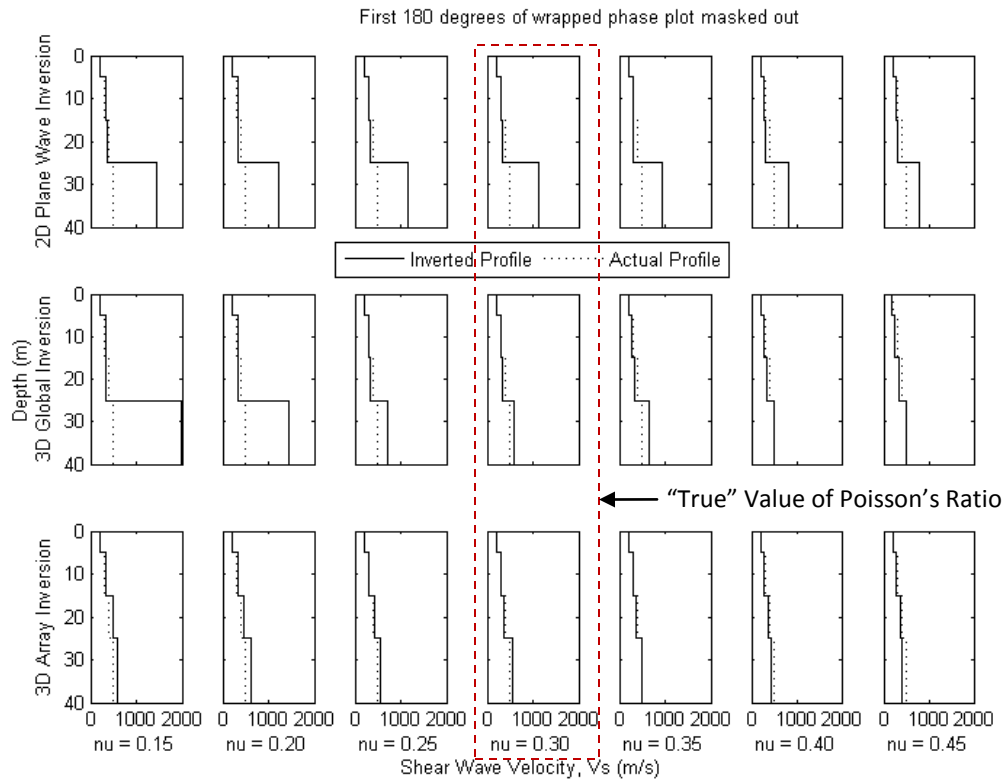


**Figure 4.46** Comparison of the “true”  $V_s$  profile for Case C with  $V_s$  profiles inverted by 2D Global, 3D Global and 3D Array methods – these data were processed by the 180° filtering criteria

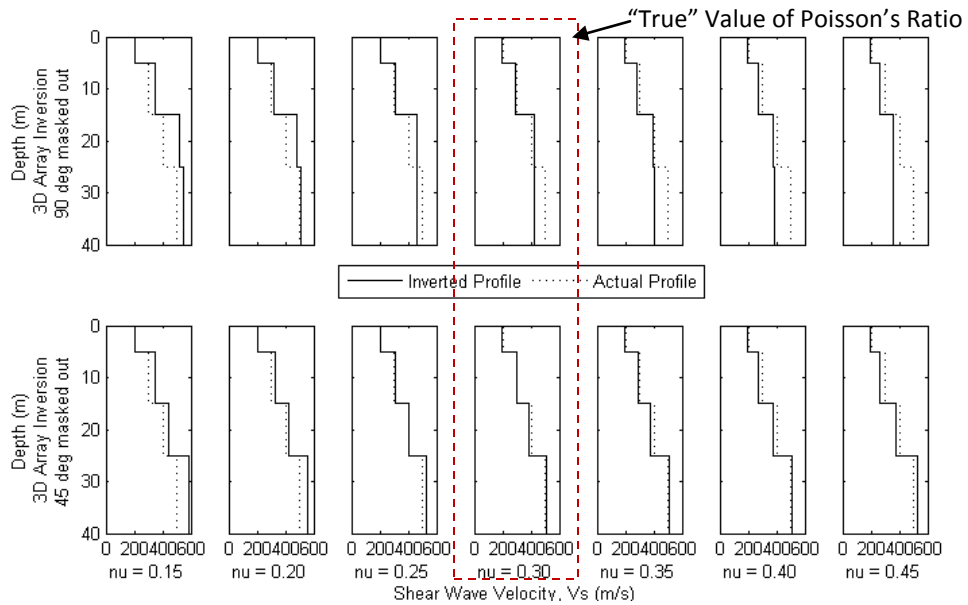


**Figure 4.47** Comparison of the “true”  $V_s$  profile for Case C with  $V_s$  profiles inverted by 2D Global, 3D Global and 3D Array methods – these data were processed by alternative filtering criteria including more near-field (90° top row and 45° bottom row)

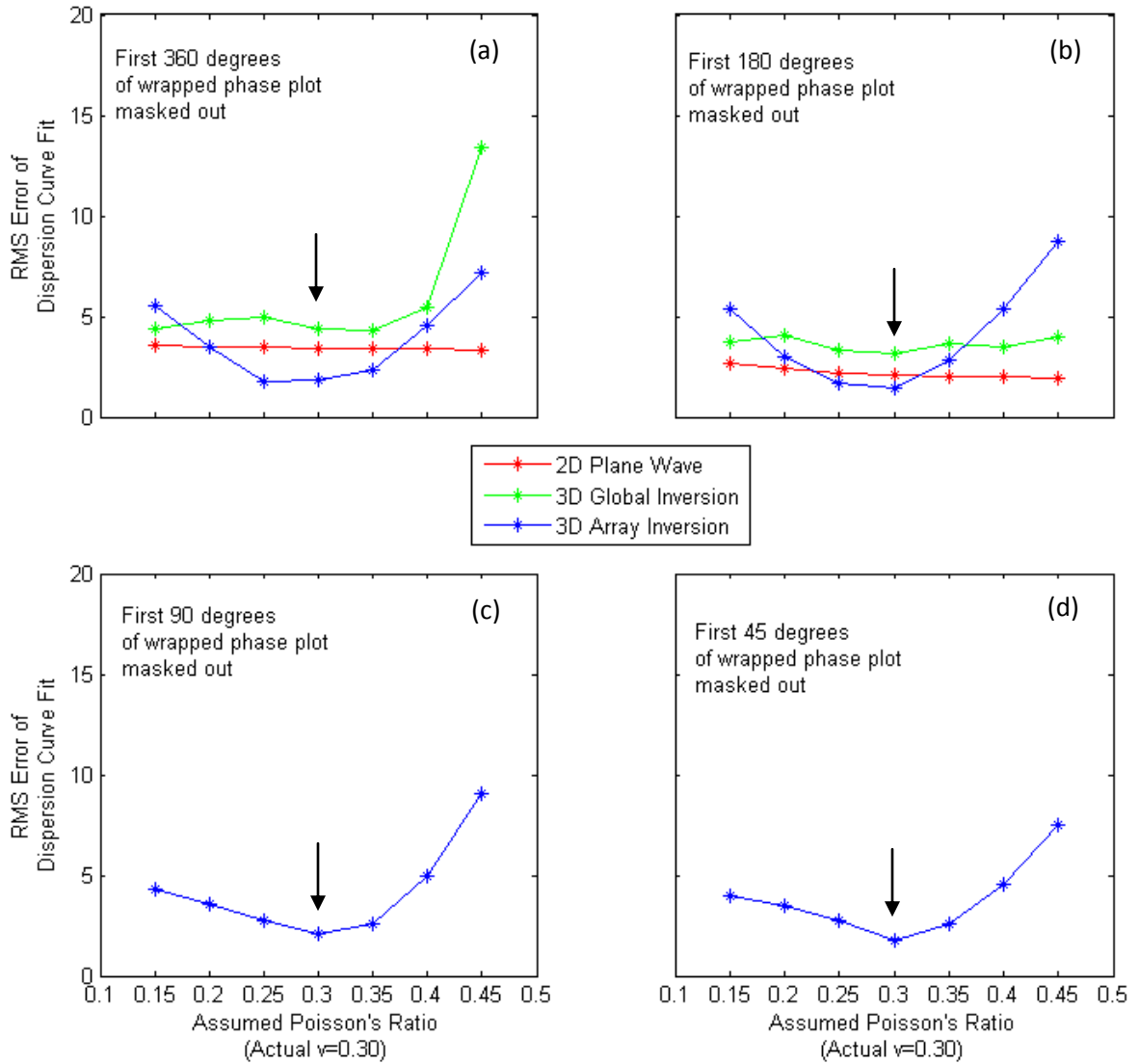


**Figure 4.48** RMS error in fit between theoretical and experimental dispersion curves for Case C, covering the range of inversion methods, filtering criteria, and Poisson's ratio values encompassed by Figure 4.45, Figure 4.46, and Figure 4.47 – arrows indicate abscissa location of the “true” Poisson's ratio

#### 4.3.3.4 Case D – Steep Power Function $V_S$ Profile ( $\nu = 0.30$ )

Results of the Poisson’s ratio study for the case of a steep power function  $V_S$  profile (Case D) are presented in four different figures as described herein – three sets of  $V_S$  profiles and a plot of RMS error versus Poisson’s ratio.  $V_S$  profiles derived from all inversion analyses are compared with the “true” Case D profile over seven different values of Poisson’s ratio. Specifically,  $V_S$  profiles derived from the 360° and 180° filtering criteria in Figure 4.49 and Figure 4.50, respectively, while those derived from the 90° and 45° filtering criteria are shown together in Figure 4.51.  $V_S$  profiles derived from inversion analysis are shown with a solid line, while the “true” Case D profile is shown with a dashed line. The root-mean-squared (RMS) error in fit between theoretical and experimental dispersion curves is plotted versus the value of Poisson’s ratio in Figure 4.52: a separate curve is plotted for each inversion approach (2D Global, 3D Global, and 3D Array) and each subplot corresponds to one of the four filtering criteria (360°, 180°, 90°, and 45°). Each curve in Figure 4.52 corresponds to an individual row of  $V_S$  profiles in Figure 4.49, Figure 4.50, and Figure 4.51.

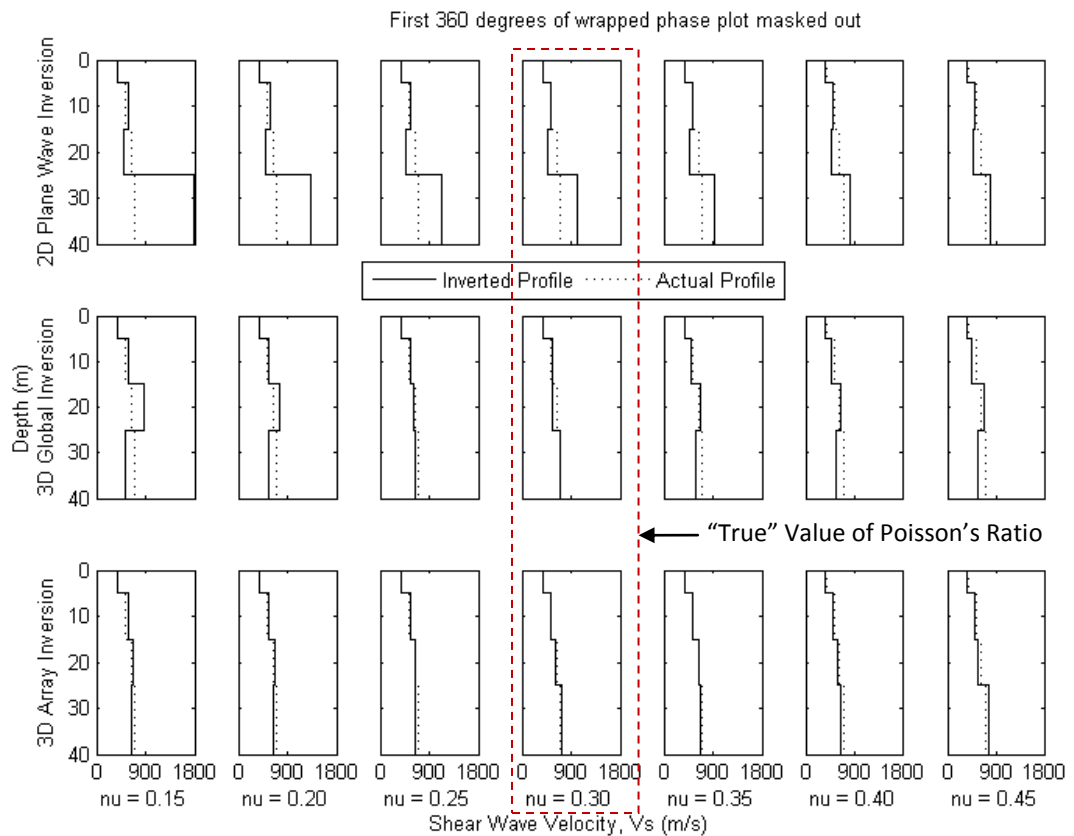


**Figure 4.49** Comparison of the “true”  $V_S$  profile for Case D with  $V_S$  profiles inverted by 2D Global, 3D Global and 3D Array methods – these data were processed by the 360° filtering criteria

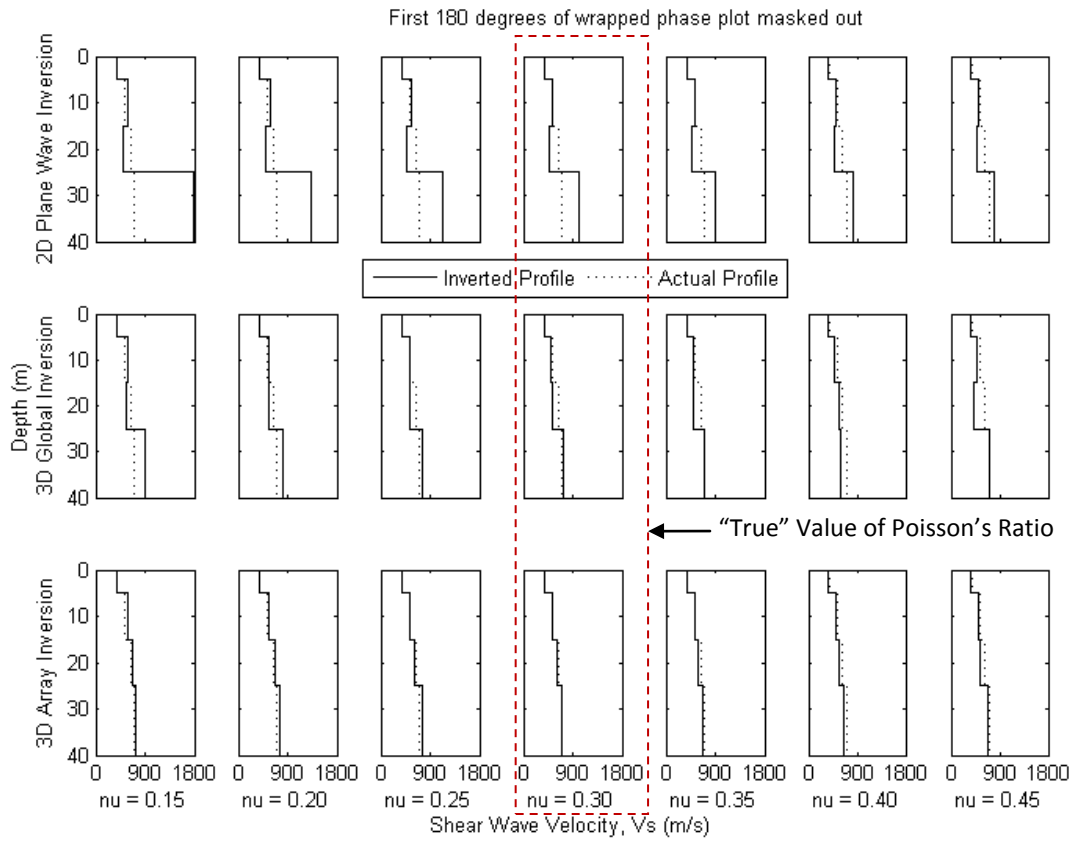


**Figure 4.50** Comparison of the “true”  $V_s$  profile for Case D with  $V_s$  profiles inverted by 2D Global, 3D Global and 3D Array methods – these data were processed by the 180° filtering criteria

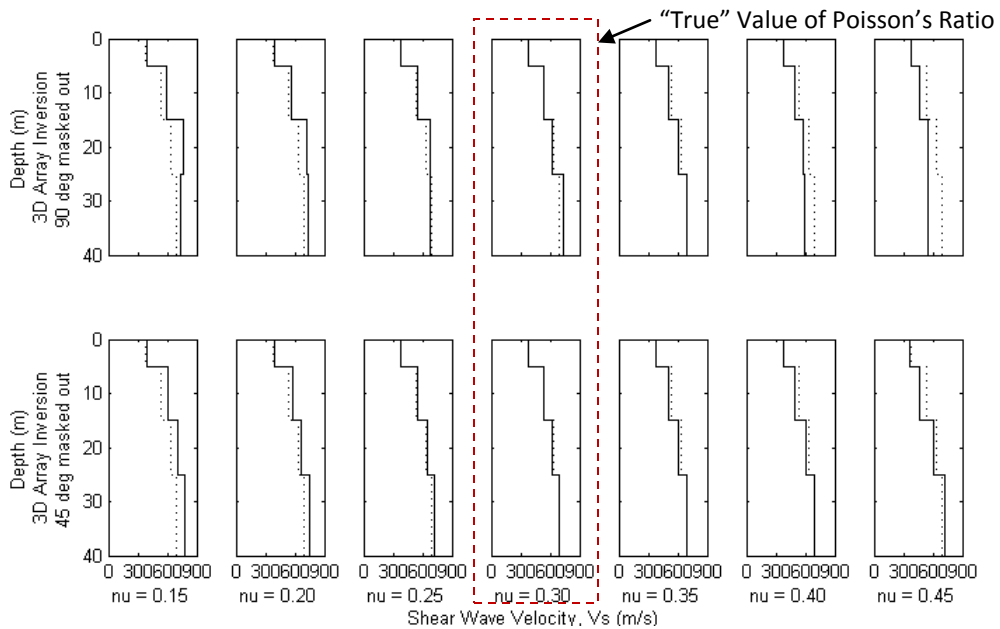


**Figure 4.51** Comparison of the “true”  $V_s$  profile for Case D with  $V_s$  profiles inverted by 2D Global, 3D Global and 3D Array methods – these data were processed by alternative filtering criteria including more near-field (90° top row and 45° bottom row)

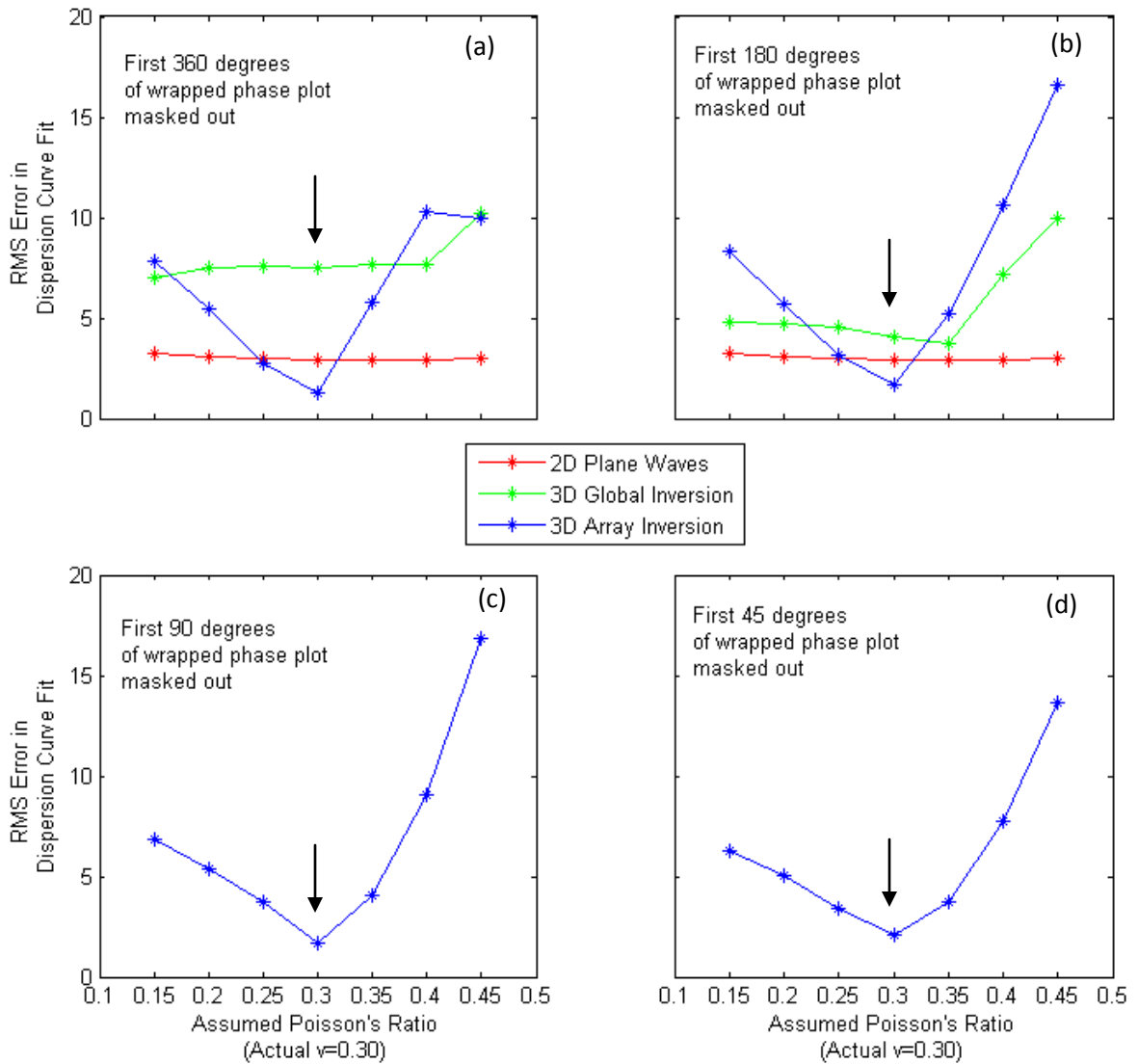


**Figure 4.52** RMS error in fit between theoretical and experimental dispersion curves for Case D, covering the range of inversion methods, filtering criteria, and Poisson’s ratio values encompassed by Figure 4.49, Figure 4.50, and Figure 4.51 – arrows indicate abscissa location of the “true” Poisson’s ratio value

**4.3.3.5 Case B\* – “Saturated” Power Function  $V_s$  Profile ( $\nu = 0.45$ )**

Results of the Poisson’s ratio study for the case of a “saturated” power function  $V_s$  profile (Case B\*) are presented in four different figures as described herein – three sets of  $V_s$  profiles and a plot of RMS error versus Poisson’s ratio.  $V_s$  profiles derived from all inversion analyses are compared with the “true” Case B\* profile over seven different values of Poisson’s ratio. Specifically,  $V_s$  profiles derived from the 360° and 180° filtering criteria in Figure 4.53 and Figure 4.54, respectively, while those derived from the 90° and 45° filtering criteria are shown together in Figure 4.55.  $V_s$  profiles derived from inversion analysis are shown with a solid line, while the “true” Case B\* profile is shown with a dashed line. The root-mean-squared (RMS) error in fit between theoretical and experimental dispersion curves is plotted versus the value of Poisson’s ratio in Figure 4.56: a separate curve is plotted for each inversion approach (2D Global, 3D Global, and 3D Array) and each subplot corresponds to one of the four filtering criteria (360°, 180°, 90°, and 45°). Each curve in Figure 4.56 corresponds to an individual row of  $V_s$  profiles in Figure 4.53, Figure 4.54, and Figure 4.55.

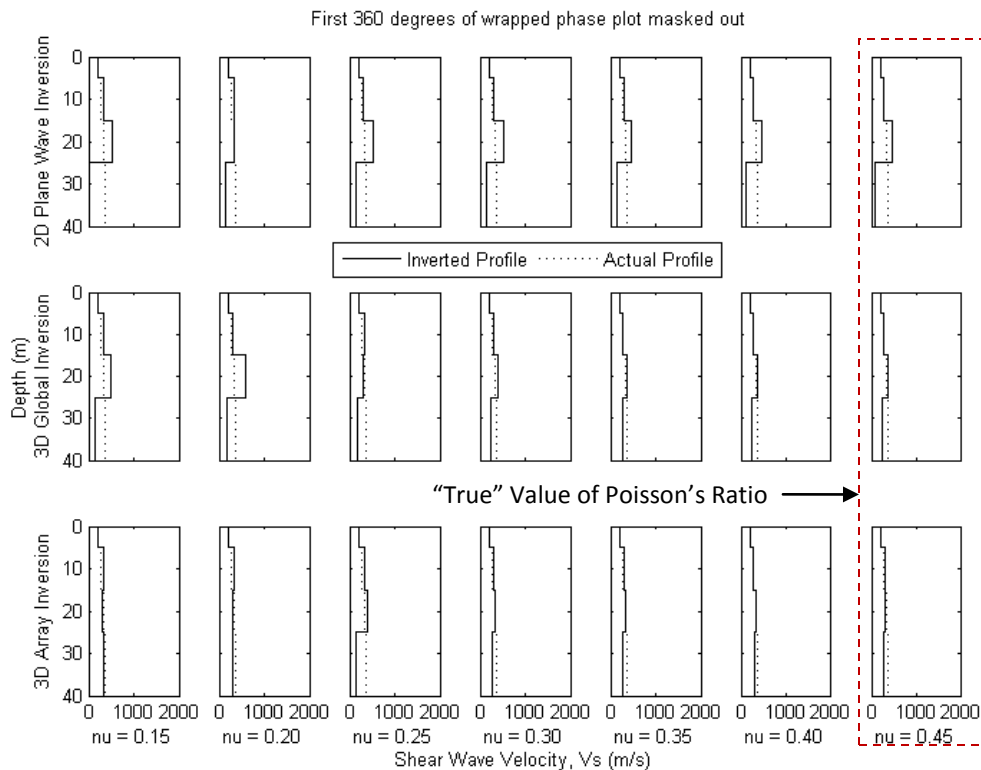


**Figure 4.53** Comparison of the “true”  $V_s$  profile for Case B\* - a saturated version of Case B - with  $V_s$  profiles inverted by 2D Global, 3D Global and 3D Array methods – these data were processed by the 360° filtering criteria

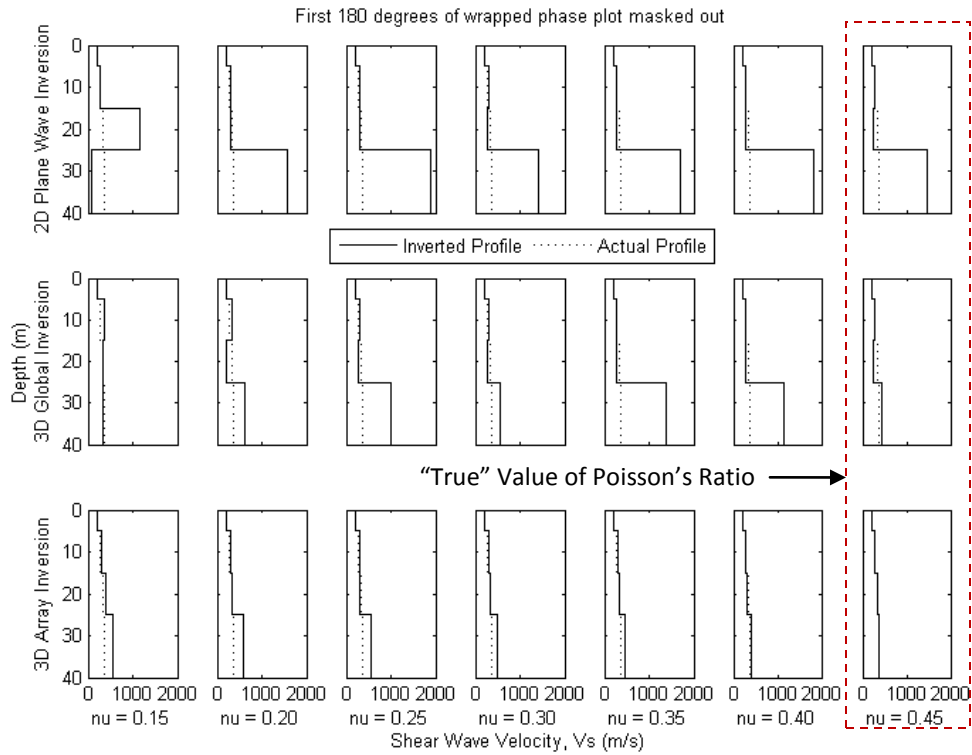


**Figure 4.54** Comparison of the “true”  $V_s$  profile for Case B\* - a saturated version of Case B - with  $V_s$  profiles inverted by 2D Global, 3D Global and 3D Array methods – these data were processed by the 180 ° filtering criteria

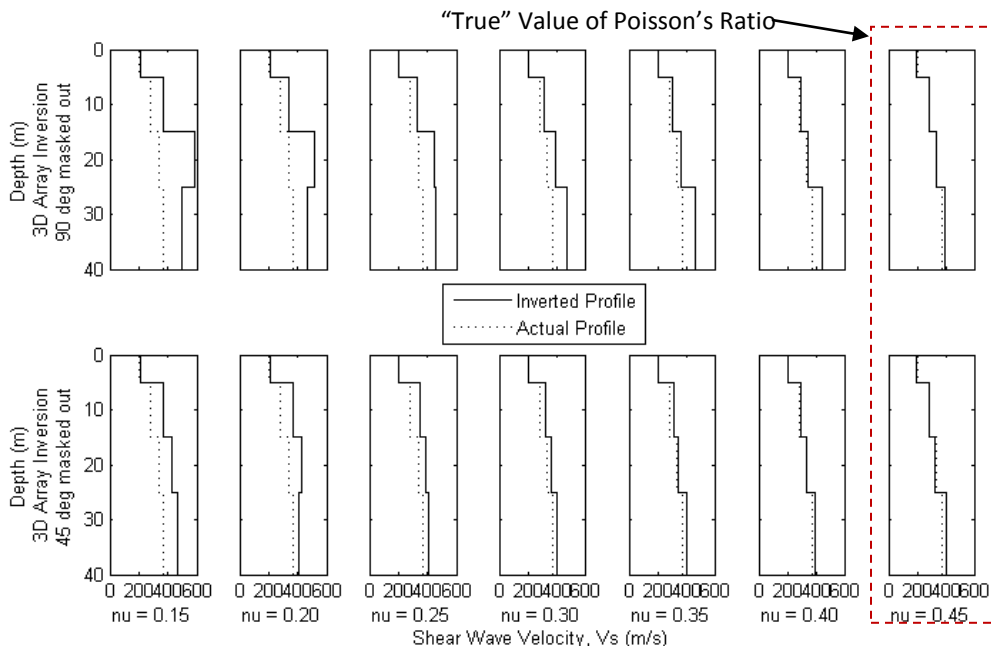


**Figure 4.55** Comparison of the “true”  $V_s$  profile for Case B\* - a saturated version of Case B - with  $V_s$  profiles inverted by 2D Global, 3D Global and 3D Array methods – these data were processed by alternative filtering criteria including more near-field (90° top row and 45° bottom row)

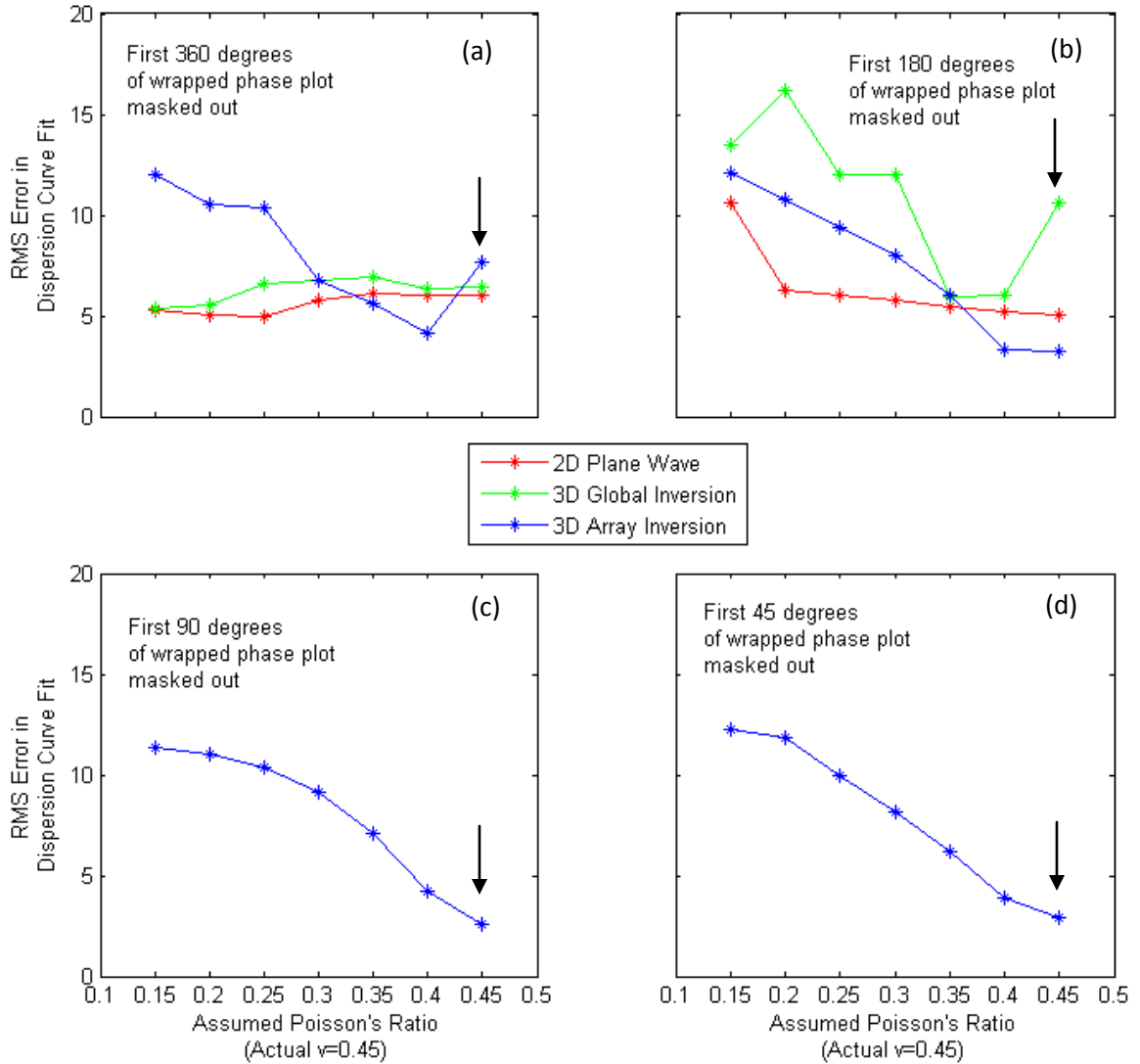


**Figure 4.56** RMS error in fit between theoretical and experimental dispersion curves for Case B\* - a saturated version of Case B - covering the range of inversion methods, filtering criteria, and Poisson's ratio values encompassed by Figure 4.53, Figure 4.54, and Figure 4.55 – arrows indicate abscissa location of the “true” Poisson's ratio value

#### 4.3.4 Discussion of Poisson's Ratio Study with Simulated SASW data

The results of the Poisson's ratio study presented in Section 4.3.3 demonstrate the effectiveness of various inversion approaches to infer the "true" value of Poisson's ratio. This study was motivated by the results of the preliminary sensitivity study (Section 4.2.1), which indicated that the shape of the dispersion curve appears to be sensitive to the value of Poisson's ratio when near-field effects are included in the analysis. The Poisson's ratio study considered the same combination of profile conditions, filtering criteria, and inversion approaches as the profile recovery study (Section 0). This study essentially expanded upon the latter by performing inversion analyses with seven different *assumptions* of Poisson's ratio, ranging from 0.15 to 0.45, since the value of Poisson's ratio is typically not known in practice and must be assumed. The assumed values were selected such that one assumed value corresponds to the "true" value in each case – this was the exact condition assessed in the profile recovery study. The "true" values of Poisson's ratio are 0.30 (for Cases A, B, C, and D) and 0.45 (for Case B\*). Even though each inversion analysis started with a different assumed value of Poisson's ratio, shear wave velocity was the only parameter inverted. The layering system and all other parameters had identical values to those used to generate the simulated data and were held constant throughout the analysis.

A number of useful observations can be derived from the shear wave velocity profiles and RMS error versus Poisson's ratio plots presented in Section 4.3.3. In these results, the dominant trends are most evident in the RMS error versus Poisson's ratio plots (i.e. Figure 4.40, Figure 4.44, Figure 4.48, Figure 4.52, and Figure 4.56). The plots of RMS error versus Poisson's ratio show the same three trends for all profile conditions: (1) the curve for the 2D global inversion is almost completely flat, (2) the curve for the 3D global inversion may have slight undulations at some values of Poisson's ratio, but is for the most part flat, and (3) the curve for the 3D array inversion dips sharply to the lowest RMS error, which is almost always at the "true" value of Poisson's ratio. The same three trends are evident in the results for all simulated profiles, regardless of the filtering criterion applied. The "flat" shape of the curve for the 2D and 3D global inversions indicates that the RMS error is approximately the same at different values of Poisson's ratio, which implies that these approaches are largely insensitive to the "true" value of Poisson's ratio. In other words, the same quality of fit can be achieved regardless of whether the correct Poisson's ratio is assumed. However, as is evident in the comparison of  $V_s$  profile, and incorrect assumption of Poisson's ratio will result in a lower quality prediction of the  $V_s$

profile. For the 3D array inversion, however, the steep slope of the curve indicates a distinct sensitivity to the “true” value of Poisson’s ratio – with the lowest RMS error corresponding very well to this value. It is interesting to note that there is much greater sensitivity as Poisson’s ratio increases. In other words, it is easier to differentiate a Poisson’s ratio value of 0.35 from 0.5, as compared to 0.2 to 0.35.

There is a slight anomaly in the results associated with the 360° filtering criterion: In the 3D array inversion results for Case B\*, the RMS error at a Poisson’s ratio of 0.45 (the “true” value) appears to be somewhat higher than that at a Poisson’s ratio of 0.40, which would lead one to believe that 0.40 is the “true” value. This is likely due to the shape of the dispersion curves associated with the longest simulated receiver spacings, which is a similar issue to that noted in Section 4.3.2 (see Figure 4.34). Here, some of the dispersion curves have a distinct “kink” at long wavelengths, as shown in Figure 4.57, which is quite severe for the longest spacing. This may be attributed to the interaction of near-field effects and a high Poisson’s ratio value. In any case, the kink will have a significant effect on the way that both global and array average curves are generated and, ultimately, the fit of the theoretical dispersion curve in the inversion analysis. For the same range of wavelengths, the results for the 180° filtering criterion were less affected by this phenomenon, and the results for the 90° and 45° criteria seemed to be unaffected. These criteria expand the near-field portion of the dispersion curve (i.e. right of the kink), so data from some of the longer spacings can be omitted while maintaining the same wavelength range in the composite dispersion curve. A composite dispersion curve generated for the same profile (Case B\*) with a 45° filtering criterion is shown in Figure 4.58 for comparison.

Three key conclusions were derived from the Poisson’s ratio study. First, Poisson’s ratio cannot be inferred by inversion methods based on a global average of the experimental dispersion curve, as these methods do not exhibit sensitivity to the value of Poisson’s ratio. The 2D global approach produced similar fit quality (RMS error) for all assumed values of Poisson’s ratio, while the 3D global approach yielded unpredictable results (even showing a “false sensitivity” in some cases). This result was expected and it is consistent with the current practice of assuming a value of Poisson’s ratio and accepting the resulting error in the computed  $V_s$  profile. Second, the value of Poisson’s ratio can be accurately inferred, for the profile conditions examined in this study, by use of the 3D array inversion approach. A distinct trend emerged from multiple 3D array inversions of the same data using different assumed values of Poisson’s

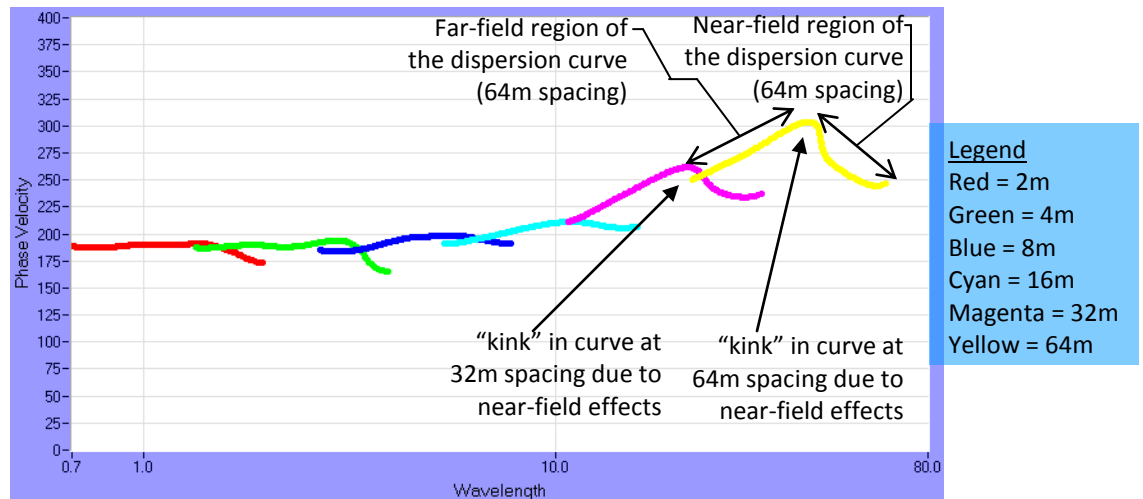


**Figure 4.57** WinSASW screenshot of the composite dispersion curve for Case B\*, with a 360° filtering criterion, showing the sharp “kinks” in the curves of the longer spacings required for this criterion

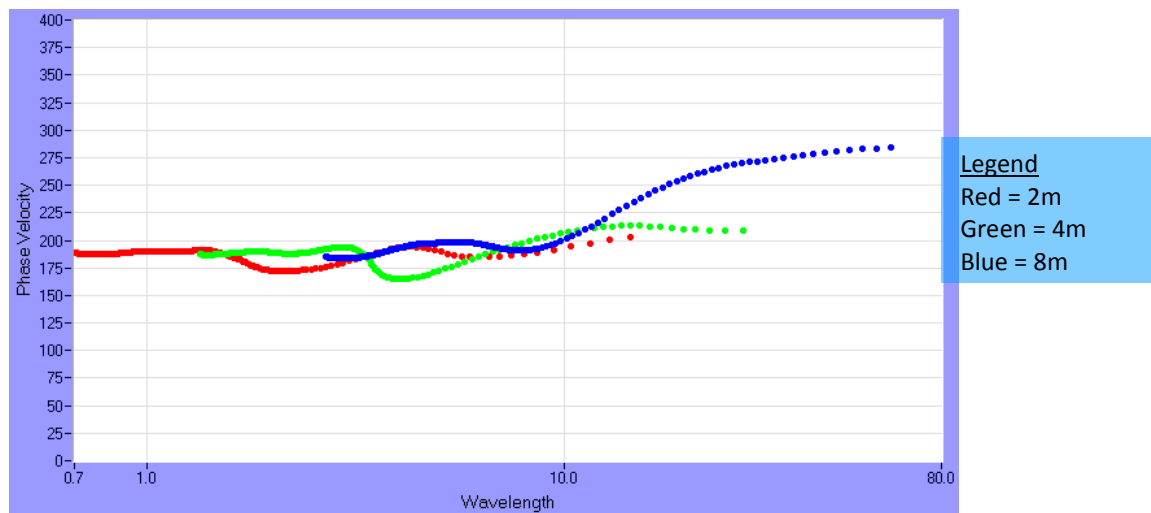


**Figure 4.58** WinSASW screenshot of the composite dispersion curve for Case B\*, with a 45° filtering criterion, showing the gradual undulations in the near-field region of each curve

ratio, where the “true” value of Poisson’s ratio was correctly identified from the inversion producing the lowest RMS error in dispersion curve fit (which also produced the best quality  $V_s$  profile). Third, filtering criteria used to mitigate the near-field had little to no effect on the process of inferring Poisson’s ratio by the 3D array inversion, with less restrictive criteria providing a slightly better result. The 360° and 180° criteria did produce ambiguous results in some cases (e.g. Case C and Case B\*), while the 90° and 45° criteria produced consistent sensitivity trends for all simulated profiles, even for the saturated conditions of Case B\*. This last point also suggests that near-field effects are present in all cases, and filtering criteria

allowing for more of the near-field can be implemented without affecting the inference of Poisson's ratio from the 3D array inversion. In practice, this could be implemented by performing multiple inversions using a range of Poisson's ratio values to identify the case that provided the best fit to the dispersion data. This would produce both a prediction of Poisson's ratio for the profile and the best prediction of the  $V_S$  profile.

Therefore, it has been demonstrated that a value which must be assumed in current practice (i.e. Poisson's ratio) can be inferred from experimental data, substantially increasing the effectiveness of surface wave measurements. The benefits of accurately inferring Poisson's ratio for in-situ conditions also extend beyond surface wave analyses (e.g. Poisson's ratio is an important *a priori* input for many geotechnical analyses). Future work may focus on the development of an SASW inversion program capable of simultaneously inverting for both shear wave velocity and Poisson's ratio with depth.

#### **4.3.5 Results from Analysis of Simulated Multi-channel Data**

This section presents results of a study performed with simulated multi-channel data, which extended the previously-described profile recovery and Poisson's ratio studies by considering the response of multi-channel data to similar inversion techniques. Multi-channel analysis was performed to allow comparisons between the SASW method and the multi-channel method which is now the most common approach used in current practice. The goal of this study was to examine how results from current multi-channel methods compare with the SASW results derived in this study. Ground motions were simulated for the 30 receiver locations shown in Figure 3.24 and processed as described in Section 3.4. Inversion was performed using the 2D (plane wave) model, which is the predominant approach to multi-channel analyses in current practice. The array inversion approach is not applicable, as multi-channel methods produce only a single continuous dispersion curve. The scope of the multi-channel study was limited to simulations of Cases A, B, C, and D, where the "true" value of Poisson's ratio was 0.30 for all profiles. Similar to the previous studies, the same data from each profile was inverted with different *assumed* values of Poisson's ratio. For this study, the results are presented in the form of a three-part plot. On each of the following figures, part (a) shows the inverted and "true" shear wave velocity profiles for each assumed value of Poisson's ratio, while part (b) shows a plot of RMS error versus Poisson's ratio similar to those of the Poisson's ratio study, and part (c) shows a layer-specific profile error plot similar to those of the profile recovery study.

**4.3.5.1 Case A – Uniform  $V_S$  Profile, ( $\nu = 0.30$ )**

Results of the study with simulated multi-channel data for the case of a uniform  $V_S$  profile (Case A) are shown in Figure 4.59. Figure 4.59a shows  $V_S$  profiles derived from 2D Global inversion analyses (solid line), which are compared with the “true” Case A profile (dashed line) over seven different *assumed* values of Poisson’s ratio, as the exact value is often unknown *a priori*. The quality of fit between the experimental and theoretical dispersion curve is quantified for each case using RMS error and plotted in Figure 4.59b – the “true” value of Poisson’s ratio (indicated by the red dashed rectangle) was known to be 0.30 *a priori*. Percent error between the inverted and “true” values of  $V_S$  for each layer is shown in Figure 4.59c – this comparison was made possible by the fact that the layering system was known *a priori*.

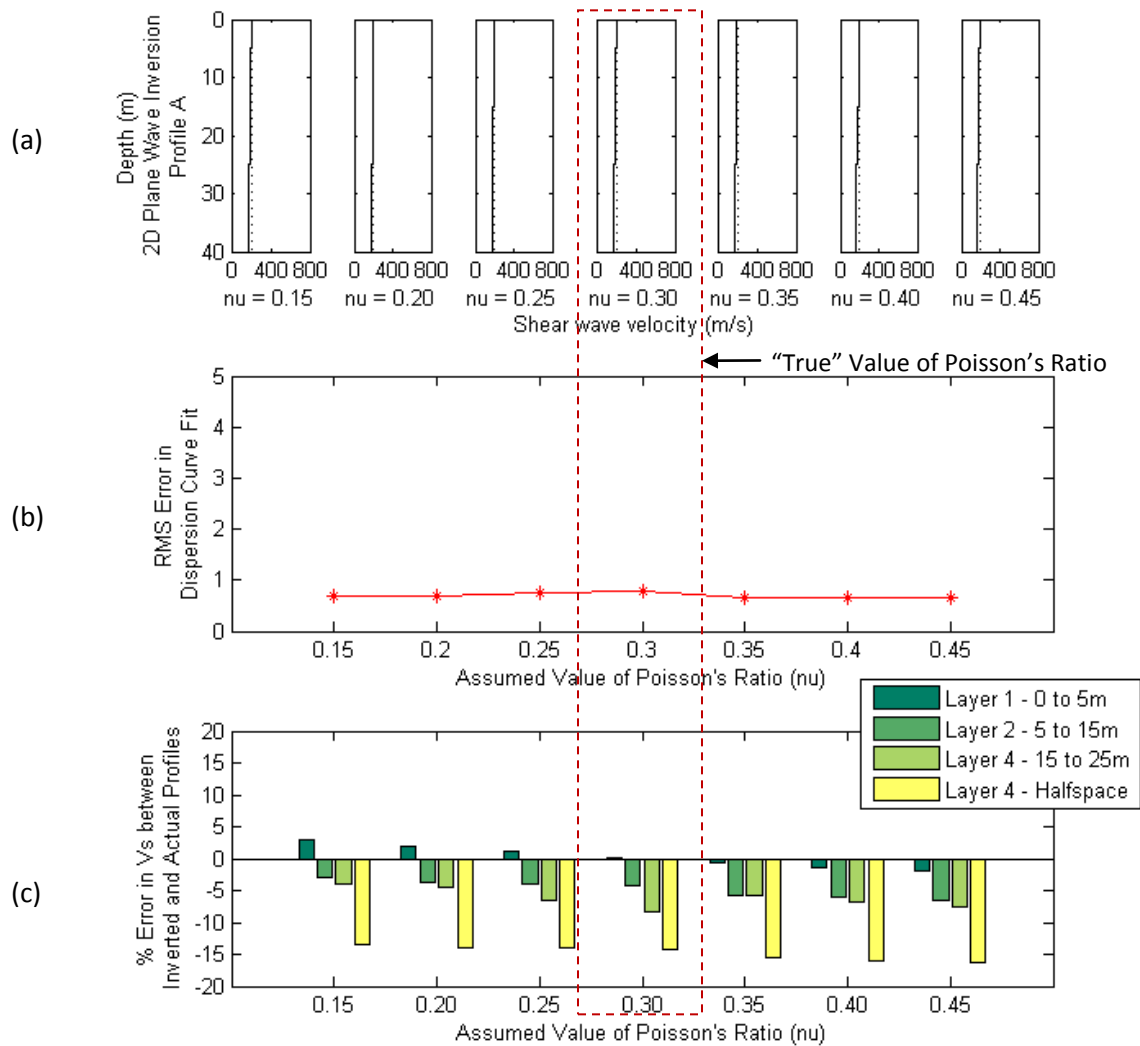


**Figure 4.59** Comparison of the “true”  $V_S$  profile for Case A with  $V_S$  profiles inverted from multi-channel data by 2D Global and 3D Global methods

#### 4.3.5.2 Case B – Power Function $V_S$ Profile ( $\nu = 0.30$ )

Results of the multi-channel inversion study for the case of a uniform  $V_S$  profile (Case B) are shown in Figure 4.60. Figure 4.60a shows  $V_S$  profiles derived from 2D Global inversion analyses (solid line), which are compared with the “true” Case B profile (dashed line) over seven different assumed values of Poisson’s ratio, as the exact value is often unknown *a priori*. The quality of fit between the experimental and theoretical dispersion curve is quantified for each case using RMS error and plotted in Figure 4.60b – the “true” value of Poisson’s ratio (indicated by the red dashed rectangle) was known to be 0.30 *a priori*. Percent error between the inverted and “true” values of  $V_S$  for each layer is shown in Figure 4.60c – this comparison was made possible by the fact that the layering system was known *a priori*.

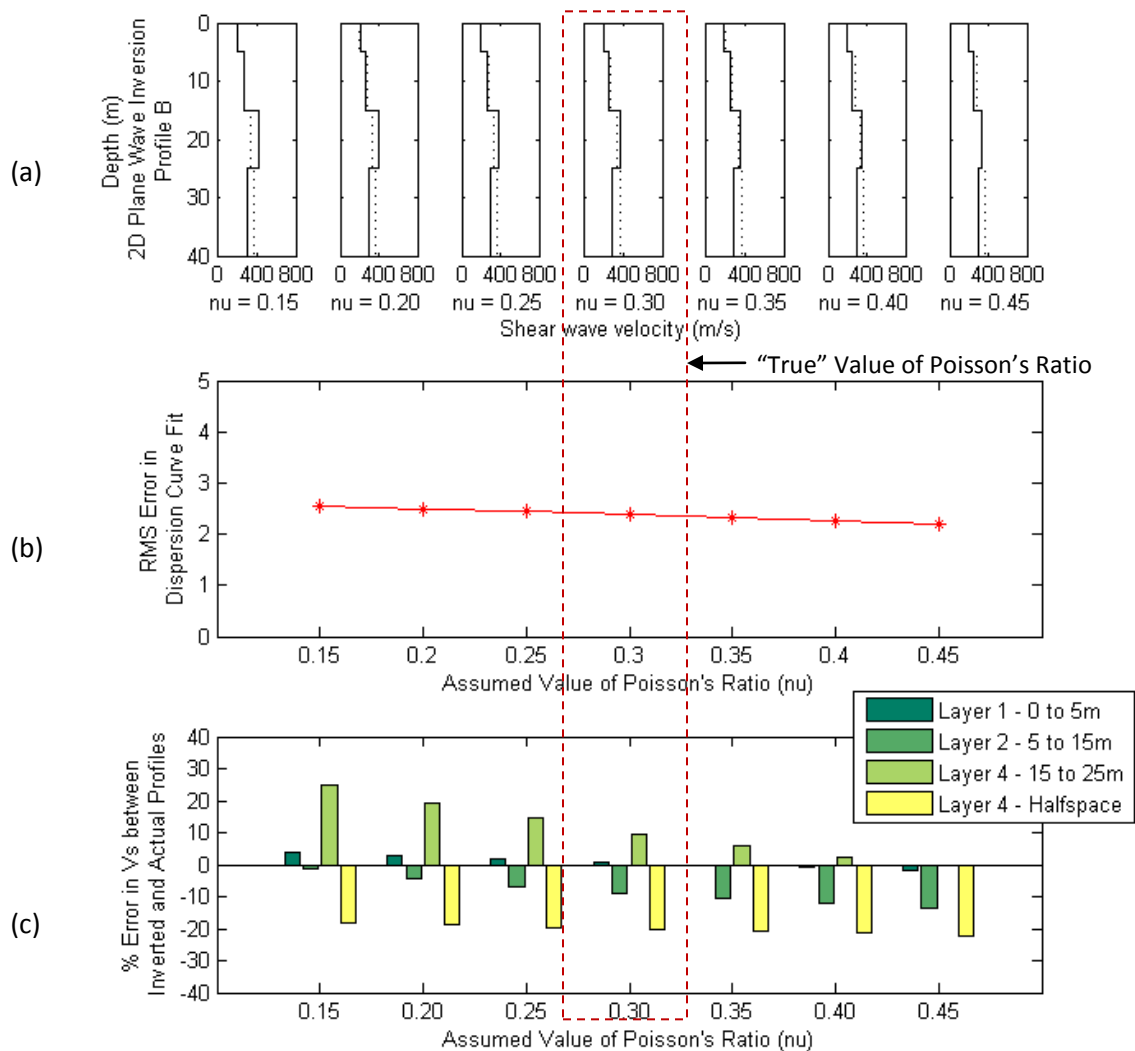


**Figure 4.60** Comparison of the “true”  $V_S$  profile for Case B with  $V_S$  profiles inverted from multi-channel data by 2D Global and 3D Global methods

**4.3.5.3 Case C – Linear  $V_s$  Profile ( $\nu = 0.30$ )**

Results of the multi-channel inversion study for the case of a uniform  $V_s$  profile (Case C) are shown in Figure 4.61. Figure 4.61a shows  $V_s$  profiles derived from 2D Global inversion analyses (solid line) are compared with the “true” Case C profile (dashed line) over seven different assumed values of Poisson’s ratio, as the exact value is often unknown *a priori*. The quality of fit between the experimental and theoretical dispersion curve is quantified for each case using RMS error and plotted in Figure 4.61b – the “true” value of Poisson’s ratio (indicated by the red dashed rectangle) was known to be 0.30 *a priori*. Percent error between the inverted and “true” values of  $V_s$  for each layer is shown in Figure 4.61c – this comparison was made possible by the fact that the layering system was known *a priori*.

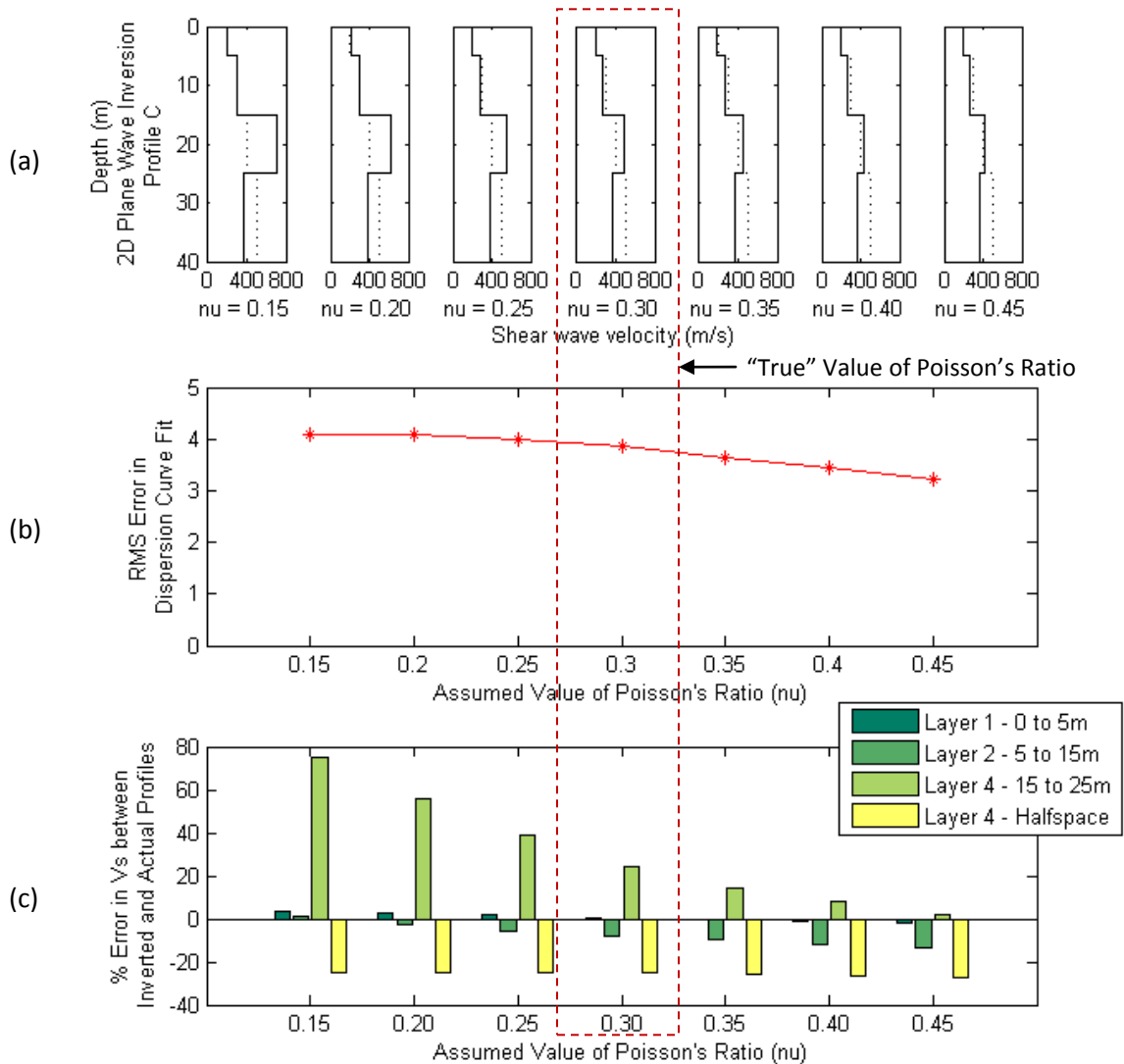


**Figure 4.61** Comparison of the “true”  $V_s$  profile for Case C with  $V_s$  profiles inverted from multi-channel data by 2D Global and 3D Global methods

**4.3.5.4 Case D – Steep Linear  $V_s$  Profile ( $\nu = 0.30$ )**

Results of the multi-channel inversion study for the case of a uniform  $V_s$  profile (Case D) are shown in Figure 4.62. Figure 4.62a shows  $V_s$  profiles derived from 2D Global inversion analyses (solid line), which are compared with the “true” Case D profile (dashed line) over seven different assumed values of Poisson’s ratio, as the exact value is often unknown *a priori*. The quality of fit between the experimental and theoretical dispersion curve is quantified for each case using RMS error and plotted in Figure 4.62b – the “true” value of Poisson’s ratio (indicated by the red dashed rectangle) was known to be 0.30 *a priori*. Percent error between the inverted and “true” values of  $V_s$  for each layer is shown in Figure 4.62c – this comparison was made possible by the fact that the layering system was known *a priori*.

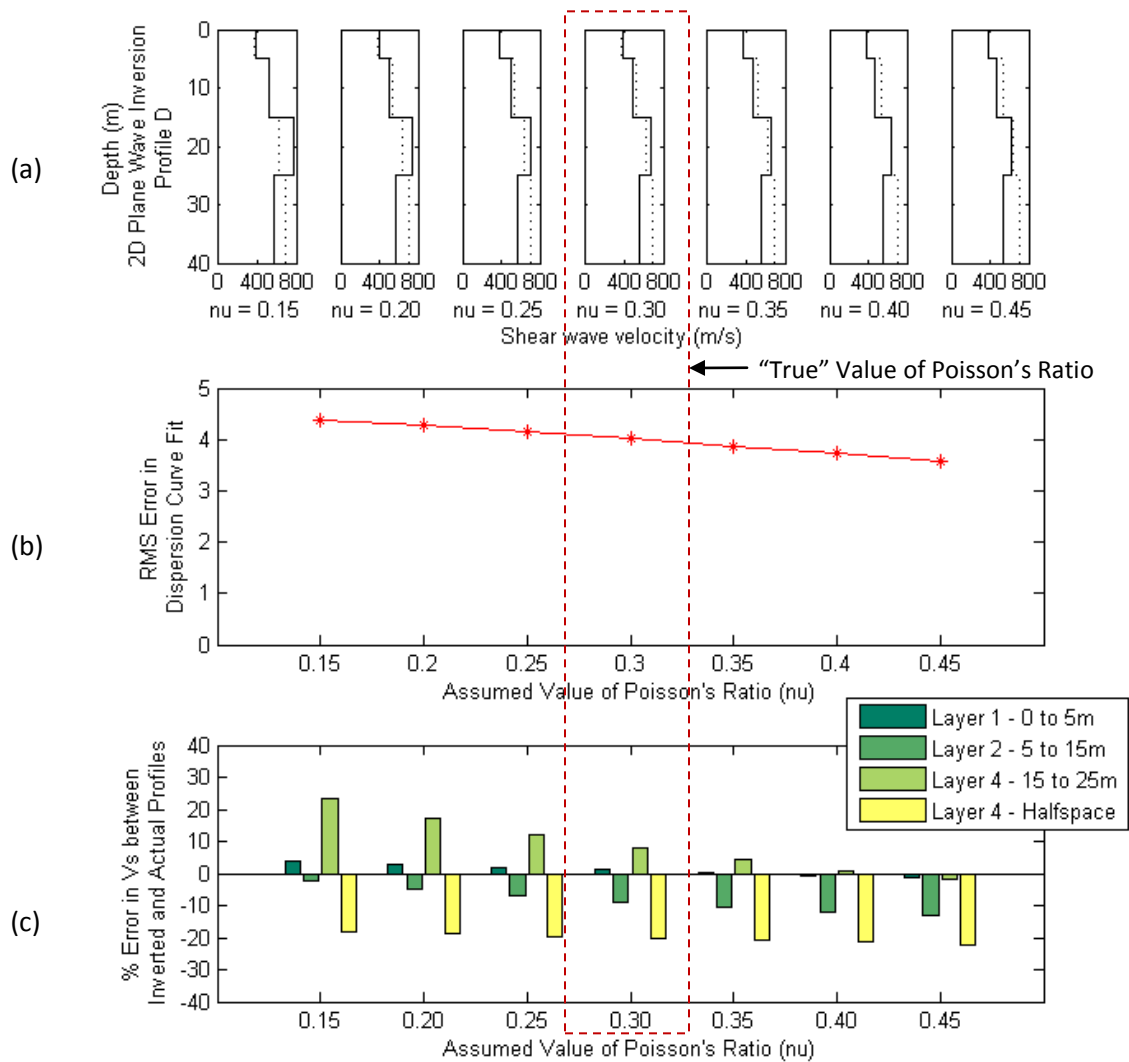


**Figure 4.62** Comparison of the “true”  $V_s$  profile for Case D with  $V_s$  profiles inverted from multi-channel data by 2D Global and 3D Global methods

#### 4.3.6 Discussion of Surface Wave Analysis with Simulated Multi-channel Data

Similar to the profile recovery (Section 0) and Poisson's ratio (Section 4.3.3) studies with SASW data, the multi-channel study (Section 4.3.5) considered potential applications of surface wave analyses in recovering the "true"  $V_s$  profile and inferring the "true" value of Poisson's ratio. This study used simulated multi-channel data, which were generated for the same Case A, B, C, and D profiles used in the previous two studies, processed by the FDBF approach (see Section 3.4), and inverted by the 2D global approach. Similar to the previous studies, Poisson's ratio was studied by multiple inversions of the same data with seven different assumptions of the Poisson's ratio value, ranging from 0.15 to 0.45. In each case, one of the assumed Poisson's ratio values also corresponded to the "true" value of 0.30. Even though each inversion analysis started with a different assumed value of Poisson's ratio, shear wave velocity was still the only value to be changed during the inversion process. All other parameters, including the layering system, had identical values to those used to generate the simulated data and were held constant throughout the analysis.

Considering the multi-channel results presented in Section 4.3.5, key observations arise in three areas: (1) profile recovery when Poisson's ratio is assumed correctly, (2) profile recovery when Poisson's ratio is assumed incorrectly, and (3) the sensitivity of the quality of fit (i.e. RMS error) to the Poisson's ratio assumption. First, when the value of Poisson's ratio is assumed correctly, the multi-channel results demonstrate a trend of systematic error with a significant under-estimation of the halfspace velocity in all cases. Other layers were over-/under-estimated to the same or a lesser degree in all cases, with the linear profile (Case C) showing the worst overall profile recovery. Perhaps the best explanation for these issues is incompatibility between the experimental data and theoretical model, in that a 2D theoretical model (which does not simulate the near-field) is being used to fit experimental data "collected" in the near-field. This effect was clearly illustrated by Li (2011) for the Case C profile with the same receiver array, as shown in Figure 4.63, where the near-field and far-field curves diverge sharply at low frequencies/long wavelengths. Second, for multi-channel analyses, an incorrect assumption of Poisson's ratio does not appreciably alter the (poor) quality of the profile. In some cases (especially Case C), using a Poisson's ratio smaller than the "true" value can result in a profile estimate which is worse than that derived from the "true" value. This is also likely to be a function of the model incompatibility issue. Third, the quality-of-fit (i.e. RMS error) results for the multi-channel study show a trend of either constant or slightly decreasing error with

changes in Poisson's ratio, indicating that this approach is largely insensitive to the assumed value of Poisson's ratio. Although these results show a decreasing trend of RMS error in some cases, the minimum RMS error does not occur at the "true" value. In the Poisson's ratio study for SASW, the quality-of-fit for the 3D array inversion changed quite significantly for different assumptions of Poisson's ratio, which led to inferring the value of Poisson's ratio. Poisson's ratio must, therefore, be known or assumed for multi-channel analyses, since it cannot be inferred from the dispersion curve fit.

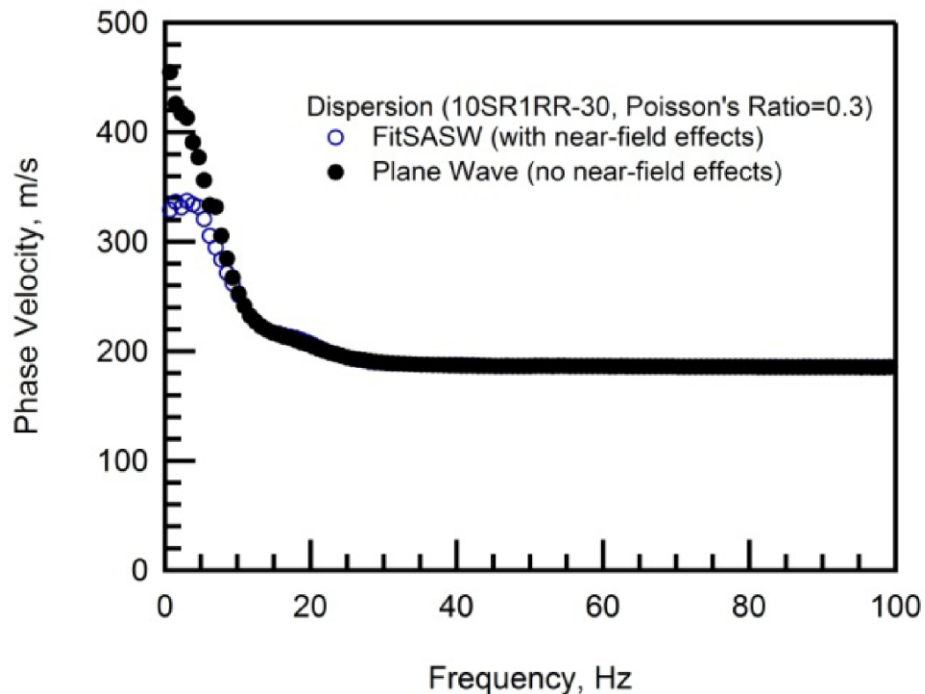


**Figure 4.63** Normalized dispersion curves for Case C with a multi-channel array having a 10m source-to-first-receiver distance, a receiver-to-receiver of 1m and 30 total receivers (i.e. 10SR1RR-30) from Li 2011

Therefore, three key conclusions were derived from the multi-channel study with simulated data. First, the common approach to multi-channel analyses (i.e. 2D global inversion) causes systematic errors in profile recovery when used with experimental data collected in the near-field. The issue of "model incompatibility" is likely the main cause of these errors, as the 2D model does not account for the near-field effects inherent in most experimental data. The SASW results for the 2D and 3D global inversions demonstrated similar profile recovery issues on account of the global averaging approach. Second, a comparison of SASW and multi-channel results (i.e. compare Figure 4.37 and Figure 4.59a; Figure 4.41 and Figure 4.60a; Figure 4.45 and Figure 4.61a; Figure 4.49 and Figure 4.62a) reveals that the multi-channel approach provides

better profile recovery than SASW with same inversion approach, 2D global. Despite this improvement, both approaches are still affected by the model incompatibility issue with the 2D model. The 3D array approach with SASW is significantly more accurate in profile recovery than the multi-channel approach with the 2D model. Third, the quality-of-fit (i.e. RMS error) for multi-channel analyses is largely insensitive to changes in the value of Poisson's ratio. In contrast, a distinct sensitivity to Poisson's ratio was evident in the SASW quality-of-fit results for the 3D array inversion, from which the "true" in-situ value of Poisson's ratio was correctly inferred. A "3D array" approach for multi-channel would theoretically combine the best elements of both SASW and multi-channel approaches, but, at present, has not yet been developed due to the extensive computational requirements.

## 5 RESULTS AND DISCUSSION – EXPERIMENTAL STUDY

### 5.1 Introduction

The key findings from the study using simulated data and discussed in Chapter 4 were: (1) using the array inversion approach, less restrictive near-field criteria (and shorter receiver arrays) can be used without sacrificing the quality of the  $V_S$  profile prediction, and (2) using the array inversion approach, Poisson's ratio of the profile can be inferred from the quality of fit between experimental and theoretical dispersion curves. In this Chapter, these two findings are tested using real experimental data collected as part of a previous study in the Mississippi Embayment region of the central United States. Experimental data were collected, processed and inverted as described in Chapter 3 (see Section 3.7). Section 5.2 presents the results of the array inversion analysis using minimal near-field masking (i.e.  $90^\circ$  criteria) of SASW (Section 5.2.1) and analysis of multi-channel methods (Section 5.2.2). The resulting profiles are compared to the profile obtained by Rosenblad et al. (2010) using traditional SASW procedures. Section 5.3 discusses these results as they relate to the practicality of including the near-field in surface wave analyses.

### 5.2 Results from the Analysis of Mississippi Embayment Data

#### 5.2.1 Results from SASW Analyses using Alternative Near-field Filtering

Results of the SASW inversion using real surface wave data from the field site in the Mississippi Embayment are presented below. In this case, the  $90^\circ$  filtering criteria was used to mask the SASW data, allowing for a maximum wavelength of about 300 m to be generated from a receiver spacing of only 80 m. Figure 5.1, below, shows the experimental dispersion curve used in this analysis. The final shear wave velocity profiles were obtained from the analyses performed using assumed Poisson's ratio values of 0.20, 0.30, 0.40, and 0.45, plus the "saturated" case (where the p-wave velocity was set equal to 1600 m/s), are shown in Figure 5.2. The  $V_S$  profiles are shown to a depth of 150m, as the longest wavelength was approximately 300 m. As noted in Section 3.7, this site is saturated below the first few meters, so the "saturated" case should best represent the true profile conditions at this site. Figure 5.3 shows a comparison of the  $V_S$  profile obtained for the saturated condition ( $V_p = 1600$  m/s) using the alternative masking approach ( $90^\circ$  criteria) to the  $V_S$  profile obtained by Rosenblad et al. (2010)

using the traditional masking approach (180° criteria). The root-mean-squared (RMS) error in fit between theoretical and experimental dispersion curves is plotted versus the value of Poisson’s ratio in Figure 5.4. The open circle in Figure 5.4 corresponds to the “saturated” case, where  $V_p = 1600$  m/s, and are shown with an average value of Poisson’s ratio. Figure 5.5 shows an example of the dispersion curve obtained for this “saturated” case.

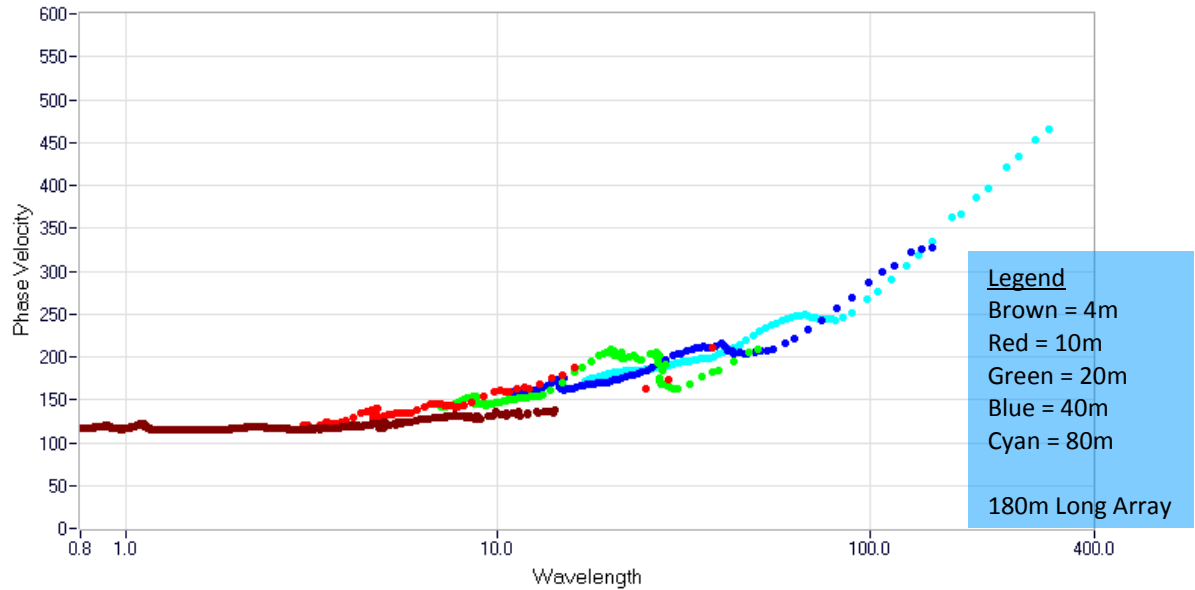


**Figure 5.1** Experimental dispersion curve generated from the Mississippi Embayment data using a 90° filtering criteria with a 180m long array

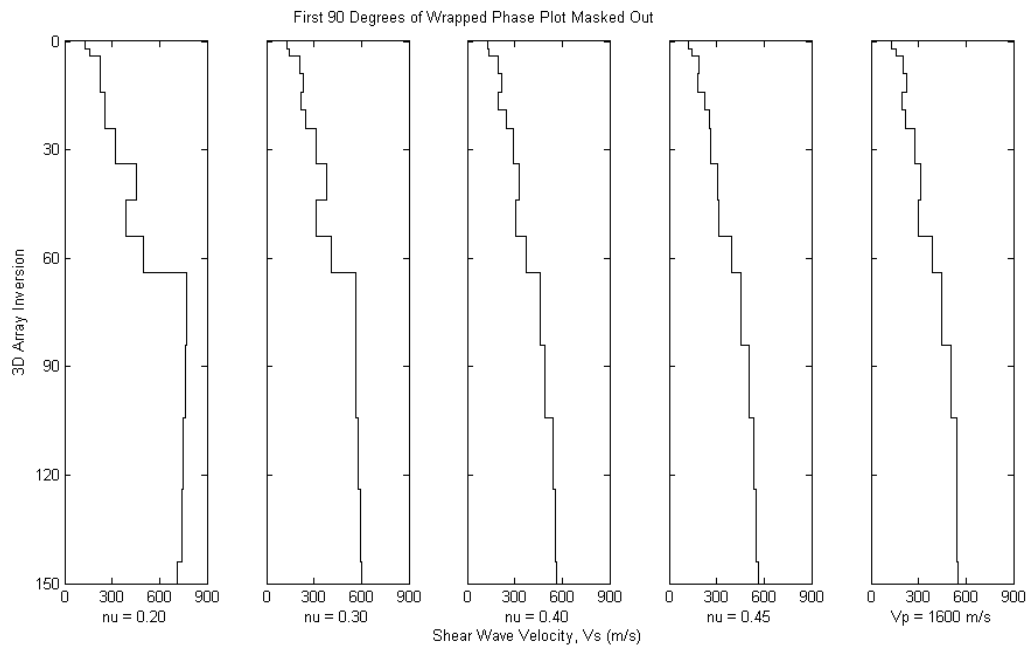


**Figure 5.2**  $V_s$  profiles inverted from the Mississippi Embayment data by the 3D array method using alternative filtering criteria including more of the near-field

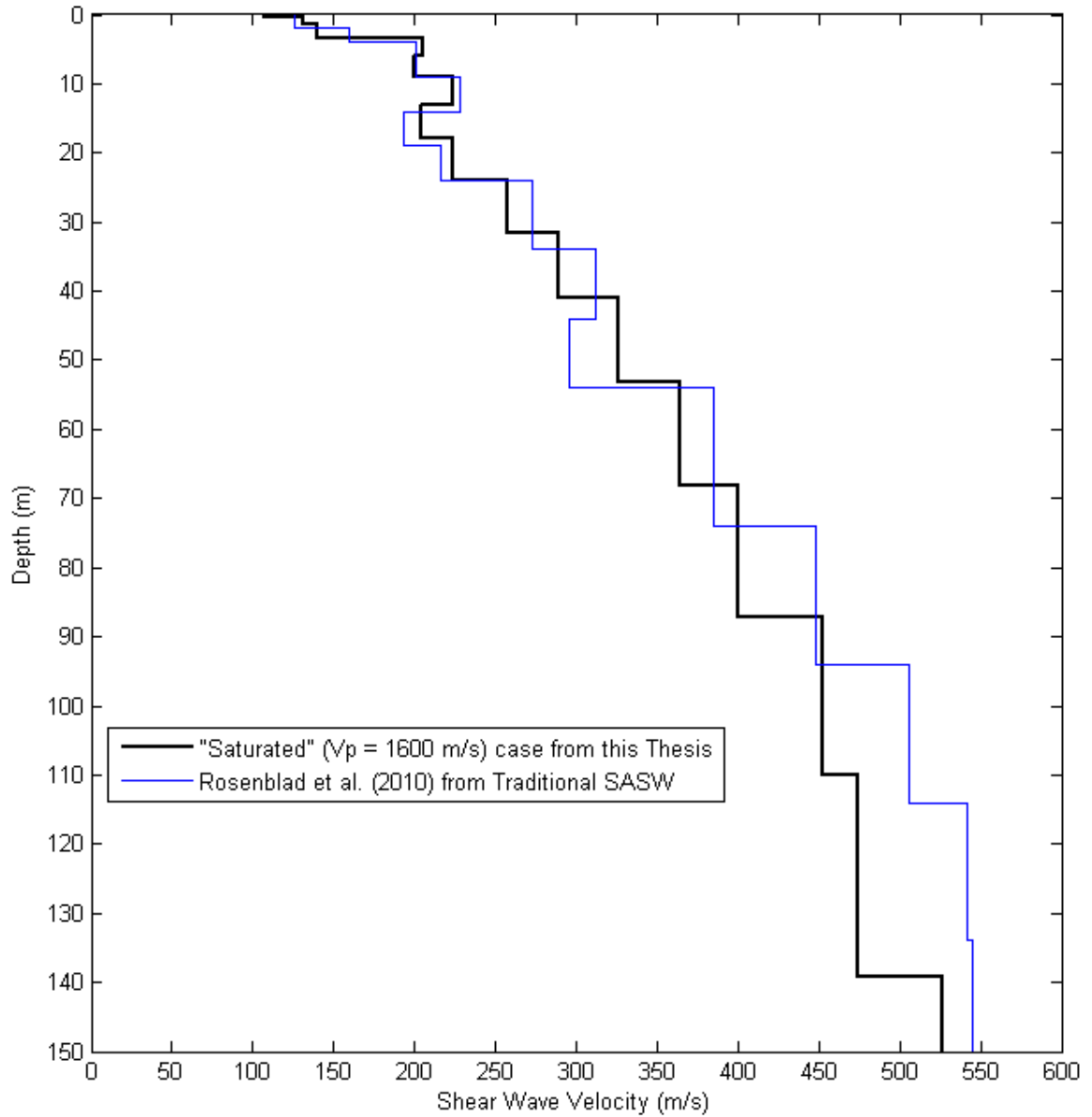


**Figure 5.3** Comparison of the  $V_s$  profile derived for the "saturated" ( $V_p = 1600$  m/s) case with the profile determined by Rosenblad et al. (2010), who processed the same experimental dataset with traditional SASW criteria

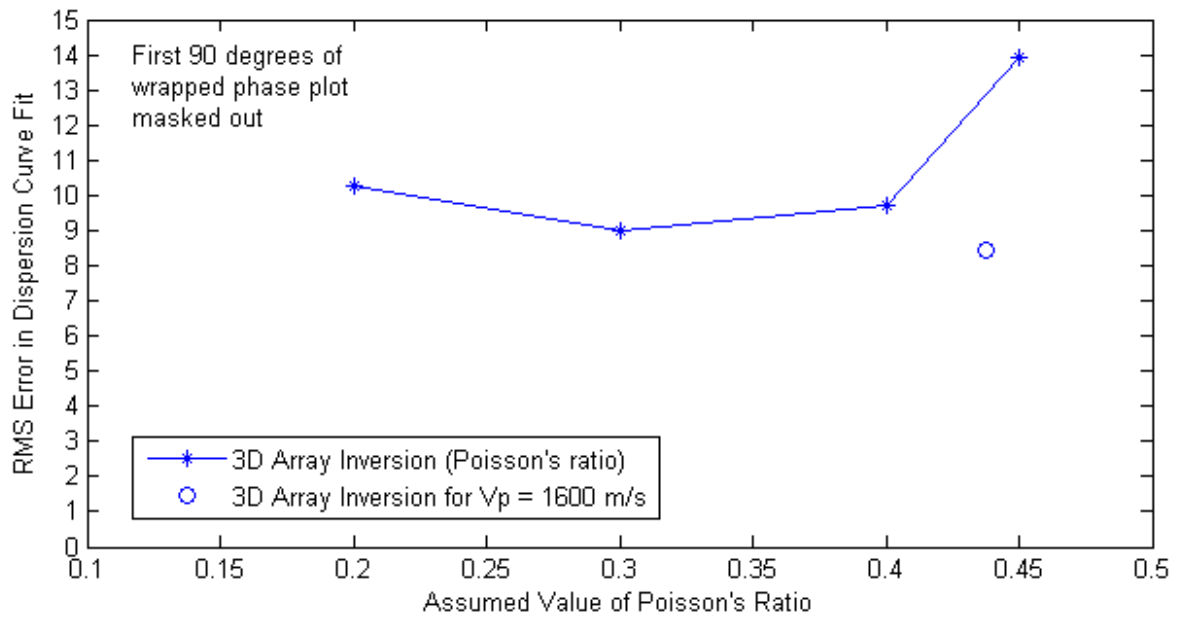


**Figure 5.4** RMS error in fit between theoretical and experimental dispersion curves from Mississippi Embayment data, for the inversion methods and Poisson's ratio values encompassed by Figure 5.2 – average Poisson's ratio values are plotted for the saturated case ( $V_p = 1600$  m/s)

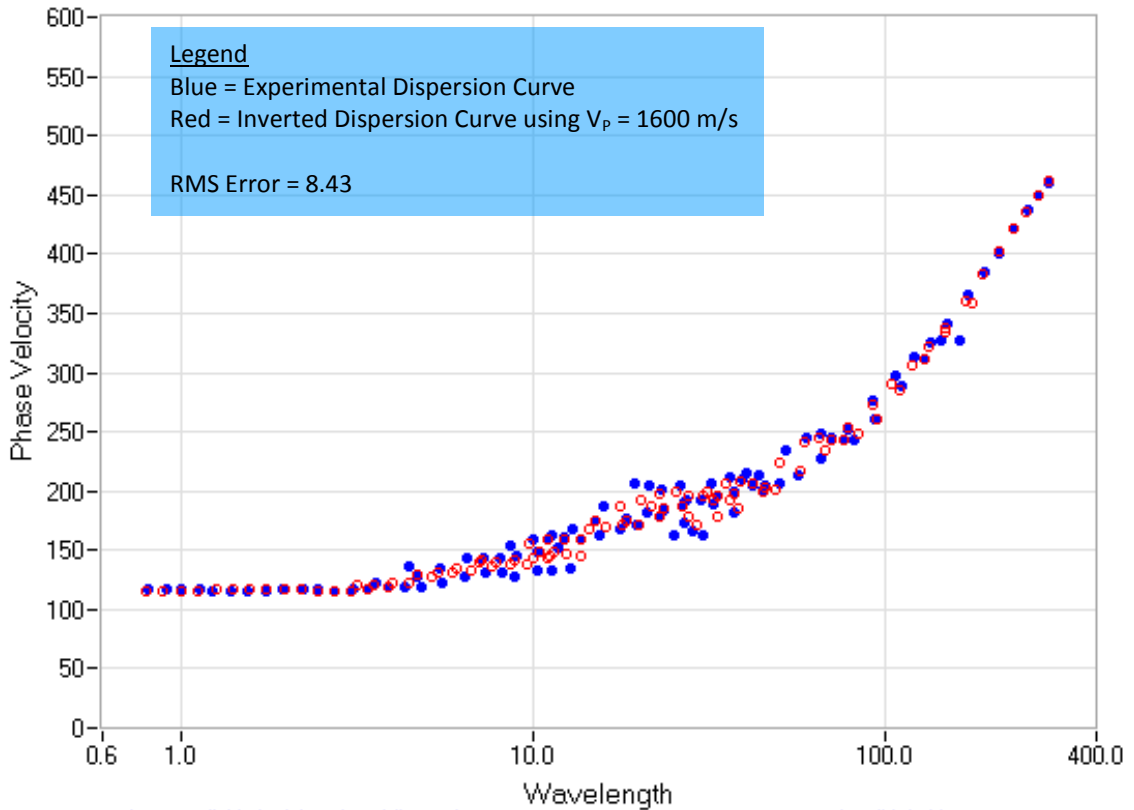


**Figure 5.5** Comparison of experimental and inverted dispersion curves for the "saturated" ( $V_p = 1600$  m/s) case

### 5.2.2 Results of Multi-channel Analyses with Real Data

Results of the multi-channel inversion study using real multi-channel data from the field site in the Mississippi Embayment are shown in Figure 5.6. The upper row of Figure 5.6 shows  $V_s$  profiles derived from experimental data collected with the “short” array, while the lower row corresponds to the “long” array (see Table 3.5 and Figure 3.34 for array definitions). Only the 2D plane wave inversion was used for this study. The quality-of-fit, in terms of root-mean-squared (RMS) error is plotted versus the value of Poisson’s ratio in Figure 5.7, where a separate curve is plotted for each of the two array configurations.

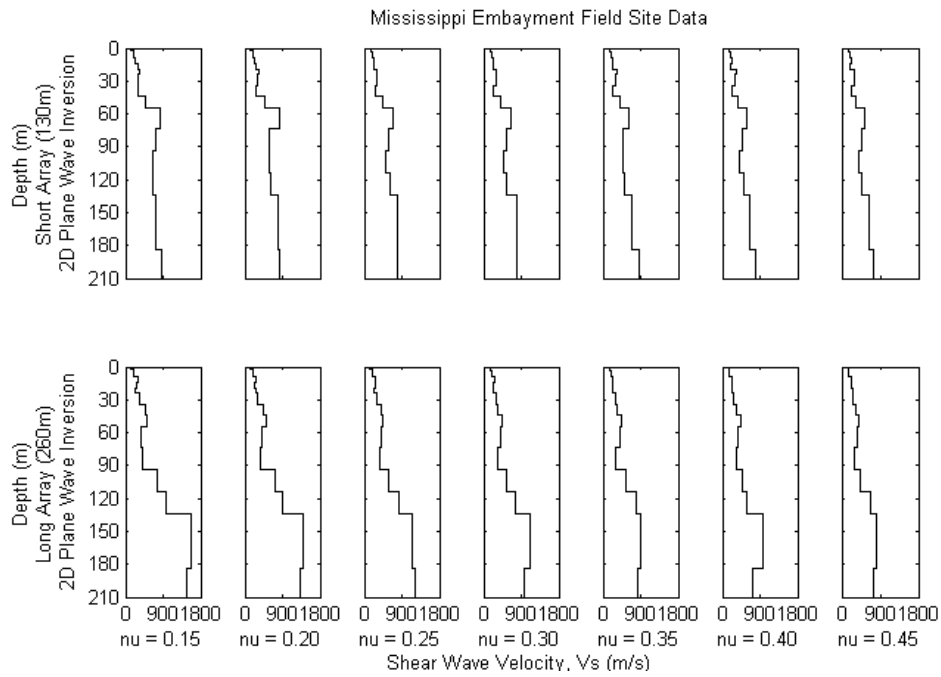


Figure 5.6  $V_s$  profiles inverted from real multi-channel data by 2D Global and 3D Global methods

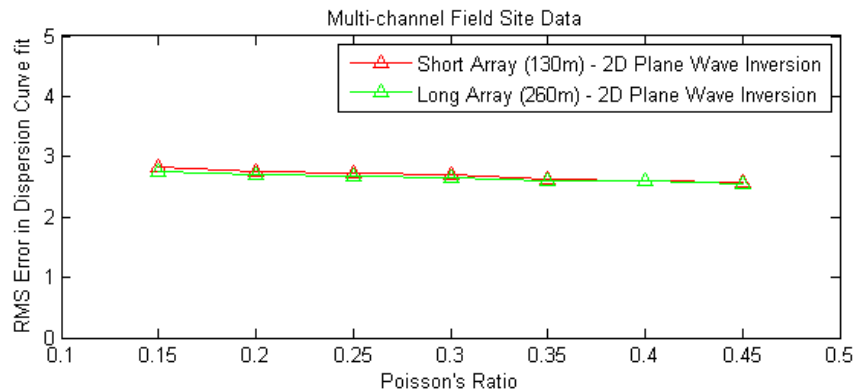


Figure 5.7 RMS error in fit between theoretical and experimental dispersion curves for real multi-channel data

### 5.3 Discussion of Analyses with Mississippi Embayment Data

The surface wave analysis results presented in Section 5.2 used the SASW-based method of inferring Poisson's ratio developed in Chapter 4 with real experimental data from the "MORT" site in the Mississippi Embayment (Section 3.7). The purpose of this study was to validate the "alternative SASW" method for potential use in practice, where data are often imperfect and the profile conditions are not known *a priori*. Both SASW and multi-channel arrays were used to collect experimental data at the MORT site as described in Section 3.7.1. SASW data were processed as described in Section 3.7.2, while the multi-channel data were processed as described in Section 3.4. Surface wave data from both approaches were inverted as described in Section 3.7.3. Results for SASW and multi-channel methods are compared to assess the extent to which current practice could be improved by using more of the near-field.

Key observations on the use of real data can be derived from the results of the SASW real data study (Section 5.2.1) and the multi-channel real data study (Section 5.2.2). Using conditions that are expected at the site, the alternative SASW method provided an estimate of the  $V_s$  profile that was essentially equivalent to that obtained in a previous study (Figure 5.3), where the traditional approach was used. This agrees well with the results of the simulation study, where the quality of the inverted profile was not affected by the level of near-field filtering, in cases where the array inversion approach was used (e.g. compare 3D array results for Figure 4.53, Figure 4.54, and Figure 4.55). In this particular case, profiling to a depth of 150 m with the traditional approach required a total array length of 640 m (Rosenblad et al. 2010), while the alternative SASW approach profiled to the same depth with an array length of 180m, with no apparent loss in profile quality. Results from multi-channel inversion performed using multiple values of Poisson's ratio (Figure 5.7) showed a generally flat trend of RMS error, indicating that the quality of the dispersion fit was not greatly affected by the selection of the correct value Poisson's ratio. This result is generally consistent with the findings of the simulation study (e.g. Figure 4.60b). Results from the SASW analysis performed using multiple values of Poisson's ratio (Figure 5.4) did not show the expected trend of RMS error values when the "true" Poisson's ratio value was used. Although the saturated case did show the lowest value of RMS error, it was only slightly lower and the trend was not consistent with the results of the simulation study (Figure 4.56c).

The higher RMS errors at Poisson's ratio values of 0.40 and 0.45 in Figure 5.4 could be explained by an unrealistic estimate of P-wave velocity ( $V_p$ ) produced by the forward model used in WinSASW. Given an assumed value of P-wave velocity, the forward model calculates Poisson's ratio and, given an assumed value of Poisson's ratio, the model calculates P-wave velocity. For the fully saturated case, the P-wave velocity was set to 1600 m/s for all but the top two layers, where a Poisson's ratio of 0.25 was applied to simulate an unsaturated zone above the water table. In all other layers, the exact value of Poisson's ratio would be calculated in the inversion process. For the cases where Poisson's ratio was specified, however, the value was set for the entire profile and the inversion process computed the P-wave velocity. For deep profiles and large values of Poisson's ratio, such as were present here, the forward model yields  $V_p$  values far in excess of 1600 m/s, which produces a slightly higher RMS error. Poisson's ratio is not typically constant with depth.

Two key conclusions were derived from this study involving experimental data from a real field site. First, the results of this study validated the simulation study finding that SASW analysis produces similar quality profiles for all filtering criteria, when the array inversion is used. Unfortunately, the results of this study did *not* conclusively validate the practical application of the (Poisson's ratio) inference technique developed in Chapter 4. Second, the multi-channel results for this study agreed well with the results of the simulation study, indicating that the multi-channel approach is largely insensitive to Poisson's ratio. Third, great care must be taken to ensure that reasonable values of all profile parameters are maintained throughout the inversion process, especially when inverting profiles with Poisson's ratio values close to 0.50. Unrealistic P-wave velocities, greater than the P-wave velocity of water (i.e.  $V_p = 1600$  m/s), may develop when Poisson's ratio values are set to fixed values, especially so in deeper layers.

Therefore, even though the results of this study did not conclusively validate the simulation study, they do provide a starting point for future research. The simulation study clearly demonstrated the effectiveness of the alternative SASW approach in inferring Poisson's ratio, so it would be unwise to discard the approach based on the uncertain results from this one site. Future research should focus on collecting and processing data from several well-characterized sites, to examine the practicality of inferring Poisson's ratio for a wide range of subsurface conditions. This work should also include sites having lower "true" values of Poisson's ratio to validate the inference approach for those conditions.

## 6 SUMMARY AND CONCLUSIONS

### 6.1 Summary

The primary objective of this study was to investigate potential benefits of including the near-field in surface wave data collection and analysis. First, it was hypothesized that limiting criteria currently used to remove near-field effects from surface wave measurements could be greatly reduced without affecting the quality of surface wave results – if a theoretical model incorporating the near-field was used. Second, it was hypothesized that the near-field portion of the dispersion curve would be more sensitive to changes in additional profile parameters than the far-field portion used in current practice. Three different studies were performed for this research, including: (1) a preliminary sensitivity study to identify which profile parameters are most sensitive to the near-field, (2) surface wave analysis with simulated experimental data, to assess both profile recovery and the possibility of inferring an additional profile parameter (i.e. Poisson's ratio), and (3) surface wave analysis with real data to validate the profile recovery and parametric inference techniques of the simulated data study with real data. Experimental data collected/simulated from both the spectral-analysis-of-surface-waves (SASW) method and multi-channel surface wave methods, but the primary focus was the SASW method.

All analyses for this research were performed using the commercial software program WinSASW, which was developed by Joh (1996). This program was used to perform most of the data processing and inversion analyses for this research. The preliminary sensitivity study made extensive use of the forward modeling module in WinSASW. For the surface wave analyses involving simulated data, simulated experimental data were generated in a separate program, FitSASW, and imported into WinSASW for analysis. For the surface wave analyses involving real data, data collected as part of a previous study at a field site near Mooring, Tennessee in the Mississippi Embayment were processed and analyzed using WinSASW. Multi-channel data processed by the frequency-domain beamformer (FDBF) approach were also inverted using WinSASW.

Results of the preliminary sensitivity study are presented as dispersion curves, in terms of both phase velocity versus frequency and percent difference in phase velocity (relative to a baseline curve) versus frequency. Results of the surface wave analysis studies are presented as

shear wave velocity ( $V_s$ ) profiles (i.e.  $V_s$  versus depth), layer-specific percent error plots for inverted versus “true” profiles, and quality-of-fit plots in terms of the root-mean-squared (RMS) error between theoretical and experimental dispersion curves versus Poisson’s ratio.

## 6.2 Conclusions

The principal conclusions drawn from this research are summarized below:

- (1) An alternative approach to SASW using a single receiver spacing and more of the near-field in the data collection and processing was considered in the preliminary sensitivity study. It was found that this approach yielded comparable results to those of the traditional SASW approach (which, in this case, used four receiver spacings to cover the same range of wavelengths). Although this alternative approach produced dispersion curves with significantly lower phase velocities than the traditional SASW method, the two methods showed similar sensitivity to changes in profile parameters.
- (2) The near-field portion of the dispersion curve has a distinct sensitivity to changes in the value of Poisson’s ratio, in terms of both the velocity values and the shape of the dispersion curve. All three of the simple profiles considered in the preliminary sensitivity study (i.e. uniform, “soft-over-stiff”, and linear) demonstrated similar levels of sensitivity to changes in the velocity profile, as were observed using the far-field portion of the dispersion curve. Sensitivity was observed for changes at layer transitions, but the sensitivity was small in both of the cases studied.
- (3) The “3D Array” approach to inversion analysis yields a superior estimate of the  $V_s$  profile when analyzing SASW data. Under the same conditions, the “2D Global” and “3D Global” inversion approaches produced  $V_s$  profile estimates that decrease in quality (as measured by comparing to the known profile) with depth, which is primarily due to the presence of near-field effects in the experimental data, even when very restrictive filtering criteria are applied.
- (4) If the 3D Array approach is used, much less restrictive near-field criteria can be used without impacting the quality of the  $V_s$  profile estimate. This allows for the use of much shorter arrays and smaller sources. The simulations performed in this study showed good results using an array that was one-quarter the size of that used in a typical SASW analysis.

- (5) The Poisson's ratio study (with simulated data) demonstrated that it is possible to correctly infer the in-situ value of Poisson's ratio by successive applications of the 3D Array inversion. With this approach, the value of Poisson's ratio producing the lowest RMS error (in the fit between theoretical and experimental dispersion curves) is consistent with the correct value – which also corresponds to the best  $V_s$  profile estimate. In contrast, the 2D and 3D Global inversions show no apparent sensitivity to the value of Poisson's ratio. Results from the study using real data did not show this same definitive trend.
- (6) Throughout this research, four different SASW filtering criteria (360°, 180°, 90°, and 45°) were used to produce an experimental dispersion curve from either real or simulated experimental data. The filtering criteria ranged from very restrictive criteria (i.e. 360° and 180°) originally developed to limit the near-field to the very inclusive criteria (i.e. 90° and 45°) allowing more of the near-field, as considered in this research. The surface wave analyses performed in this study were largely unaffected by the filtering criterion selection, except that the criteria allowing more of the near-field produced better results overall.
- (7) The  $V_s$  profiles produced from multi-channel data were of higher quality than those produced from SASW data when using the 2D global inversion. Even so, the  $V_s$  profiles produced from SASW data using the 3D Array inversion produced superior predictions of the  $V_s$  profile as compared to multi-channel analysis. Systematic errors were evident in the multi-channel data (especially in half-space velocity), likely owing to the model incompatibility issue, where the model without near-field contributions is used to invert data with near-field effects.

### 6.3 Significance and Future Research

This study has demonstrated the potential benefits of including the near-field in active-source surface wave measurements. It has been shown, first of all, that the near-field need not be completely avoided, at least not to the extent suggested by current practice, if the appropriate model is used in the theoretical analysis. Moreover, it has also been shown that near-field effects in experimental data can even be leveraged to good effect with the right inversion model (i.e. 3D Array). Furthermore, it is also feasible to infer the in-situ value of certain profile parameters (i.e. Poisson's ratio) by successive applications of an inversion approach that can

accurately account for near-field effects (i.e. 3D Array). This was clearly demonstrated using simulated data, but not with the real experimental data from the single site examined in this thesis. It is hoped that the conclusion of this study is only the beginning of several opportunities for future research.

The real experimental data used in this study came from a single site with a shallow groundwater table (i.e. mostly saturated). Given the uncertain results from this one site, future research should focus on collecting and processing data from several well-characterized sites including sites having lower values of Poisson's ratio to validate the approach to inferring Poisson's ratio for those conditions. Secondly, this study focused on "simple" sites, so future work should extend the simulated data study to include complex and "stiff-over-soft" profile conditions where higher mode contributions may be significant. Instead of seeking a minimum offset distance to avoid the near-field, future research can quantify the minimum extent to which filtering criteria can be reduced (i.e. where it is no longer sensitive to the deep soil properties). If filtering criteria are pushed too far (too close to the source), the receivers would be measuring only the dynamic "deflection bowl" produced by the source (e.g. falling weight deflectometer testing of pavements).

Perhaps the greatest contribution that future research could derive from this work would be the development of an SASW inversion program that can simultaneously invert for both the shear wave velocity profile and the Poisson's ratio profile, essentially automating the process of successive 3D array inversions. The results from this study suggest that this may be possible. Another area that holds promise for future research, as technology continues to advance and computers become more powerful, is the development of a "3D Array inversion" for multi-channel methods – perhaps an inversion that can also simultaneously invert for both shear wave velocity and Poisson's ratio. Current multi-channel processing techniques can produce a three-dimensional "dispersion image" or "dispersion surface" from multi-channel experimental data, so the approach would be to develop a theoretical model (based on the "Green's Function" principle of the 3D array approach) and resulting dispersion curve which includes near-field effect that can be fit to the experimental curve. Such a solution may be very computationally demanding. Until technology develops to the point where this is a practical solution for geotechnical projects, research could focus on the development of "hybrid" approaches, combining the best aspects of both SASW and multi-channel methods (i.e. SASW with four receivers, multi-channel with 8 receivers, etc.).

## **Appendix**

The appendix documents the results of the preliminary sensitivity study for all profile conditions studied. Dispersion curves are presented in terms of both phase velocity versus frequency and percent difference in phase velocity (from the baseline profile) versus frequency.

### A. Variations in Halfspace (i.e. "Layer 2") Shear Wave Velocity

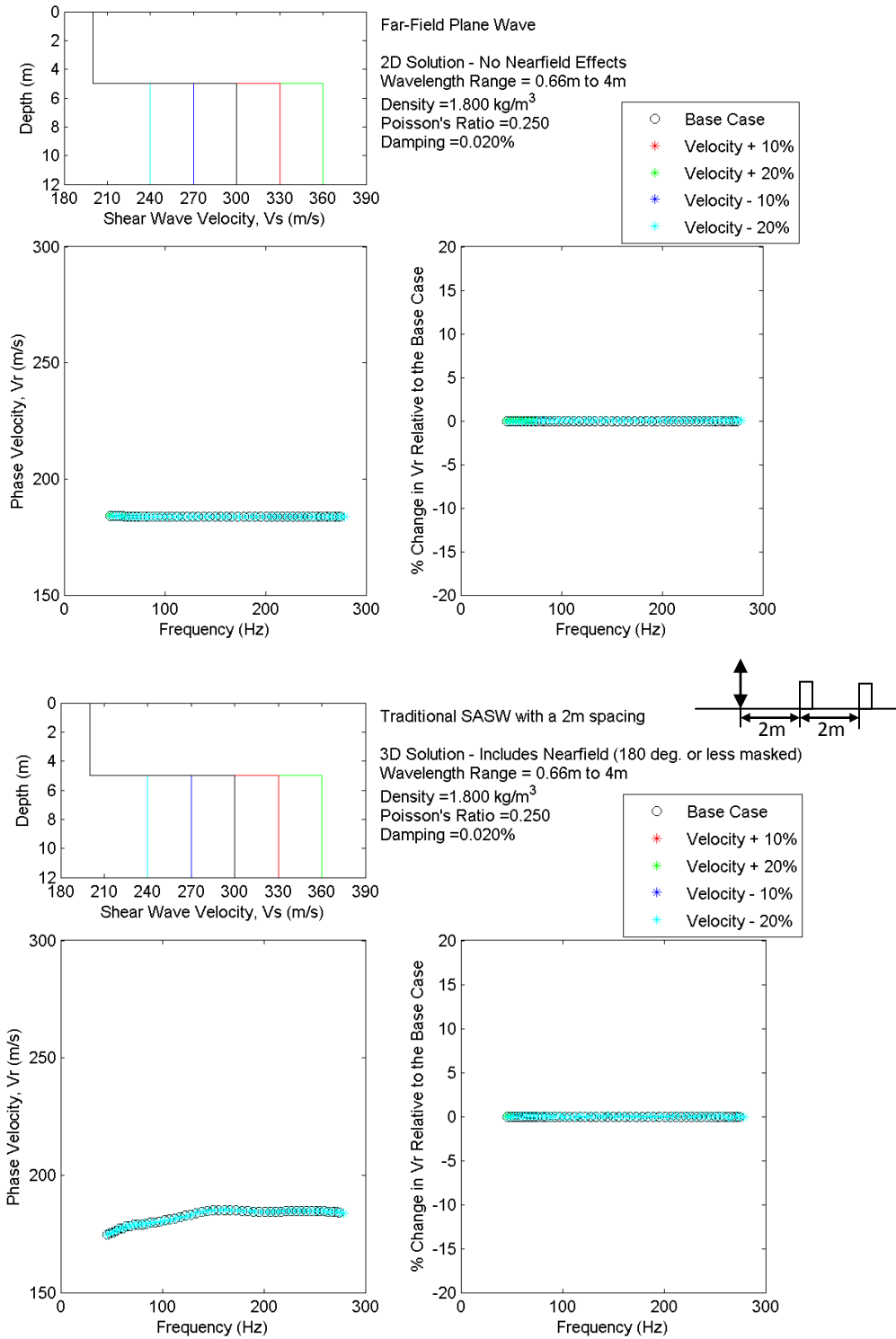


**Figure A.1** Sensitivity study results for a "soft-over-stiff" profile with a variable lower layer  $V_s$ , comparing results from the 2D solution (at top) and 3D solution (at bottom) for a wavelength range of 1/3m to 4m.

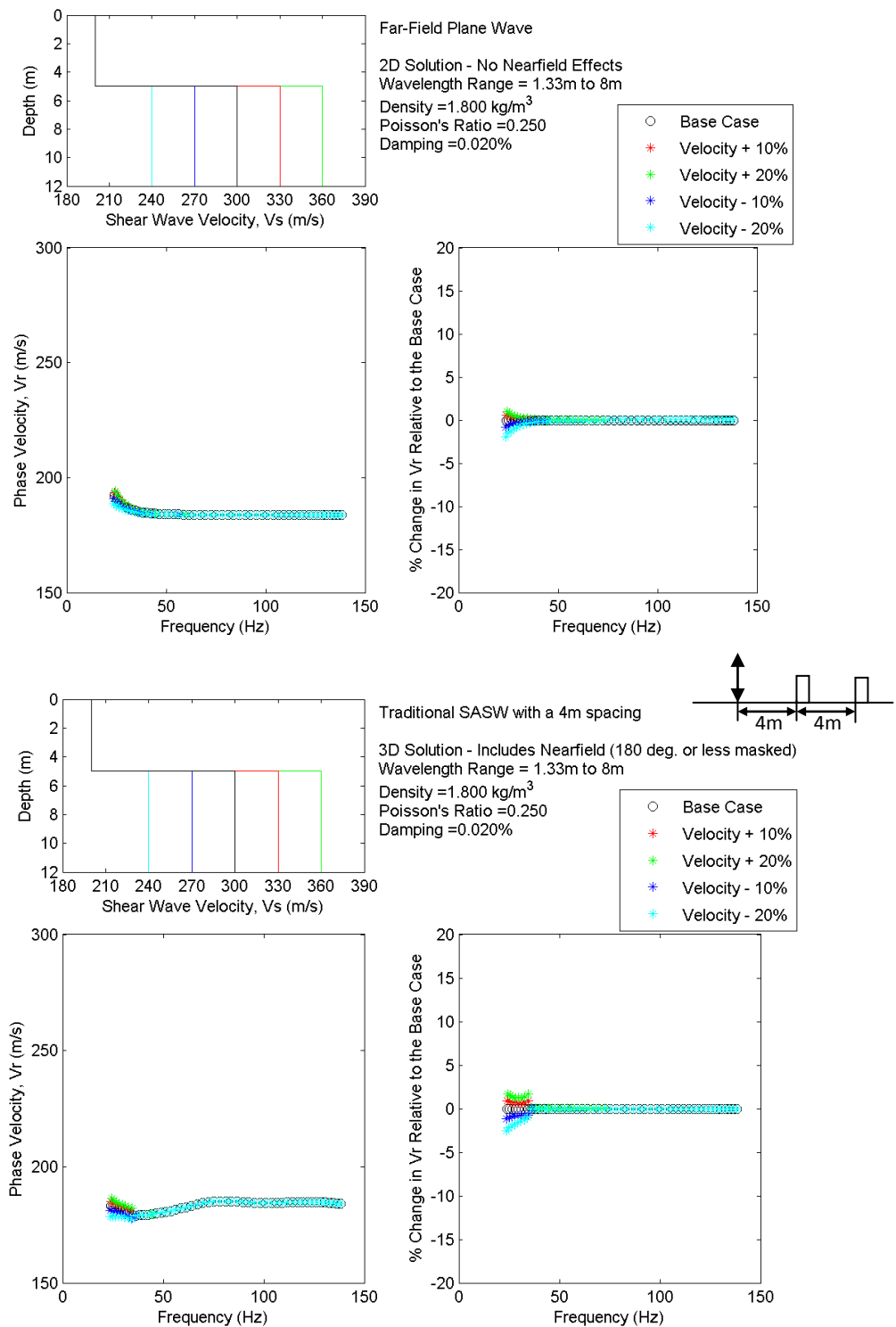


**Figure A.2** Sensitivity study results for a “soft-over-stiff” profile with a variable lower layer  $V_s$ , comparing results from the 2D solution (at top) and 3D solution (at bottom) for a wavelength range of 4/3m to 8m.

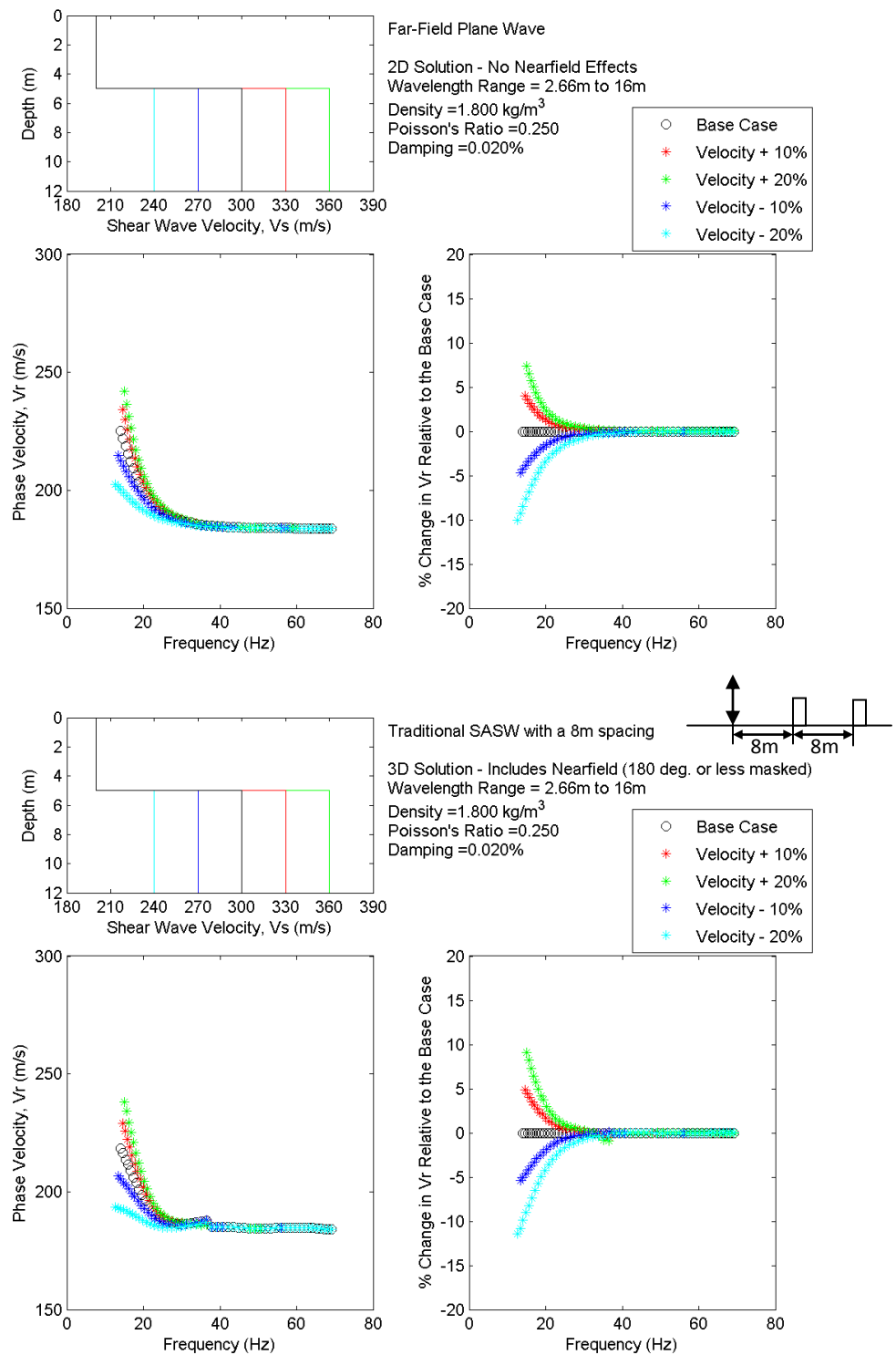


**Figure A.3** Sensitivity study results for a “soft-over-stiff” profile with a variable lower layer  $V_s$ , comparing results from the 2D solution (at top) and 3D solution (at bottom) for a wavelength range of 8/3m to 16m.

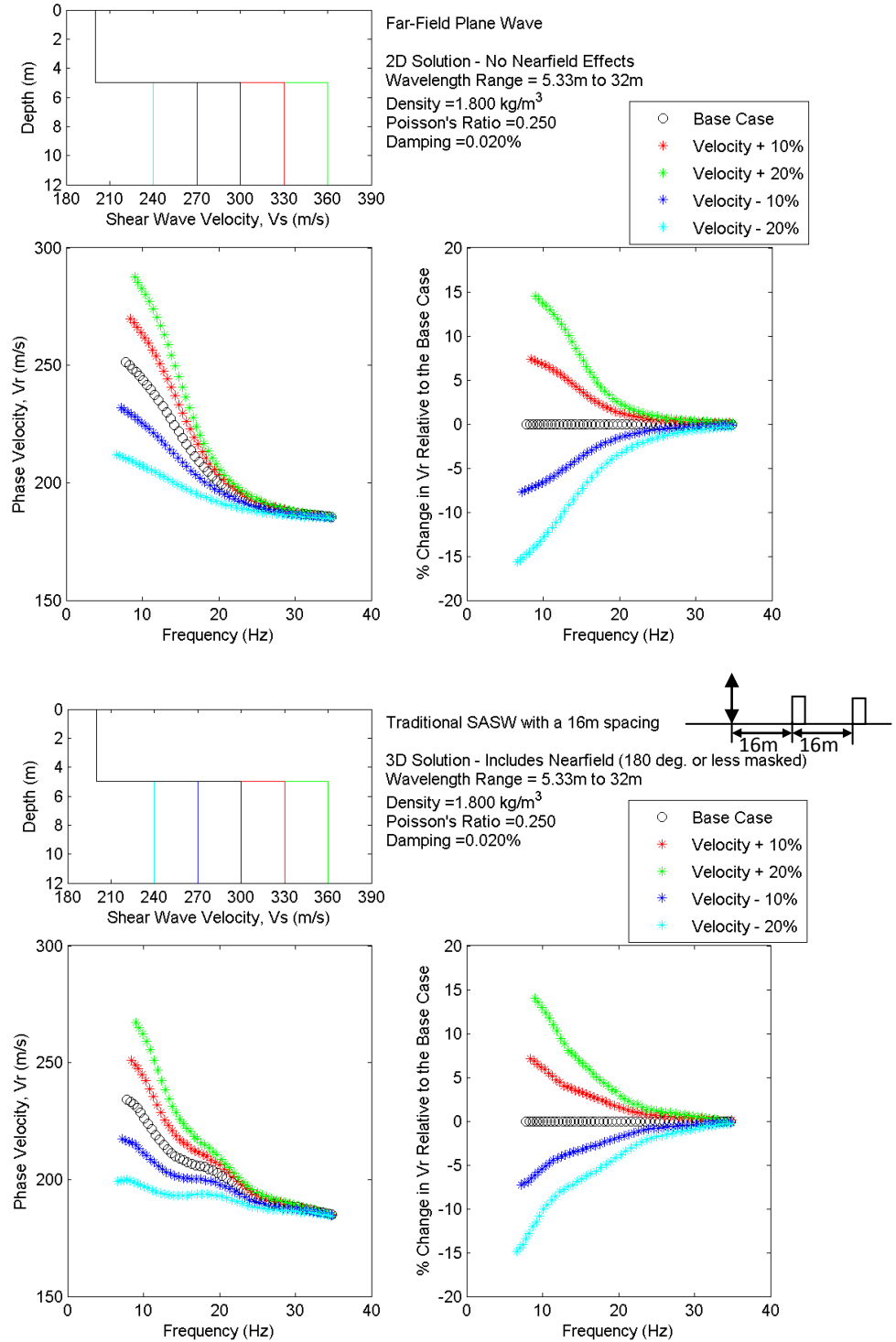


**Figure A.4** Sensitivity study results for a “soft-over-stiff” profile with a variable lower layer  $V_s$ , comparing results from the 2D solution (at top) and 3D solution (at bottom) for a wavelength range of 16/3m to 32m.

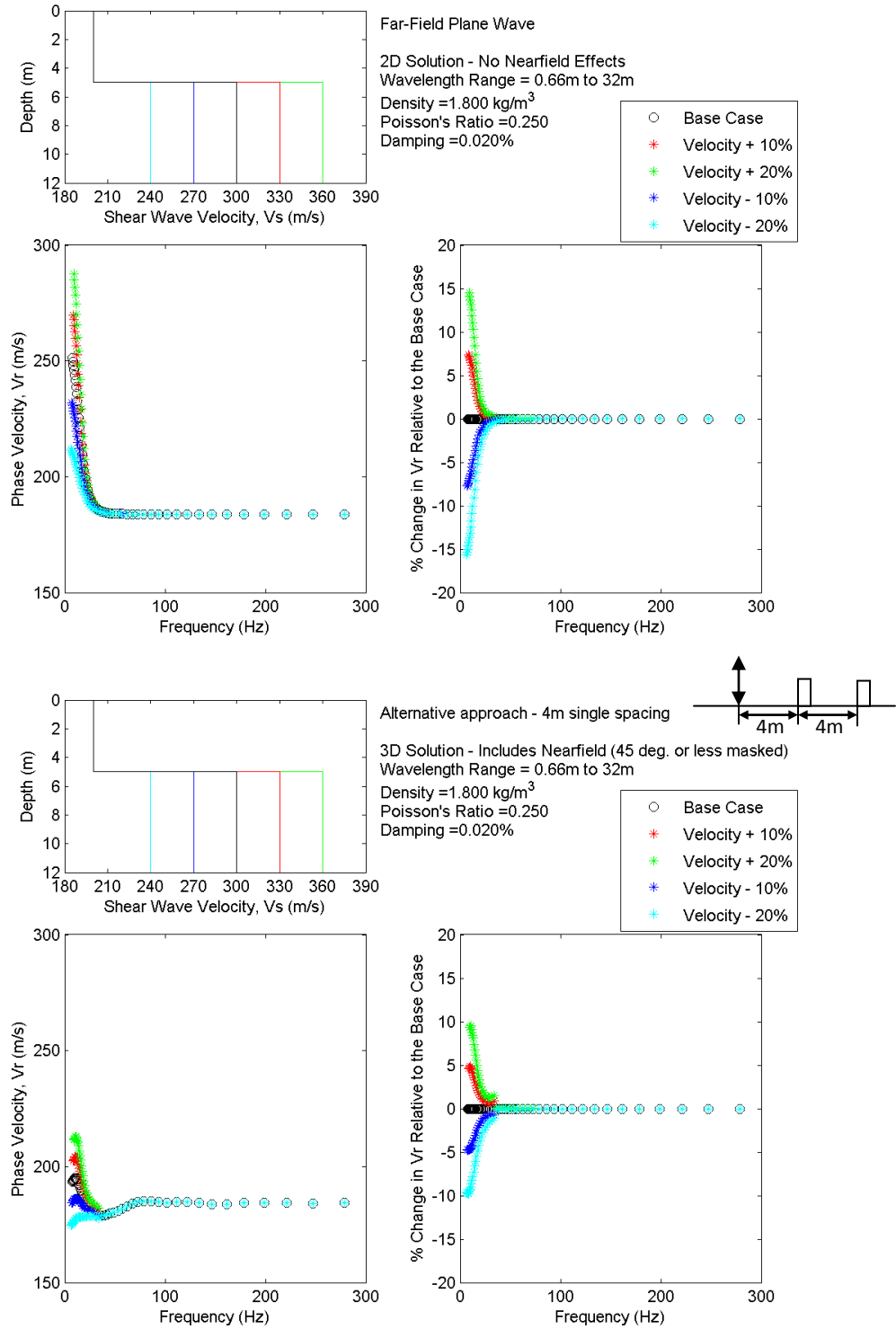


**Figure A.5** Sensitivity study results for a “soft-over-stiff” profile with a variable lower layer  $V_s$ , comparing results from the 2D solution (at top) and 3D solution (at bottom) for a wavelength range of 1/3m to 32m.

### B. Variations in the Shear Wave Velocity Gradient for Linear Profiles

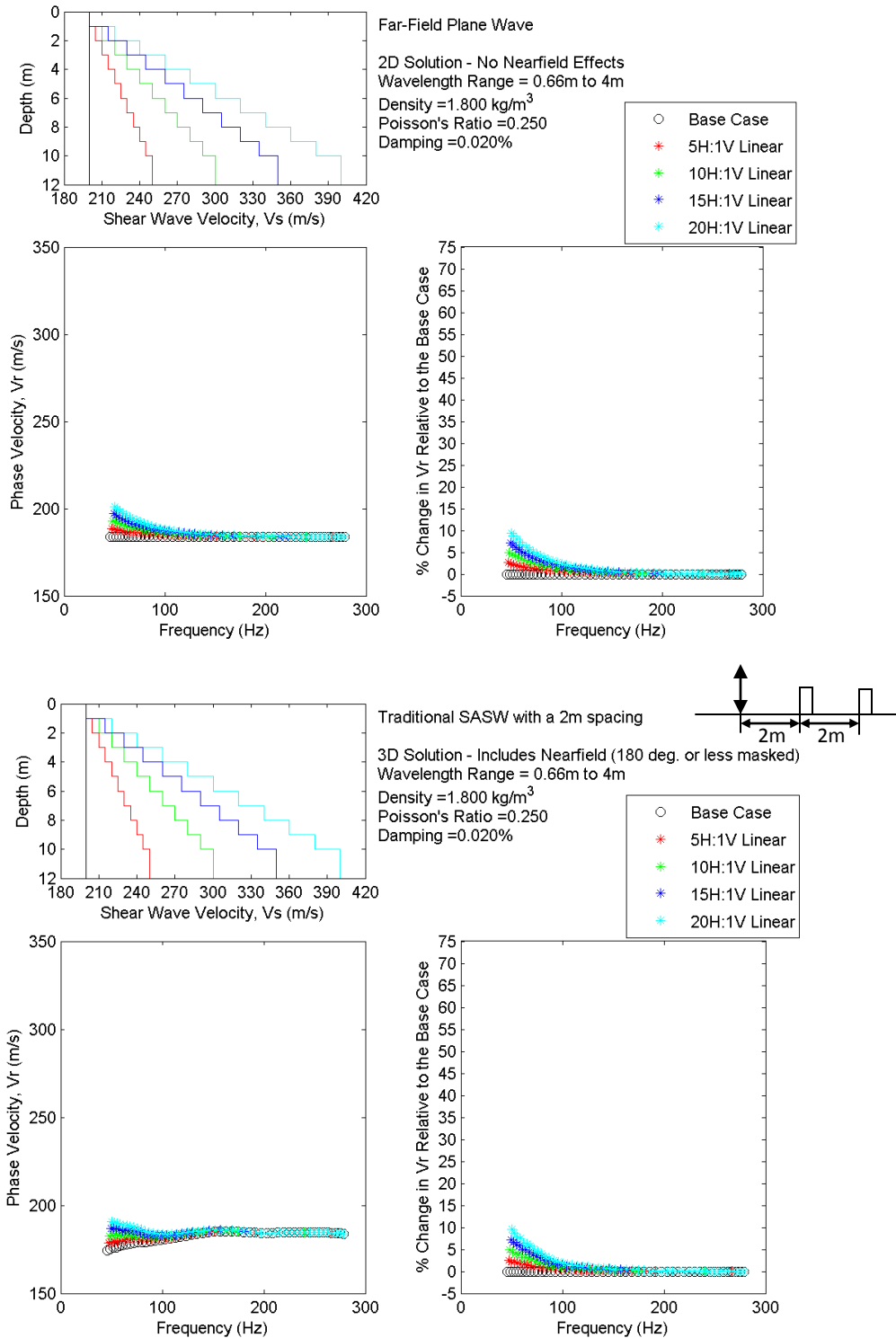


**Figure B.1** Sensitivity study results for a variable  $V_s$  profile transition gradient, comparing results from the 2D solution (at top) and 3D solution (at bottom) for a wavelength range of 1/3m to 4m.

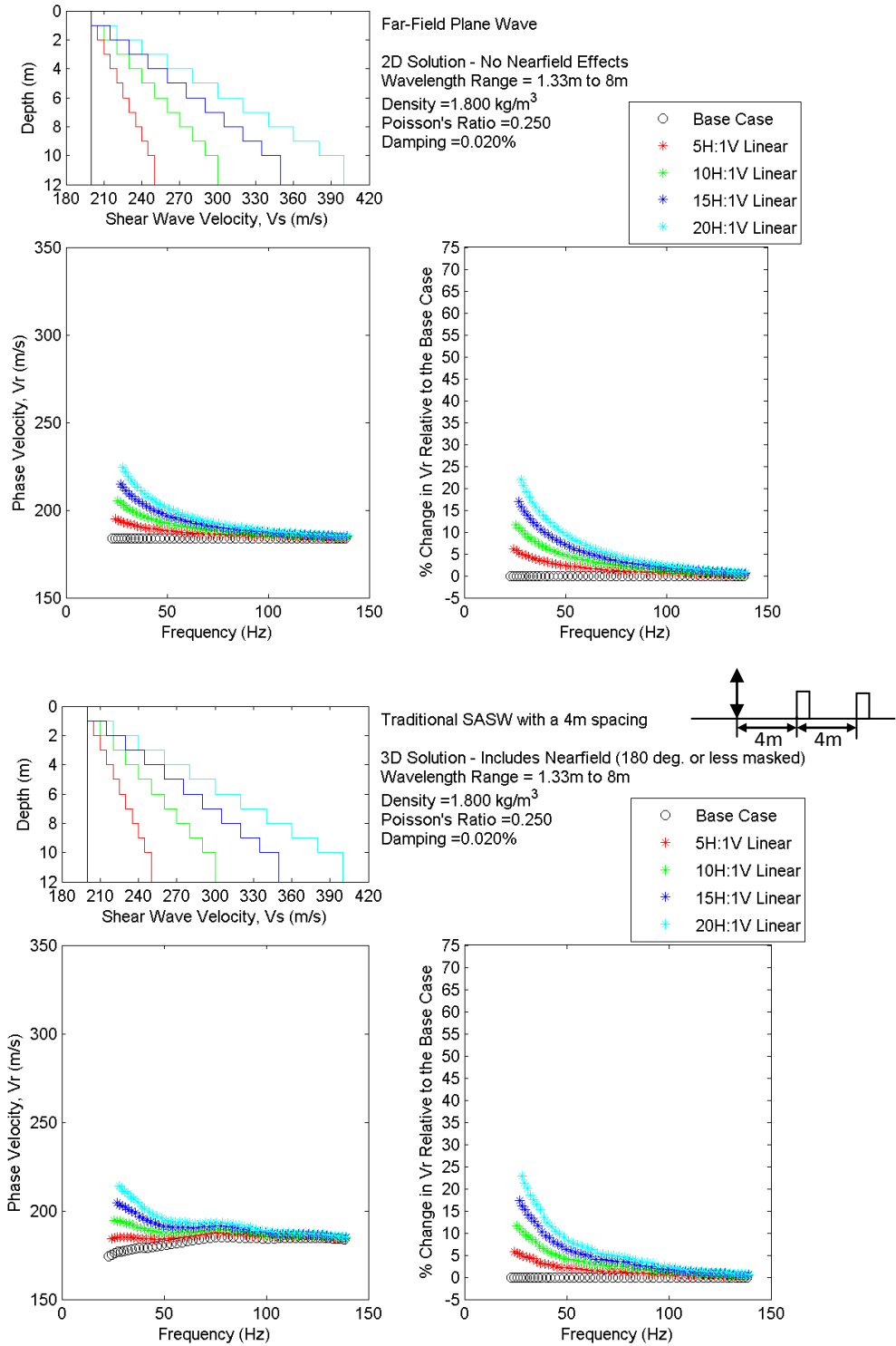


**Figure B.2** Sensitivity study results for a variable  $V_s$  profile transition gradient, comparing results from the 2D solution (at top) and 3D solution (at bottom) for a wavelength range of 4/3m to 8m.

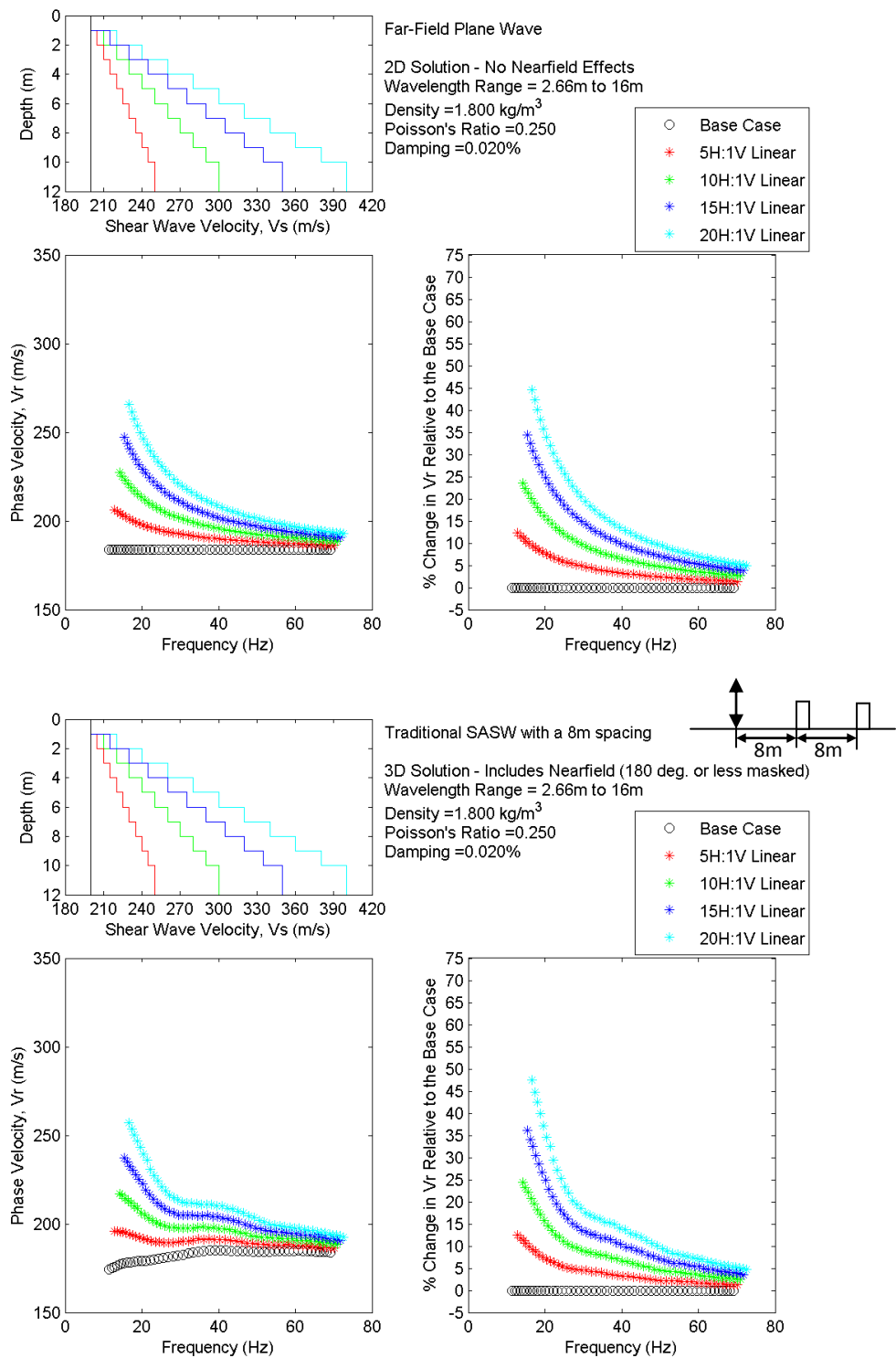


**Figure B.3** Sensitivity study results for a variable  $V_s$  profile transition gradient, comparing results from the 2D solution (at top) and 3D solution (at bottom) for a wavelength range of 8/3m to 16m.

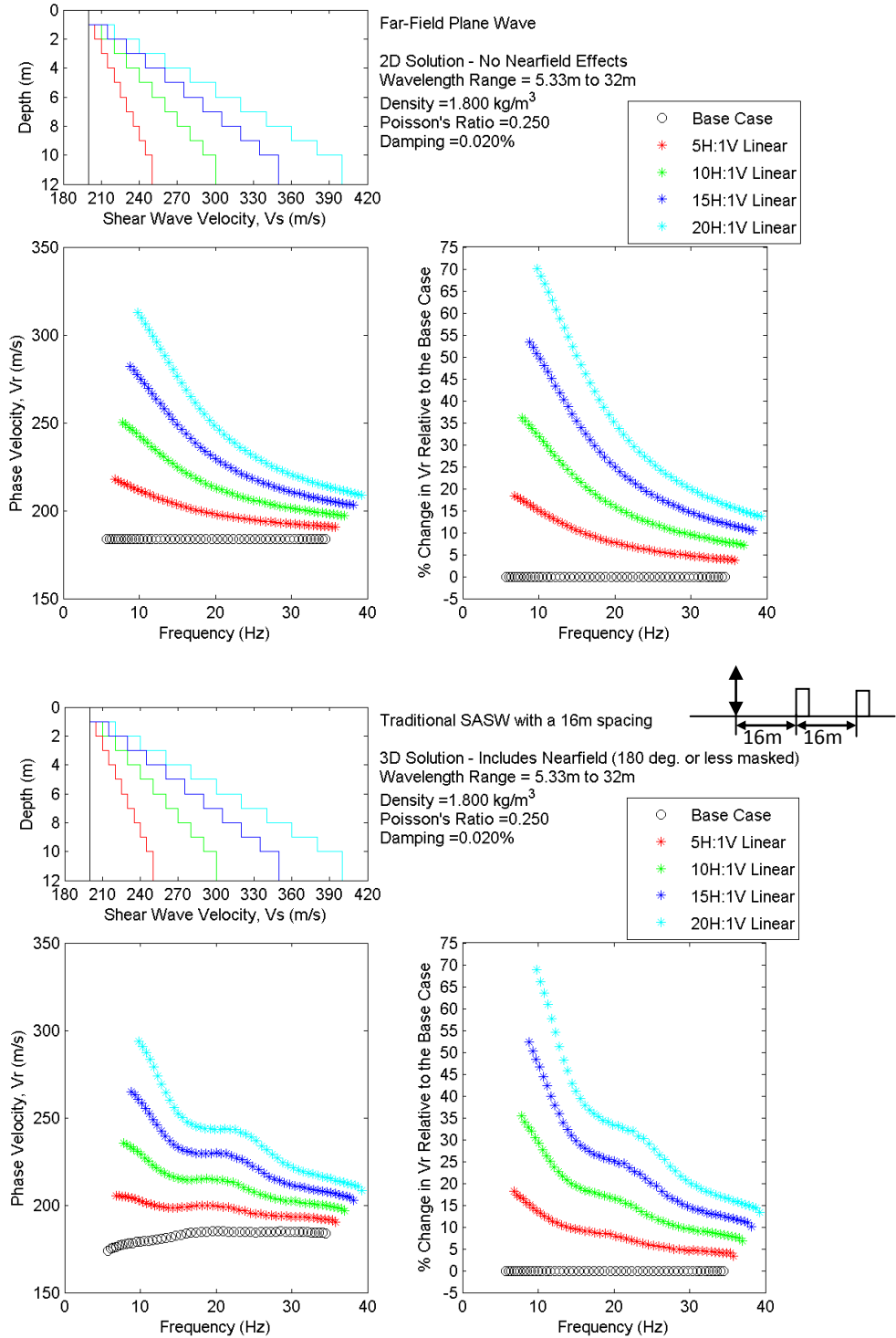


**Figure B.4** Sensitivity study results for a variable  $V_s$  profile transition gradient, comparing results from the 2D solution (at top) and 3D solution (at bottom) for a wavelength range of 16/3m to 32m.

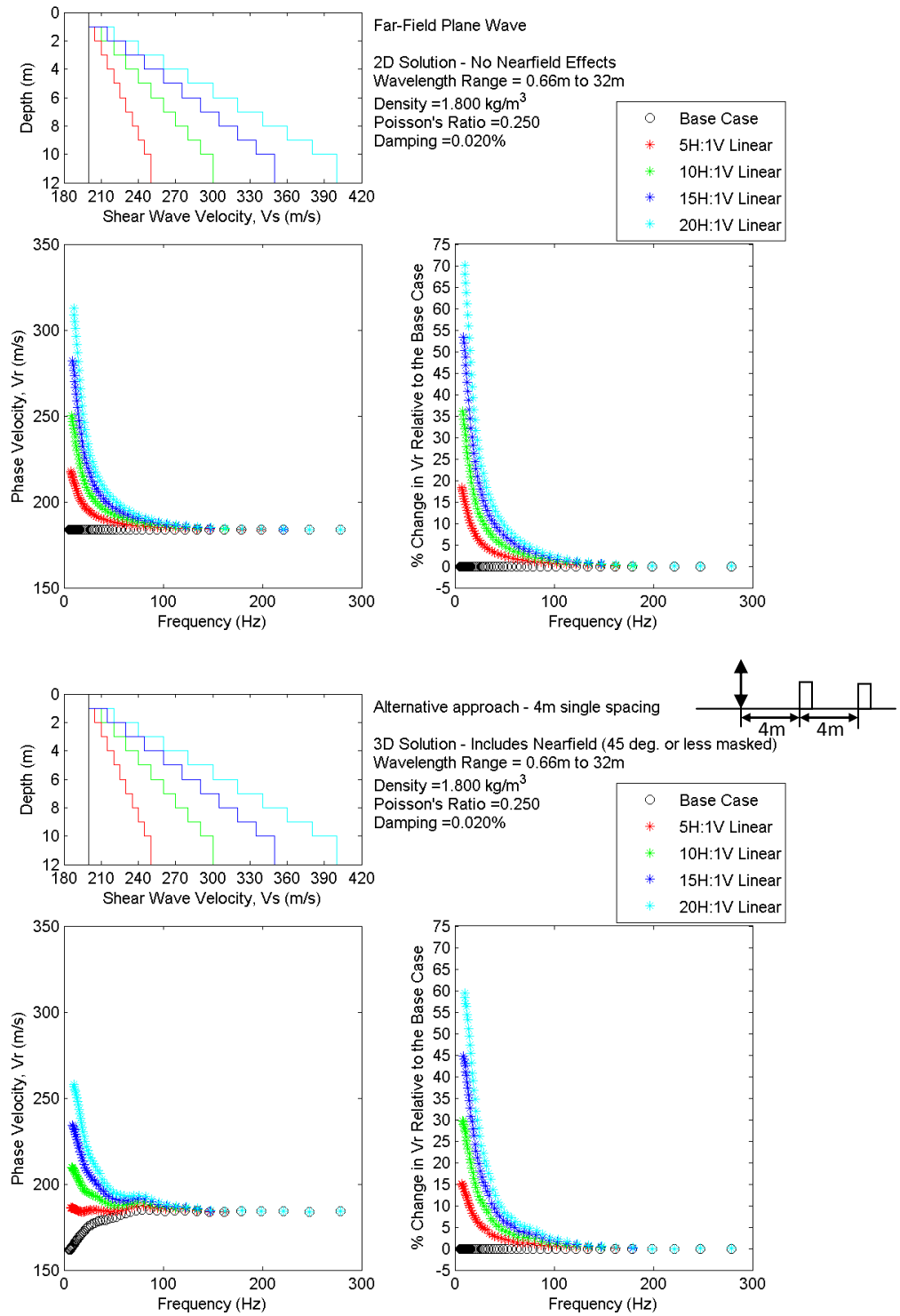


**Figure B.5** Sensitivity study results for a variable  $V_s$  profile transition gradient, comparing results from the 2D solution (at top) and 3D solution (at bottom) for a wavelength range of 1/3m to 32m.

### C. Variations in Halfspace (i.e. “Layer 2”) Depth

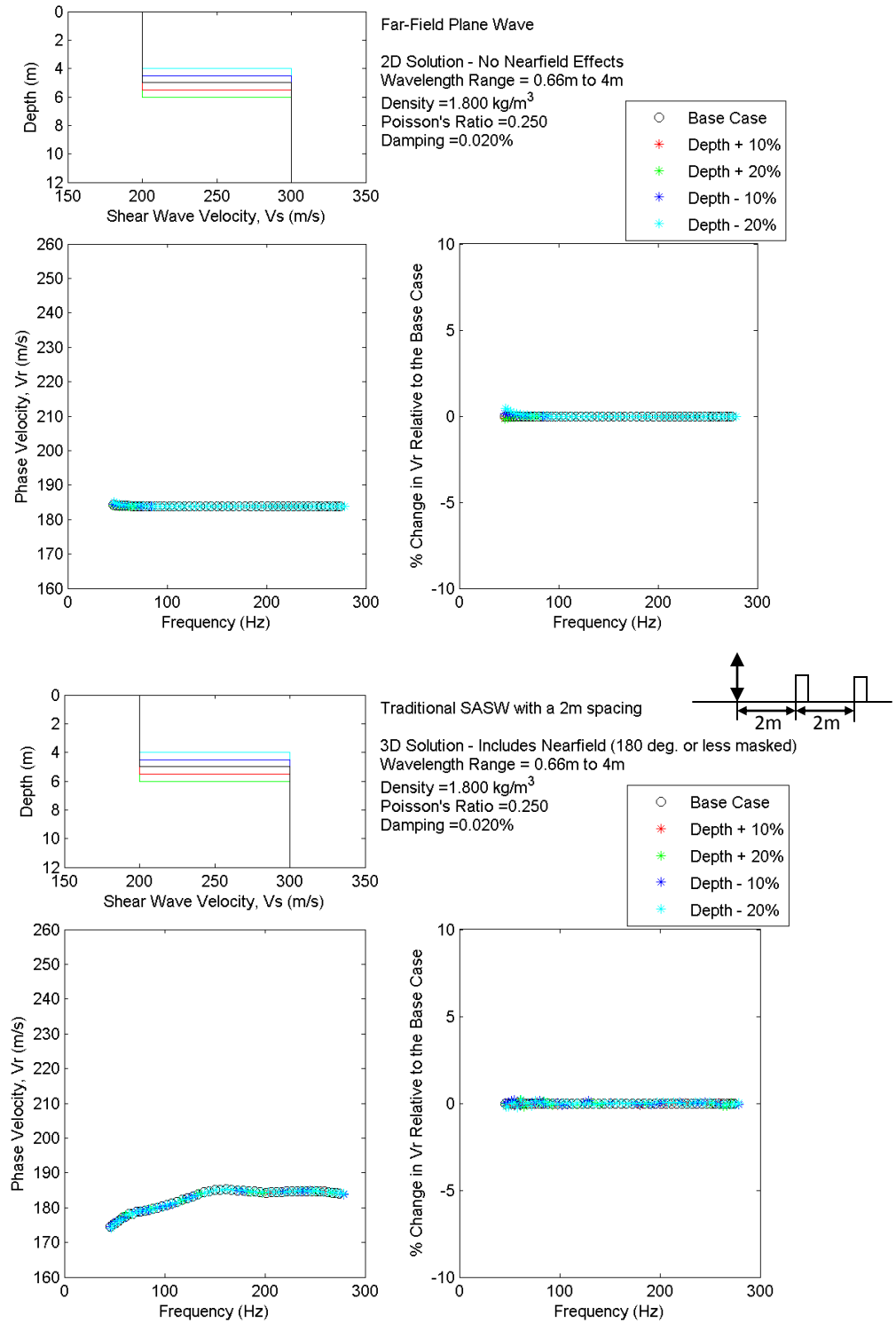


**Figure C.1** Sensitivity study results for a “soft-over-stiff” profile with a variable lower layer depth, comparing results from the 2D solution (at top) and 3D solution (at bottom) for a wavelength range of 1/3m to 4m.

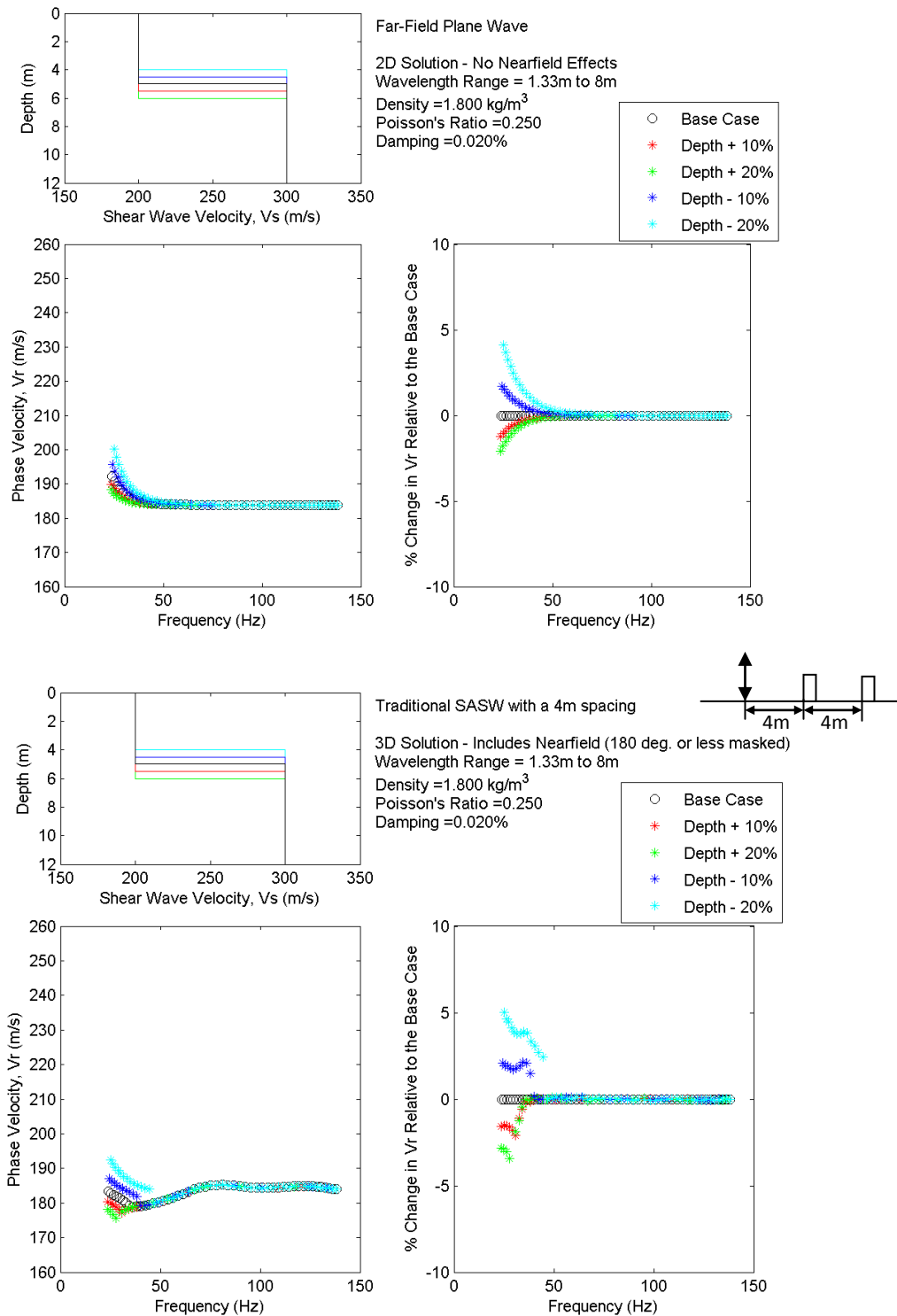


**Figure C.2** Sensitivity study results for a “soft-over-stiff” profile with a variable lower layer depth, comparing results from the 2D solution (at top) and 3D solution (at bottom) for a wavelength range of 4/3m to 8m.

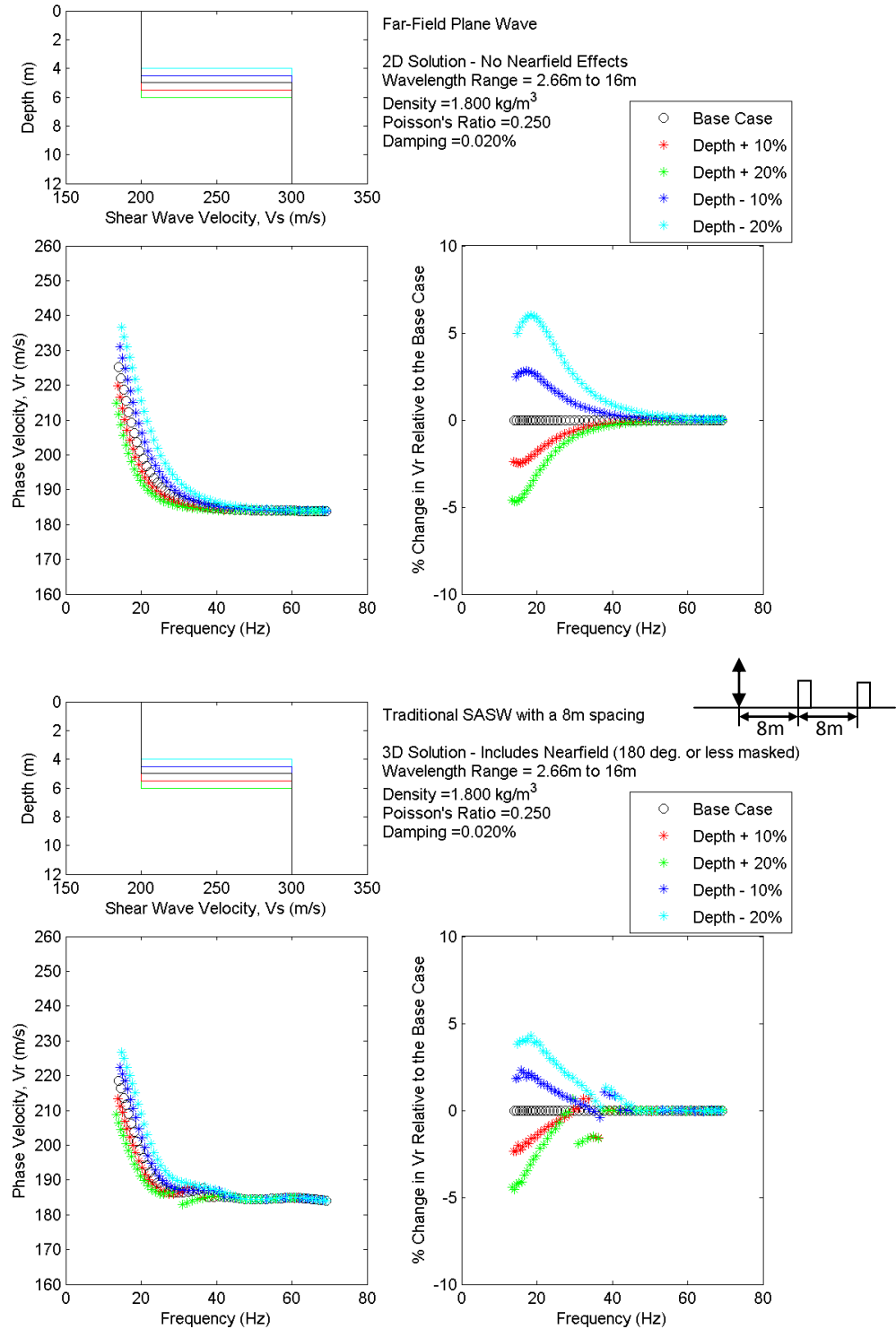


**Figure C.3** Sensitivity study results for a “soft-over-stiff” profile with a variable lower layer depth, comparing results from the 2D solution (at top) and 3D solution (at bottom) for a wavelength range of 8/3m to 16m.

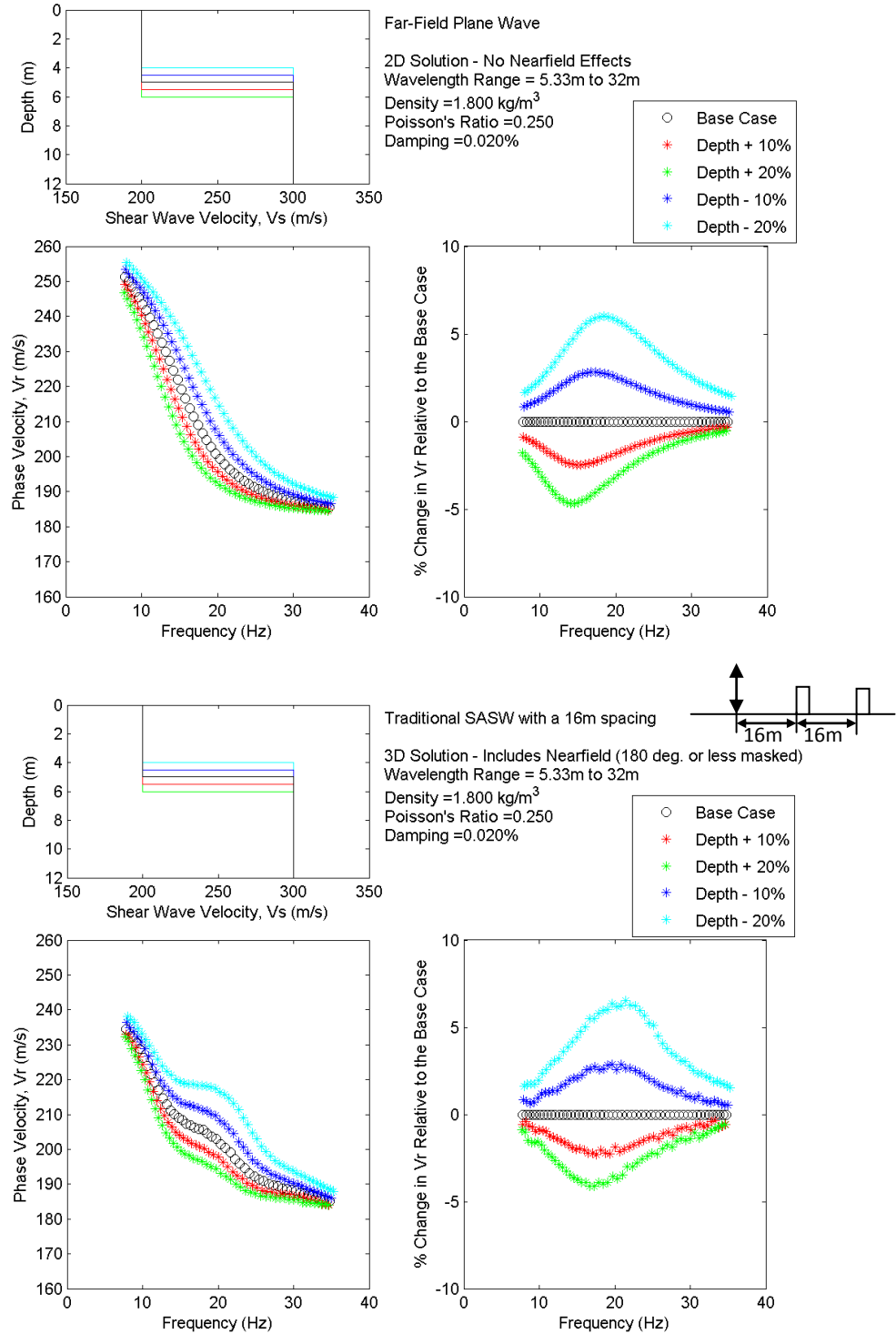


**Figure C.4** Sensitivity study results for a “soft-over-stiff” profile with a variable lower layer depth, comparing results from the 2D solution (at top) and 3D solution (at bottom) for a wavelength range of 16/3m to 32m.

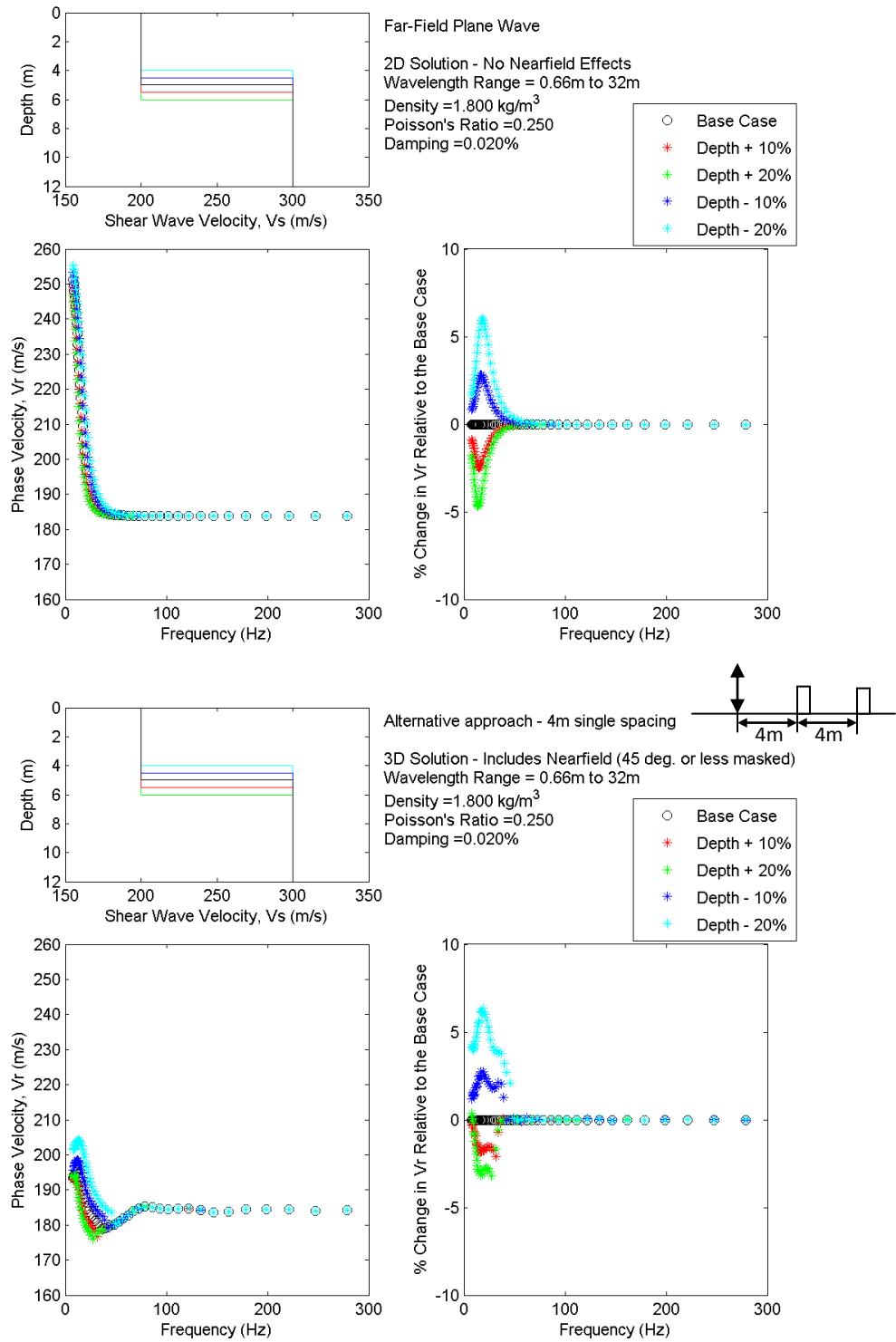


**Figure C.5** Sensitivity study results for a “soft-over-stiff” profile with a variable lower layer depth, comparing results from the 2D solution (at top) and 3D solution (at bottom) for a wavelength range of 1/3m to 32m.

### D. Variations in the Layer Transition Gradient

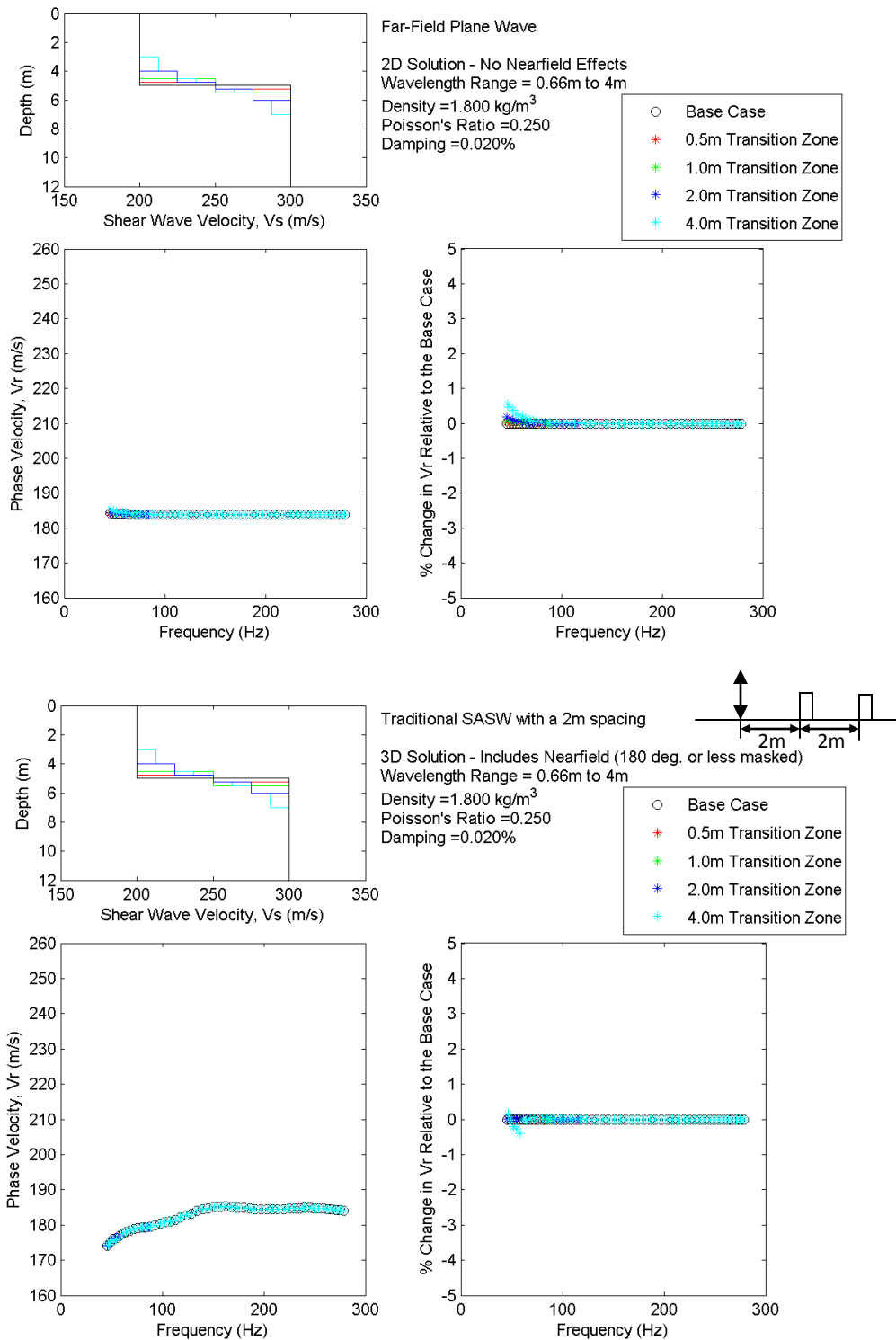


**Figure D.1** Sensitivity study results for a “soft-over-stiff” profile with a variable layer transition gradient, comparing results from the 2D solution (at top) and 3D solution (at bottom) for a wavelength range of 1/3m to 4m.

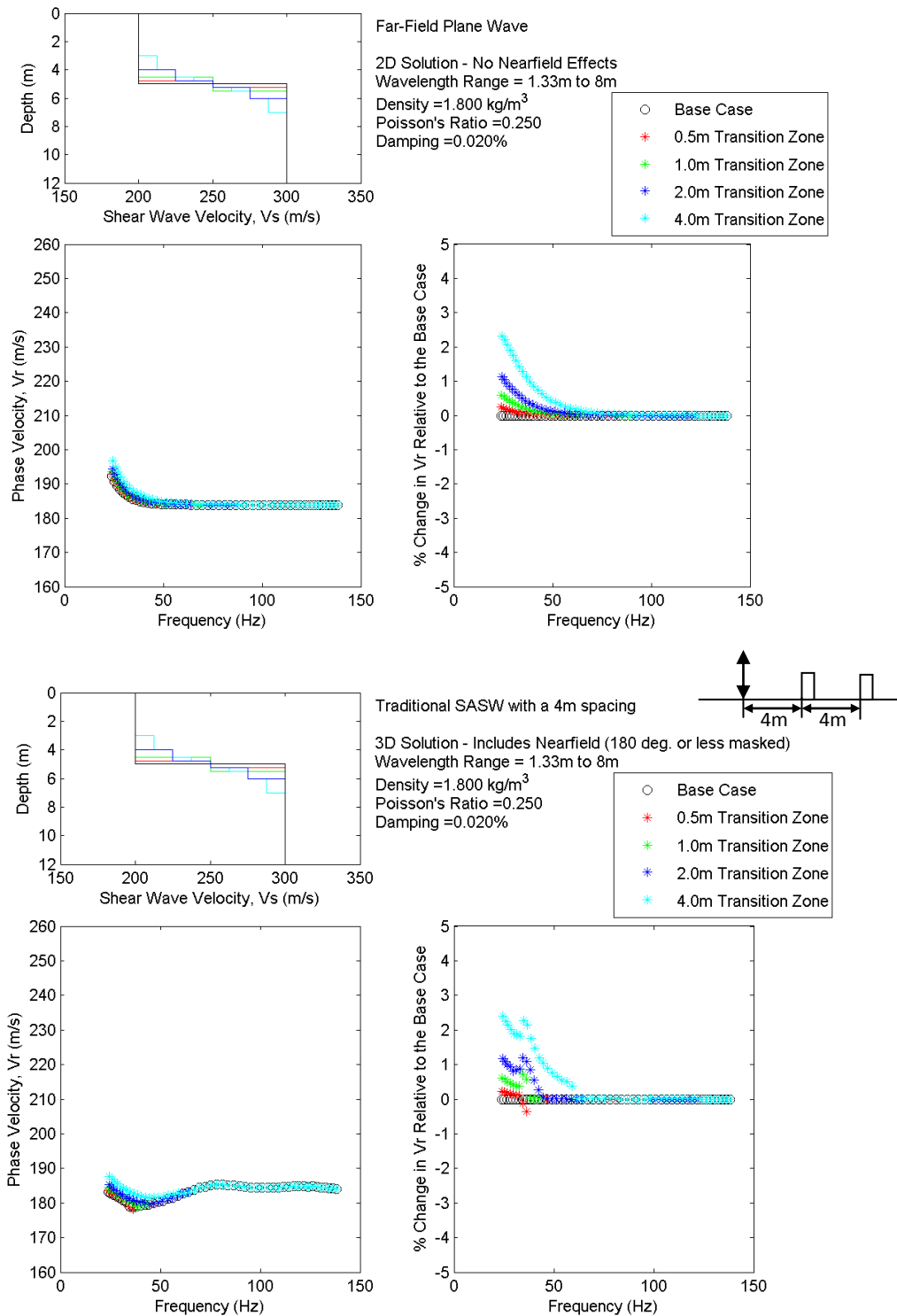


**Figure D.2** Sensitivity study results for a “soft-over-stiff” profile with a variable layer transition gradient, comparing results from the 2D solution (at top) and 3D solution (at bottom) for a wavelength range of 4/3m to 8m.

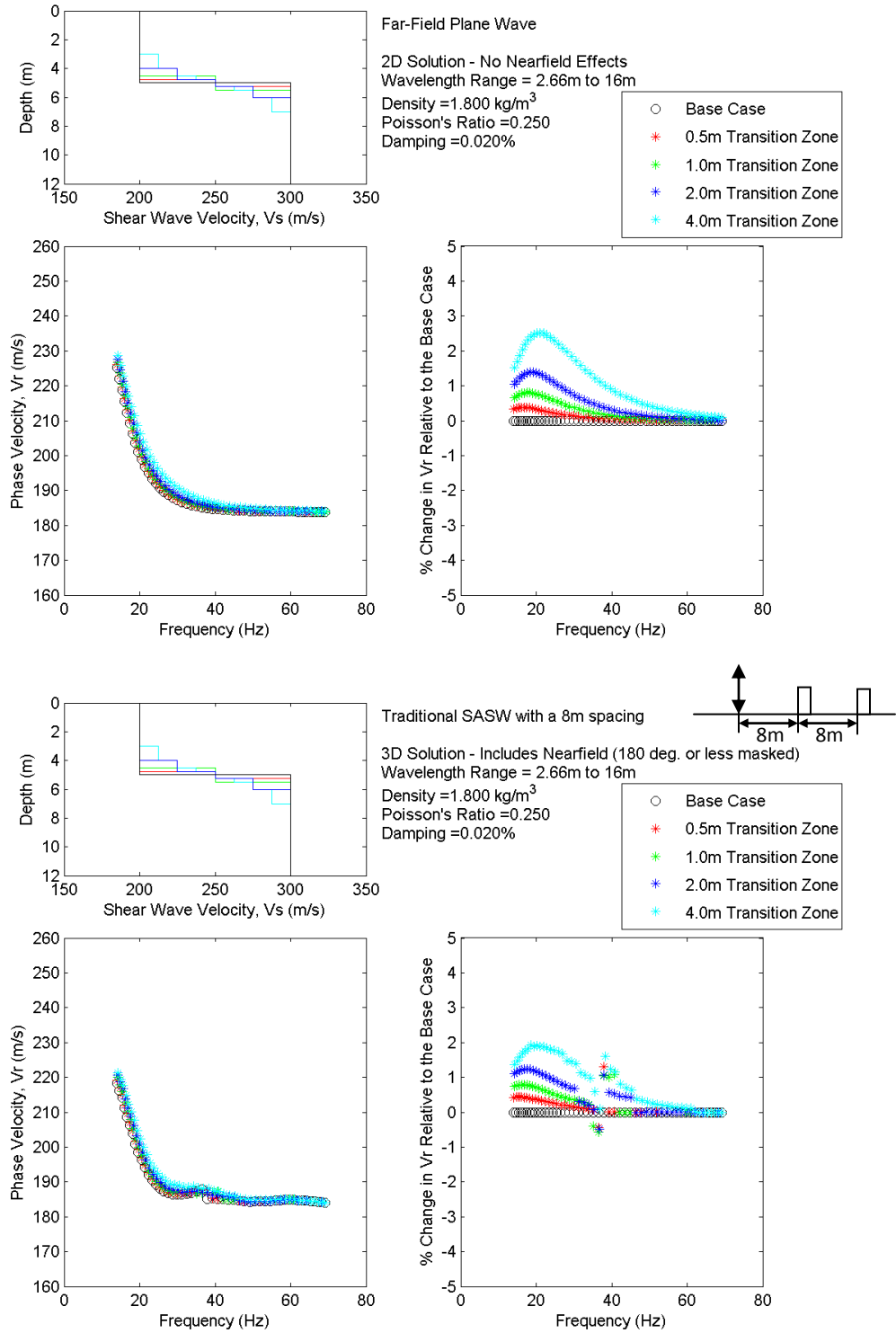


**Figure D.3** Sensitivity study results for a “soft-over-stiff” profile with a variable layer transition gradient, comparing results from the 2D solution (at top) and 3D solution (at bottom) for a wavelength range of 8/3m to 16m.

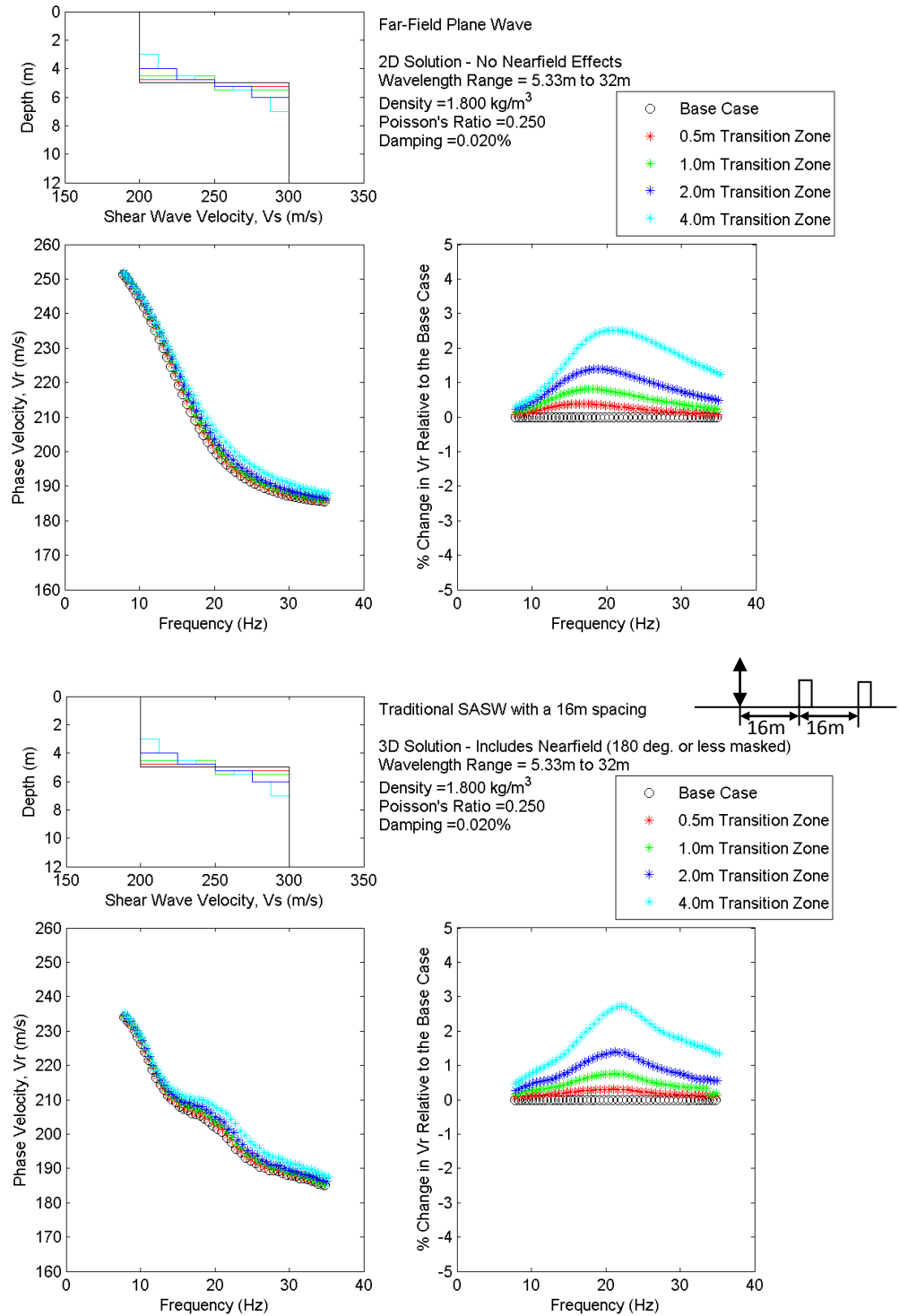


**Figure D.4** Sensitivity study results for a “soft-over-stiff” profile with a variable layer transition gradient, comparing results from the 2D solution (at top) and 3D solution (at bottom) for a wavelength range of 16/3m to 32m.

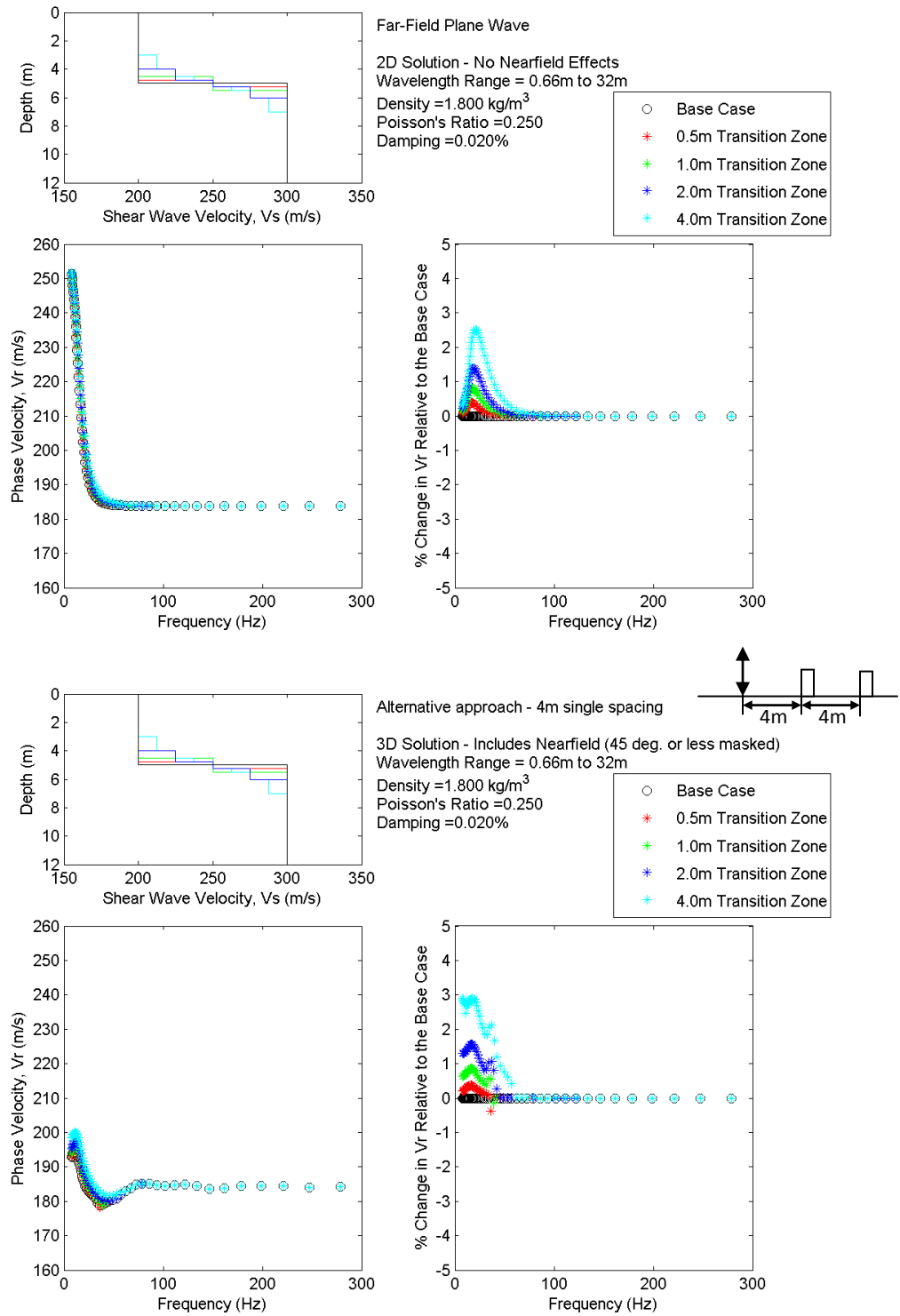


**Figure D.5** Sensitivity study results for a “soft-over-stiff” profile with a variable layer transition gradient, comparing results from the 2D solution (at top) and 3D solution (at bottom) for a wavelength range of 1/3m to 32m.

### E. Variations in Poisson's Ratio for a Uniform Profile

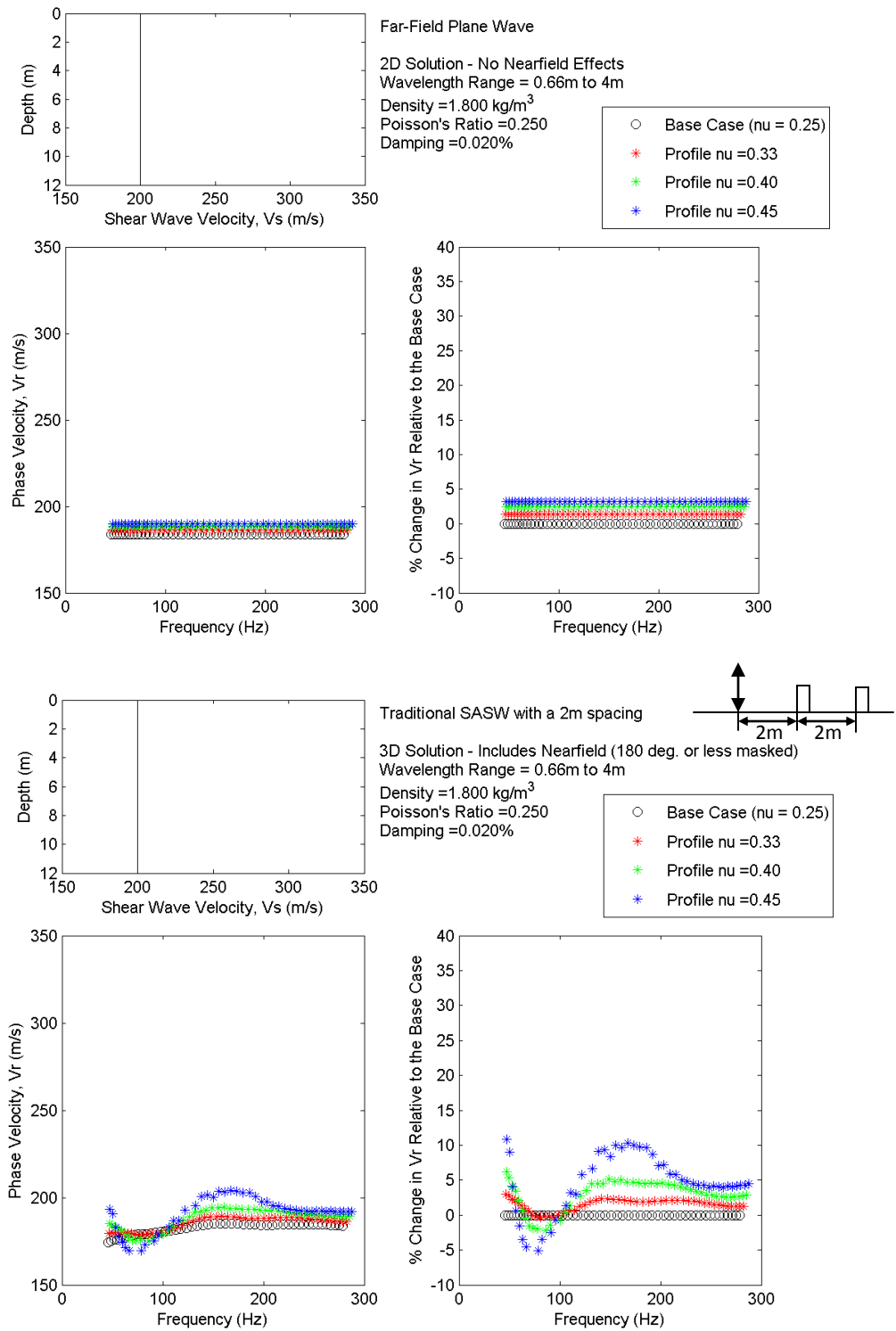


**Figure E.1** Sensitivity study results for a uniform  $V_S$  profile with a variable Poisson's ratio, comparing results from the 2D solution (at top) and 3D solution (at bottom) for a wavelength range of 1/3m to 4m.

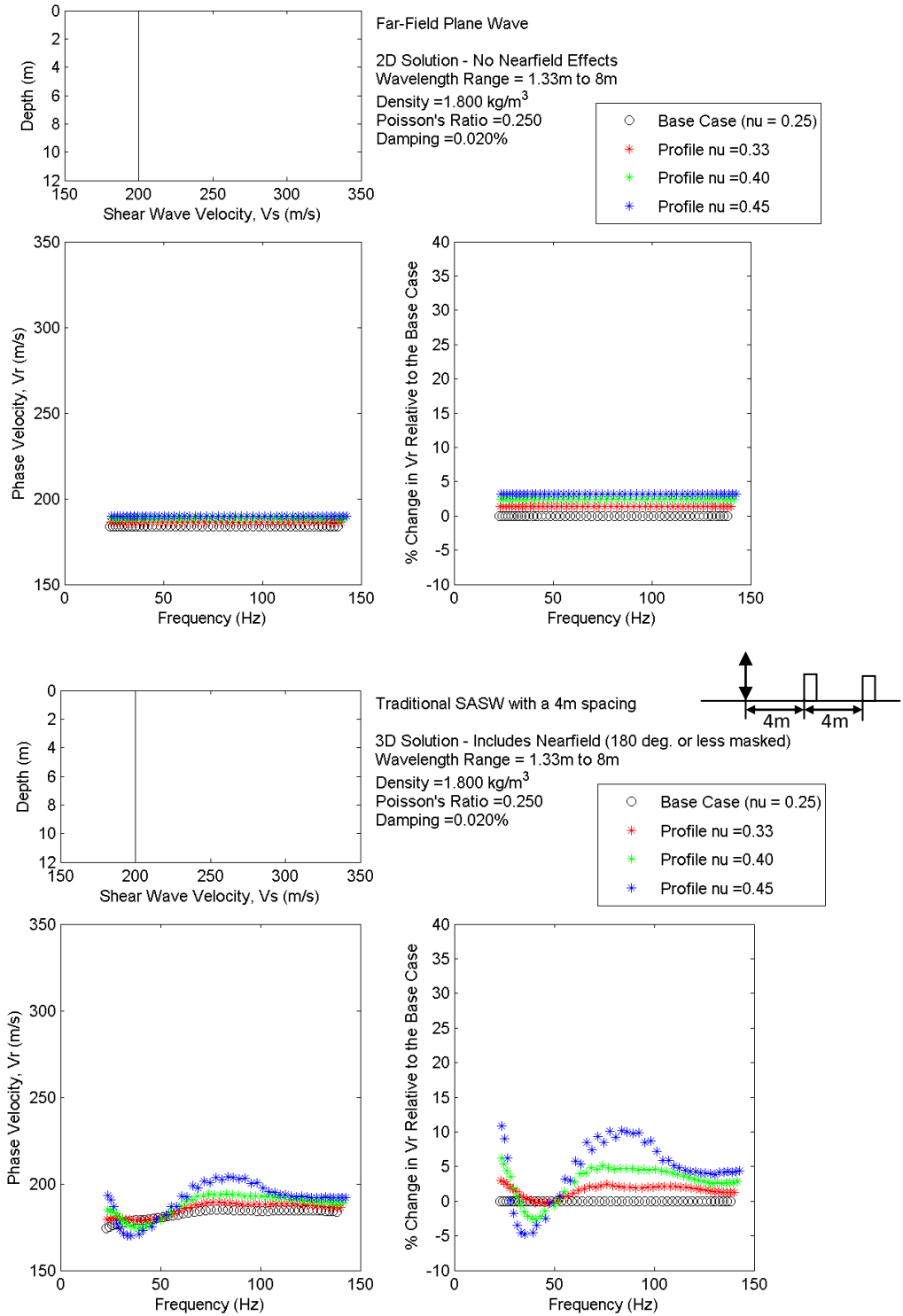


**Figure E.2** Sensitivity study results for a uniform  $V_s$  profile with a variable Poisson's ratio, comparing results from the 2D solution (at top) and 3D solution (at bottom) for a wavelength range of 4/3m to 8m.

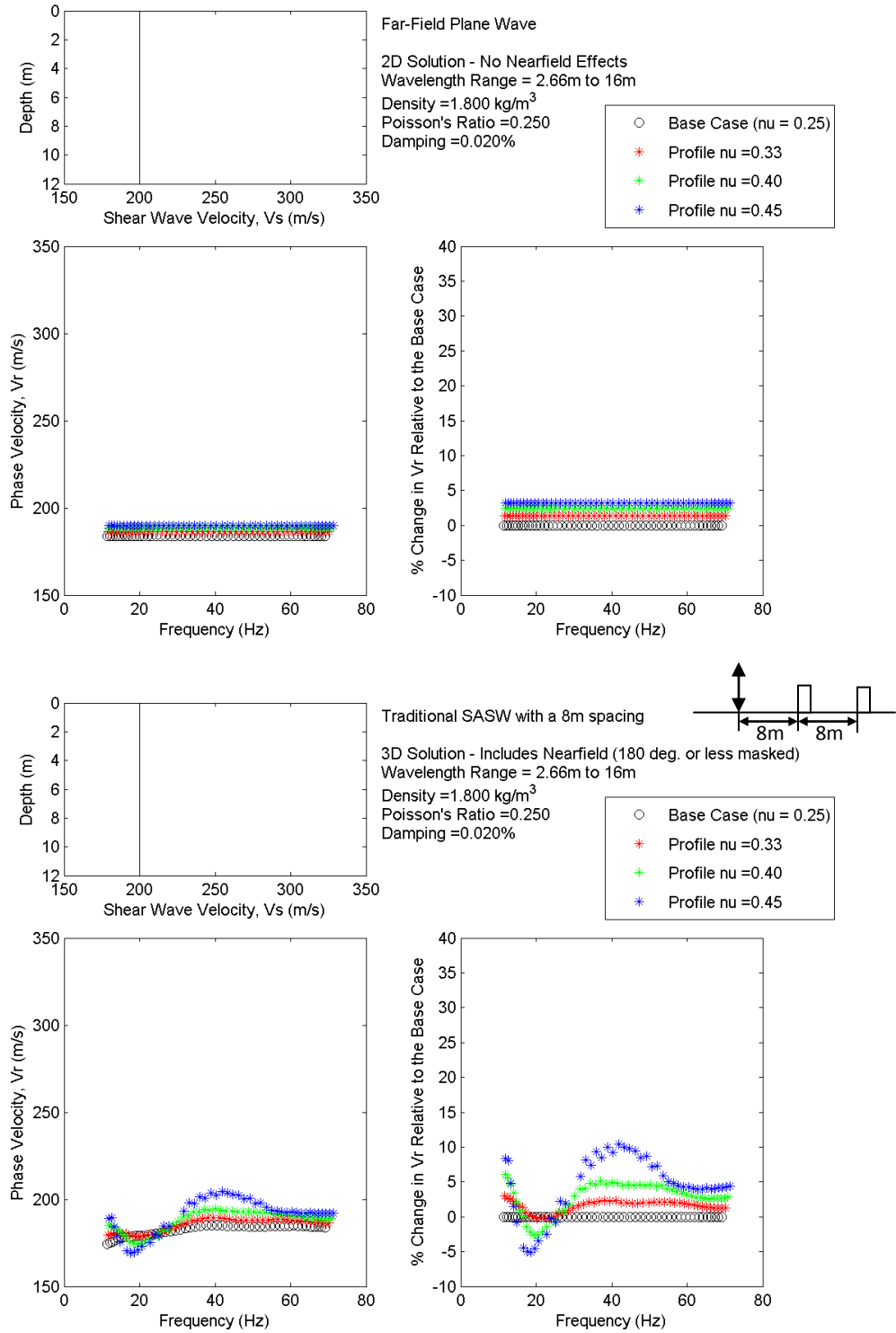


**Figure E.3** Sensitivity study results for a uniform  $V_s$  profile with a variable Poisson's ratio, comparing results from the 2D solution (at top) and 3D solution (at bottom) for a wavelength range of 8/3m to 16m.

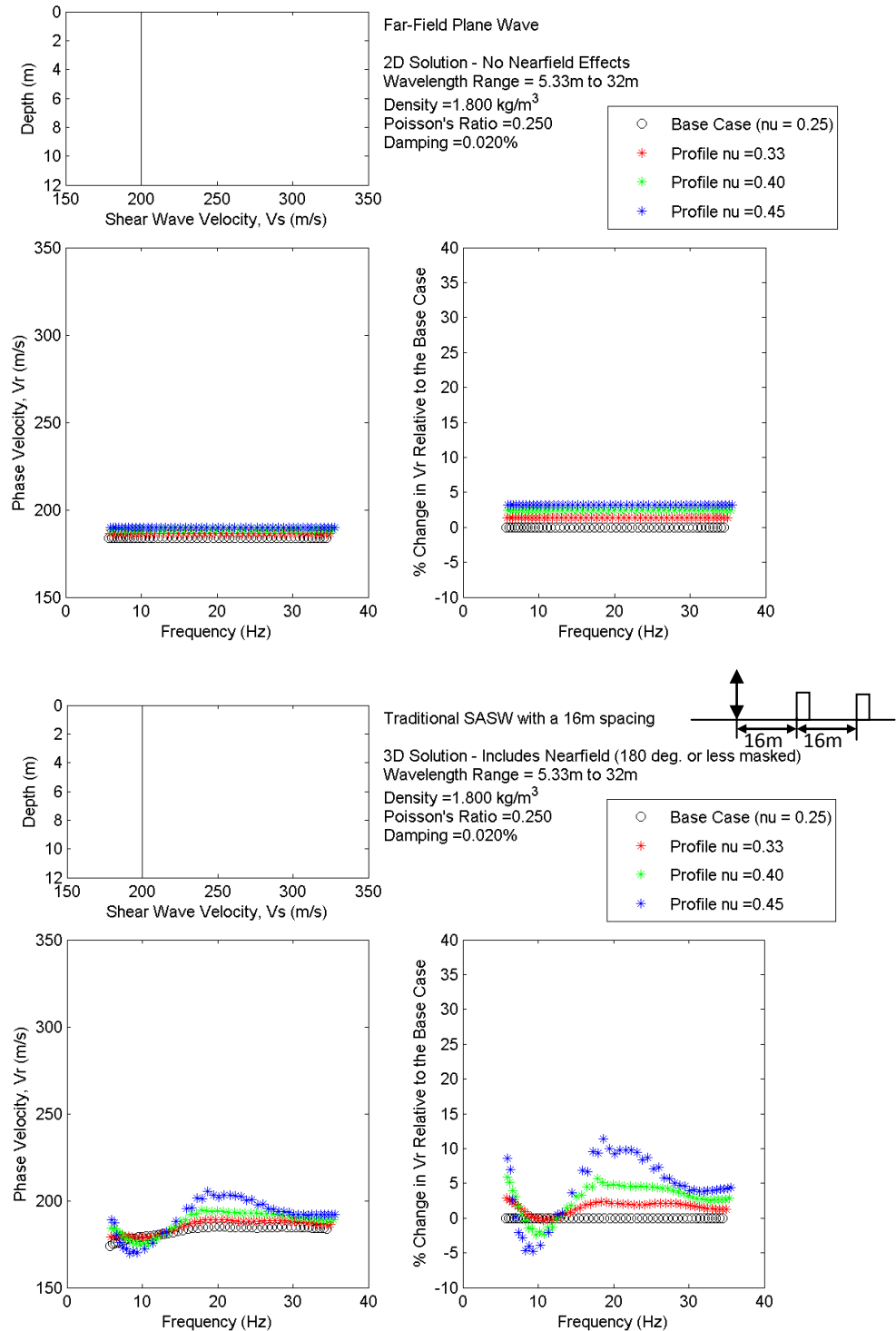


**Figure E.4** Sensitivity study results for a uniform  $V_s$  profile with a variable Poisson's ratio, comparing results from the 2D solution (at top) and 3D solution (at bottom) for a wavelength range of 16/3m to 32m.

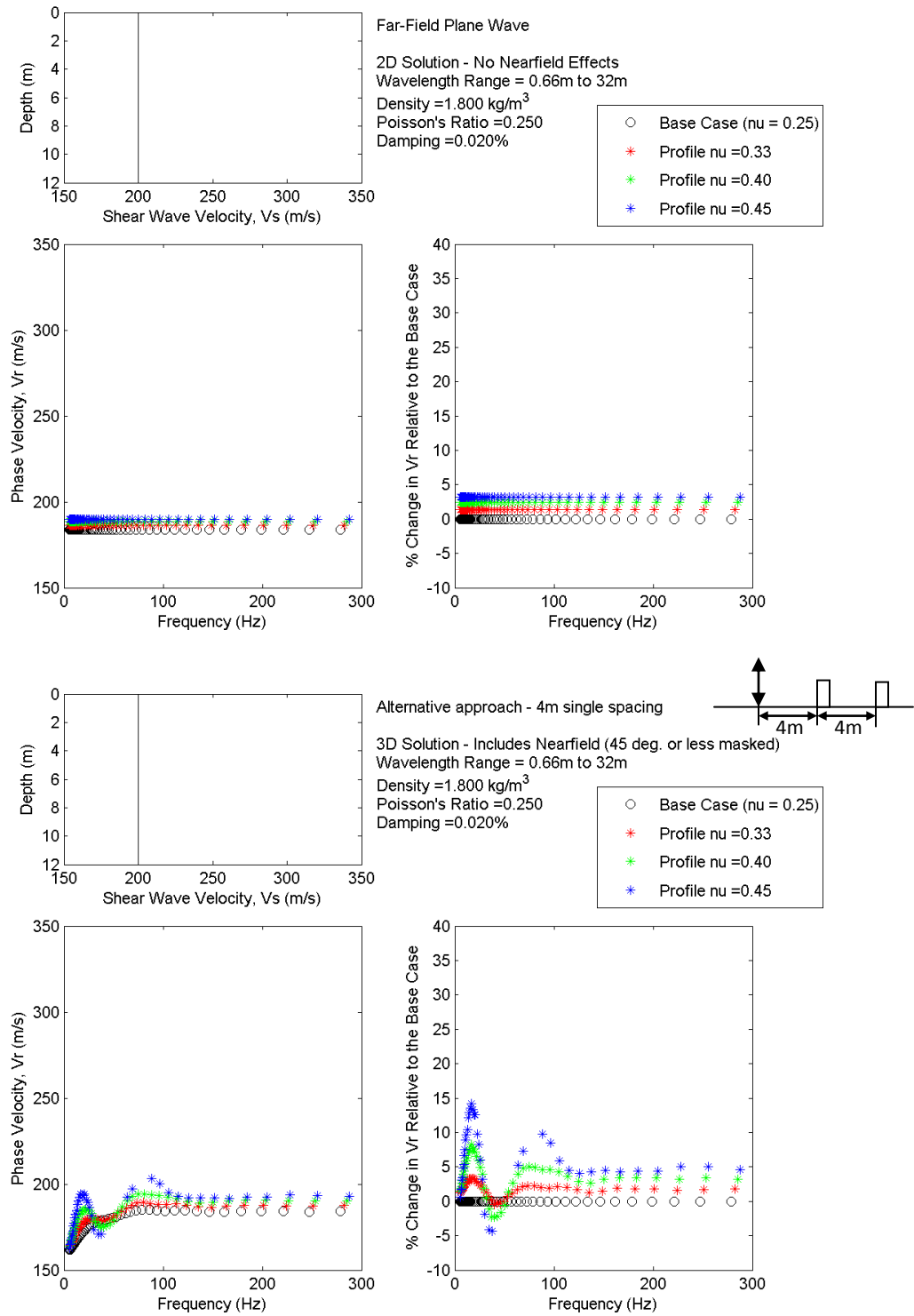


**Figure E.5** Sensitivity study results for a uniform  $V_s$  profile with a variable Poisson's ratio, comparing results from the 2D solution (at top) and 3D solution (at bottom) for a wavelength range of 1/3m to 32m.

### F. Variations in Poisson’s Ratio for a “Soft-Over-Stiff” Profile

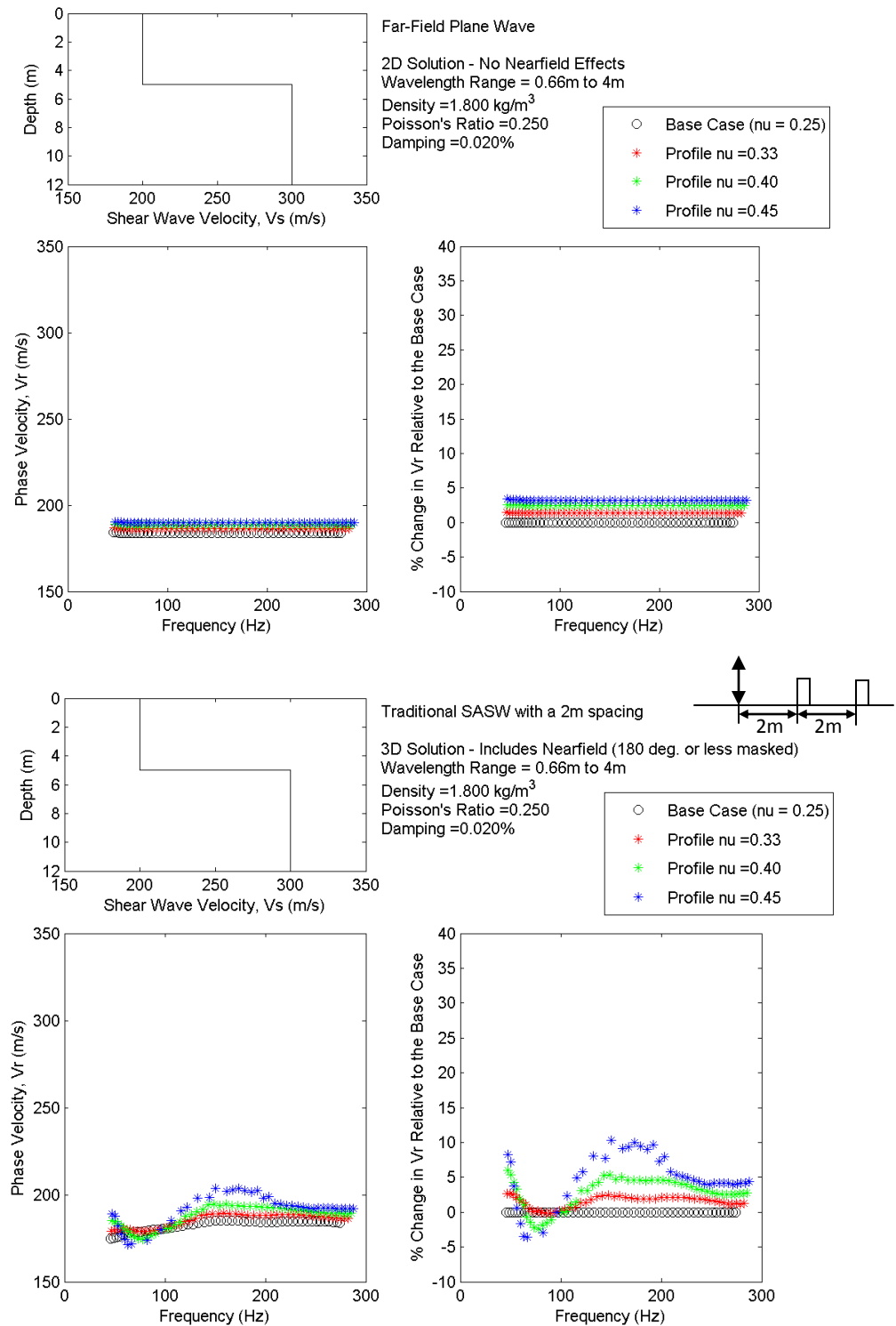


**Figure F.1** Sensitivity study results for a “soft-over-stiff” profile with a variable Poisson’s ratio, comparing results from the 2D solution (at top) and 3D solution (at bottom) for a wavelength range of 1/3m to 4m.

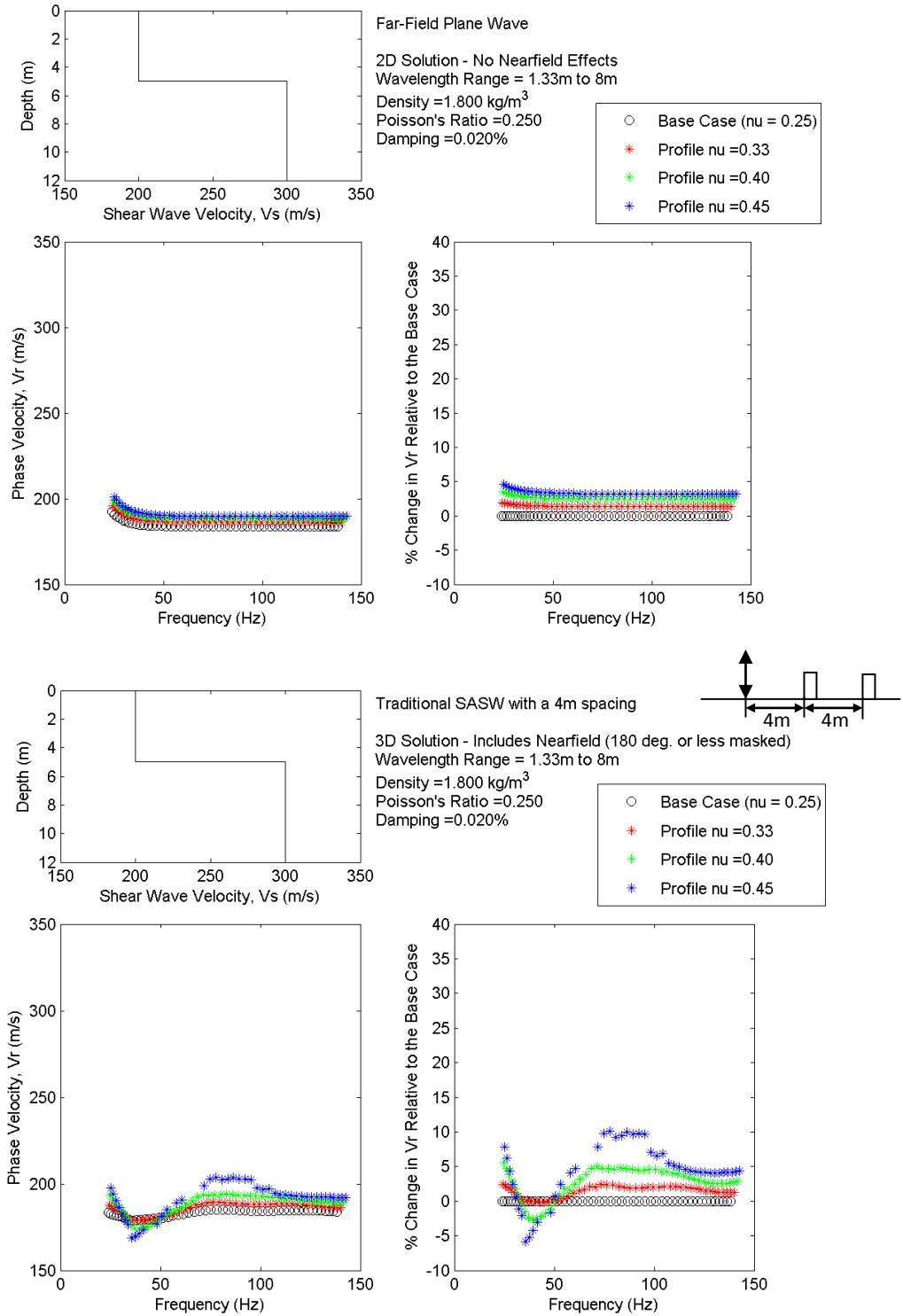


**Figure F.2** Sensitivity study results for a “soft-over-stiff” profile with a variable Poisson’s ratio, comparing results from the 2D solution (at top) and 3D solution (at bottom) for a wavelength range of 4/3m to 8m.

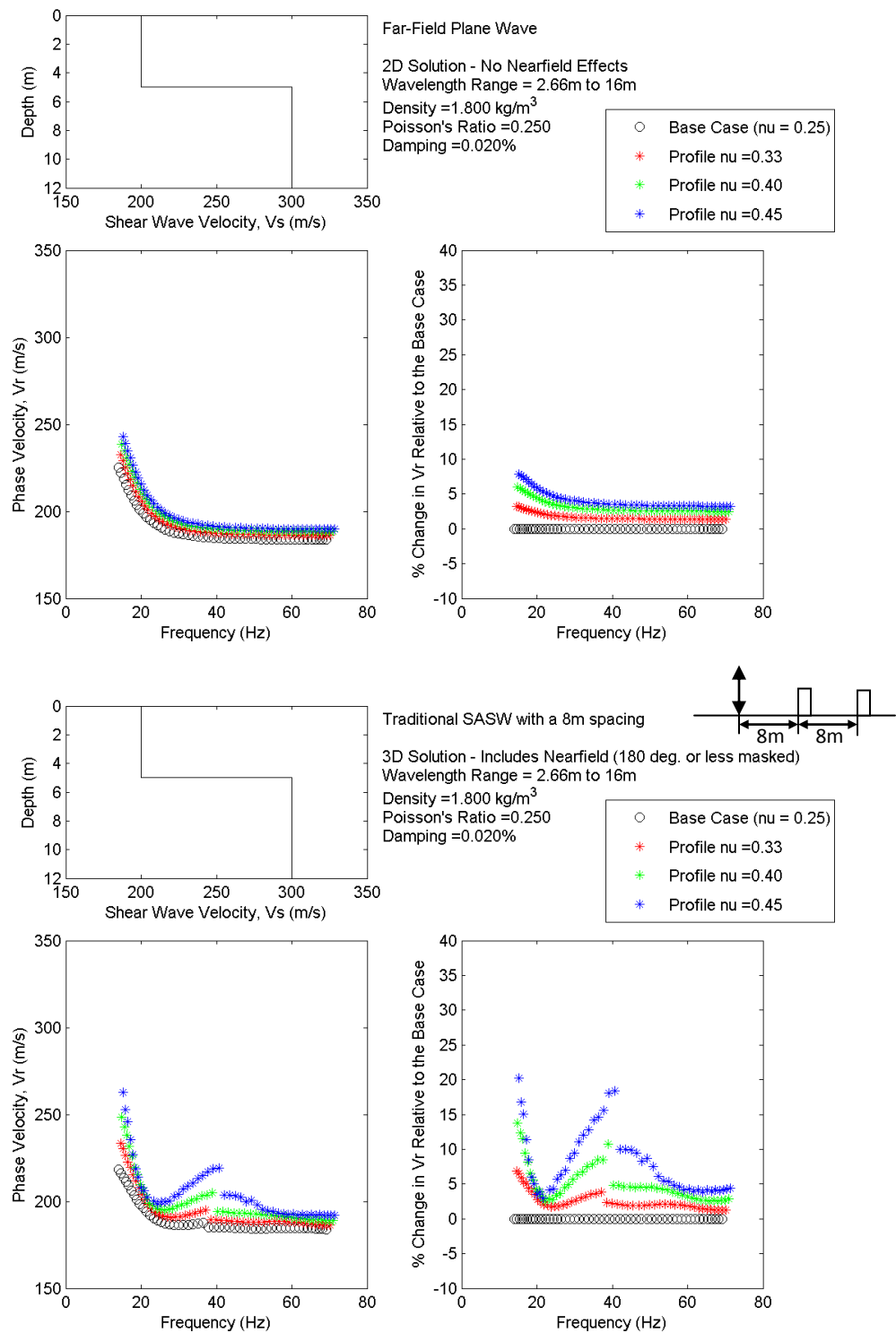


**Figure F.3** Sensitivity study results for a “soft-over-stiff” profile with a variable Poisson’s ratio, comparing results from the 2D solution (at top) and 3D solution (at bottom) for a wavelength range of 8/3m to 16m.

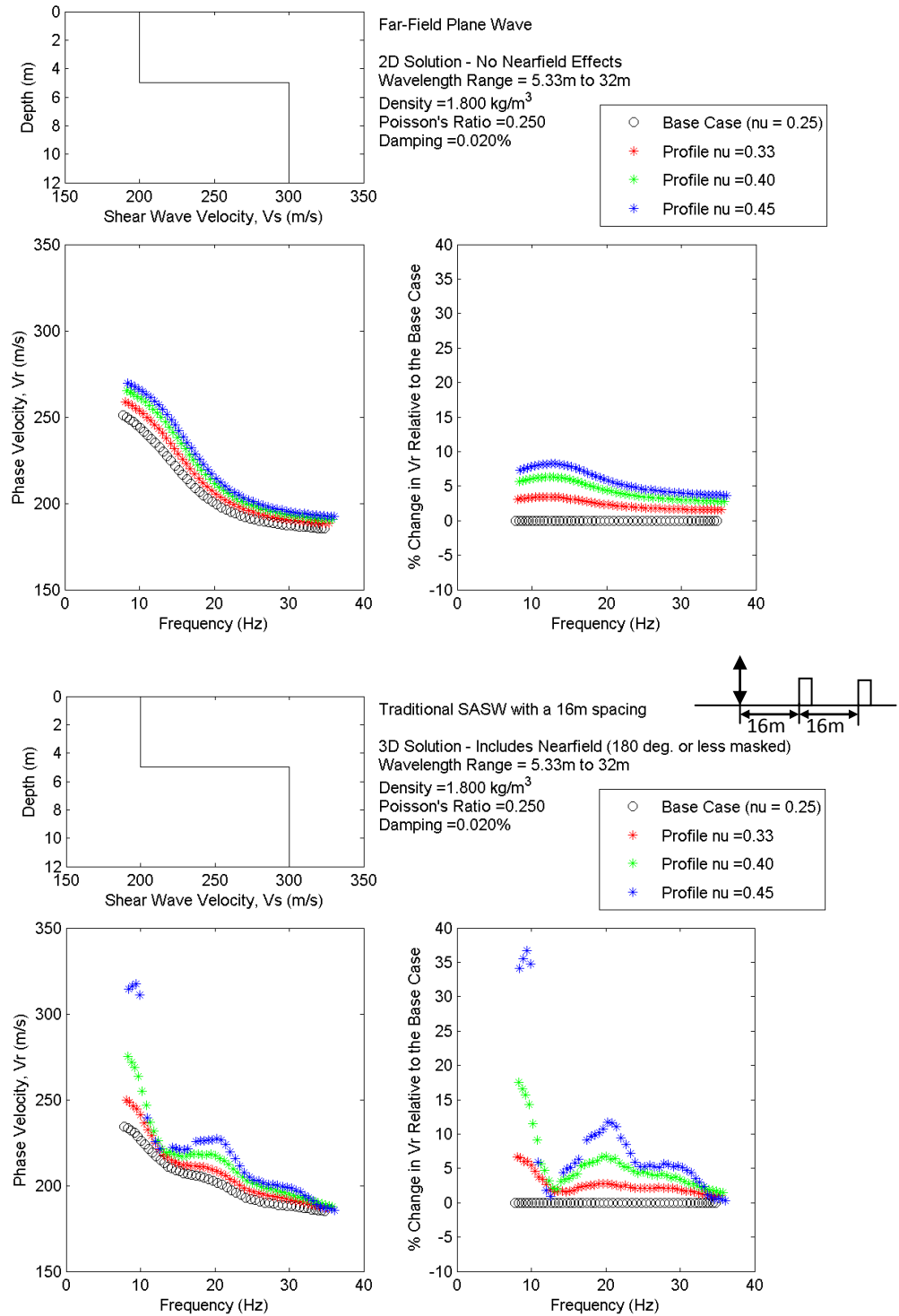


**Figure F.4** Sensitivity study results for a “soft-over-stiff” profile with a variable Poisson’s ratio, comparing results from the 2D solution (at top) and 3D solution (at bottom) for a wavelength range of 16/3m to 32m.

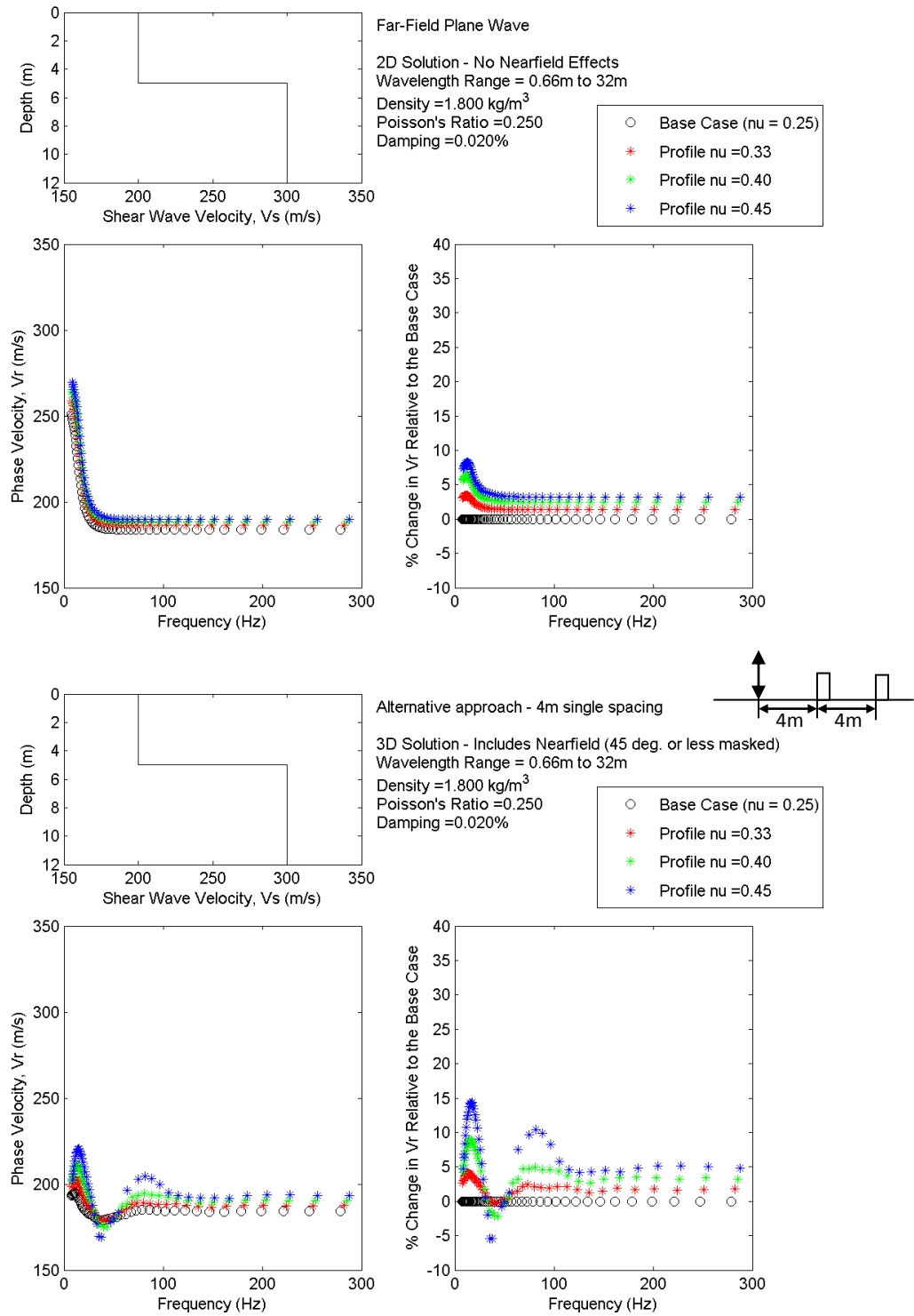


**Figure F.5** Sensitivity study results for a “soft-over-stiff” profile with a variable Poisson’s ratio, comparing results from the 2D solution (at top) and 3D solution (at bottom) for a wavelength range of 1/3m to 32m.

### G. Variations in Poisson's Ratio for a Linear Profile

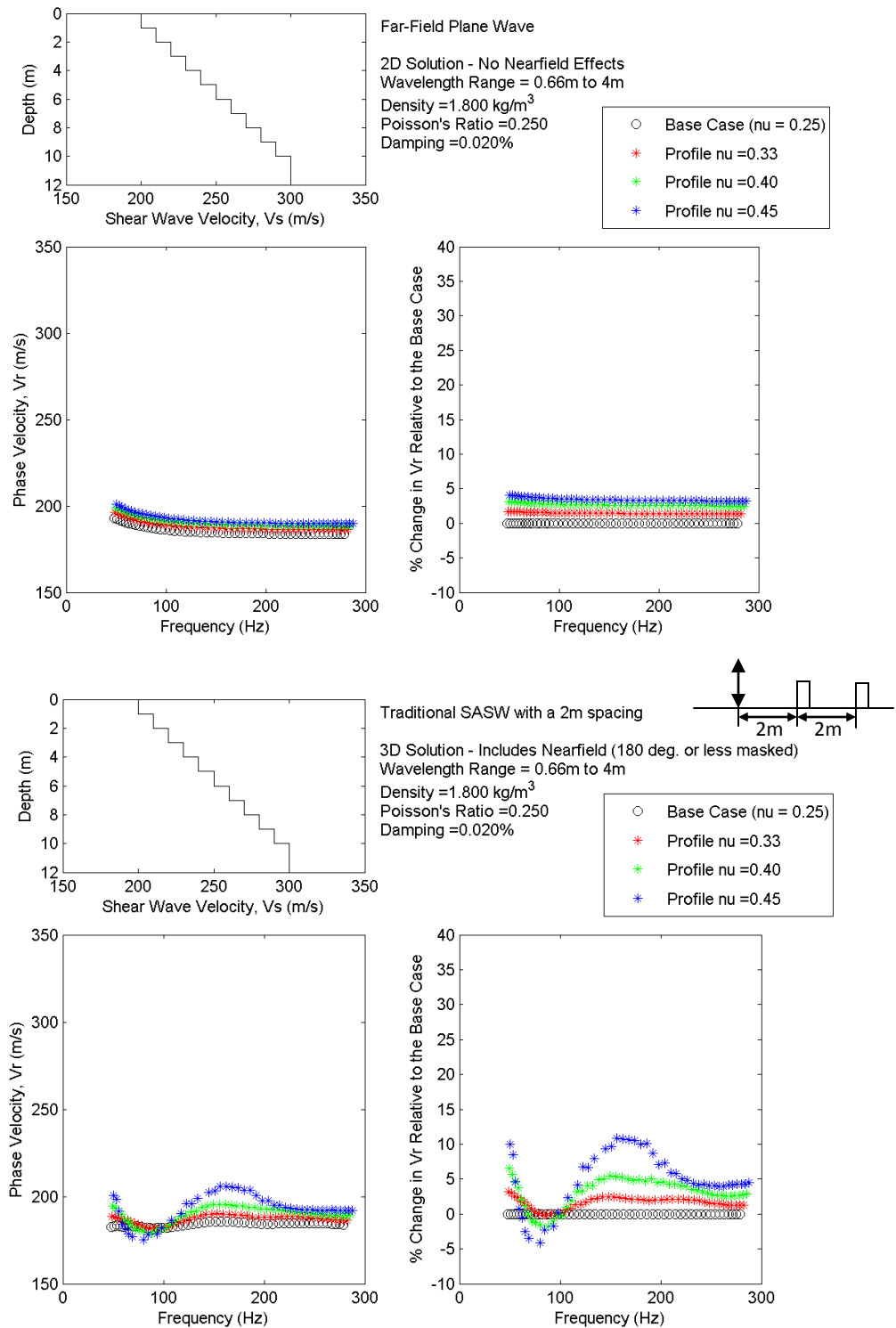


**Figure G.1** Sensitivity study results for a linear  $V_s$  profile with a variable Poisson's ratio, comparing results from the 2D solution (at top) and 3D solution (at bottom) for a wavelength range of 1/3m to 4m.

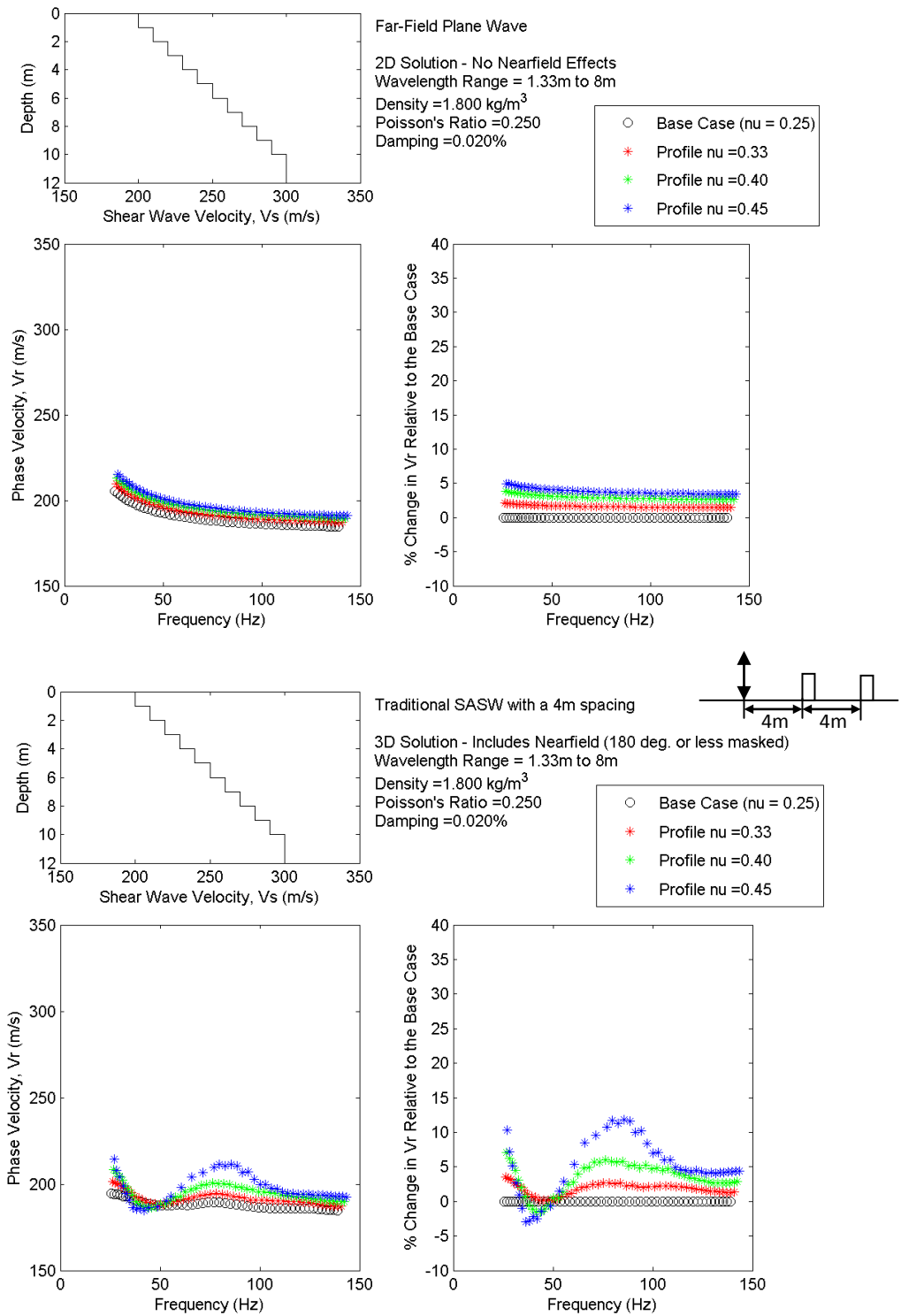


**Figure G.2** Sensitivity study results for a linear  $V_s$  profile with a variable Poisson's ratio, comparing results from the 2D solution (at top) and 3D solution (at bottom) for a wavelength range of 4/3m to 8m.

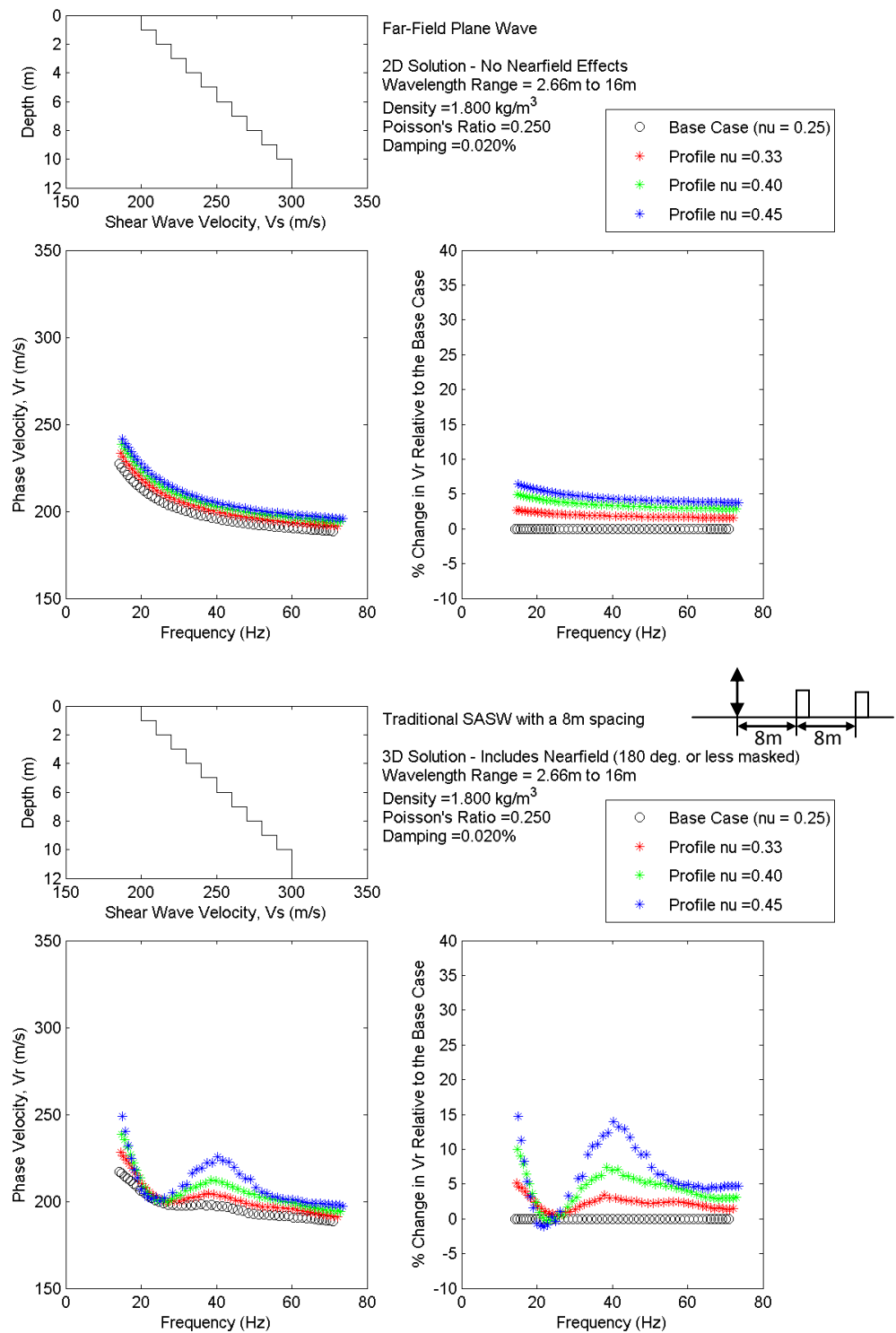


**Figure G.3** Sensitivity study results for a linear  $V_s$  profile with a variable Poisson's ratio, comparing results from the 2D solution (at top) and 3D solution (at bottom) for a wavelength range of 8/3m to 16m.

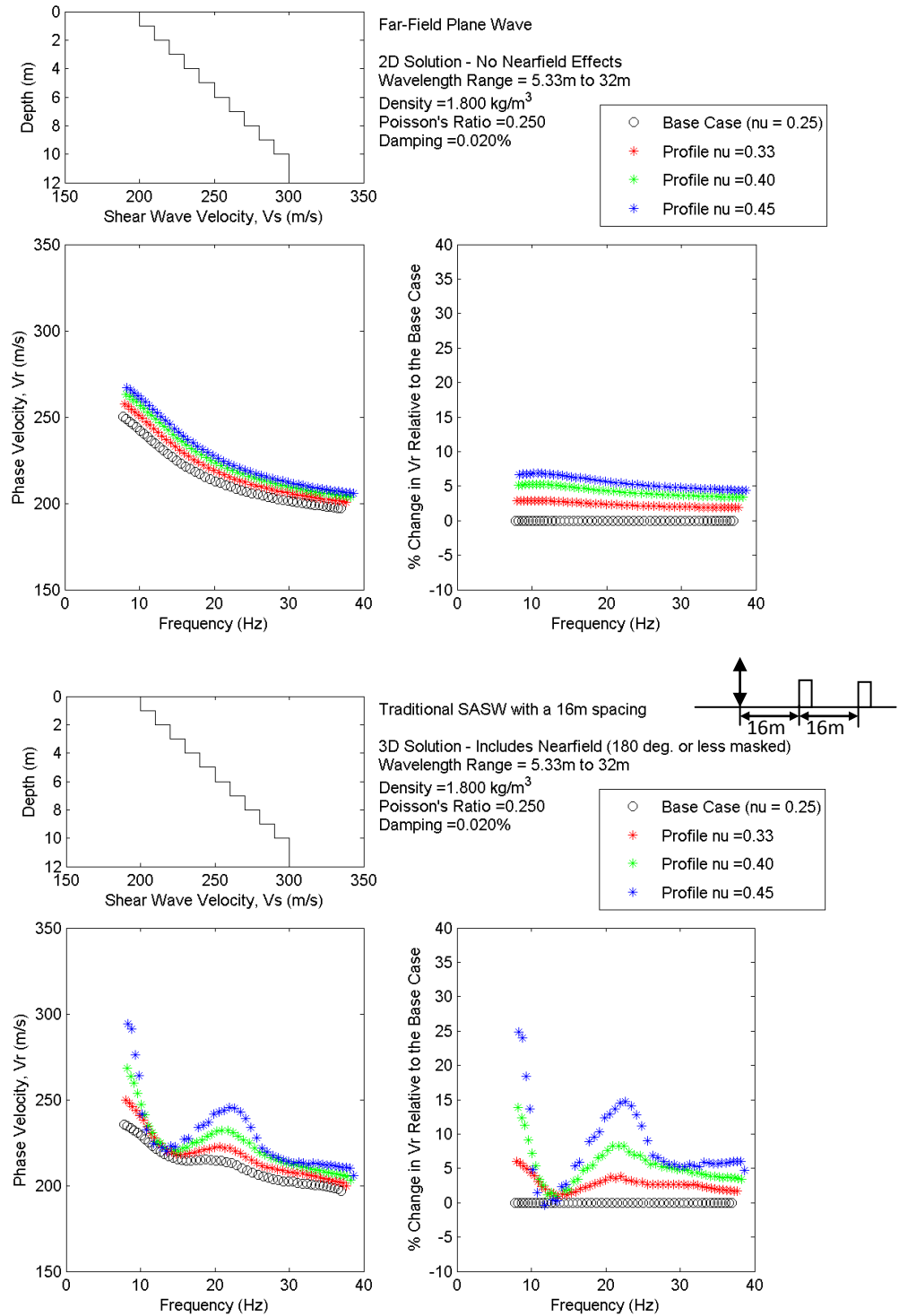


**Figure G.4** Sensitivity study results for a linear  $V_s$  profile with a variable Poisson's ratio, comparing results from the 2D solution (at top) and 3D solution (at bottom) for a wavelength range of 16/3m to 32m.

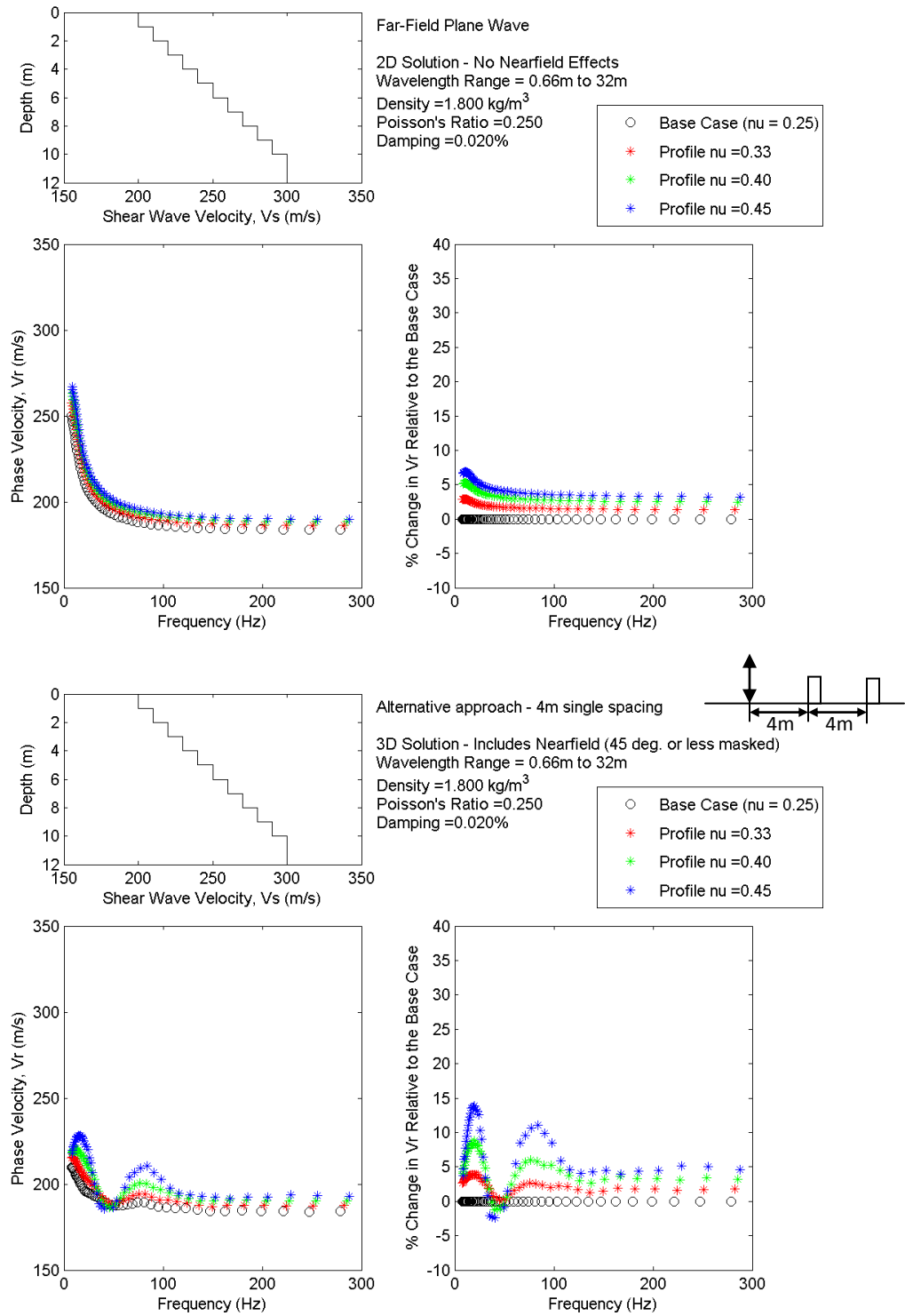


**Figure G.5** Sensitivity study results for a linear  $V_s$  profile with a variable Poisson's ratio, comparing results from the 2D solution (at top) and 3D solution (at bottom) for a wavelength range of 1/3m to 32m.

## REFERENCES

- Al-Hunaidi, M. O. (1993). "Insights on SASW nondestructive testing method." *Canadian Journal of Civil Engineering*, 20(6), 940-950.
- Avar, B. B., and Luke, B. A. (1999). "Roadside application of seismic surface waves over abandoned mines." *Proceedings of the Symposium on the Application of Geophysics to Environmental and Engineering Problems (SAGEEP)*, 1999, 31-40.
- Bailey, J. P. (2008). "DEVELOPMENT OF SHEAR WAVE VELOCITY PROFILES IN THE DEEP SEDIMENTS OF THE MISSISSIPPI EMBAYMENT USING SURFACE WAVE AND SPECTRAL RATIO METHODS." Master's Thesis, University of Missouri - Columbia, Columbia, MO.
- Bodet, L., Abraham, O., and Clorennec, D. (2009). "Near-offset effects on Rayleigh-wave dispersion measurements: Physical modeling." *Journal of Applied Geophysics*, 68(1), 95-103.
- Chen, L., Zhu, J., Yan, X., and Song, C. (2004). "On arrangement of source and receivers in SASW testing." *Soil Dynamics and Earthquake Engineering*, 24(5), 389-396.
- Ewing, W. M., Jardetzky, W. S., and Press, F. (1957). *Elastic Waves in Layered Media*, McGraw-Hill Book Co., New York.
- Exploratorium (2014). "Faultline: Seismic Science at the Epicenter." *Exploratorium: The Museum of Science, Art and Human Perception*, <<http://www.exploratorium.edu/faultline/basics/waves.html>>. (April 28, 2014).
- Gucunski, N., and Woods, R. D. (1992). "Numerical simulation of the SASW test." *Soil Dynamics & Earthquake Engineering*, 11(4), 213-227.
- Haskell, N. A. (1953). "The Dispersion of Surface Waves on Multilayered Media." *Bull. Seimol. Soc. Am.*, 43, 17-34.
- Heisey, J. S., Stokoe, K. H., and Meyer, A. H. (1982). "Moduli of Pavement Systems from Spectral Analysis of Surface Waves." *Transportation Research Record*(853).
- Hiltunen, D. R., and Woods, R. D. (1990). "Variables affecting the testing of pavement by the surface wave method." *Transportation Research Record*, 1260, 42-52.
- Ivanov, J., Miller, R. D., Peterie, S., and Dunbar, J. B. (2010). "Practical focusing of surface-wave inversion to image levees in southern New Mexico." *Proceedings of SAGEEP*, 2010, 97-102.
- Ivanov, J., Park, C. B., Miller, R. D., and Xia, J. (2000). "Mapping Poisson's ratio of unconsolidated materials from a joint analysis of surface-wave and refraction events." *Proceedings of the Symposium on the Application of Geophysics to Environmental and Engineering Problems (SAGEEP)*, 2000, 11-19.
- Joh, S.-h. (1996). "Advances in the Data Interpretation Technique for Spectral-Analysis-of-Surface-Waves (SASW) Measurement." Doctor of Philosophy, University of Texas at Austin, Austin, TX.
- Johnson, D. H., and Dudgeon, D. E. (1993). *Array signal processing: concepts and techniques*, PTR Prentice-Hall, Inc., Upper Saddle River, NJ.
- Karray, M., and Lefebvre, G. (2008). "Significance and evaluation of Poisson's ratio in Rayleigh wave testing." *Canadian Geotechnical Journal = Revue Canadienne de Geotechnique*, 45(5), 624-635.
- Kausel, E., and Peek, R. (1982). "Dynamic loads in the interior of a layered stratum: an explicit solution." *Bull. Seimol. Soc. Am.*, 71, 1743-1761.

- Kausel, E., and Roesset, J. M. (1981). "Stiffness matrices for layered soils." *Bull. Seimol. Soc. Am.*, 71(6), 1743-1761.
- Kavazanjian, E., Jr., Matasovic, N., Stokoe, K. H., and Bray, J. D. "In situ shear wave velocity of solid waste from surface wave measurements." *Proc., Environmental geotechnics*, A.A. Balkema, Rotterdam, Netherlands, 97-102.
- Lamb, H. (1904). "On the propagation of Tremors over the Surface of an Elastic Solid." *Philosophical Transactions of the Royal Society*, Ser. A, Vol. 203, pp. 1-42.
- Li, C.-H. (2011). "Influence of Site Conditions on Near-field Effects in Multi-Channel Surface Wave Measurements." Master of Science, University of Missouri, Columbia, MO.
- Li, J.-H. (2008). "STUDY OF SURFACE WAVE METHODS FOR DEEP SHEAR WAVE VELOCITY PROFILING APPLIED IN THE UPPER MISSISSIPPI EMBAYMENT." Ph.D Dissertation, University of Missouri-Columbia, Columbia, MO.
- Li, J., and Rosenblad, B. (2011). "Experimental study of near-field effects in multichannel array-based surface wave velocity measurements." *Near Surface Geophysics*, 9(4), 357-366.
- Lin, C.-P., Chang, C.-C., and Chang, T.-S. (2004). "The use of MASW method in the assessment of soil liquefaction potential." *Soil Dynamics and Earthquake Engineering (1984)*, 24(9-10), 689-698.
- Love, A. E. H. (1911). *Some problems of geodynamics; an essay to which the Adams Prize in the University of Cambridge was adjudged in 1911*, Cambridge University Press, Cambridge, England.
- Menke, W. (1984). *Geophysical Data Analysis: Discrete Inverse Theory*, Academic Press, New York.
- Mera, R. F. (1991). "Analytical Study and Inversion for the Spectral Analysis of Surface Waves Method." Thesis, The University of Texas at Austin.
- Mera, R. F. (1995). "Dynamic Nondestructive Testing of Pavements." Doctor of Philosophy, University of Texas at Austin, Austin, TX.
- Nazarian, S., Stokoe, K. H., Briggs, R. C., and Rogers, R. (1988). "Determination of pavement layer thicknesses and moduli by SASW method." *Transportation Research Record*(1196), 133-150.
- Oh, Y., Jeong, H., Lee, Y., and Shon, H. (2003). "Safety evaluation of rock-fill dam by seismic (MASW) and resistivity methods." *Proceedings - Symposium on the Application of Geophysics to Engineering and Environmental Problems (SAGEEP)*, 2003, 1377-1386.
- Park, C. B., Ivanov, J., Miller, R. D., Xia, J., and Ryden, N. (2001). "Seismic investigation of pavements by MASW method; geophone approach." *Proceedings - Symposium on the Application of Geophysics to Engineering and Environmental Problems (SAGEEP)*, 2001.
- Park, C. B., Miller, R. D., and Xia, J. (1999). "Multichannel analysis of surface waves." *Geophysics*, 64(3), 800-808.
- Park, C. B., and Shawver, J. B. "MASW survey using multiple source offsets." *Proc., 22nd Symposium on the Application of Geophysics to Engineering and Environmental Problems 2009, SAGEEP 2009, March 29, 2009 - April 2, 2009*, J and N Group, Ltd., 15-19.
- Pelekis, P. C., and Athanasopoulos, G. A. (2011). "An overview of surface wave methods and a reliability study of a simplified inversion technique." *Soil Dynamics and Earthquake Engineering*, 31(12), 1654-1668.
- Phillips, C., Cascante, G., and Hutchinson, J. (2000). "Detection of underground voids with surface waves." *Proceedings of the Symposium on the Application of Geophysics to Environmental and Engineering Problems (SAGEEP)*, 2000, 29-37.

- Pulli, J. J., Krumhansl, P. J., and Bunks, C. (2000). "Modeling and field measurements of the seismic response of shallow unexploded ordnance." *Proceedings of the Symposium on the Application of Geophysics to Environmental and Engineering Problems (SAGEEP)*, 2000, 757-763.
- Rayleigh, L. (1885). "On wave propagated along the plane surface of an elastic solid." *London Mathematical Society Proc.*, 17, 4-11.
- Richart, F. E., Hall, J. R., and Woods, R. D. (1970). *Vibrations of Soils and Foundations*, Prentice-Hall, Englewood Cliffs, NJ.
- Roesset, J. M., Chang, D. W., and Stokoe, K. H. (1991). "Comparison of 2-D and 3-D models for analysis of surface wave tests." *Soil Dynamics and Earthquake Engineering*, 5, 111-126.
- Roesset, J. M., Chang, D. W., Stokoe, K. H., and Aouad, M. (1990). "Modulus and thickness of the pavement surface layer from SASW tests." *Transportation Research Record*, 1260, 53-63.
- Roesset, J. M., and Foinquinos, R. (1991). *User's guide to SASWFI, a program for forward modeling and inversion analysis for the surface waves*, The University of Texas at Austin, Austin, TX.
- Rosenblad, B., Bailey, J. P., Csontos, R., and Van Arsdale, R. (2010). "Shear wave velocities of Mississippi embayment soils from low frequency surface wave measurements." *Soil Dynamics and Earthquake Engineering*, 30(8), 691-701.
- Rosenblad, B. L., and Li, C.-H. "Influence of Poisson's ratio on surface wave near-field effects." *Proc., Geo-Frontiers 2011: Advances in Geotechnical Engineering, March 13, 2011 - March 16, 2011*, American Society of Civil Engineers (ASCE), 2554-2563.
- Ryden, N., and Mooney, M. A. "Surface wave testing to investigate the nature of roller determined soil stiffness." *Proc., 20th Symposium on the Application of Geophysics to Engineering and Environmental Problems: Geophysical Investigation and Problem Solving for the Next Generation, SAGEEP 2007, April 1, 2007 - April 5, 2007*, J and N Group, Ltd., 1261-1267.
- Sanchez-Salinerio, I., Roesset, J., Shao, K.-Y., Stokoe, K., and Rix, G. (1987). "ANALYTICAL EVALUATION OF VARIABLES AFFECTING SURFACE WAVE TESTING OF PAVEMENTS." *Transportation Research Record*(1136), 86-95.
- Smith, R. T., Tomeh, A. A., Alyateem, S., and Sartipi, K. "Applications of surface waves to enhance subsurface boring exploration in the delineation of undocumented landfill cells." *Proc., 25th Symposium on the Application of Geophysics to Engineering and Environmental Problems 2012, SAGEEP 2012, March 25, 2012 - March 29, 2012*, J and N Group, Ltd., 524-533.
- Stokoe, K. H., Cox, B. R., Lin, Y.-C., Jung, M. J., Menq, F.-Y., Bay, J. A., Rosenblad, B., and Wong, I. "Use of intermediate to large vibrators as surface wave sources to evaluate Vs profiles for earthquake studies." *Proc., 19th Symposium on the Application of Geophysics to Engineering and Environmental Problems: Geophysical Applications for Environmental and Engineering Hazards - Advances and Constraints, SAGEEP 2006, April 2, 2006 - April 6, 2006*, Environmental and Engineering Geophysical Society (EEGS), 1241-1258.
- Stokoe, K. H., and Nazarian, S. "USE OF RAYLEIGH WAVES IN LIQUEFACTION STUDIES." *Proc., Measurement and Use of Shear Wave Velocity for Evaluating Dynamic Soil Properties. Proceedings of a session held in conjunction with the ASCE Convention.*, ASCE, 1-17.
- Tarantola, A. (1987). *Inverse Problem Theory: Methods for Data Fitting and Model Parameter Estimation*, Elsevier, New York.
- Thompson, W. T. (1950). "Transmission of Elastic Waves through a Stratified Solid Medium." *Journal of Applied Physics*, 21(2), 89-93.

- Woods, R. D., and Stokoe, K. H. "SHALLOW SEISMIC EXPLORATION IN SOIL DYNAMICS." *Proc., Richart Commemorative Lectures. Proceedings of a session held in conjunction with the ASCE Convention.*, ASCE, 120-156.
- Xia, J., Xu, Y., Luo, Y., Miller, R. D., Cakir, R., and Zeng, C. (2012). "Advantages of Using Multichannel Analysis of Love Waves (MALW) to Estimate Near-Surface Shear-Wave Velocity." *Surveys in Geophysics*, 33(5), 841-860.
- Xu, Y., Xia, J., and Miller, R. D. (2006). "Quantitative estimation of minimum offset for multichannel surface-wave survey with actively exciting source." *Journal of Applied Geophysics*, 59(2), 117-125.
- Yoon, S. (2005). "Array-based measurements of surface wave dispersion and attenuation using frequency-wavenumber analysis." Ph.D. dissertation, Georgia Institute of Technology.
- Yoon, S., and Rix, G. J. (2009). "Near-Field Effects on Array-Based Surface Wave Methods with Active Sources." *Journal of Geotechnical and Geoenvironmental Engineering*, 135(3), 399-406.
- Zywicki, D. J., and Rix, G. J. (2005). "Mitigation of near-field effects for seismic surface wave velocity estimation with cylindrical beamformers." *Journal of Geotechnical and Geoenvironmental Engineering*, 131(8), 970-977.

**VITA**

Alexander T. McCaskill, the son of Stuart and Patricia McCaskill, was born in Beaver Dam, WI on August 25, 1987. Growing up in Kansas City, MO, he graduated from Oak Park High School in 2006 and proceeded to attend local Maple Woods Community College, where he obtained both an Associate in Arts (General Studies) degree and an Associate in Engineering degree. He then transferred to the University of Missouri – Kansas City to complete his undergraduate studies and later (May 2012) graduated Cum Laude with a Bachelor of Science in Civil Engineering (BSCE) degree. From December 2009 to August 2012, Alexander was employed as an engineering intern/technician with The Judy Company, a geotechnical specialty contractor. In August 2012, he entered the geotechnical engineering program at the University of Missouri – Columbia to pursue a Master of Science (MS) degree. In July 2014, he was employed as a full-time engineer with the Chicago office of GRL Engineers, Inc., a deep foundations testing and analysis firm.

Forwarding address:     Alexander McCaskill  
                                  155 W. Wayne Pl.  
                                  Wheeling, IL 60090